Jet Shapes in Charm Photoproduction at HERA

Dissertation
zur Erlangung des Doktorgrades
des Fachbereichs Physik
der Universität Hamburg

vorgelegt von

MÁRIA MARTIŠÍKOVÁ
aus Bratislava

Hamburg
2005

Gutachterin und Gutachter der Dissertation:	Prof. Dr. B. Naroska Prof. Dr. P. Schleper
Gutachterin und Gutachter der Disputation:	Prof. Dr. B. Naroska Dr. H. Jung
Datum der Disputation:	15.12.2005
Vorsitzender des Prüfungsausschusses:	Dr. H. D. Rüter
Vorsitzender des Promotionsausschusses und Dekan des Fahchbereichs Physik:	Prof. Dr. G. Huber

Mojim rodičom

Abstract

The aim of this study is the investigation of charm production in positron-proton collisions at a centre-of-mass energy of 318 GeV in the kinematic regime of photoproduction. Dijet events are analysed, which were collected with the H1 experiment in the years 1999-2000 and correspond to an integrated luminosity of 48 pb^{-1}. Events are selected by requiring two jets with transverse momentum of the jet larger than 7 and 6 GeV in the central rapidity range. One jet is tagged by a muon to be initiated by a charm quark. In order to shed light on the production mechanism of charm events in *ep* collisions the shape of the other jet is studied to estimate to what extent it is initiated by a quark or a gluon. The jet shapes are measured as a function of kinematic variables such as the transverse momentum, energy and pseudorapidity of the jet and x_γ^{obs}, the photon energy fraction entering the partonic production process. The shapes are found to be well described by the leading order plus parton shower Monte Carlo simulation PYTHIA in the region of large x_γ^{obs}, where according to the simulation the jets are dominantly charm quark initiated. Deviations of PYTHIA from the data are observed for small x_γ^{obs}, where resolved photon events are expected to contribute significantly and more gluon jets are expected. No such deviations are observed in a flavour inclusive photoproduction sample without muon requirements, which is dominated by light quark production.

Zusammenfassung

Das Ziel dieser Studie ist die Untersuchung der Charmproduktion in Positron-Proton Kollisionen bei einer Schwerpunktsenergie von 318 GeV im kinematischen Bereich der Photoproduktion. Aus der Charmproduktion stammende Zweijetereignisse wurden untersucht, die mit dem H1 Experiment in den Jahren 1999-2000 aufgezeichnet wurden und einer integrierten Luminosität von 48 pb^{-1} entsprechen. Es wurden Ereignisse mit zwei Jets im zentralen Rapiditätsbereich selektiert mit Transversalimpulsen größer als 7 und 6 GeV. Einer der beiden Jets wird durch ein Myon als Charmjet identifiziert. Um den Produktionsmechanismus von Charmquarks in *ep* Kollisionen zu untersuchen, wurde die Form des anderen Jets untersucht, um zu bestimmen, in wieweit er auf ein Quark bzw. ein Gluon als primäres Parton zurückgeht. Die Jetform wird als Funktion der kinematischen Variablen Transversalimpuls, Energie and Pseudorapidität des Jets und x_γ^{obs}, dem Anteil der Photonenergie im partonischen Produktionsprozess. Die Daten werden mit dem Monte Carlo Simulationsprogramm PYTHIA verglichen, das auf Rechnungen in führender Ordnung der Störungstheorie, kombiniert mit Partonschauern, beruht. Die Messergebnisse werden im Bereich grosser Werte von x_γ^{obs} gut beschrieben, wo laut Simulation der größte Anteil der Jets durch Quarks induziert wird. Abweichungen zwischen den Ergebnissen und PYTHIA werden für kleine x_γ^{obs} beobachtet, wo ein signifikanter Beitrag so genannter aufgelöster Photonen und mehr Gluonjets erwartet werden. Solche Abweichungen wurden in einem flavourinklusiven Datensatz, in dem kein Myon verlangt wurde, nicht beobachtet. Dieser Datensatz enthält vor allem Photoproduktion leichter Quarks.

Abstrakt

Cieľom tejto práce je vyšetrovanie produkcie charmových kvarkov v pozitrón-protónových zrážkach pri ťažiskovej energii 318 GeV v kinematickom režime fotoprodukcie. Použitá vzorka dát bola nazbieraná experimentom H1 na urýchľovači HERA v rokoch 1999 a 2000 a zodpovedá integrovanej luminozite 48 pb^{-1}. Selektované eventy obsahujú dva jety v oblasti centrálnej rapidity s priečnou hybnosťou väčšou ako 7 a 6 GeV, pričom jeden z nich bol označený myónom ako jet pochádzajúci z c-kvarku. S cieľom preveriť mechanizmus produkcie charmu vo fotoprodukcii sme v práci študovali tvar neoznačeneho jetu aby sme zistili nakoľko je iniciovaný kvarkom alebo gluónom. Tvar neoznačeného jetu sme študovali ako funkciu pseudorapidity, priečnej hybnosti, energie jetu a premennej x_γ^{obs}, predstavujúcej podiel energie fotónu v partónovom produkčnom procese. Tvary jetov sú dobre popísané Monte Carlo simuláciou PYTHIA, založenou na prvom ráde poruchovej teórie kombinovanej s partónovými spŕškami, v oblasti veľkých x_γ^{obs}, kde sú podľa simulácie jety prevažne iniciované charmovým kvarkom. Rozdiely medzi dátami a PYTHIOU boli pozorované pre malé x_γ^{obs}, kde sú očakávané značné príspevky od 'resolved' fotónu a tým aj viac gluónovych jetov. Žiadne také odchýlky neboli pozorované vo flavour-inkluzívnom fotoprodukčnom dátovom súbore bez myónovej požiadavky, kde prevažuje produkcia ľahkých kvarkov.

Contents

Introduction

Presently the world of elementary particles is described very successfully by the Standard Model, which consists of the strong and the electroweak interaction parts. Quantum Chromodynamics (QCD), as one part of the Standard Model, is the theory of strong interactions between quarks and gluons. Calculations of production cross sections in QCD are performed in perturbation theory, where the strong coupling constant α_s is used as an expansion parameter. In the presence of a hard scale α_s is small. This ensures the convergence of the perturbation series. In heavy quark production this hard scale can be provided by the mass of the heavy quark. The study of heavy quark production thus offers possibilities to test QCD calculations. In particular the different approximations which are necessary to perform the calculations can be checked for their validity in different kinematic regions.

The charm production mechanism in *ep* collisions at HERA is dominated by boson-gluon fusion processes. In photoproduction the exchanged photon is quasi-real and, in addition to direct photon processes, resolved photon processes can contribute significantly, where the photon acts as a source of quarks and gluons which participate in the hard interaction, as shown in figure 1. It was found in previous analyses that the so called excitation component, where the charm quark originates from the resolved photon, is needed to describe the data. Many measurements of charm production cross sections at HERA are adequately described by Monte Carlo models based on QCD predictions. However, the agreement is worse in the region where resolved processes are expected to contribute.

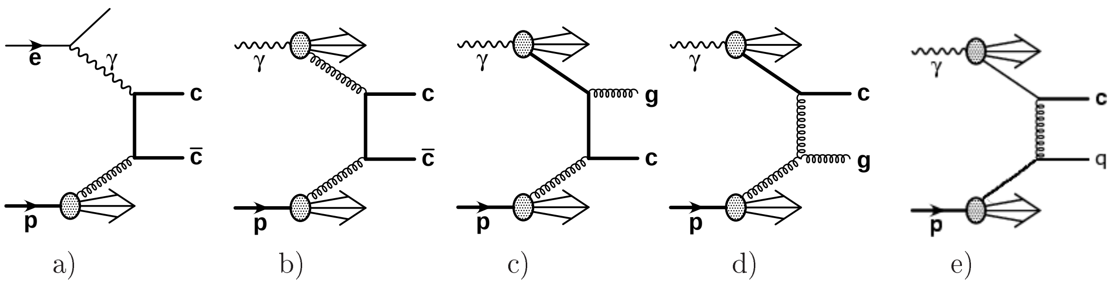

Figure 1: *Charm quark production processes in leading order pQCD: direct process a) and resolved processes b) - e). Figures c) - e) show the charm excitation processes.*

Having measured the cross sections, the next step in the investigation of charm production is to disentangle the contribution of different processes to the cross section, particularly, to which extent charm production can be attributed to the excitation processes. In perturbative QCD at leading order only the charm-excitation process produces a hard gluon in addition to a hard charm quark, while the direct photon and other resolved processes lead to the production of two quarks as outgoing partons of the hard subprocess. Therefore one of the experimental questions is whether charm production accompanied by a hard gluon can be observed.

Although the outgoing partons from the direct and excitation processes are different, they are hidden to us by color confinement. Due to confinement quarks and gluons are not directly observable as free particles but they form jets of colorless hadrons. At low energies, when the non-perturbative behavior dominates, the hadrons are continously distributed in space. The first evidence for jet-like structure in high energy physics events was found in hadron production in e^+e^- annihilation at the SPEAR collider at SLAC in 1975 [1]. The observations of jets give a clear experimental evidence of the partons coming from the hard interactions. Measurements of the jet directions give a picture of the original parton's directions. The investigation of e^+e^- collisions at PETRA in the late seventies led to the observation of three jet events [2], as shown in figure 2. The origin of the third observed jet was explained as being caused by the radiated gluon in the process $e^+e^- \to q\bar{q}g$. The question can be turned around: Can one recognize partons initiating the jets and so constrain the contributing physics processes?

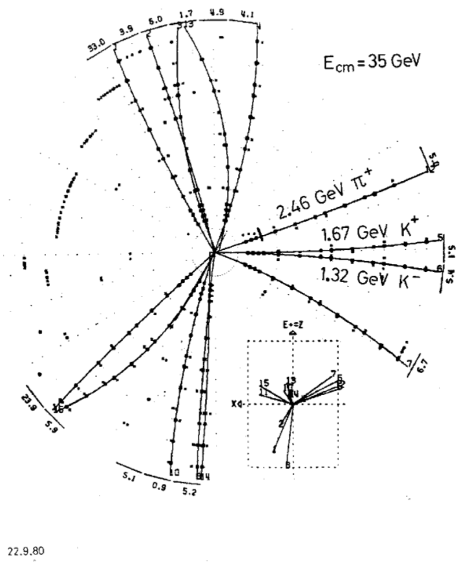

Figure 2: *Three jet event ($e^+e^- \to qqg$) as measured at PETRA.*

In the present understanding jets result from chains of elementary splitting processes of the initial quarks or gluons. Since the relative strengths of $g \to gg$, $q \to qg$ and $g \to q\bar{q}$ splittings, determined by the QCD color factors, are different, the structure of gluon and quark induced jets differs. Gluon jets are broader than quark jets at the same energy and they consist of more particles with softer p_t spectra. Differences in the structure of gluon and quark initiated jets, as predicted by QCD, have been observed at LEP. Although the jets at HERA energies have lower transverse momenta than those produced typically at LEP, there are still visible differences expected. Thus, the internal structure of a jet is one of the promising tools for distinguishing the primary partons. Recent measurements by different experiments are based on the analysis of the jet structure and this method is also exploited in this thesis for charm production.

The aim of the present study is the distinction of events with pairs of charm quarks from those with a charm quark and a gluon as final state partons from the hard scattering process. The analysis is performed in the kinematic region of photoproduction. This analysis uses the data recorded in the years 1999-2000 by the H1 experiment at HERA, corresponding to an integrated luminosity of $48\,\mathrm{pb}^{-1}$. Dijet events in which one jet is tagged as being initiated by a charm quark are used to study the shape of the other jet. A well established variable called 'integrated jet shape' is chosen as a tool for the jet shape study. The charm quark initiated jet is tagged by a muon, in contrast to other analyses which use a D^* meson for charm tagging. A flavour inclusive sample is analysed as well to compare to the situation in the light quark dominated sector.

This thesis is organised as follows: In the first chapter an overview of the theoretical background and a description of electron-proton collisions is summarised. Particular attention is given to the heavy quark production mechanisms and discussion of the different properties of quark and gluon induced jets. Monte Carlo generators are shortly introduced. In the second chapter the analysis method is explained in detail. The third chapter is dedicated to the H1 experiment where those detector parts are emphasised which are especially important for this analysis. Reconstruction of the analysis objects, like muons, electrons, hadronic final state particles and jets in the framework of the object oriented H1 software is explained in detail in chapter four. In the fifth chapter the selection of the dijet photoproduction data samples (flavour inclusive and charm enriched) is described. Particular details about the measurement are given in the chapter six. Results of the jet shape measurement are presented in chapter seven. The discussion of the results then follows in chapter eight. Finally an outlook closes the thesis.

Chapter 1

Theoretical Background

1.1 The Standard Model

The Standard Model of particle physics (SM) describes our current knowledge of the particles and forces in nature. Although it cannot explain everything, it survived decades of testing successfully. It says that matter is composed of elementary fermions - leptons and quarks [3], interacting with each other through fields. The particles associated with the interaction fields are bosons. Four types of interactions have been distinguished: electromagnetic, weak, strong and gravitational interaction. On the scales of particle physics, gravitational forces are insignificant. Gravitation is described by general theory of relativity which is a classical field theory. The quanta of the electromagnetic interaction between electrically charged fermions are the massless photons. The quanta of the weak interaction fields between fermions are the charged $W^{\pm}$ bosons and the neutral Z^0 boson. Since these carry mass, the weak interaction is short ranged. The quanta of the strong interaction field are the massless gluons. They carry color and therefore can couple together. Quarks are confined in compound systems of the size of about 1 fm. The most elementary quark systems are hadrons, compound of a quark and an antiquark (mesons) or of three quarks (baryons). The most common example is a proton, consisting of uud quarks.

In this thesis the **charm quark**[1] is of a particular interest. It was discovered in November 1974 [4] at the same time at SLAC and in Brookhaven, as a constituent of a $c\bar{c}$ bound state with a mass of about 3.1 GeV, later named J/ψ (see Fig.1.1). The charm quark is a heavy quark with a mass of about 1.5 GeV. It carries an electric charge of $+2/3\,e$, where e is the elementary charge.

1.2 Quantum Chromodynamics

Quantum Chromodynamics (QCD) is the theory of the strong interactions between color charged particles. The fundamental idea of QCD is that hadronic matter is made of quarks. The interactions of quarks and gluons are described by a non-Abelian gauge theory based on the $SU(3)_c$ color symmetry group. The gauge bosons associated with this gauge symmetry are gluons. They are electrically neutral and form a color octet. The QCD properties make it much more difficult to work with theoretically than electroweak theory. Large value of the strong coupling constant α_s, used as an expansion parameter, makes the convergence of the perturbative series problematic. Higher order contributions cannot be neglected.

[1]Later in this thesis 'charm quark' denotes both charm quark and charmed antiquark.

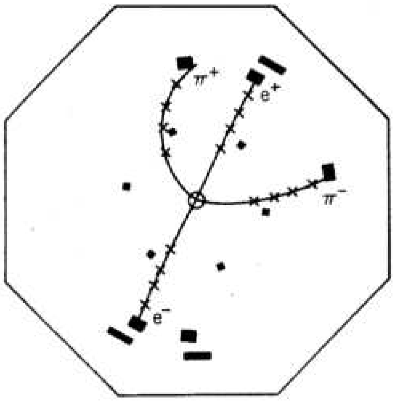

Figure 1.1: *Spark-chamber event display of a ψ' to J/ψ decay from the Mark I detector at SPEAR collider at SLAC. Pictures as this one often resembled the shape of the Greek letter ψ.*

In addition to the fermion loops also gluon loops occur, as shown in figure 1.2, which exist due to the gluon self-interaction. These result in an anti-screening effect, causing the strong coupling constant to behave differently from the electromagnetic fine structure constant. It becomes large at large distances corresponding to small momentum transfer. In one loop approximation α_s at the scale $\mu > \Lambda_{QCD}$ is given by

$$\alpha_s(\mu^2) = \frac{1}{b\ \ln\left(\frac{\mu^2}{\Lambda^2_{QCD}}\right)}, \qquad b = \frac{33 - 2n_f}{12\pi} \tag{1.1}$$

where Λ_{QCD} is the scale where α_s gets large and perturbative theory is not applicable anymore. This fundamental parameter of QCD depends on the renormalisation scheme (see section 1.5) and on the number of active flavors. The value of $\Lambda_{QCD}(\overline{MS})$ was determined experimentally to be about 215 MeV [3].

The **running of the coupling constant** as a function of the scale is shown in figure 1.3. It has important consequences: **confinement and asymptotic freedom** of partons. 'Confinement' means that quark and gluon degrees of freedom are not observed as states which propagate over macroscopic distances.

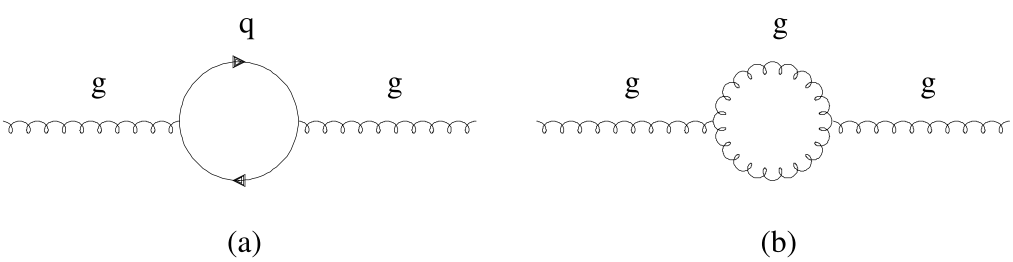

Figure 1.2: *Higher order corrections to diagrams with exchanged gluons: (a) a quark anti-quark loop, (b) a gluon loop.*

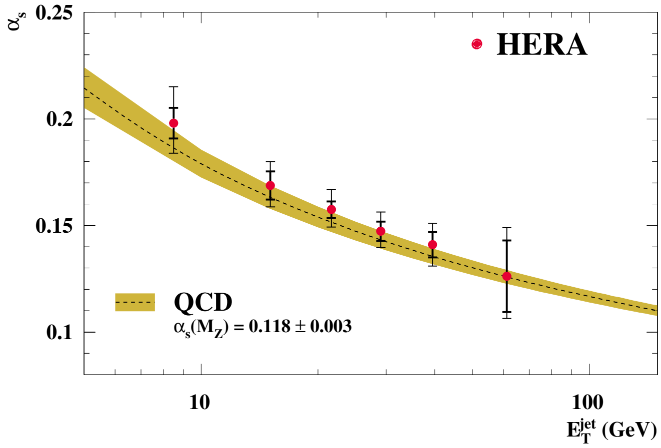

Figure 1.3: *Running of the effective coupling constant α_s as a function of the transverse jet energy. Combined ZEUS and H1 measurement and the QCD prediction [5].*

'Asymptotic freedom' describes the fact that at small distances partons behave as free particles. This explains why the method of perturbation theory is useful at high energy.

Heavy quark production is an excellent testing ground for pQCD, because the high mass of the heavy quark, together with p_t of the quarks and/or Q^2 provide a hard scale. The presence of the hard scale enables the convergence of the perturbation series present in the calculations.

1.3 High Energy *ep* Collisions at HERA

At HERA high energy leptons (positrons or electrons) are scattered off a proton beam at a centre-of-mass energy of 318 GeV. The process can be described in leading order by the exchange of a single virtual gauge boson (γ, Z^0 or $W^{\pm}$), as shown in figure 1.4. According to the boson charge **neutral current (NC) processes** ($ep \to eX$) and **charged current (CC) processes** ($ep \to \nu_e X$) are distinguished.

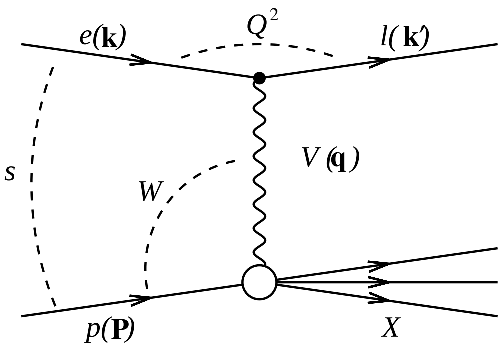

e:	positron
p:	proton
l:	scattered lepton (e or ν_e)
V:	exchanged boson (γ, Z^0 or $W^{\pm}$)
X:	hadronic final state

Figure 1.4: *Deep inelastic positron-proton scattering at HERA in the single boson exchange picture. In NC processes γ or Z^0 bosons are exchanged and the scattered lepton is a positron. In CC processes a $W^{\pm}$ boson is exchanged, resulting in an outgoing antineutrino. The four momenta of the particles are denoted in parentheses.*

For unpolarised beams at a given centre-of-mass energy

$$\sqrt{s} = \sqrt{(k+P)^2} \tag{1.2}$$

only two variables are needed to completely describe the kinematics of inclusive lepton proton scattering. Usually they are selected from the following Lorentz invariant quantities:

$$Q^2 = -q^2 = -(k-k')^2 \tag{1.3}$$

$$y = \frac{P \cdot q}{P \cdot k}, \; (0 \leq y \leq 1) \tag{1.4}$$

$$x = \frac{Q^2}{2\,P \cdot q}, \; (0 \leq x \leq 1) \tag{1.5}$$

where Q^2 is the negative squared transfer of four momentum from the incoming lepton to the proton. It can be interpreted as a measure of the resolving power of the exchanged boson, where large Q^2 means high resolution. In the proton rest frame, the inelasticity y represents the fractional energy transferred from the lepton to the proton. The momentum fraction of the proton carried by the struck parton is characterised by x. Neglecting the lepton and proton masses, the variables are related by the following equation

$$Q^2 = x \cdot y \cdot s \tag{1.6}$$

The regime of small momentum transfer ($Q^2 \approx 0$) is called **photoproduction**. The ep interaction is in this case mediated by quasi-real photons. At H1 photoproduction is usually selected by $Q^2 < 1\,\mathrm{GeV}$. The regime of large Q^2 is called Deep Inelastic Scattering (DIS).

1.4 Cross Sections and Structure Functions

The complete differential neutral current cross section for $e^+p \to e^+X$ processes incorporating both γ and Z^0 exchange can be written as

$$\frac{d^2\sigma^{NC}}{dxdQ^2} = \frac{4\pi\alpha^2}{xQ^4} \cdot \left[F_2(1+(1-y)^2) - xF_3(1-(1-y)^2) - y^2 F_L\right] \tag{1.7}$$

where $F_2(x,Q^2)$, $F_3(x,Q^2)$, $F_L(x,Q^2)$ are the **proton structure functions**, which parametrize the structure of the protons as 'seen' by the virtual boson. The term containing $F_3(x,Q^2)$ describes the Z^0 exchange and the γZ^0 interference. Due to the large mass of the Z^0 boson it can be neglected in this photoproduction analysis, since it contributes only at very large Q^2 where the γZ^0 interference becomes important.

The longitudinal structure function $F_L(x,Q^2)$ is related to the exchange of a longitudinally polarised photon. Due to the factor y^2 in front of F_L its contribution is kinematically suppressed. It can lead to sizeable effect only for large inelasticities.

From the measurements of the cross section of NC DIS events one can extract the proton structure function $F_2(x, Q^2)$. In the naive **Quark Parton Model** (QPM) [6], the proton consists of (quasi) free point-like objects called partons. Once they are resolved, the increase of the momentum transfer Q^2 will not make any new detail visible in this picture. Thus the structure functions are expected to be independent of Q^2 in this model. This effect is known as **scaling** [6]. The structure functions in this approximation depend only on the dimensionless variable x. The data at HERA and fixed target experiments show (see Fig. 1.5) that this is really the case for $x \sim 0.1$. But the data show as well that at low x F_2 rises sharply with increasing Q^2, a sign of **scaling violations**. As one can see in Fig. 1.5, QCD can accommodate this behavior in the whole kinematic region of the measurements. The independence of F_2 on Q^2 at $x \sim 0.1$ is interpreted as scattering mainly off the valence quarks. The rise of F_2 toward high Q^2 at low x is associated with the increase of the gluon density as x gets smaller.

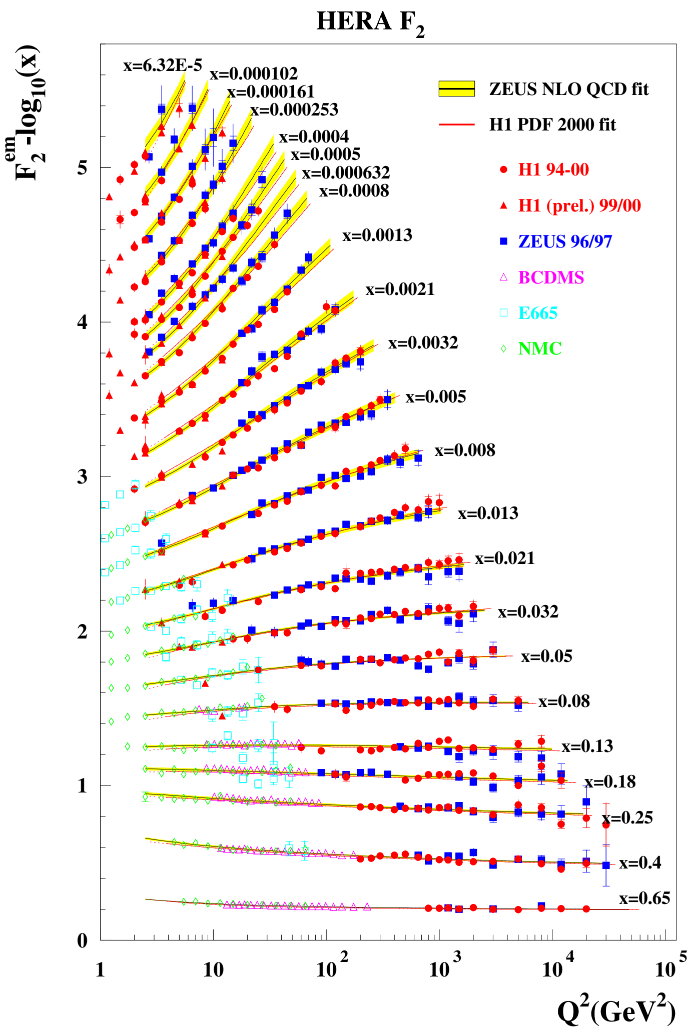

Figure 1.5: *Measurement of the proton structure function $F_2(x, Q^2)$ as a function of Q^2 at fixed values of x by various fixed target and collider experiments. The lines correspond to QCD fits performed by the ZEUS and H1 experiments.*

Another problem of the otherwise successful QPM was that, as the experiments show, only about 50 % of the proton momentum is carried by the charged valence quarks. This fact together with the observation of scaling violations confirms, that also gluons and gluon-induced quark-antiquark pairs (so called 'sea quarks') have to be considered as proton constituents.

Heavy quark production is sensitive to the gluon density in the proton, since the main production mechanism for heavy quarks at HERA is boson-gluon fusion (see section 1.8).

1.5 Factorisation Theorem

The factorisation theorem introduces a separation of the **short distance part** (hard processes) and the **long distance part** (soft processes) of the scattering process. The QCD factorisation theorem [7] states that in the presence of a hard scale the cross section can be decomposed as

$$\sigma \sim f_{i/p}(x_1, \mu_F^2) \otimes \hat{\sigma}_{ij}(\hat{s}, \alpha_s(\mu_R), \mu_R, \mu_F) \otimes f_{j/\gamma}(x_2, \mu_F^2) \otimes D(z), \tag{1.8}$$

where $f_{i/p}$ and $f_{j/\gamma}$ are parton density functions of the proton and photon, respectively. $\hat{\sigma}_{ij}$ denotes the cross section of the hard subprocess. $D(z)$ is the fragmentation function and z stands for the fraction of the original longitudinal momentum of the parton carried by the hadron which contains that parton. μ_F and μ_R are factorisation and renormalisation scales, respectively. See also figure 1.6.

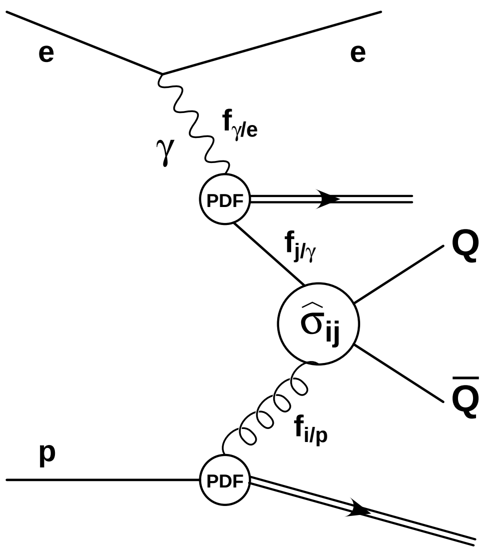

Figure 1.6: *Schematic diagram illustrating the ep scattering process motivated by the factorisation theorem for the photoproduction case.*

The cross section of the hard subprocess $\hat{\sigma}_{ij}$ is calculable in perturbative QCD. The other terms absorb the long-range non perturbative processes. These parts are presently not calculable and therefore have to be determined experimentally, for example the fragmentation function $D(z)$.

The fluxes of the incoming particles depend on the **parton density functions** (PDFs) $f_{i/p}$ and $f_{j/\gamma}$. They represent the probability to find a particular parton (i or j) having a momentum fraction of the mother particle in the range of $(x,\, x + dx)$. Thus $f_{i/p}(x_1)dx_1$ gives the probability to find the parton i in the proton carrying a fraction x_1 of its momentum.

The QCD factorisation theorem allows to write the following relation between the structure function F_2 and the parton density functions

$$F_2(x, Q^2) = \sum_{i=q,\bar{q},g} \int_x^1 dz\, C^i\left(\frac{x}{z}, \frac{Q^2}{\mu^2}, \frac{\mu_F^2}{\mu^2}, \alpha_s(\mu^2)\right) f_{i/p}(z, \mu_F, \mu^2). \tag{1.9}$$

The coefficient functions C_i can be computed in pQCD. PDFs are not physical observables in contrast to structure functions which are observables . Figure 1.7 shows parton densities of the proton as a function of x, as they are predicted by the CTEQ5L set [8] for the scale relevant in this analysis.

The factorisation procedure introduces a **factorisation scale** μ_F, which defines the boundary between the perturbative and non-perturbative regions. Formally, the μ_F dependence of the PDFs arises from the absorption of collinear divergences into the PDFs according to a certain 'factorisation scheme'. For a given choice of factorisation scheme and scale, the proton PDFs are considered to be universal, i.e. independent of the actual reaction the proton takes part in.

By introducing the arbitrary **renormalisation scale** $\mu_R > \Lambda_{QCD}$ the ultraviolet divergences coming from the calculation of virtual corrections (see appendix D), which yield divergent integrals, are absorbed into the definition of the parameters of the theory. The renormalisation scale can be viewed as the momentum at which the subtraction, which removes the divergences arising in the momentum limit $p \to \infty$, is performed. Several renormalisation schemes are used. The most important are the *minimal subtraction scheme* ($\overline{MS}$) and the *deep inelastic scattering scheme* (DIS).

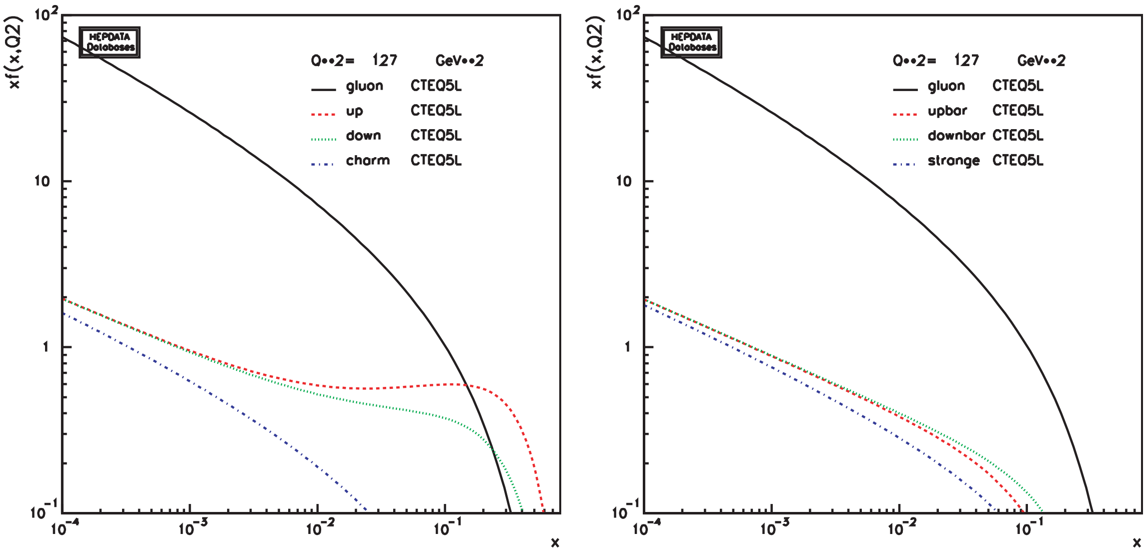

Figure 1.7: *Parton densities of the proton as a function of x as given by the CTEQ5L parton density function [8], which has been used in the Monte Carlo generator PYTHIA. The scale is given by $\hat{p}_t^2 + m_c^2 = 127\,\mathrm{GeV}^2$.*

1.6 Parton Evolution Models

The parton densities discussed in the previous section contain the soft processes up to the factorisation scale μ_f and depend on the scale. Although pQCD does not predict the parton density functions, the scale dependence of the PDFs can be calculated within pQCD. This means that if the $f_{i/p}(x, \mu_0)$ is obtained from the experimental data at a certain scale μ_0, the evolution to any other scale $\mu_f > \mu_0$ is possible. The evolution equations are derived considering the parton radiation and splitting processes, as shown in figure 1.12. The evolution is performed by parton evolution models, which are expected to be valid only in certain regions of phase space. The calculation simplifies considerably if some approximations in the calculations are used. The summation over particular terms can be interpreted as a kinematical ordering [9].

DGLAP Evolution

The DGLAP[2] approach [10] is based on summing terms proportional to $\alpha_s \ln Q^2$. This approximation leads to strong ordering in the transverse momenta of the emitted partons (see Fig. 1.8):

$$k_{t,0} \ll k_{t,1} \ll \ldots \ll k_{t,n-1} \ll k_{t,n} \ll k_{t,n+1} \ll Q^2 \tag{1.10}$$

Then the integration of the parton densities over k_t and x can be carried out. Therefore the factorisation within this approximation is called 'collinear factorisation'.

The DGLAP equations are a set of coupled integro-differential equations for parton density functions $f_{i/p}$ which can be written as

$$\frac{df_{i/p}(x, \mu^2)}{d\ \ln \mu^2} = \sum_b \int_x^1 \frac{dz}{z} P_{ij}(z, \alpha_s(\mu^2)) f_{i/p}(x/z, \mu^2). \tag{1.11}$$

Splitting functions P_{ij} give the probability for a parton j to emit a parton i with momentum $p_i = zp_j$. They will be discussed in more detail in section 1.10. The DGLAP approximation is expected to be valid in the region where Q^2 is large and x is not too small. The DGLAP approach describes successfully the scaling violations of the structure functions observed at HERA down to the smallest accessible x.

BFKL Evolution

The evolution in the BFKL[3] model [11] is performed in x and the leading $\alpha_s \ln(1/x)$ terms are resummed. This approach is expected to be valid for moderate Q^2 and small x. This approach leads to strongly ordered longitudinal momenta $z_i = x_i/x_{i-1}$. The transverse momenta k_t are free and one considers the unintegrated (over the parton k_t) parton densities. This approach is called 'k_t-factorisation'.

[2] Dokshitzer, Gribov, Lipatov, Altareli, Parisi
[3] Balitsky, Fadin, Kuraev, Lipatov

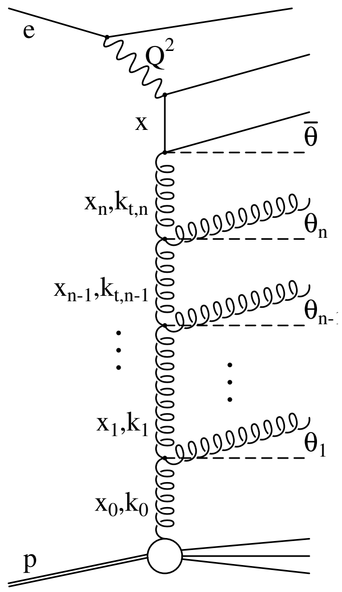

Figure 1.8: *Gluon ladder illustrating the evolution of partons with momentum fractions x, virtualities k_t and emission angles θ.*

The behavior of the structure function F_2 in the HERA kinematical region is not sensitive enough to discriminate between DGLAP and BFKL. Signs of the BFKL mechanism may be observable by studying the energy dependence of jets near the proton direction.

CCFM Evolution

The CCFM[4] model [12] combines both approaches mentioned above. It is equivalent to DGLAP for large Q^2 and moderate x and equivalent to BFKL in case of small x and moderate Q^2. The CCFM approach is based on a strong angular ordering of subsequent parton emissions. The unintegrated gluon density which is used here depends on k_t.

Measurements of forward jet production [13, 14] show, that the DGLAP-based models including the resolved photon component describe the data better than the CCFM-based model. However, when in addition to the forward jet two central jets are required, the CCFM description of the data is better [14].

[4]Ciafaloni, Catani, Fiorani, Marchesini

1.7 Photoproduction at HERA

The lepton-proton cross section falls rapidly with increasing Q^2 (equation 1.7). At low Q^2 the photon propagator dominates the NC cross section and the contribution of Z^0 exchange can be neglected. In the photoproduction processes the Q^2 of the exchanged photon is small and the positron is scattered under a small angle. The positron can be regarded as the source of **almost real photons**. The inclusive ep cross section is dominated by photoproduction, because the photon propagator leads to the behaviour of the cross section as $\sim 1/Q^4$.

In photoproduction the hard scale of the interaction cannot be identified with Q^2. Instead the transverse energy of the hard outgoing partons and/or the mass of the heavy quark, if present, can be used.

Photon Structure

In the Standard Model the photon is considered as an elementary and color-neutral particle. But it can indirectly participate in strong interactions via fluctuation into a quark-antiquark pair. This partonic structure of the photon, described by the photon parton density functions, is especially relevant in the photoproduction domain. The hadronic constituents of the photon lead to the so called **resolved photon events** (see section 1.8).

1.8 Heavy Quark Production

Heavy flavors refer here to charm and beauty quarks, because their masses $m_c \approx 1.5\,\text{GeV}$ and $m_b \approx 4.5\,\text{GeV}$ are considerably larger than those of the light quarks (up, down, strange). The HERA centre-of-mass energy is not high enough for top quarks to be produced in pairs. The Standard Model single top production mechanism has a very low cross section.

Heavy quark production represents a significant contribution to the total inclusive cross section at HERA energies. Because of the high mass of the charm quark, it is produced predominantly dynamically in **boson-gluon fusion** (BGF) processes, as shown in figure 1.9. Gluon splitting to a heavy quark pair $g \to Q\overline{Q}$ and the production of heavy quarks in fragmentation processes is suppressed at HERA due to the high quark masses.

In the direct process (Fig. 1.9 a) a photon emitted from the incoming electron interacts with a gluon from the proton and a heavy quark pair is produced. In photoproduction in addition to the direct processes, the **resolved processes** give a sizeable contribution. In the so called '**normal resolved**' processes (Fig. 1.9 b) a gluon out of the photon interacts with a parton of the proton. In the '**excitation processes**' (Fig. 1.9 c-e), which are also subsumed under resolved processes, a heavy quark out of the photon takes part in the hard interaction. It should be noted that the separation of the direct and resolved processes is only unambiguous in the LO picture.

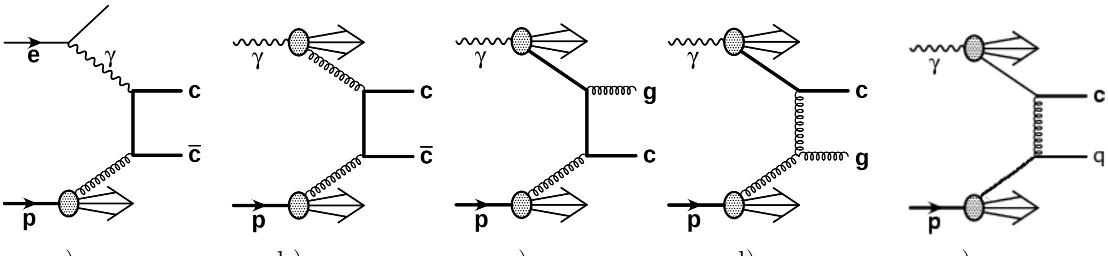

Figure 1.9: *Charm quark production processes in leading order pQCD: direct process a) and resolved processes b) - e). Figures c) - e) show the charm excitation processes.*

The **direct BGF cross section in leading order** can be calculated as [15]

$$\hat{\sigma}_{\gamma g \to Q\overline{Q}}(\hat{s}, m_Q^2) = \frac{\pi e_Q^2 \alpha \alpha_s}{\hat{s}} \left[(2 + 2\omega - \omega^2) \ln \frac{1+\chi}{1-\chi} - 2\chi(1+\chi) \right] \tag{1.12}$$

where

$$\omega = 4m_Q^2/\hat{s}, \quad \chi = \sqrt{1-\omega}$$

The squared centre-of-mass energy is denoted as $\hat{s}$, e_Q is the heavy quark's electric charge. The χ-terms describe the threshold behavior of heavy quark production. Thus the kinematic region close to the charm production threshold is strongly favored, which is reflected in typically small charm quark transverse momenta with respect to the beam axis. Due to larger mass and smaller charge of the beauty quark in comparison to the charm quark, the beauty production is in photoproduction suppressed with respect to the charm production by a factor of about 200, depending on the phase space selection.

It is assumed that the mass of the charm quark provides a sufficient **hard scale** ($m_c \gg \Lambda_{QCD}$). Therefore charm production is a good testbasis of the pQCD predictions, even in absence of any other hard scale. Additionally it provides information about the parton content of the photon and proton, especially gluon structure, because the cross section is expected to be dominated by gluon-induced processes. Due to the hard fragmentation of heavy quarks, the parton and hadron levels are closely related.

This analysis studies the **open charm production** where the partons from the produced $c\bar{c}$ pair hadronise independently and build jets. In the hidden charm production the $c\bar{c}$ pair forms a bound state like for example J/ψ, which can than decay hadronically or leptonically.

1.9 Hadronisation Models

In Monte Carlo two partons are produced in the hard process in case of BGF. Subsequently, they undergo a parton shower, which is carried out by the evolution equation (see section 1.6) as a sequence of particle branchings. From a certain threshold α_s is so large that the use of pQCD is not possible anymore. In order to describe hadronisation processes, phenomenological fragmentation models are used. A number of such models have been developed. Two of them, which are used in this analysis, are discussed here:

- **The String fragmentation** (Lund model) [16] is used in JETSET. The $q\bar{q}$ pairs and the color field between them form 'strings'. Gluons are represented by kinks in the strings. If the potential energy stored in the string becomes large enough (the QCD potential is proportional to the distance at large distances), the string breaks up into two string pieces and a new $q\bar{q}$ pair is formed (see Fig. 1.10). When no energy for further pair production is left, the process stops and the resulting string fragments are combined into hadrons.

- For heavy quark fragmentation **Independent fragmentation** is widely used as implemented in the Peterson model [17]. In this model partons hadronise independently (figure 1.11) and the probability of the transition of a quark Q to the hadron H carrying a fraction z of the parton's longitudinal momentum is given by

$$D_Q^H(z) = \frac{N}{z\left[1 - \frac{1}{z} - \frac{\epsilon_Q}{1-z}\right]^2}. \tag{1.13}$$

  At leading order the common choice of the parameter ϵ_Q is $\epsilon_c \approx 0.058$ and $\epsilon_b \approx 0.0069$ at next-to-leading $\epsilon_c \approx 0.035$ and $\epsilon_b \approx 0.0033$ [18]. The additional quarks (antiquarks) needed to form the hadron are from the vacuum $q\bar{q}$ pairs, with the remaining quark (antiquark) continuing hadronisation. The branching is repeated until the available energy is exhausted. This model is generally used in the NLO calculations.

For heavy quark fragmentation at HERA string fragmentation is often used in the LO event generators to create hadrons and the momenta of the heavy hadrons are determined using the Peterson fragmentation function. This is the case also in this analysis.

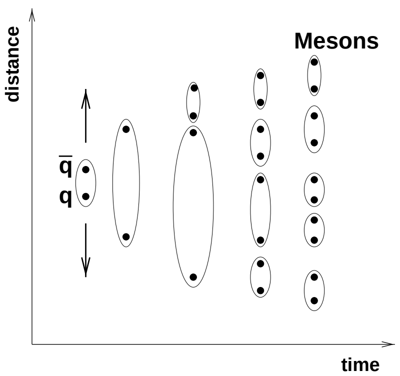

Figure 1.10: *Creation of mesons in the Lund string model. The kinks representing strings are not shown.*

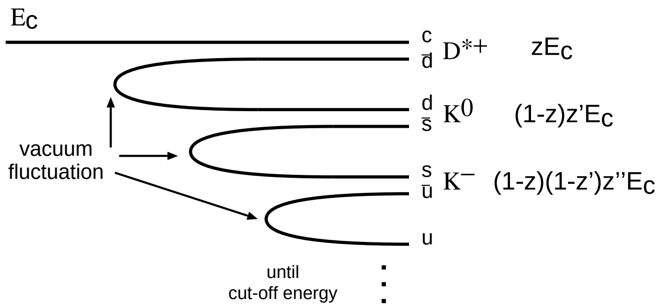

Figure 1.11: *Meson creation according to the independent fragmentation model.*

1.10 Jet Structure

In the present picture jets result from a chain of elementary splitting processes (parton branchings). Each branching is characterised by the value of Q^2 representing the negative squared four momentum transfer in that branching. As the parton shower develops, Q^2 in the particular branching processes decreases and thus α_s rises. Therefore the processes can be described by perturbative QCD only up to a certain cut-off value of the parton virtuality. After that the hadronisation of the created partons, discussed in the previous section, takes over. In Monte Carlo calculations the factorisation scale μ_f represents the boundary between these two regimes. The lower is the available energy, the higher is the role of nonperturbative effects. Internal jet structure is sensitive to both soft and hard contribution from QCD, thus it can be used to probe both of them.

Internal jet structure is expected to depend mainly on the primary parton type and less on the particular hard scattering process. The differences between quark and gluon jets arise from the SU(3) group structure of QCD. Relative strengths of different splittings (see figure 1.12) lead to different branching probabilities for quark and gluon and thus to different properties of quark and gluon induced jets. The strengths of the splittings are given by the QCD color factors C_A, C_F and T_R:

$$C_A = N_c = 3 \tag{1.14}$$

$$C_F = \frac{N_c^2 - 1}{2N_c} = \frac{4}{3} \tag{1.15}$$

$$T_R = \frac{1}{2}, \tag{1.16}$$

where N_c denotes the number of colors.

In the following differences between quark and gluon induced jets will be discussed in terms of multiplicity of the jet particles and angular jet size.

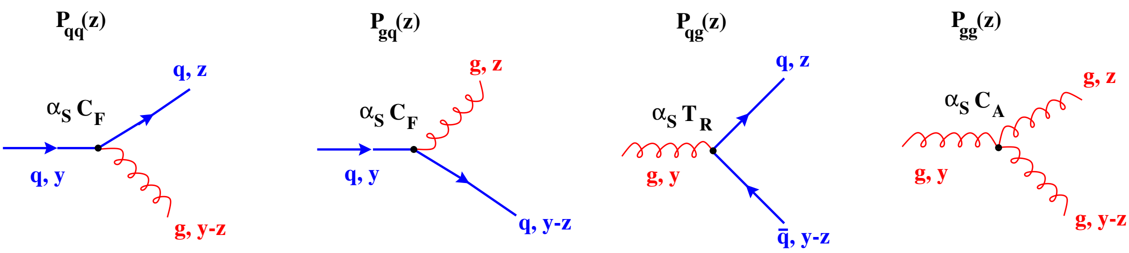

Figure 1.12: *Branching processes of quarks and gluons.*

Multiplicity of Jet Particles

As explained in [19], in pQCD the average number of hadrons of type h in a jet initiated by a parton i at scale t is given by

$$\langle n_h(t) \rangle_i = \int_0^1 dx D_i^h(x,t). \tag{1.17}$$

The scaled hadron energy is given by $x = E_h/E_{jet}$. The fragmentation function $D_i^h(x,t)$

represents the probability for the parton i to form a jet that contains the hadron h carrying the longitudinal momentum $p_L^h = xp_L^i$. $D_i^h(x,t)$ cannot be computed in perturbation theory, since it describes a non perturbative process. But as in case of parton density functions, the evolution with scale t can be computed. The change of $D_i^h(x,t)$ when $t \to t + dt$ can occur only via the splitting of a parton of type i in this interval. Therefore $D_i^h(x,t)$ satisfies evolution equations like those for particle densities.

$$t\frac{\partial}{\partial t}D_i^h(x,t) = \sum_j \int_x^1 \frac{dz}{z}\frac{\alpha_S}{2\pi}P_{ji}(z,\alpha_S(t))D_j^h(x/z,t) \tag{1.18}$$

It enables to predict the value of $D_i^h(x,t)$ at an arbitrary scale t once they have been parametrised at some scale t_0. $P_{ji}(z)$ are called splitting functions. They give the probability for an initial parton i to emit a parton j with momentum $p_j = zp_i$. Splitting processes relevant for jet development are shown up to order α_s in figure 1.12. At leading order in α_s the splitting functions are given by

$$P_{qq}^0(z) = C_F\Big[\frac{1+z^2}{1-z} + \frac{3}{2}\delta(1-z)\Big] \tag{1.19}$$

$$P_{gq}^0(z) = C_F\Big[\frac{1+(1-z)^2}{z}\Big] \tag{1.20}$$

$$P_{qg}^0(z) = T_R\Big[z^2 + (1-z)^2\Big] \tag{1.21}$$

$$P_{gg}^0(z) = 2C_A\Big[\frac{z}{1-z} + \frac{1-z}{z} + z(1-z)\Big] + \delta(1-z)\frac{11C_A - 4N_fT_R}{6} \tag{1.22}$$

Thus, the probability for each branching is proportional to the QCD color factors C_A, C_F and T_R mentioned above. Already from equation 1.21 one can see that gluon splitting to quarks is the least important process contributing to building of jets at HERA since T_R is the smallest from the three factors. Since $C_A/C_F = 9/4 > 1$, more branchings are expected for jets originating from gluons. Therefore gluon jets are on average broader than quark jets with the same p_t.

A more rigorous approach by solving DGLAP equations (1.18) (see for example [19]) results in a relation between the mean multiplicities:

$$\langle n_h(t)\rangle_q \sim \frac{C_F}{C_A}\langle n_h(t)\rangle_g. \tag{1.23}$$

This relation is valid at a scale $t \gg t_0$. These differences arise from the greater absolute effective color charge of the gluon, which is proportional to $\sqrt{C_A}$ as opposed to $\sqrt{C_F}$ for the quark. The following model from [19] illustrates this difference: The dominant asymptotic contribution to the multiplicity of a quark jet comes from the emission of a highly virtual gluon by the initial quark. This gluon then generates a gluon jet with an energy lower than the original quark energy. Thus one factor of C_A in the cascade is replaced by C_F leading to a reduction in the average multiplicity by a factor C_A/C_F. The whole situation is shown in figure 1.13. However, this is an asymptotic behavior at very high scales (energies) [20].

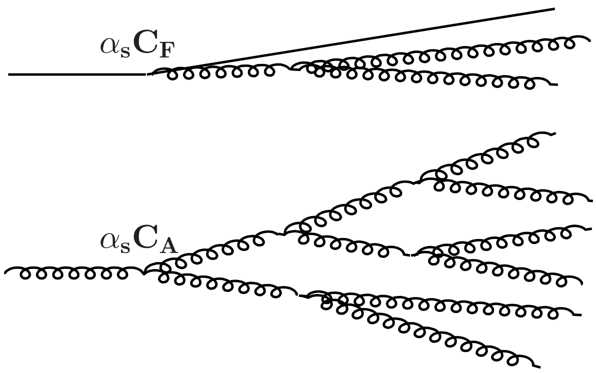

Figure 1.13: *Typical structure of quark and gluon induced jets. Gluon jets are broader and contain more partons than quark jets. A quark radiates typically one gluon, which then develops a gluon jet.*

In addition, the lower is the energy the higher is the influence of non-perturbative effects which cause smearing of the differences.

Such effects were studied in three jet events in e^+e^- annihilation. In recent studies [21] agreement was also found between theory describing finite scales and experimental measurements in a special event configuration.

Angular Jet Size

In one of the first attempts to define jet cross sections for e^+e^- collisions in perturbation theory [22] the following definition of the two-jet final state was used: The final state is classified as two-jet like if all but a fraction ϵ of the total available energy is contained in a pair of cones of half-angle δ (see Fig. 1.14). Using this definition the angular size of quark/gluon jets for a given small ϵ in lowest order can be shown to be

$$\delta_q \sim \exp \frac{\pi(1-f_2)}{4C_F\alpha_S(s)|\ln\epsilon|} \tag{1.24}$$

$$\delta_g \sim \exp \frac{\pi(1-f_2)}{4C_A\alpha_S(s)|\ln\epsilon|} \tag{1.25}$$

$$f_2 = \frac{\sigma_{2jet}}{\sigma_{tot}} \tag{1.26}$$

Therefore

$$\delta_g \sim \delta_q^{C_F/C_A}. \tag{1.27}$$

Since $C_F/C_A < 1$, the angular size of a gluon jet is larger than that of a quark jet, as shown schematically in figure 1.15.

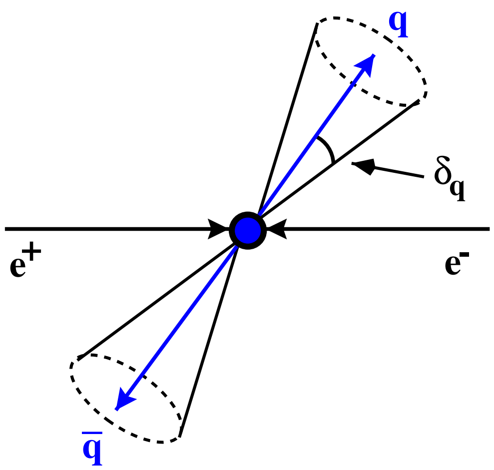

Figure 1.14: *Sketch of a two jet final state in e^+e^- annihilation.*

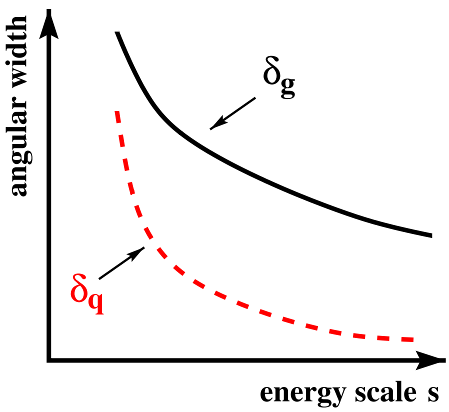

Figure 1.15: *Schematic illustration of the decrease of the angular width for quark and gluon induced jets as a function of the energy scale s.*

Summary of the Quark - Gluon Jet Differences

For quark and gluon jets of equal energy produced under the same circumstances, the **average multiplicity** of any type of object in a gluon jet is predicted by QCD to be larger than that of a quark jet. Therefore the **particle spectrum** is softer and the jet energy is distributed at larger **mean angles with respect to the jet axis**. A further consequence of the higher multiplicity is a softer **fragmentation function** of a gluon jet with respect to a quark jet. The fragmentation of the beauty quark into charged hadrons including the weak decay products of the beauty flavored hadron is expected to be substantially softer than that of the other quarks. This is caused by the large mass difference between the beauty and charm quark which results in many produced particles. A smaller effect is expected in charm quark fragmentation, since the mass difference between the charm and strange quark is not as large as in the beauty case.

Differences between light quark and gluon jets predicted by QCD were confirmed by measurements at LEP. See for example [20, 21, 23] and section 2.6. The results of the e^+e^- collider experiments concerning the mean charged multiplicity were found to be consistent with the measurements performed for the current jet at HERA [24]. In addition, different distributions for flavour inclusive jets and charm induced jets were studied at PETRA [25]. Spectra of charged particle multiplicities in the jets, as well as thrust and sphericity of the jets were found to be similar for both kinds of jets.

In this thesis the jet structure will be used as a tool to study the contribution of gluon and quark jets to the final state and thus to discriminate between processes contributing to charm photoproduction.

1.11 Physics Simulation

Theoretical predictions implemented in Monte Carlo simulation programs form an integral part of any high energy physics experiment. They help to design the detectors and to define the experimental strategies. To serve such a purpose, these predictions must reproduce the possible collision processes taking place in real detectors as closely as possible. Simulation of the physics is based on the factorisation theorem (see section 1.5), which says that the scattering process with a hard scale can be factorised in a hard and a soft part. The scales for the calculation of the hard scattering process in heavy quark production are defined by the heavy quark mass in combination with p_t of the heavy quark (in photoproduction and DIS) or Q^2 (in DIS).

Two different types of programs will be discussed here: event generators and cross section integration programs. Event generators are used to produce hypothetical events with distributions predicted by theory, i.e. the frequency we expect the events to appear in nature. On the other side, cross section integration programs predict distributions in a limited number of observables according to the theoretical calculations. For a more detailed explanation and examples see [26].

Calculation Schemes

Heavy quark production presents a challenge in pQCD because the heavy quark mass provides an additional hard scale to p_t or Q^2, which complicates the situation. Presently there are two main schemes available for calculating heavy quark production, which represent two different ways of reducing the two-scale problem to an effective one-scale problem:

- **Fixed order (FO) massive approach:**
  In this fixed-flavour-number-scheme (FFNS) heavy quarks are not considered to be active partons in the proton and in the photon. Charm and beauty quarks are produced via boson-gluon fusion mechanism. This approach is valid near the threshold, i. e. for p_t of the heavy quark of the order of the quark mass. Feynman diagrams corresponding to heavy quark production in the massive scheme are shown in figure 1.16. The massive scheme is implemented in the FMNR program [27] for photoproduction and in the HVQDIS program [28] for DIS regime calculations. In this case, the NLO diagrams are of order α_s^2, which are much more complicated to calculate than the diagrams of the second approach.

- **Resummed calculations (RS) - massless approach:**
  It is implemented in the zero-mass-variable-flavour-number-scheme (ZM-VFNS). This approach is reliable at large scales (p_t of the heavy quark much larger than the quark mass), where the heavy quarks can be treated as zero mass partons, like up, down and strange quarks. Thus in the ZM-VFNS heavy quarks are active flavors in photon and proton and heavy quark excitation processes are possible, as is shown in figure 1.17. There are leading order Monte Carlo programs are based on this approach.

- The most reliable pQCD prediction at low and intermediate p_t might obtained by the **Matched scheme** (FO+NLL) [29]. It combines the two previous approaches, utilizing the most appropriate scheme at a given energy scale Q^2. The massive scheme is used near the threshold and the massless scheme (with $m_c \neq 0$) is applied for large scales. This scheme is commonly referred to as the variable-flavour-number-scheme (VFNS).

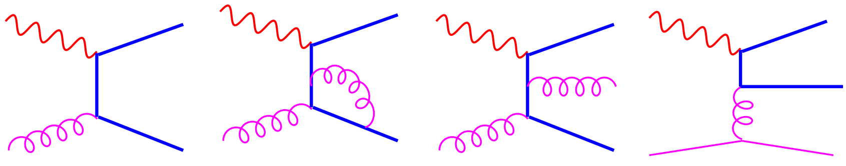

Figure 1.16: *Examples of partonic processes for heavy quark production in the massive scheme: a) LO contribution, b) virtual contribution and c), d) show NLO radiative processes. The straight lines represent the heavy quarks.*

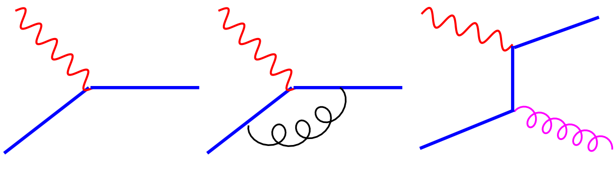

Figure 1.17: *Examples of partonic processes for heavy quark production in the massless scheme: a) LO contribution, b) virtual contribution and c), d) show NLO radiative processes. The straight lines represent the heavy quarks.*

The measurements of $F_2^{c\bar{c}}$ and $F_2^{b\bar{b}}$ at high Q^2 [30] performed at H1 were compared to NLO QCD predictions for both ZM-VFNS and VFNS. Both approaches were found to be similar and compatible with the data.

Event Generators

Event generators generate four vectors of final state particles. Usually they are based on leading order calculations of the hard subprocess and the higher orders are simulated using parton showers. Event generators use the following separate stages, as shown in figure 1.18, to describe the physics events:

- The starting point are the **PDFs**, which were discussed in section 1.5. PDFs used in this analysis are listed in table 1.2.
- The **hard scattering process** is described by a matrix element. It involves a hard scale, and is calculated using perturbation theory. In the present MC generators leading order matrix elements are implemented only.
- Gluon radiation may give large corrections to the overall topology of the event. Therefore they are simulated using the **parton shower** (PS) method, in which both initial and final state radiation is simulated by an arbitrary number of branchings

of one parton into two partons ($a \to bc$). Once formed, the daughters b and c may branch as well, and so on. In the event generators used in this analysis final parton showers are implemented via the JETSET program [31]. The shower evolution is cut off at some scale, where the hadronisation process takes over.

- The colored partons are transformed into colorless partons in the process of **hadronisation**. Nowadays only phenomenological models exist. Two of them are described in section 1.9. Hadronisation is also implemented in JETSET using the string model. In this analysis the Peterson fragmentation function, which is derived for independent fragmentation, is used additionally for heavy quarks. That means that the hadrons are created according to the Lund model, but the longitudinal momentum is assigned to them according to the Peterson fragmentation function. See section 1.9 for details about both hadronisation models.

- The **beam remnant** forms part of the hadronic system, which is color-connected to the hard interaction. It needs to be reconstructed and connected to the rest of the event. In addition, in collisions of composite particles there is a possibility that several parton pairs undergo separate hard or semihard scatterings. They are referred to as **'multiple interactions'**. The event generators use phenomenological models and parametrisations from existing data to simulate effects on the hadronic final state.

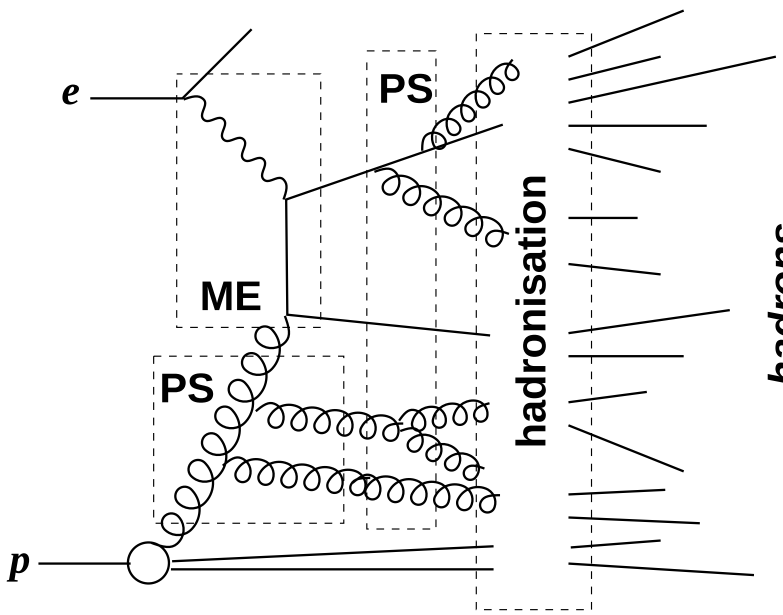

Figure 1.18: *A schematic illustration of an event generator with initial and final parton shower (PS), matrix element (ME) and hadronisation.*

The final state particles (hadrons) characterised by their four momenta are passed in the second step to the **simulation of the detector and trigger response**. The H1 detector simulation (H1SIM) is based on GEANT 3 [32] and includes a description of the detector components, the materials they are made of, their geometry and positions. Possible changes of the geometry from run to run are considered. Trajectories of the particles through the detector are calculated taking into account physics processes such as energy loss and multiple scattering. Particle decays are simulated according to particle lifetimes. Subsequently, the detector response is simulated. The output of the simulation has the same format as the real data recorded by the detector and can therefore be run through the same event reconstruction and physics analysis chain. In this way the Monte Carlo model predictions include the detector acceptance and efficiency and thus can be compared directly to the experimental data.

In this analysis two MC generators are used, PYTHIA 6.1 [31] and CASCADE 1.0 [33, 34]. The **PYTHIA Monte Carlo** implements the DGLAP evolution (see section 1.6) and on-shell matrix elements. PYTHIA is run in an 'all inclusive' mode and all processes are generated using massless matrix elements. The direct and resolved photon processes are simulated including excitation processes, in which one heavy quark (c or b) originates from the resolved photon or the proton. The CTEQ5L [8] parton densities are used for the proton and those of GRVG-LO [35] for the photon. Event samples for the processes $ep \to ec\bar{c}X$, $ep \to eb\bar{b}X$ and inclusive (light quark dominated) production were generated. The charm sample is compared to the measured charm data. The light quark sample and beauty sample are used to simulate the templates for background subtraction. The light quark sample simulates the background from fake muons, i.e. hadrons misidentified as muons and decays of light mesons into muons. For comparison with the flavour inclusive sample an inclusive PYTHIA data set is used. The probabilities of various processes as simulated by PYTHIA for the charm MC and inclusive MC are shown in table 1.1.

Process	PYTHIA No.	Name	Type	$x_\gamma^{obs} \leq 0.75$		$x_\gamma^{obs} > 0.75$	
				Charm Sample [%]	Flavour Inclusive Sample [%]	Charm Sample [%]	Flavour Inclusive Sample [%]
$\gamma g \to Q\bar{Q}$	135	direct	d	16.2	4.7	72.0	43.4
$gg \to Q\bar{Q}$	53	norm. res.	r	1.5	1.5	0.2	0.34
$Qg \to Qg$ +c.c.	28	excitation	r	61.0	56.8	17.0	33.7
$Qq \to Qq$ +c.c.	11	uds comp.	r	19.2	12.5	5.3	7.7
$q\bar{q} \to Q\bar{Q}$	12	-	r	0.55	0.16	0.1	0.1
$\gamma Q \to gQ$ +c.c.	131	-	d	1.59	0.85	5.3	8.5
$gg \to gg$	68	-	r	-	23.3	-	6.1
$q\bar{q} \to gg$	13	-	r	-	0.2	-	0.1

Table 1.1: *The most important processes and their probability according to the PYTHIA simulation for the charm sample and flavour inclusive sample in two regions of x_γ^{obs}. Q denotes the heaviest quark in the process, q a light quark, γ stands for photon and g for gluon. Type 'd' denotes direct photon and 'r' resolved photon events. See next section for the definition of x_γ^{obs}.*

The **CASCADE Monte Carlo** generator is based on the CCFM evolution model (see section 1.6). CASCADE uses unintegrated parton densities and off-shell matrix elements. In this analysis the JS2001 set [33] is used. Resolved photon processes are not simulated separately, because k_t-factorisation includes partially a hadronic photon component. The final state parton showers, proton remnant treatment and hadronisation are adopted from JETSET which is part of the PYTHIA program. CASCADE is used as a cross check for comparisons between data and theory for the charm sample.

An overview of the properties and settings used for both Monte Carlo models is given in table 1.2. In both simulations the mass of the charm quark of 1.5 GeV is used as well as Lund string fragmentation supplemented with the Peterson fragmentation for heavy quarks, as mentioned above.

MC	PYTHIA	CASCADE
Evolution scheme	DGLAP	CCFM
Factorisation scheme	collinear	k_t
Matrix element	on-shell	off-shell
Version	6.1	1.0
Mode	massless (35 % excitation)	-
$\Lambda_{QCD} [GeV]$	0.192	0.2
Renormalisation scale	$m_q^2 + p_{t\,q\bar{q}}^2$	$4m_q^2 + p_{t\,q\bar{q}}^2$
Factorisation scale	$m_q^2 + p_{t\,q\bar{q}}^2$	$\hat{s} + Q_t^2$
Proton PDF	CTEQ5L	unintegrated JS2001
Photon PDF	GRV-LO	-

Table 1.2: *Overview of properties and settings used for MC models with leading order matrix elements and parton showers. Here m_q denotes the heavy quark masses, $p_{t\,q\bar{q}}$ the average of the transverse momenta of the two heavy quarks, $\hat{s}$ is the centre-of-mass energy squared and Q_t is the tranverse momentum of the heavy quark.*

Cross Section Integration Programs

Perturbative QCD calculations of heavy quark production in next-to-leading order are available in Monte Carlo integration programs. For photoproduction of heavy quarks the FMNR program [27, 36, 37] is used, which implements a massive scheme calculation. The output includes only the (two or three) parton four vectors. For a comparison with data in a limited phase-space these have to be evolved to hadron level and the decay of hadrons has to be modeled. Only then the kinematics of the decay products can be included in the definition of visible cross sections. More details about the FMNR program as well as the principle of Monte Carlo integration programs can be found in appendix D. The results of this analysis are at present not compared to any NLO calculation.

Chapter 2

Analysis Method

The aim of this analysis is to shed light on the production mechanisms involved in charm photoproduction at HERA, which are in leading order QCD represented by direct, resolved and excitation processes, as discussed in the previous chapter. In the direct processes ($\gamma g \rightarrow c\bar{c}$) and in the 'normal resolved' processes ($gg \rightarrow c\bar{c}$) a charm quark pair is produced in the hard interaction. In contrast to that, in the excitation processes ($cg \rightarrow cg$ and $cq \rightarrow cq$), which are supposed to represent the largest fraction of the resolved photon processes [38], the products of the hard interaction are a charm quark and a gluon.

A **charm enriched event sample** is studied, which consists of dijet events where one jet is tagged by a muon to originate from a charm quark. The origin of the second jet is investigated by exploiting its internal jet structure. The structure of this 'other jet' is expected to depend mainly on the type of the primary parton, as explained in the previous chapter. The 'other jet' can originate from a charm quark, a gluon or from a light quark. Thus this approach is sensitive to differences between cg and $c\bar{c}$ type of events.

Different methods to investigate the jet structure were studied. Results of the studies are discussed in appendix A. A variable called mean integrated jet shape was chosen to be used in this analysis. It will be explained in section 2.5. For comparison a sample of flavour inclusive dijet events is selected in tagged photoproduction. Such **flavour inclusive event sample** is dominated by light quark events. In both samples the dependence of the integrated jet shape is studied as a function of different jet variables like p_t^{jet}, η^{jet1}, E^{jet} and as a function of the x_γ^{obs} variable. In addition, direct enriched and resolved enriched events are investigated separately.

The results of the measurement for both samples, after background subtraction (in charm enriched case only), corrected to hadron level are compared to the pQCD predictions implemented in the Monte Carlo models. The most important aspects of the analysis are discussed in the following sections.

2.1 Investigated Jets

Jets are in this analysis reconstructed from the hadronic final state objects (see section 4.3) using the k_t-clustering algorithm with the p_t-weighted recombination scheme. Details of the jet reconstruction are discussed in section 4.4, jet selection is given in section 5.2. In case of charm enriched sample only the structure of the jet without muon is studied ('other jet'). This is not biased by the muon cuts. In case of flavour inclusive sample both jets are studied.

[1] The pseudorapidity η, corresponding to a polar angle θ, is given by $-\ln tan(\theta/2)$.

2.2 Tagging of Heavy Quarks Using the Semimuonic Decay Channel

Traditionally charm enriched events are tagged using D^* **mesons**, reconstructed via the golden decay channel ($D^{*\pm} \rightarrow K^{\mp}\pi^{\pm}\pi_s^{\pm}$). In the data taking period 1999-2000 there was no dedicated trigger at H1 to trigger D^* photoproduction events. Charm photoproduction tagged by D^* mesons could only be triggered via the scattered electron at a low angle, which limits the kinematic range and the statistics of the D^* sample [39]. Another possibility to tag charmed photoproduction is to tag charm events by a **lepton with a high transverse momentum**. In the present analysis a muon tag is used which leads to a larger number of events to be studied in comparison to the D^* tagged charm production. There is a dedicated trigger to trigger events containing a muon. However, background is also higher since the muon tag is not as clean as the D^* tag.

In frame of charm production so called 'open' and 'hidden' charm production is distinguished. In case of the open charm production heavy quarks fragment into hadrons containing only one charm quark, since in case of the hidden charm production bound $c\bar{c}$ states are created. Charm hadrons decay with a probability of almost 1.0 into hadrons containing a strange quark. The decay of a c-quark into a d-quark is strongly suppressed since the $|V_{cd}|$ element of the Cabibbo-Kobayashi-Maskawa Matrix is much smaller than the $|V_{cs}|$ element [3]. Typically the charm quark transforms via radiation of a W-boson into a strange quark. The charged W-boson can decay into a muon and a neutrino, which escapes detection. Such decay of a charm meson is schematically shown in figure 2.1. The branching ratio $c \rightarrow \mu X$ has been measured by the LEP experiments to be 0.098 ± 0.005 [40]. This branching ratio is large enough to be used in this analysis and the decay muon provides a clean experimental signature. This is desired since charm quark production is suppressed by about a factor of 5 with respect to the production of lighter quarks, due to its high mass.

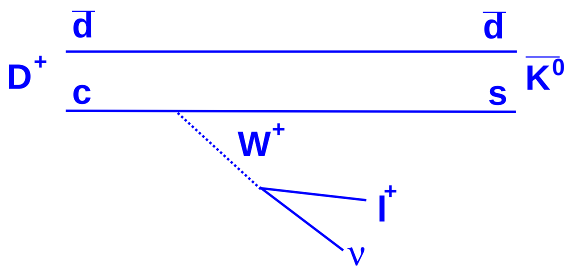

Figure 2.1: *Example of a semileptonic decay of a charmed hadron.*

In case of charm enriched event sample the jet algorithm provides an association of the muon to a jet. According to the charm PYTHIA MC, in 2% of charm events the muon is not included in any jet with other particles, but forms its own jet. Such events are excluded from the analysis. Muon associated to the jet enables us to define **variable** p_t^{rel}

$$p_t^{rel} = \frac{|\vec{p_\mu} \times (\vec{p_{jet}} - \vec{p_\mu})|}{|\vec{p_{jet}} - \vec{p_\mu}|}, \quad (2.1)$$

where $\vec{p_{jet}}$ and $\vec{p_\mu}$ are the momentum vectors of the muon and the jet, respectively. p_t^{rel} represents relative momentum of the muon with respect to the axis of the rest of the jet which contained the muon. This variable is used for enrichment of charm events, as explained in the next section.

2.3 Background Types

An event selection requiring dijet events containing a muon does not result in a pure charm sample. There are various background processes producing similar final state topologies. The two main sources are open beauty production and events from the production of light quarks, u, d and s.

- **Open beauty production** results in topologies which are very similar to open charm production. Muons can appear directly as decay products of beauty hadrons (on the quark level $b \to \mu X$) or via cascade decays ($b \to cX$ where $c \to \mu Y$) with a total branching ratio of about 20 %. The cross section for the production of beauty quarks at HERA is about 200 times lower than the one for charm production. However, the high p_t muon requirement also enriches beauty events and they become an important background for the charm measurement.

  Since the beauty quark has an approximately three times higher mass than the charm quark, beauty decays are characterised by higher p_t^{rel} values in contrast to charm decays, where the mass difference between the charm and strange quark is smaller. Therefore we select events with low p_t^{rel} to reduce the beauty contamination of the sample. Details are discussed in section 5.2.

- A study of the **light quark originated muon background** was performed at H1 [41] for dijet + muon type of events. The modeling of the fake muon background distributions was investigated using the flavour inclusive Monte Carlo samples. It was found that the majority, i.e. about 90 %, of the selected muons in the light quark event sample originates from charged kaons and pions, which leave the the central tracker volume undecayed. The remaining 10 % are muons which result from inflight decays of charged kaons and pions inside the beam pipe (5 %) or in the active volume of the central track detector and central silicon tracker (5 %). See section 3.2.1 for the description of the detectors.

- **Other background sources**: Studies performed in [42] show that the required topology (two jets and a muon) is an unlikely one for heavy vector meson decays as well as for overlay of dijet events with a cosmic muon. Therefore these sources of background can be neglected.

The remaining background in the charm enriched sample is subtracted from the data on a statistical basis. Details of background determination and subtraction will be discussed in sections 5.2 and 6.2.

2.4 Experimental Signature of Resolved Processes

Direct and resolved processes differ in the way in which the photon participates in the hard interaction. In direct processes the photon enters the hard interaction directly, while in resolved processes the photon interacts via hadronic states. The structure of the photon is resolved and only one parton takes part in the hard subprocess (see figure 1.9). The difference between these two types of photon interactions are reflected in the fraction of the photon momentum entering the hard interaction. The **variable** x_γ^{obs} representing the fraction of the incoming photon energy which participates in the production of the two highest p_t jets is in this analysis defined as

$$x_\gamma^{obs} = \frac{\sum_{h \in Jet_1}(E - p_z) + \sum_{h \in Jet_2}(E - p_z)}{\sum_h (E - p_z)}. \tag{2.2}$$

The sums in the numerator run over the particles associated with the two jets and that in the denominator over all detected hadronic final state particles. This equation is discussed in detail in section 4.5.

Direct and resolved processes tend to populate different regions in the x_γ^{obs} distribution. For the direct process x_γ^{obs} approaches unity, because the hadronic final state consists of only the two hard jets and the proton remnant in the forward region which contributes little to $\sum_h (E - p_z)$. In resolved processes x_γ^{obs} can be small.

In this analysis we investigate the jet structure in direct enriched and resolved enriched events defined by $x_\gamma^{obs} > 0.75$ and $x_\gamma^{obs} \leq 0.75$, respectively. This enables to study separately direct and resolved processes.

2.5 Jet Shape Analysis Strategy

The main idea of the analysis is to distinguish processes using the differences in the jet structure of quark and gluon initiated jets. The most common way of resolving the internal jet structure, inspired by the cone-type algorithms, is to measure the energy distribution perpendicular to the jet axis direction. The physical observables used for this purpose are the **integrated jet shape** $\psi(r)$ and **differential jet shape** $\rho(r)$ [43]. $\psi(r)$ is defined as the fraction of the jet transverse momentum deposited within a cone of the radius r around the jet axis relative to the transverse momentum of the jet deposited in a bigger cone with radius $R = 1$:

$$\psi(r) = \frac{\sum_{i, r_i < r} p_{t,i}}{\sum_{i, r_i < R} p_{t,i}}, \tag{2.3}$$

where the sums run over the hadronic final state objects. $\rho(r)$ is defined as the fraction of the jet transverse momentum deposited within two cones of the radii r and Δr around the jet axis relative to the total transverse momentum of the jet

$$\rho(r) = \frac{d\psi(r)}{dr} = \frac{\sum_{i, r_i \in (r, r+\Delta r)} p_{t,i}}{\sum_{i, r_i < R} p_{t,i}}. \tag{2.4}$$

Visualisations of both definitions are shown in figure 2.2. Transverse momenta of the particles $p_{t,i}$ are measured with respect to the beam axis. The distances of the individual particles forming the jet to the jet axis are defined as $r_i = \sqrt{\Delta\eta_i^2 + \Delta\phi_i^2}$, where $\Delta\eta_i$ and $\Delta\phi_i$ are the distances to the jet axis in pseudorapidity η and azimuthal angle ϕ, respectively. Generally, the parameter r can vary between 0 and R. In this analysis $R = 1$, according to the resolution parameter R_0 in the k_t-clustering jet algorithm (see section 4.4), which is in this analysis equal to 1. Note that in case of the k_t-clustering jet algorithm particles can occur which belong to the jet, although the distance to the jet axis is $r_i > R_0$. Those are not taken into account in this analysis. It was checked that considering those particles in the $\psi(r)$ and $\rho(r)$ definitions does not change the conclusions obtained without them.

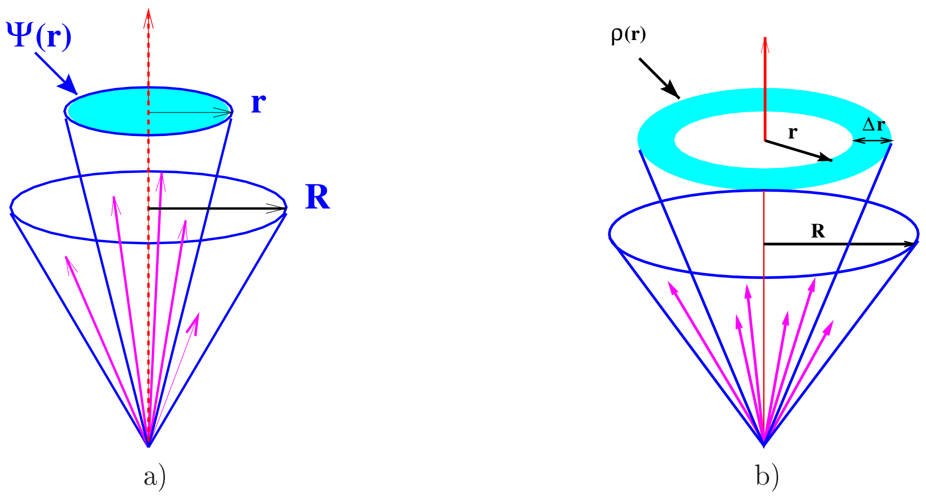

Figure 2.2: *Visualisation of the integrated jet shape a) and differential jet shape b).*

In this analysis the **mean integrated jet shape** is measured as

$$\langle\psi(r)\rangle = \frac{1}{N_{events}} \sum_{events} \psi(r), \tag{2.5}$$

where the mean is calculated over all investigated jets from all events of the selected data sample. Analogically the **mean differential jet shape** is measured. The averaging over events means to consider one jet per event in the charm enriched sample and two jets per event in the flavour inclusive sample. Close to the jet axis, the jet shape is dominated by collinear gluon emission, whereas at large angles from the jet axis, the jet shape reflects large angle gluon emissions, which can be calculated perturbatively.

Due to differences in the formation processes of charm and gluon jets the latter are expected to be broader and contain more particles [19]. Narrower jets are characterised by larger values of $\langle\psi(r)\rangle$. Therefore one expects

$$\langle\psi(r)\rangle_{quark} > \langle\psi(r)\rangle_{gluon} \;\; (for \;\; r < R), \tag{2.6}$$

because for gluon jets the full transverse momentum is reached more slowly and at a given radius the value is on average smaller. This kind of difference between gluon and quark jets is also reflected in the distributions of the mean differential jet shape. Distribution of $\langle\rho(r)\rangle_{gluon}$ is shifted to larger values of r than $\langle\rho(r)\rangle_{quark}$.

2.6 Measurements by Other Experiments

The method of the jet shape measurement has been already used by other experiments.

- The mean integrated jet shape for gluon, light quark and beauty quark initiated jets was measured by OPAL [23]. Figure 2.3 a) shows the differences in the $\langle\psi(r)\rangle$ distributions of light quark and gluon jets, as observed for high jet energies in e^+e^- collisions at LEP. Large differences are observed. The gluon jets were found to be much broader than the quark jets, as predicted by pQCD. The jet energies in the present analysis are lower but still high enough to expect significant differences in the jet shapes of gluon and charm initiated jets. The shape of the charm quark initiated jets is expected to be similar to the light quark jets, because the mass difference between the charm and the strange quark is not too high. In contrast to that, beauty quark initiated jets were measured to be broader than light quark jets and very similar to gluon jets (Fig. 2.3 b). This behavior is caused by the large mass difference between the beauty and the charm quark.

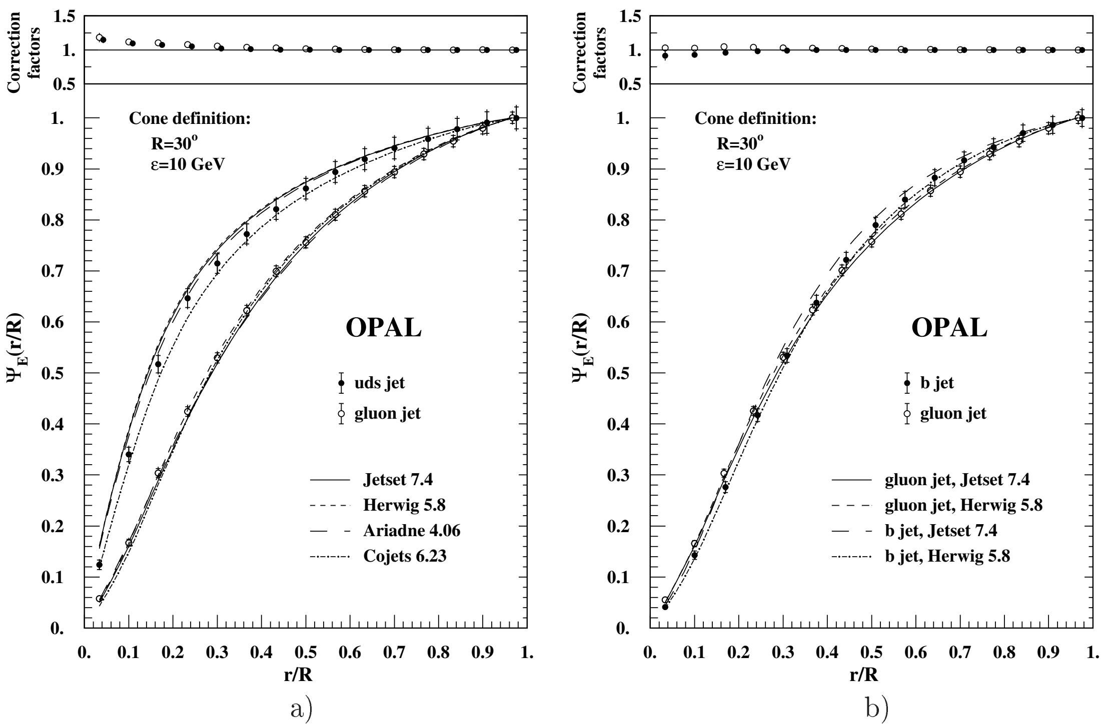

Figure 2.3: *Mean integrated jet shape (here labeled $\Psi_E(r/R)$) for a) light quark and gluon jets and b) beauty and gluon jets as measured by OPAL [23].*

► The integrated jet shape was measured by H1 for a flavour inclusive DIS dijet event sample [44] (Fig. 2.4) and it was found to be reasonably described by the Monte Carlo model LEPTO, which predicts a fraction of $\approx 80\,\%$ photon-gluon fusion events with two quarks in the partonic final state. Thus the observed jets are consistent with being mainly initiated by quarks, as expected in DIS.

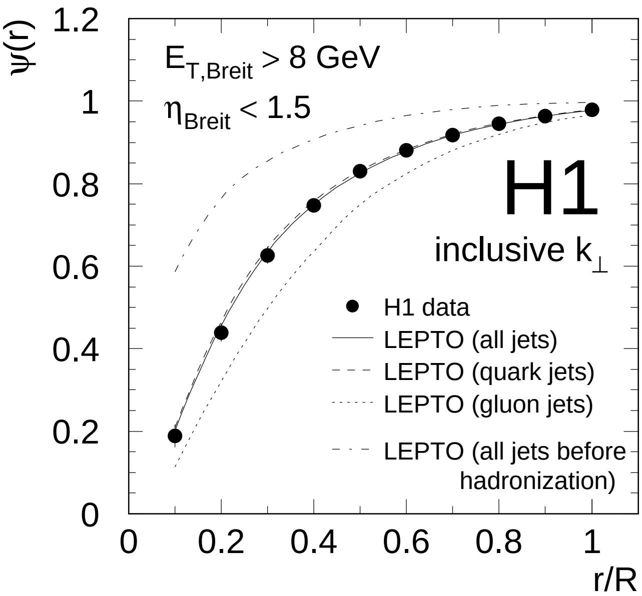

Figure 2.4: *Jet shape measured by H1, for jets produced in the range* $10 < Q^2 \lesssim 120\,GeV^2$ *and comparison to the Monte Carlo models [44].*

► A similar flavour inclusive measurement was performed by ZEUS for photoproduction events [45] (Fig. 2.5 a). The observed broadening of jets as η^{jet} increases is consistent with an increase of the fraction of gluon initiated jets. There one concludes that the prediction of PYTHIA, including resolved and direct processes, fails to describe the strong broadening of the measured jet shape for forward rapidities. The present analysis does however not cover this forward η^{jet} region, in this analysis $|\eta^{jet}| < 1.73$.

► ZEUS also measured the integrated jet shape for the 'other jet' in a D^*-tagged dijet photoproduction sample [46] (Fig. 2.5 b). A difference between the total and the direct-enriched sample in the highest η^{jet} bin was observed. They conclude that the measurement in the highest η^{jet} bin is consistent with the presence of $cg \to cg$ processes.

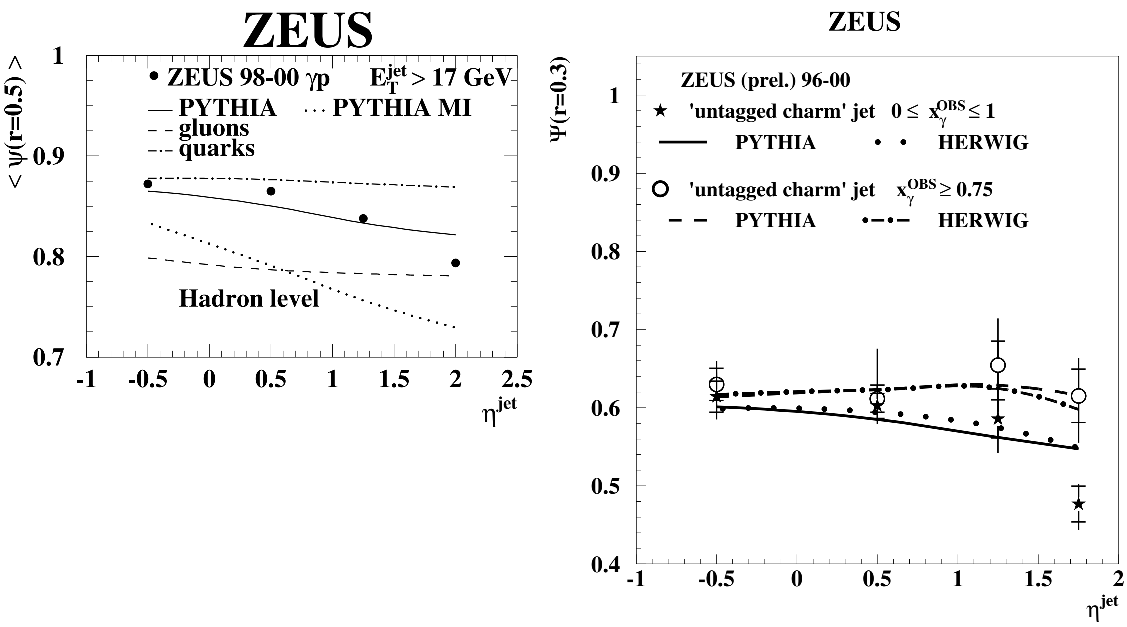

a) b)

Figure 2.5: *a) Integrated jet shape as measured by ZEUS for photoproduction events [45]. b) Integrated jet shape measured at fixed value of r=0.3 as a function of* η^{jet} *for the 'untagged charm' jet from the* D^* *tagged charm events as measured by ZEUS [46]. Shown are the total and direct enriched data samples for jets with* $p_t^{jet} > 7(6)\,\mathrm{GeV}$ *in photoproduction in the central region.*

The analysis presented in this thesis selects a similar kinematic range of charm production as the ZEUS analysis. Only the η^{jet} range is restricted to more central region. The fundamental difference is the charm tagging method (muon versus D^*), which causes a completely different composition of background and thus provides an independent approach. Since we are especially interested in the contribution of gluon jets in resolved processes in comparison to direct processes, we compare directly jet shapes for high and low x_γ^{obs} values.

Chapter 3

The H1 Experiment at HERA

In this chapter the electron-proton collider HERA is introduced briefly. Then a short description of the H1 detector components most important for this analysis follows, including tracking, calorimetry, detection of muons, luminosity system and trigger system.

3.1 The HERA Collider

The electron-proton storage ring HERA (Hadron Elektron Ring Anlage) is situated at DESY (Deutsches Elektronen Synchrotron) in Hamburg, Germany. Before injection into the HERA storage ring both the electrons and the protons are accelerated in pre-accelerators which are shown in figure 3.1 a). Further are electrons and protons accelerated in two independent accelerators in HERA tunnel, which is 6.3 km in circumference and $10 - 25$ m under ground. In HERA (see figure 3.1 b) 27.5 GeV positrons[1] were collided with 920 GeV protons in the years 1999-2000, resulting in a centre-of-mass energy $\sqrt{s} \approx 320$ GeV.

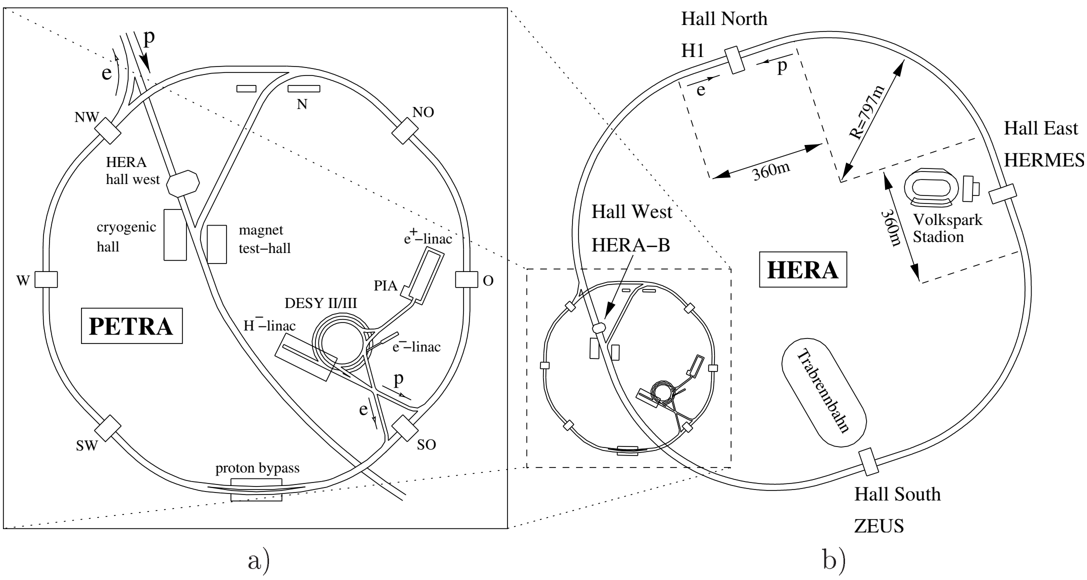

Figure 3.1: *The injectors and pre-accelerators of the HERA storage ring a) and the electron-proton collider itself with the four experiments b).*

[1]Further in this thesis the term electrons is used to denote both electrons and positrons.

The magnets of the proton storage ring produce a magnetic field of 4.7 T for bending the high momentum proton beam through the ring. These superconducting magnets operate at a temperature of 4.4 K. The magnets of the electron storage ring contain normal conductors producing a magnetic field of 0.165 T and operate at room temperature. The protons and electrons are stored in up to 220 bunches of $10^{10} - 10^{11}$ particles. A small number of non-colliding bunches, called 'pilot bunches', is usually preserved for studying beam induced background arising from interactions of the beam with the residual gas in the beampipe, or with its wall. The proton beam lifetime is rather large, of the order of 100 h, while the positron beam lifetime of about $10 - 20$ h limits the typical duration of luminosity fills to less than 15 h. When the beams have reached their final energy, they are tuned to collide each 96 ns at very small angles in the interaction regions of the H1 and ZEUS experiments dedicated to the measurement of electron and proton collisions. In addition there are two beam-target experiments, HERMES studying the spin structure of the nucleons and HERA-B focused on fixed target heavy flavour production.

3.2 The H1 detector

The analysis described in this thesis is based on a data sample collected with the H1 detector in the years 1999-2000. The H1 detector is described in detail in [47]. The H1 experiment (see figure 3.2) is a **typical multi-purpose collider detector** with approximate dimensions $12 \times 15 \times 10\,\mathrm{m}^3$ and a weight about 2800 t. The momentum and energy of particles produced in an *ep* interaction are measured. The identification and precise energy measurement of the scattered electron, a high resolution for the hadronic system measurement and a good hermicity to recognize missing transverse energy were of importance in designing the detector. The unequal beam energies are taken into account in an asymmetric detector configuration, namely its enhanced instrumentation in the proton direction. The fine granularity liquid argon calorimeter enables the measurement of both charged and neutral hadrons, photons and for high Q^2 events the scattered electrons. Since the electron most likely scatters in backward direction, the SpaCal calorimeter has been built there in order to support the electron identification. It also servers for measurement of photons. The tracking system as well as the calorimeters are located inside the superconducting coil, which produces a magnetic field of ~ 1.15 T for momentum measurement. This layout minimizes the dead material in front of the calorimeter. The whole apparatus is surrounded by an iron yoke to return the magnetic flux of the solenoid. The iron yoke is instrumented and used as central muon detector.

H1 uses a **right-handed coordinate system**. The origin of the coordinate system is located at the nominal interaction point. The positive z-direction is defined by the beam axis in the direction of the proton beam, called the forward direction. The positive x-axis points to the ring centre, the positive y-axis points upwards. The polar angle θ is defined with respect to the positive z-axis and the azimuthal angle ϕ in the xy-plane such that $\phi = 0$ points to the positive x-axis.

In the following the components of the experiment relevant for the present analysis will be briefly described.

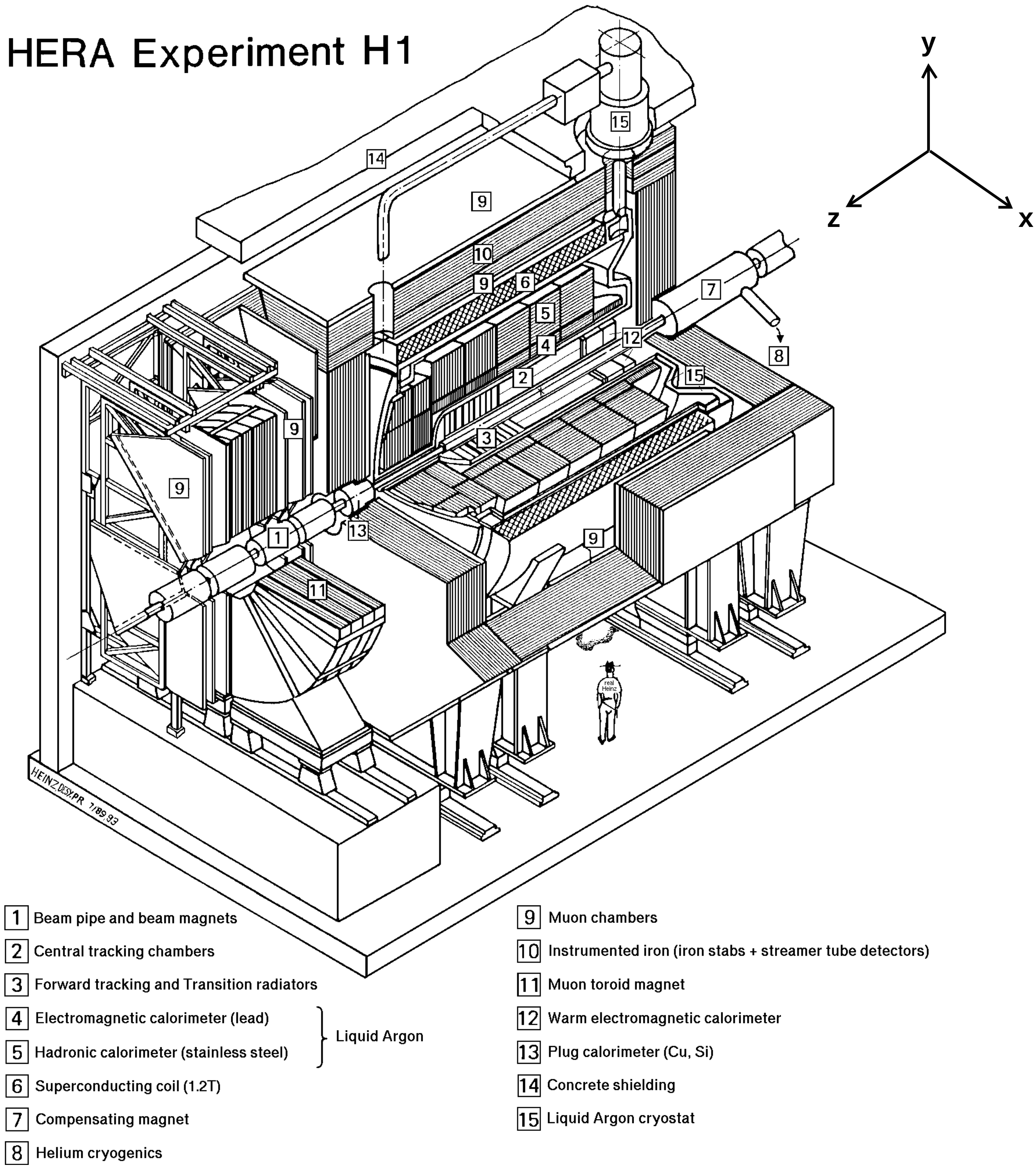

Figure 3.2: *Schematic view of the H1 detector and definition of the coordinate system.*

3.2.1 Tracking Detectors

The purpose of the tracking chambers is the reconstruction of charged particles trajectories. In addition, information on event vertices, i.e. the position of the *ep* interaction point (primary vertex) and decays of long-lived particles (secondary vertices), is obtained by extrapolating the reconstructed tracks back to the beam axis.

The H1 tracking system consists of the Forward Track Detector (FTD) and the Central Track Detector (CTD) (see Fig. 3.3). For this analysis only the CTD is used, covering a polar angular range of $15° \lesssim \theta \lesssim 165°$. The CTD consists of the Central Silicon Tracker (CST), the Central Jet Chamber (CJC) and the Central Inner and Outer z-Drift Chamber (CIZ and COZ), which are shown in a radial view in figure 3.4. The CTD provides a good angular and vertex resolution as well as the charge determination of the particle tracks.

The Central Inner and Outer Proportional Chamber (CIP and COP) are used for triggering purposes only. Part of the FTD is also used by triggers. More details about the tracking detectors can be found in [48].

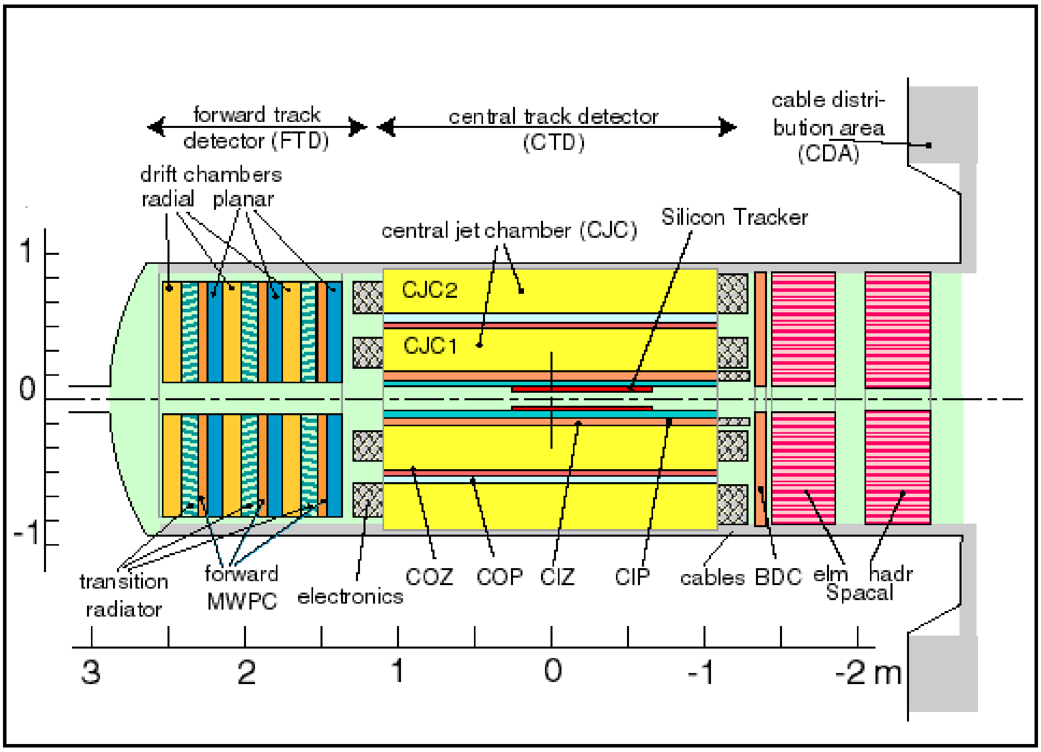

Figure 3.3: *Side view of the H1 tracking system. In addition to the Forward Track Detector (FTD) and Central Track Detector (CTD) the backward calorimeter SpaCal is also shown.*

Central Jet Chamber (CJC)

The CJC is the main tracking device, as shown in figure 3.3, consisting of two gas-filled coaxial cylindrical drift chambers CJC1 and CJC2. It covers the polar angular range of $26^\circ \lesssim \theta \lesssim 155^\circ$. The momentum and direction of the charged particles are measured via ionisation in a gas. The drift velocity and the time at which the charge collected by the sense-wires is measured, define the position of the hits in the $r-\phi$ plane. CJC1 (2) is built of 30 (60) drift cells with 24 (32) sense wires each. The sense wires of the chambers are strung parallel to the beam axis to give accurate resolution in the $r-\phi$ plane. The drift cells are tilted by about 30° with respect to the radial direction. 'Lorentz angle', which is the angle between the electrical field and the drift direction of the electrons, is approximately compensated by this tilt. Therefore the electrons liberated by the charged particles drift approximately perpendicular to the particle's direction of the flight. This results in optimum track resolution and solves drift ambiguities caused by mirror track segments.

The spatial resolution of the CJC in the $r-\phi$ plane is measured to be about $170\,\mu$m and the time resolution is about 0.5 ns. The transverse momentum of charged tracks can be determined with precision up to $\sigma_{p_t}/p_t^2 = 0.01/\text{GeV}$. The sense wires are read out at both ends and thus allowing determination of the z-coordinate by means of charge division. However, the z-resolution achieved with this method is only a few centimeters.

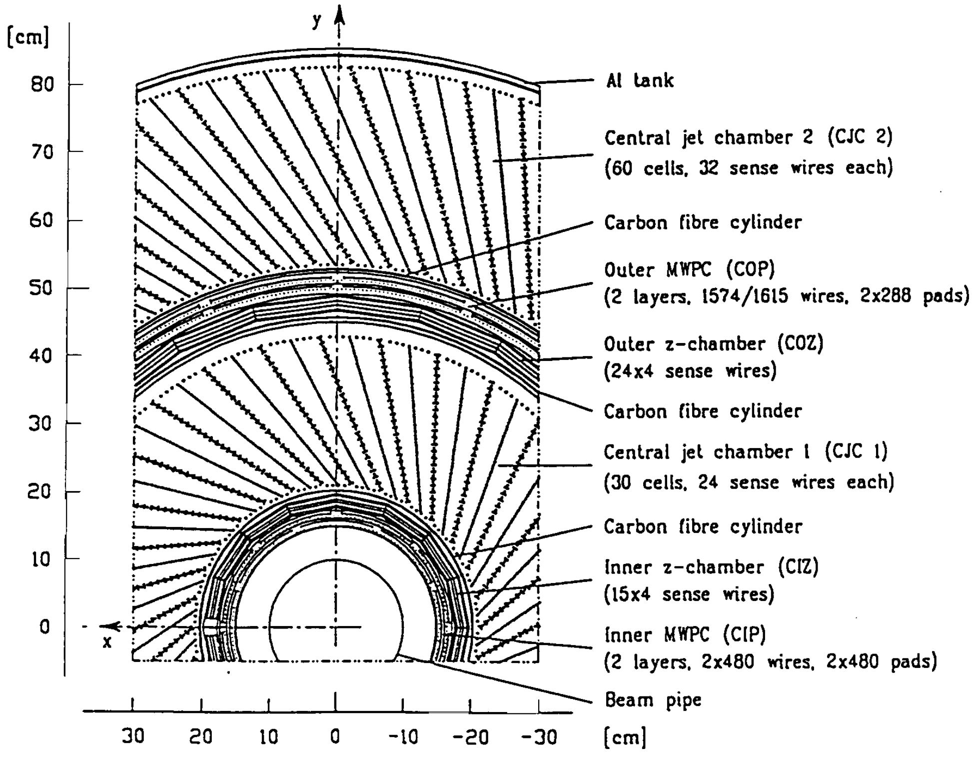

Figure 3.4: *Cross section of the central tracking chambers perpendicular to the beam direction.*

Central Inner and Outer z-Drift Chambers (CIZ and COZ)

The measurement of the z-coordinate is mainly performed with the z-drift chambers CIZ and COZ. Their signal wires are perpendicular to the z-axis. These two thin drift chambers (see Fig. 3.4) sandwiching the CJC1 yield a z-resolution of about $\approx 300\,\mu$m. The chambers cover the polar angular range $16° \lesssim \theta \lesssim 169°$ (CIZ) and $25° \lesssim \theta \lesssim 156°$ (COZ). The CIZ consists of 15, the COZ of 24 similar rings, which are arranged along the beam axis, each ring containing four sense wires. The sense wire planes of the CIZ are tilted by 45° with respect to the radial direction, while those of the COZ are oriented perpendicular to the beam axis.

Central Inner and Outer Proportional Chambers (CIP and COP)

The multiwire proportional chambers CIP and COP, shown in figure 3.4, are cylindrical double layer chambers. The CIP, covering a polar angular range of $8° \lesssim \theta \lesssim 172°$, consists of pad cathodes, which are 60-fold segmented in z and eight-fold in ϕ. Both layers are rotated by 22.5° against each other in order to achieve an effective 16-fold segmentation. The pads of the COP are 18-fold segmented in z and 16-fold in ϕ. They provide a fast timing signal with a better time resolution than the HERA bunch crossing interval and are used for triggering. A four-fold coincidence of pads of both double layer chambers leads to a first estimation of the z-position of the vertex. For more detail about the z-vertex trigger see section 5.1.

Forward Track Detector

The FTD serves for track measurement in the forward direction. It covers the angular range of $5° \leq \theta \leq 30°$ and consists of three supermodules, as shown in figure 3.3. Each supermodule contains a forward proportional chamber (FPC), radial and planar drift chambers and a transition radiator. The FPCs consist of multiwire proportional chambers which provide fast signals used for triggering purposes.

Central Silicon Tracker (CST)

The CST consists of two cylindrical layers of double sided semiconductor (silicon) sensors, as shown in figure 3.5. It has an inner radius of 5.57 cm and an outer radius of 9.7 cm. The CST covers the polar angular range of $30° \leq \theta \leq 150°$. The inner (outer) layer contains 12 (20) identical and slightly overlapping 'ladders', which are arranged around the z-axis. Each ladder consists of six silicon sensors in the z-direction and readout electronics at both ends. Due to the voltage between the inner and outer surface of the sensors, the electrons and holes, produced by the charged particles, drift to the inner or outer side. Here strips are mounted, from where the deposited charge is read out. Since the strips of both sides are perpendicular to each other it is possible to measure the $r - \phi$ -coordinate as well as the z-coordinate. A hit in three dimensional space is determined from the position of the sensor and the two coordinates. In the $r - \phi$ plane a resolution of 12 μm is achieved and in the z-coordinate a resolution of up to 22 μm is obtained. Possible CST hits are assigned to the tracks measured in the CJC and improved track parameters are found. More details about the CST can be found in [49].

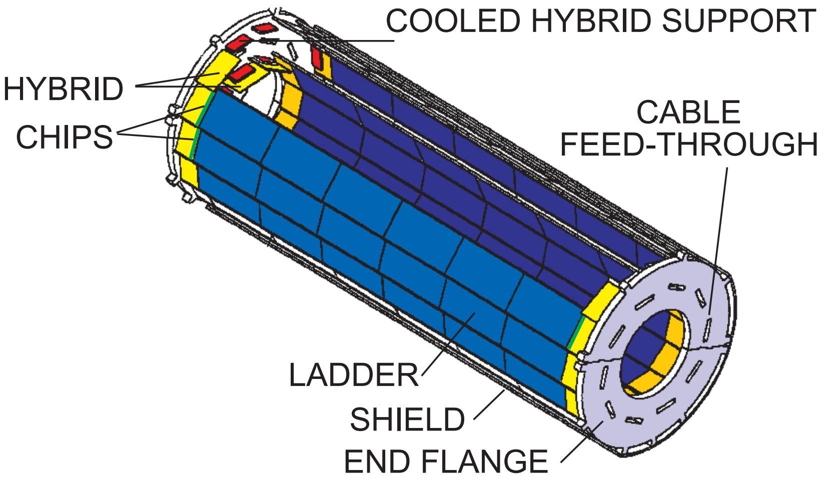

Figure 3.5: *Construction of the Central Silicon Tracker.*

3.2.2 Calorimetry

The main calorimeters in H1 are: the Liquid Argon Calorimeter (LAr), the Spaghetti Calorimeter (SpaCal), the Tail Catcher and the Plug Calorimeter. While the LAr is important for the reconstruction of the hadronic final state and measurement of the scattered electron at $Q^2 \gtrsim 100\,\mathrm{GeV}^2$, the SpaCal is used mainly to detect and measure the scattered electron in the low Q^2 regime. The Tail Catcher will be mentioned in section (3.2.3). The Plug Calorimeter, closing the gap between the LAr and the beam pipe in the forward direction, will be not described here.

Liquid Argon Calorimeter (LAr)

The LAr encloses the forward and central part of the detector with a polar angle coverage of $4° \leq \theta \leq 154°$ and with full azimuthal acceptance. The highest granularity is in the forward direction. It is situated inside of the magnetic coil in order to minimize the passive material improving the electron and the hadronic energy measurement. It is segmented along the beam axis in eight wheels, as shown in figure 3.6 and each wheel is constructed from identical octants. It has almost 45000 readout channels in total, called calorimeter cells. Particles deposit their energies via different mechanisms, which requires the LAr to be divided in an inner electromagnetic section and an outer hadronic section. The electromagnetic and hadronic sections use lead and stainless steel absorber plates respectively. In both cases liquid argon is used as the active medium, because of its good stability, ease of calibration, possibility of fine granularity and homogenity. The depth of the electromagnetic calorimeter varies with θ between 20 and 30 radiation lengths, while the depth of the hadronic calorimeter lies between 5 and 8 interaction lengths. The energy resolution measured in test beams is $\sigma_{em}(E)/E \approx 0.11/\sqrt{E[GeV]} \oplus 0.01$ for an electromagnetic shower and $\sigma_{had}(E)/E \approx 0.50/\sqrt{E[GeV]} \oplus 0.02$ for a hadronic shower. The LAr is a non-compensating calorimeter, i.e. the response to hadrons is about 30 % lower than the response to electrons of the same energy. An energy dependent reweighting is used to equalize the response. More information about the LAr calorimeter can be found in [50].

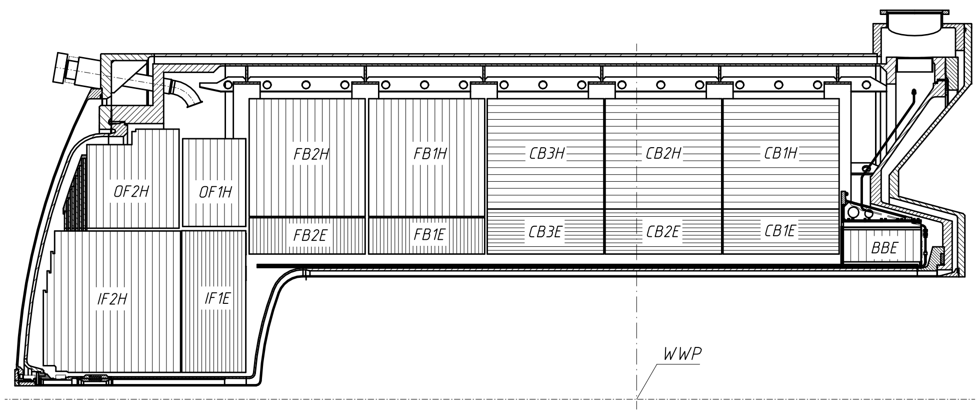

Figure 3.6: *Cross section through the upper half of the Liquid Argon Calorimeter is shown. The names of electromagnetic sections end with 'E', those of hadronic sections with 'H'. The horizontal and vertical lines indicate the orientation of the absorber plates.*

Spaghetti Calorimeter (SpaCal)

The angular region of $153° \leq \theta \leq 178°$ is covered by the SpaCal [51], a scintillating-fiber calorimeter with lead absorbers. The main design goals of the calorimeter are a good coverage of the region close to the beam pipe, high angular and energy resolution for electrons and capability of providing hadronic energy measurement. The SpaCal has an electromagnetic and a hadronic section, both 25 cm thick. Since the SpaCal is mainly used for the identification of the scattered electron, the hadronic part is only about one interaction length deep. The electromagnetic energy resolution is $\sigma_{em}(E)/E \approx 7\%/\sqrt{E[GeV]}$. In the hadronic section, energies are measured with a resolution of $\sigma_{had}(E)/E \approx 30\%/\sqrt{E[GeV]}$. High resolution in both space and time is achieved, the latter being used for triggering based on time-of-flight methods. Acceptance of the SpaCal corresponds to photon virtualities in the range $1 \leq Q^2 \leq 100\,\mathrm{GeV}^2$. In this analysis the absence of the scattered electron in the detector volume is used to select photoproduction events.

To measure measure the tracks of the scattered electrons, the Backward Drift Chamber is used, covering the region of $151° \leq \theta \leq 177.5°$.

3.2.3 Central Muon Detector

The muon system is located outside the central calorimeters, because of the high penetration power of the muons in contrast to hadrons and electrons. The iron yoke, which guides the magnetic flux produced by the superconducting coil, is instrumented with detectors which form the Central Muon System. It is divided into four regions, as can be seen in Fig. 3.7: the backward endcap ($130° \lesssim \theta \lesssim 171°$), the backward and forward barrel ($35° \lesssim \theta \lesssim 130°$) and the forward endcap ($4° \lesssim \theta \lesssim 35°$). The entire detector is split up into 64 modules. Each module consists of ten 7.5 cm thick iron plates sandwiching ten layers of limited streamer tubes and additional 6 layers are placed on the inner and outer side of the module, as shown in figure 3.8. Layers 3, 4, 5, 8 and 12 are used for trigger purposes. The individual streamer tubes have a cross section of $1 \times 1\,\mathrm{cm}^2$ and are of different length depending on the size of the module to which they belong. Eight of these tubes form a profile, two profiles build a gas tight element and several elements form a plane. The sense wires are strung parallel to the x-axis in the endcaps and in the z-direction in the barrel region. Five planes (1, 2, 7, 14, 15) are equipped with strip electrodes, while the others use pads. The strip electrodes are glued perpendicular to the sense wires in order to provide a two dimensional measurement. The strips are 1.7 cm wide, while the pads are of the size $25 \times 25\,\mathrm{cm}^2$ in the endcaps and $50 \times 40\,\mathrm{cm}^2$ in the barrel. While the wires and strips are used for muon identification the pads are mainly used to detect the energy of hadronic showers leaking out of the LAr calorimeter (Tail Catcher).

The wires and strips are read out digitally. Three dimensional tracks are reconstructed with information from 16 wire layers, 5 strip layers and 11 pad layers. A spatial resolution of $3-4$ mm for the wire and $10-15$ mm for the strip hits is achieved. The momentum resolution is estimated to be about 30 % for the particles in the barrel and the momentum measured by the CMD is not used in this analysis. More information about the myon system can be found in [52].

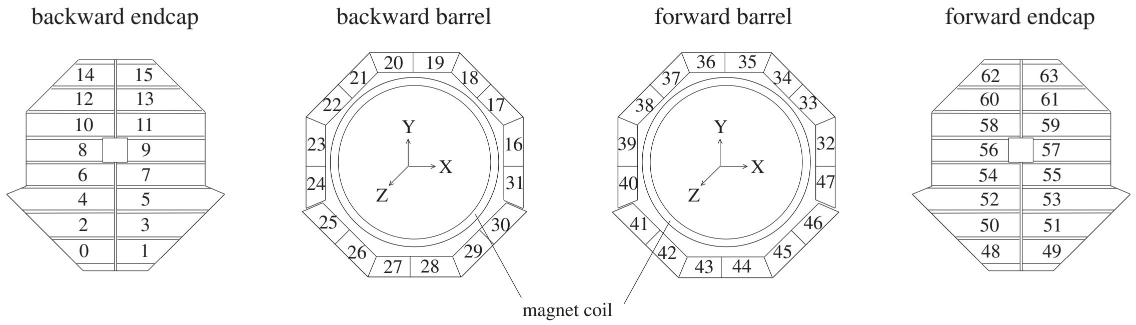

Figure 3.7: *The four parts of the Central Muon Detector, which is divided into 64 modules.*

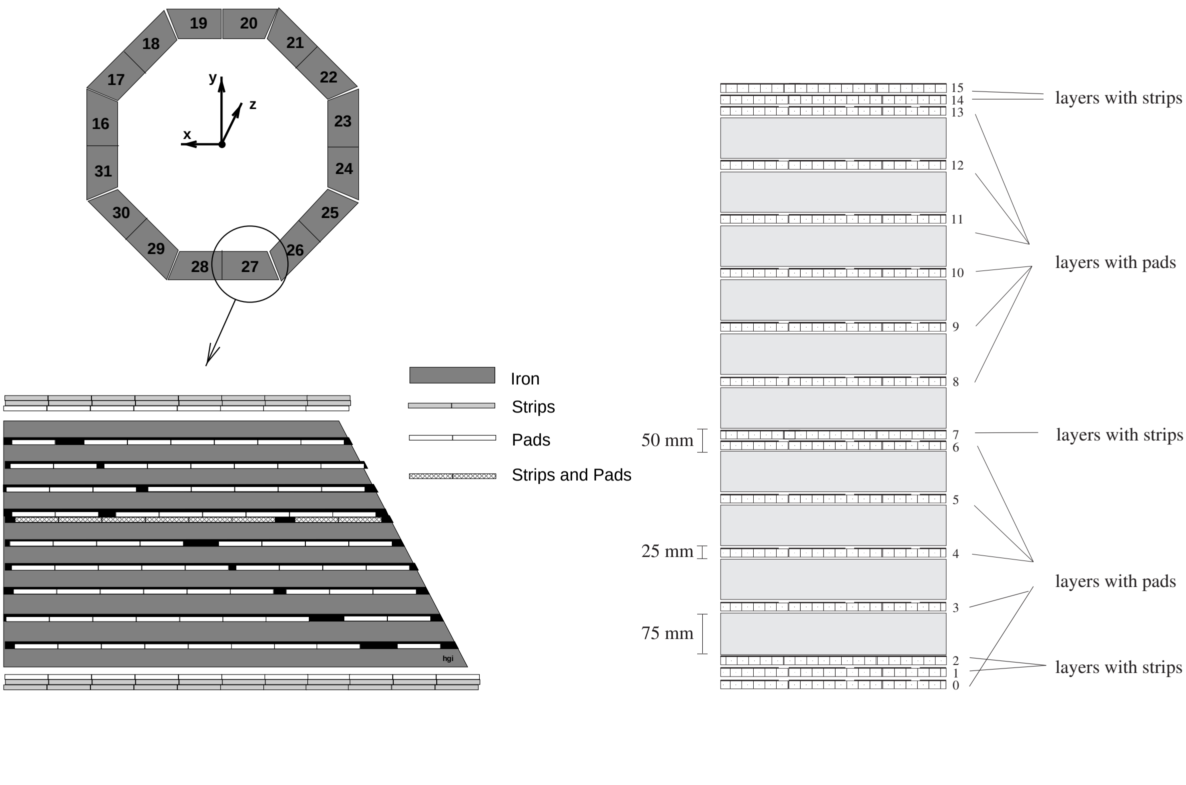

Figure 3.8: *Cross section view of an instrumented iron module. The streamer tube layers 3, 4, 5, 8, and 12 are used for trigger purposes.*

3.2.4 Luminosity System

The luminosity system of H1 is used for a fast online relative luminosity determination and to control the electron beam steering and monitoring by HERA, as well as for the absolute luminosity measurement after applying offline corrections. It consists of crystal Čerenkov calorimeters located close to the beampipe, downstream in the direction of the electron beam, as shown in figure 3.9. The luminosity is measured during the data taking by the Bethe-Heitler process $ep \to ep\gamma$, which has a large and well known cross section [53] and is insensitive to the internal proton structure. Electrons are detected in the **Electron Tagger** (ET33) at $z = -33.4\,\mathrm{m}$, photons in the **Photon Detector** (PD) at $z = -103.1\,\mathrm{m}$. For an online determination of the luminosity the rate of coincident detection in both detectors is used. After offline calibration the luminosity is determined more precisely from the photon rate in the PD only [54]. The main background comes from bremsstrahlung processes with the residual gas in the beampipe ($eA \to eA\gamma$). These events are estimated to contribute at the level of 10 % of the $ep \to ep\gamma$ rate and can be subtracted using data from the electron pilot bunches, which do not interact with corresponding proton bunches. This leads to a precision better than 2 % for the measurement of the integrated luminosity.

Furthermore, the ET33 is also used to trigger and to detect electrons in photoproduction events where the electrons are scattered under a very small angle. Electrons in events with $Q^2 < 0.01\,\mathrm{GeV}^2$ and $0.2 \lesssim y \lesssim 0.7$ can reach the ET33.

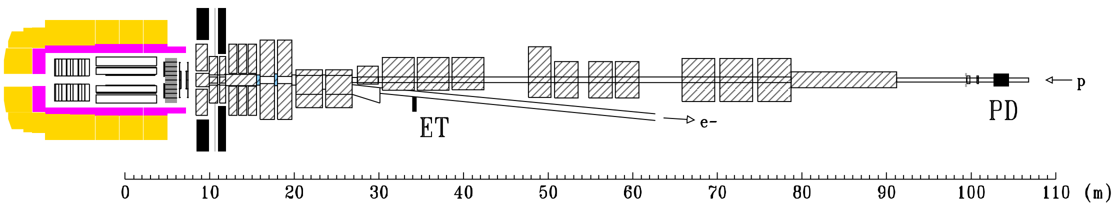

Figure 3.9: *The H1 luminosity system, consisting of an electron tagger (ET) at* $z = -33.4\,\mathrm{m}$ *and a photon detector (PD) at* $z = -103.1\,\mathrm{m}$.

3.2.5 Trigger System and Data Acquisition

Electron and proton bunches collide every 96 ns, corresponding to a frequency of 10.4 MHz. The rate of physically interesting ep interactions is much lower. In addition the rate of the background processes is several orders of magnitude higher than the ep event rate. The background arises mainly from collisions of the beam protons with the rest gas atoms within the beampipe (beam-gas interactions) and also collisions of beam particles with the beampipe or the material of the detector lead to background events (beam-wall events). Cosmic muons and synchrotron radiation have to be considered in addition. Due to the short time between two bunch crossings and limited bandwidth for the data transfer to mass storage devices, it is not possible to read out the whole detector for every bunch crossing and to select the interesting events afterwards. Thus a four level trigger system, schematically shown in figure 3.10, is used to decide whether to keep an event or not. In this way the input rate of about 100 kHz is decreased to about 10 Hz.

First trigger level (L1): Since the decision time of some detector components is significantly larger than the time between two bunch crossings, the detector information is first stored in buffers (pipelines). In case of a positive trigger decision the buffers are read out. During this time no data can be collected (dead time). The L1 decision is based on 256 special trigger signals from various detector components, called trigger elements, which are combined into 128 so called subtriggers. The trigger decision is positive if the event is accepted by at least one of the subtriggers. Depending on the run and background conditions, the L1 subtriggers are prescaled to obtain an acceptable output rate. A prescale factor of n means, that only every n-th event which fulfills the subtrigger condition is accepted by L1. The L1 reduces the rate typically from about 100 kHz to few kHz.

Second trigger level (L2): Neural networks and topological triggers are implemented on L2. In case of a negative decision on L2 the restarting sequence is initiated and then the detector is ready for the next event. Otherwise the detector readout starts. The subtriggers selected in this analysis do not require an L2 condition to be fulfilled. The L2 output rate had to be below 50 Hz, because the third level (L3) was not implemented during the HERA I data taking period 1999-2000.

Fourth trigger level (L4): The fourth trigger level is a multi-processor farm, where the online event reconstruction is performed. If the L1 and L2 trigger decisions can be validated, the events are classified into L4 classes. If the event fulfills a 'hard scale' requirement (such as a high Q^2 , high p_t track, high p_t jet, missing E_t) or passes one of the final state finders, it is accepted without prescale. Otherwise they are downscaled and acquire an L4 event weight. The maximal allowed time for the L4 decision is 100 ms.

Offline reconstruction (L5): A complete offline event reconstruction is performed using the software package H1REC [55] and the final calibration. No events are rejected on L5. The output is permanently stored on 'physics output tapes' (POT). Each recorded event is labeled by a 'run number' and an 'event number'. All events which belong to a given run have been recorded within one time period and with a constant beam conditions and trigger setup.

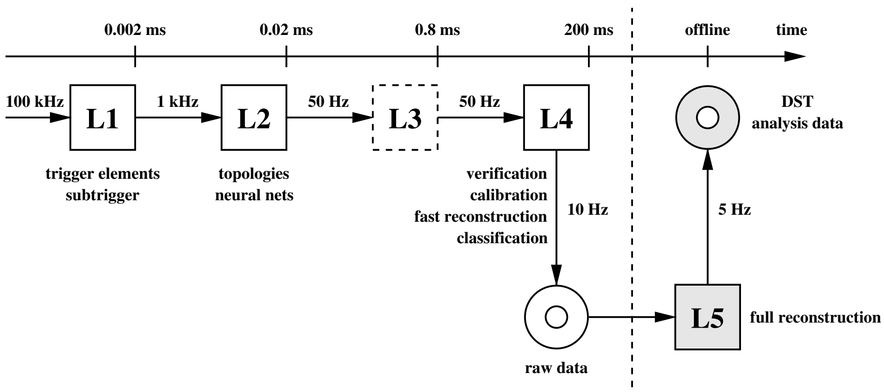

Figure 3.10: *Overview of the H1 trigger system. Shown are typical rates and decision times for each level.*

Chapter 4

Reconstruction of the Analysis Objects

In this chapter the reconstruction of muons, electrons and the hadronic final state as well as jets using the H1 Object Oriented framework will be described.

4.1 Muon Reconstruction

The **identification of muons** is based on their characteristic low energy loss when traversing matter. Muons with energies as produced at HERA lose much less energy than electrons due to Bremsstrahlung because of their higher mass. In contrast to hadrons, muons do not interact strongly either, so that they do not lose their energy in nuclear interactions. Therefore muons do not produce showers. They also lose only a small amount of energy due to ionisation and excitation, which is described by equation (4.1).

The mean energy loss of charged particles heavier than electrons in material per unit length is in general energy dependent and described by the **Bethe-Bloch formula**

$$-\frac{dE}{dx} = \frac{4\pi z^2 e^4}{m_e v^2} N_A Z \left[\ln \frac{2 m_e v^2 \gamma^2}{I} - \beta^2 - \frac{\delta}{2} - \frac{C}{Z}\right] \tag{4.1}$$

where z is the particle charge in units of the elementary charge and v denotes its velocity. m_e is the electron mass, N_A stands for the Avogadro constant and Z is the atomic number of the material. The parameter I is interpreted as a mean atomic excitation potential incorporating all excitation and ionisation processes. δ and C are the density and shell corrections respectively.

For muon energies above roughly 200 MeV, where the ionisation is minimal, the energy loss increases only logarithmically with energy and does not deviate much from the minimum. This is why muons are often called 'minimum ionizing particles'.

Typical muon energies in events with heavy quarks observed in the H1 detector are of the order of a few GeV. When such a muon passes the liquid argon calorimeter it typically traverses distances $\gtrsim 100$ cm. The energy loss due to ionisation is rather constant (about 10 MeV/cm), so the energy deposits are expected to be evenly distributed in the calorimeter and concentrated in a narrow cylinder around the muon track. If the energy is high enough ($\gtrsim 1.5$ GeV), the muon penetrates through the coil of the superconducting magnet surrounding the LAr and enters the instrumented return yoke of the magnet. The average energy loss in any of the ten iron plates is around $\sim$ 90 MeV. If the muon has enough energy, it has a good chance to pass through the iron plates as well and leave the detector. This is typically the case for $p_t^{\mu} \gtrsim 2\,\mathrm{GeV}$.

In the following the part of the **muon finding algorithm** [56], which is relevant for the present analysis, will be described. A muon is detected in H1 if it has either a minimum ionizing particle pattern in the calorimeter or a reliable signal in the instrumented iron (see below). As the high energetic muons searched for in this analysis are expected to penetrate through the calorimeter, muons identified solely in the calorimeter are not considered. The requirement for well measured muons decreases the background, what is important for an analysis studying events containing a non isolated muon like the present one.

In the instrumented iron tracks are reconstructed which are referred to as **'iron tracks'**. To reduce the non-muon background from hadrons entering the muon system a set of cuts is applied to the iron tracks. Since the hadron background is more dominant in the direction of the proton beam, harsher conditions have to be fulfilled by tracks reconstructed in the forward direction. The cuts applied to the iron tracks developed in [57] are listed in table 4.1. They are based on the number of layers, where the signal was registered as well as on the distance of the track to the nominal interaction point.

	barrel	forward endcap	backward endcap
ρ_0	$< 100\,cm$	$< 100\,cm$	$< 100\,cm$
z_0	$< 100\,cm$	$< 100\,cm$	$< 100\,cm$
n_{layers}	≥ 2	≥ 6	≥ 3
first layer	≤ 5	≤ 5	≤ 8
last layer	≥ 2	≥ 6	≥ 3

Table 4.1: *Cuts for iron tracks reconstructed in the barrel, forward endcap and backward endcap of the CMD. The variables ρ_0 and z_0 describe the distance of the extrapolated iron track to the nominal interaction point. Only streamer tube layers enclosed by the iron plates are taken into account.*

A measured track in the inner tracking chambers enables to reconstruct the muon momentum. Tracks well measured in the inner tracking chambers are at H1 also referred to as 'Lee West tracks' and the requirements for them are defined in [57]. For muons not isolated in the detector there might exist more than one possibility to link a certain iron track measured in the instrumented iron with inner tracks in the drift chambers. These ambiguities are solved by first defining so called **muon candidates** for each possible combination of tracks and then using a well defined procedure to choose from all the muon candidates the best possible set (for more details see [56]).

In this analysis only the best 'iron muons' with a good fit between inner track and iron track are used. In the linking procedure, performed by the reconstruction software H1REC [55], the inner tracks are extrapolated to the first hit in the iron system taking the energy loss according to Bethe-Bloch formula and multiple scattering into account. Then a fit between the extrapolated inner track and the iron track is performed and a χ^2 value for the fitted track parameters is calculated (more details in [58]). The **link probability**, derived from the χ^2 value, is required to exceed 10^{-4} and the combination with the largest link probability is chosen.

In this analysis we consider only muons with a significant signal in the muon detector. However, in figure 4.1 can be seen that approximately half of the selected muons left some signal also in the calorimeter. That muon quality [59] distribution is well described by the inclusive PYTHIA MC simulation. More details about lower quality muons, as are for example the calorimeter muons, can be found in [56]. Further cuts to select muons for this analysis will be explained in section 5.2.

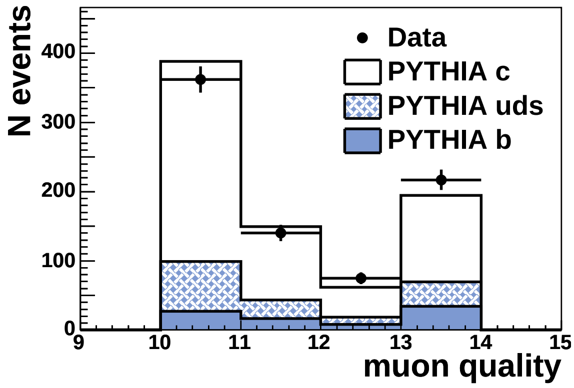

Figure 4.1: *Quality of the analysed muons and the description by the inclusive PYTHIA MC. 10 denotes 'iron muon' with the lowest calorimetric quality (no calorimeter signal), 13 denotes 'iron muon' with a very good calorimetric quality. For the definitions of the H1 calorimetric muon qualities see [59]. The data and the total PYTHIA MC prediction are normalised to the same number of events.*

4.2 Electron Reconstruction

The electron finder implemented in the H1 Object Oriented framework searches for electrons in the SpaCal and in the LAr calorimeter. A number of electromagnetic particle candidates can be created from clusters and tracks that fulfil the selection criteria. These clusters and tracks are locked and will not be used by other finders. In order to be able to calculate the kinematics using the scattered electron, one candidate is selected to be the scattered electron. The candidate with the highest p_t fulfilling additional isolation criteria is chosen to be the electron candidate. Several electron finders are run in different regions of the detector:

- The **LAr electron finder** requires transverse momentum of the electron to be larger than 3 GeV, the electron energy to be larger than 5 GeV and the number of cells of the cluster has to be larger than three. The identification of the electron is based on estimators used to characterize the electromagnetic shower like electromagnetic fraction, transverse radius and energy fraction in the 'hot' core, built of the N most energetic neighboring cells. The cut values on these estimators are θ-dependent to match the detector characteristics. For more details see [60].
  A track is associated to the electron cluster if the distance to the cluster in $\eta-\phi$ plane is less than 0.1. 'Lee West tracks' are preferred. The identified electron is defined as isolated if the calorimeter energy in a cone around the electron of radius R=0.5 is less than 5 % of the electron energy.

- The **SpaCal electron finder** looks for electron candidates with energy larger than 5 GeV and cluster radius less than 4 cm. The (x,y) position of the centre of gravity of the SpaCal clusters is calculated using logarithmic weighting. The z-position calculation is energy dependent [56]. If the distance between a track measured by the Backward Drift Chamber extrapolated into the SpaCal and the SpaCal cluster is less than 3 cm, the track extrapolation is used to define the electron candidate position.

- Additionally a **track based electron finder** is run, which is aimed for low p_t (< 5 GeV) electrons. It achieves very high purities (up to 98 %) with comparable efficiencies to the above electron finders.

In this analysis the absence of the scattered electron is used to select photoproduction events. Electrons created in the *ep* collision, apart from the scattered electron, and in decays of hadrons are also used as input for jet finding.

4.3 Reconstruction of the Hadronic Final State

For the reconstruction of the hadronic final state (HFS), the Hadroo2 algorithm is used, as described in [61]. It associates calorimeter clusters to tracks and defines the four vectors of the output particles trying to avoid energy double counting. The basic idea is to use either the track or the calorimeter information for a particular particle candidate, depending on the uncertainty of the track measurement. In principle at low p_t all tracks are kept and the cluster behind the track is ignored. At high p_t an estimate of energy compatibility and expected resolution between tracks and clusters is used to decide whether the cluster or track information is accepted. A detailed explanation of the Hadroo2 algorithm follows.

The algorithm uses the event vertex, tracks and clusters, which are not associated to isolated electron and muon candidates, as input objects. Those Lee West tracks and calorimeter clusters which are associated to isolated lepton candidates are removed first. Used are **central, forward and combined Lee West tracks** (see Fig. 4.2 for the exact definition of the angular regions). Both primary and secondary vertex fitted 'Lee West tracks' can be selected. They have to fulfil the quality criteria listed in [61].

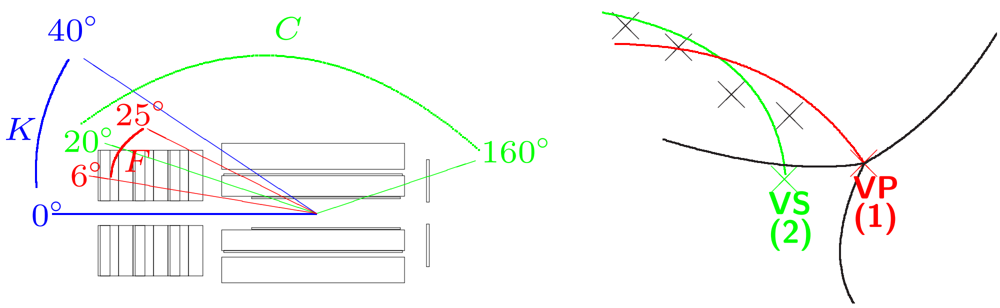

a) b)

Figure 4.2: *a) Different track types and their angular domain: C = central tracks, F = forward tracks, K = combined tracks. b) Two vertex hypotheses for a single track. Figure is from [61].*

Calorimetric clusters are only selected from LAr or SpaCal, iron and Plug clusters are not considered. The energy of a LAr cluster has to be at least 0.8 GeV (0.4 GeV) in the central (forward) region. As LAr is a non-compensating calorimeter, weighting algorithms are necessary to compensate the lower response to hadrons with respect to electrons for the same energy. SpaCal clusters have to have a cluster radius larger than 9.6 cm.

A number of **noise suppression algorithms** is run to either reject the whole event not coming from the *ep* collision or to remove unphysical clusters while keeping the event. The noise is due to detector effects such as noise in the electronics or pile-up deposition of energy coming from halo or cosmic muons.

Having selected tracks and clusters, a **cluster-track matching** can be performed. Each track is assumed to originate from a pion, with energy

$$E_{track}^2 = p_{track}^2 + m_\pi^2 = p_{t,track}^2 / \sin^2\theta + m_\pi^2. \tag{4.2}$$

As explained in [61], for each track the relative resolution of the track measurement $\frac{\sigma_{E_{track}}}{E_{track}}$ and of the calorimeter measurement $\frac{\sigma_{E_{calo}}}{E_{calo}}$ at the same energy are compared to determine which of the two detectors provides the best measurement. It is not possible to take a decision based on the measured calorimeter deposit, since this is a priori unknown due to possible contributions of neutral particles. Therefore the average relative error expected for the calorimeter measurement of the particle energy is calculated as:

$$\left(\frac{\sigma_E}{E}\right)_{LAr\ expect} = \frac{\sigma_{E\ LAr\ expect}}{E_{track}} = \frac{0.5}{\sqrt{E_{track}}}. \tag{4.3}$$

Generally the tracker measurement is better up to 25 GeV for central tracks. The selected charged tracks are ordered by increasing p_t, in order to associate first the clusters to the well measured low p_t tracks. Then the algorithm does a loop over the selected tracks and for each track compares the resolutions and tries to associate calorimetric clusters to the track.

If the relative uncertainty of the track measurement is lower, the **track is used to define a particle candidate**. In this case the calorimetric energy is suppressed partially or totally to avoid double counting. The central tracks are extrapolated into the calorimeter. The track energy E_{track} is compared to the calorimetric energy inside a cylinder of radius 25 cm (electromagnetic part) and 50 cm (hadronic part) (details in [61]), taking into account possible fluctuations of both measurements within their standard errors. If

$$E_{cylinder} < E_{track} \times \left[1 + 1.96 \sqrt{\left(\frac{\sigma_{E_{track}}}{E_{track}}\right)^2 + \left(\frac{\sigma_E}{E}\right)^2_{LAr\ expect}} \right] \tag{4.4}$$

an amount of calorimetric energy equal to $E_{cylinder}$ is suppressed completely. Otherwise only an amount of energy E_{track} is suppressed.

If the relative uncertainty of the calorimetric measurement derived using formula 4.3 is lower and if

$$E_{track} \in [E_{cylinder} - 1.96\,\sigma_{E_{cylinder}}, E_{cylinder} + 1.96\,\sigma_{E_{cylinder}}] \tag{4.5}$$

(with $\sigma_{E_{cylinder}} = 0.5\sqrt{E_{cylinder}}$) the track energy is considered to be compatible with the calorimetric deposit and the **calorimetric measurement is used to define a particle candidate**. Otherwise if

- $E_{track} < E_{cylinder} - 1.96\,\sigma_{E_{cylinder}}$, the track measurement is used and calorimetric energy is subtracted as in the case of a better track measurement.
- $E_{track} > E_{cylinder} + 1.96\,\sigma_{E_{cylinder}}$, the track is suppressed and hadron is defined using the calorimetric cluster.

Once all the tracks have been treated, particle candidates are made out of the remaining clusters using the calorimetric energies. The momentum of these clusters is obtained assuming massless particles. These particles correspond to neutral hadrons with no associated track or to charged particles with a badly measured track.

4.4 Jet Reconstruction

In high energy interactions partons are produced in the final state as a result of the hard process. Because of color confinement it is not possible to observe quarks and gluons as final state particles of the reactions. Partons outgoing from the interactions produce parton showers and finally recombine to color singlet states - hadrons. Since the transverse energies involved in the hadronisation process are typically much smaller than the hard scattering energies (typically several GeV), the final state particles are collimated around the direction of the original parton. These streams of particles, which can be measured by the detector, are called jets. The aim of reconstructing jets is to **reconstruct the direction and energy of the original partons**. An additional difficulty represents the soft underlying event. Underlying events occur, when the partons from the proton and photon remnants undergo a second interaction, in additiona to the hard subprocess. Its products can overlap with the jet formed by the hard partons.

Jet finding algorithms are used to associate particles to particular jet. After finding all the particles belonging to the jet, recombination schemes give a prescription how to calculate the momentum four vector of the jet from the momentum four vectors of the individual jet particles.

Jet Finding Algorithms

Jet finding algorithms assign particles to jets. There are different ways to define jets. Although there is no 'best' definition, there are better and worse ones in terms of reconstruction of the original parton direction or magnitude of hadronisation corrections.

According to the Snowmass Convention [62], a good jet definition has to be simple to implement in both the experimental analysis and in the theoretical calculation. It should yield a cross section that is relatively insensitive to hadronisation. It should be defined and yield finite cross section at any order of perturbation theory. More specifically, a jet finding algorithm should be **collinear and infrared safe**. This means it should be independent of a particle splitting into two partons with parallel momenta like in figure 4.3 a). Such a dependence would cause collinear divergences in the theoretical calculations. From the experimental point of view, such a property means that the jet finding is largely independent of the granularity of the detector. Particles which go in the same calorimeter cell cannot be resolved anyway. Furthermore the jet finding algorithm should be insensitive to the emission of low energetic particles (fig 4.3 b). This property avoids the infrared divergences in perturbative calculations. Experimentally, cuts to suppress the detector noise are applied to make the jet finding as independent as possible of low energy deposits.

Figure 4.3: *a) Infrared radiation and b) collinear splitting.*

There are two main types of jet finders commonly used, cone algorithms and clustering algorithms.

- **Cone algorithms** define a direction that maximizes the energy flowing into a cone around it with a fixed radius $R = \sqrt{\Delta\eta^2 + \Delta\phi^2}$. They are used mostly in hadron-hadron collisions, to solve the problem of underlying event. Typically $R \approx 0.7$. Cone algorithms are simple to implement, but they are not able to separate overlapping jets unambiguously. Hadronisation and higher order corrections are expected to be higher for cone algorithms than for clustering algorithms. Additionally there is a problem with collinear and infrared safety in higher order QCD calculations. And finally a bias arising from the choice of seeds is present in cone algorithms.

- **Clustering algorithms** are based on iterative clustering procedures in which particles are merged together into 'pseudoparticles' which build the final jets. They assign unambiguously every particle to a jet and are both collinear and infrared safe. They are used mostly by the e^+e^- collider experiments. A cluster-type algorithm was first used by the JADE collaboration [63]. The pair of particles with the smallest invariant mass was combined into a single 'pseudoparticle' and the algorithm continued recursively until all invariant masses were above a given cut-off. Undesirable features of this algorithm were improved by the QCD-inspired k_t-clustering algorithm replacing the invariant mass by the relative transverse momentum of the softer particle relative to the other. More recently, a **longitudinally invariant k_t-clustering algorithm** was proposed [64], which is used in this analysis. It combines the use of the k_t-resolution variable for e^+e^- collisions with an improved clustering procedure which is able to deal with the underlying soft event [65]. Jets built by the k_t-clustering algorithm have effective radii depending on the hardness of the jet. A diagram describing the principle of the k_t clustering algorithm is shown in figure 4.4.

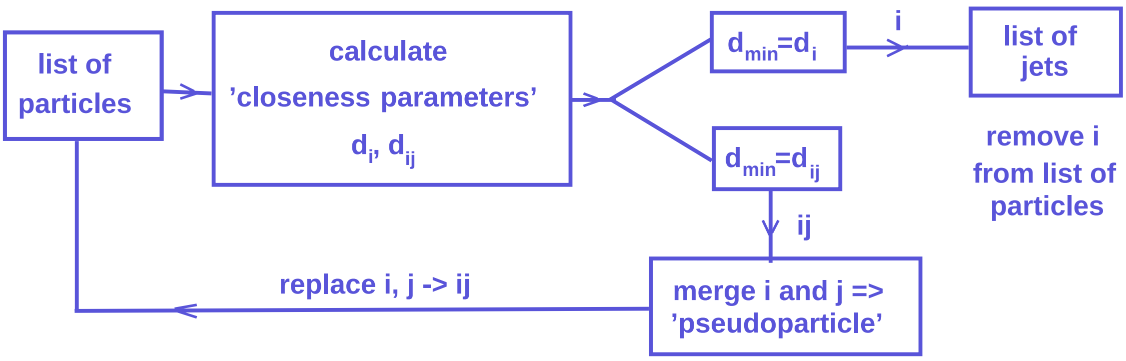

Figure 4.4: *Diagram showing the principle of the k_t-clustering algorithm. Details are explained in the text.*

The input of the k_t clustering algorithm are particles from the list of particles. The output is written in the list of jets, which is empty in the beginning. For every pair of particles a closeness parameter is calculated as

$$d_{ij} = min(p_{t,i}^2, p_{t,j}^2)[(\eta_i - \eta_j)^2 + (\phi_i - \phi_j)^2]/R_0^2 \tag{4.6}$$

The adjustable parameter R_0, characterising the with of jets, is analogous to the cone radius in case of the cone algorithm. Further for every particle is calculated

$$d_i = p_{t,i}^2. \tag{4.7}$$

Minimum of d_{ij} and d_i is labeled as d_{min}. If d_{min} belongs to the set of d_{ij}, the recombination scheme (see the next section) is used to merge particles i and j into a new 'pseudoparticle'. The particles i and j are removed from the list of particles. If d_{min} belongs to the set of d_i, the particle i is removed from the list of particles and added to the list of jets. The procedure is finished, when the list of particles is exhausted. After that, all particles are assigned to a jet.

Recombination Schemes

Recombination schemes are prescriptions to calculate the momentum four vector of the jet from the momentum four vectors of the merged jet particles. The basic recombination schemes are defined in the Snowmass Convention [62]:

$\mathbf{p_t}$**-weighted scheme**	**covariant E-scheme**
$p_t^{jet} = \sum_i p_{t,i}$	$E^{jet} = \sum_i E_i$
$\eta^{jet} = \frac{\sum_i p_{t,i}\eta_i}{\sum_i p_{t,i}}$	$p_x^{jet} = \sum_i p_{x,i}$
$\phi^{jet} = \frac{\sum_i p_{t,i}\phi_i}{\sum_i p_{t,i}}$	$p_y^{jet} = \sum_i p_{y,i}$
	$p_z^{jet} = \sum_i p_{z,i}$

The p_t-weighted scheme produces massless jets while the covariant E-scheme results in massive jets. There are also alternative, rarely used recombination schemes such as a p_t^2-weighted scheme or an E_t-scheme [66].

In this analysis jets are reconstructed by the inclusive k_t-clustering algorithm [64, 67] in the laboratory frame using the p_t-weighted recombination scheme. The algorithm, with a distance parameter in the η-ϕ plane of $R_0 = 1$ (see the previous page), is applied to all hadronic final state particles. The resulting jets are massless. The same jet finding algorithm can be applied at different levels of the analysis chain, as shown in figure 4.5. In this analysis it was applied on the final state particles in the data and in reconstructed Monte Carlo events called **'detector level'**, as well as on the level of decayed hadrons of the Monte Carlo events called **'hadron level'**, in order to determine the detector corrections.

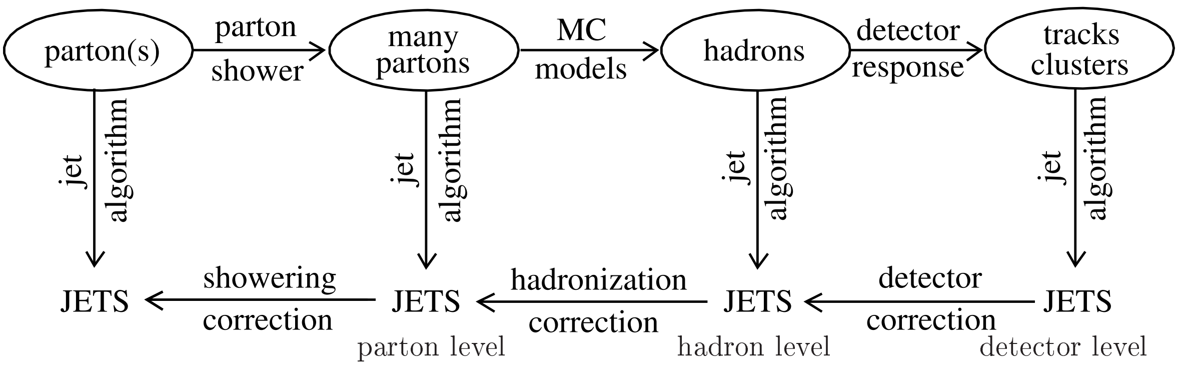

Figure 4.5: *Schematic diagram of a typical analysis using jets [68]. In the upper line the partons are produced from the hard scattering process and a parton shower is created. The hadrons deposit their energy in the detector. At each stage jet finding can be applied. This analysis is performed at the detector level and afterwards detector corrections are applied.*

4.5 Reconstruction of the variable x_{γ}^{obs}.

In this section a motivation for the definition of the variable x_{γ}^{obs} by equation 2.2 will be given. It is constructed to represent the fraction of the photon momentum entering the hard interaction. The momentum fraction carried by the incoming parton from the photon side is at leading order defined as

$$x_{\gamma}^{LO} = \frac{p_p{\cdot}p_{parton}}{p_p{\cdot}p_{\gamma}}, \tag{4.8}$$

where p_p, p_γ, and p_{parton} are the four momenta of the proton, photon and parton from the photon side participating in the hard interaction, respectively. Such defined x_{γ}^{LO} as defined by (4.8) is equal to one for direct processes and less than one for resolved processes. In the collinear approximation, i.e. when the parton has the same direction as the proton, the following equation holds:

$$x_{\gamma}^{LO} = \frac{E_{parton}}{E_{\gamma}}, \tag{4.9}$$

where E_{parton} is the energy of the parton from the photon side participating in the hard interaction. In photoproduction the energy of the photon E_γ is related to the electron beam energy E_e via the inelasticity y, $E_\gamma = yE_e$. The photon momentum fraction entering the hard interaction can be determined from the transverse energies $E_{t,j} = \sqrt{E_j^2 - p_{z,j}^2}$ and rapidities $\hat{y}_j = 1/2\ \ln[(E_j+p_{z,j})/(E_j-p_{z,j})]$ of the outgoing hard partons according to

$$x_{\gamma}^{LO} = \frac{\sum_{j=outgoing\ parton} E_{t,j}e^{-\hat{y}_j}}{2yE_e}. \tag{4.10}$$

Since partons cannot be measured directly, one needs to write equation (4.10) in terms of experimentally measurable quantities. The sum over partons is replaced by the sum over hadronic jets. For $2 \to 2$ processes, like boson-gluon fusion, the variable x_{γ}^{obs} is defined as

$$x_{\gamma}^{obs} = \frac{\sum_{jet=1,2} E_{t,jet}e^{-\hat{y}_{jet}}}{2yE_e} \tag{4.11}$$

where the sum in the numerator runs over the two highest transverse energy jets in the event. Since for a massless jet $E_{t,jet}e^{-\hat{y}_{jet}} = (E - p_z)_{jet}$, x_{γ}^{obs} can be written in terms $(E - p_z)$ of the jets

$$x_{\gamma}^{obs} = \frac{\sum_{jet=1,2}(E - p_z)_{jet}}{2yE_e}. \tag{4.12}$$

In this analysis this definition will be used in the form

$$x_\gamma^{obs} = \frac{\sum_{h \in Jet_1}(E - p_z) + \sum_{h \in Jet_2}(E - p_z)}{\sum_h (E - p_z)}, \tag{4.13}$$

where the sums in the numerator run over the particles associated with the two jets and for the denominator over all detected hadronic final state particles. The variable x_γ^{obs} defined in this way is restricted to the range $0 < x_\gamma^{obs} \leq 1$. Resolved processes tend to populate region of lower x_γ^{obs} values than the direct ones. However, an overlap between them is present. Especially parton showers and hadronisation processes cause the smearing of the direct peak at $x_\gamma^{obs} = 1$ to lower values of x_γ^{obs}. Distributions for the variable x_γ^{obs} for various processes, as simulated by the charm PYTHIA MC are shown in figure 4.6. This detector level simulation includes already the smearing effects.

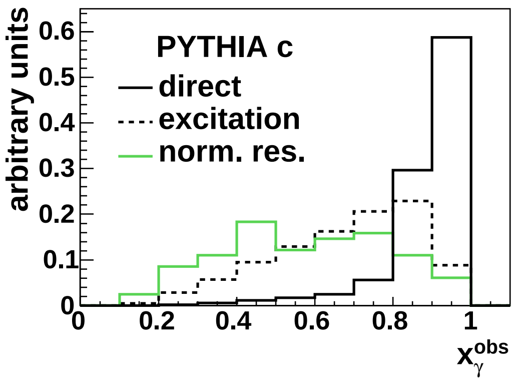

Figure 4.6: *Distributions of x_γ^{obs} for direct, excitation and normal resolved processes on detector level, after the final data selection. Distributions simulated by the charm PYTHIA MC are normalised to the total number of events.*

4.6 Analysis Environment

This analysis is performed in the H1 Object Oriented framework (H1OO). It was created by members of the collaboration in order to manage to process increasing data volumes and to satisfy increasing demands on the software used for the analysis. It is programmed in C++. The goal of H1OO is to accommodate the collaboration with a standard of event and particle reconstruction and selection. This new software framework for general analysis purposes provides a new data storage and environment for all steps of an analysis. It offers a modular and extendable framework, supporting all H1 physics analyses. H1OO standardizes the physics algorithms like kinematic reconstruction, selection criteria and particle identification and make the expert knowledge reusable by non-experts. The algorithms and the data are organised in classes, based on the ROOT package [69]. ROOT is an object oriented analysis framework programmed in C++ which provides efficient storage, analysis and graphic display facilities.

For more details about H1OO, particularly concerning the three-layer data storage design, see [56].

Chapter 5

Event Selection

This analysis is based on the event sample selected for the recent determination of the beauty production cross section [70]. The data selection was optimised to select heavy quark events that include semimuonic decays.

The data were recorded by the H1 experiment at HERA in the years 1999 and 2000 in *ep* collisions at a centre-of-mass energy of 318 GeV and correspond to an integrated luminosity of $48\,\mathrm{pb}^{-1}$.

For this analysis dijet events in photoproduction are selected. For a comparison of charm and light quark events, two samples are selected: a **charm enriched sample** and a light quark dominated **flavour inclusive sample**. The main selection difference between them is the requirement of a high p_t muon in case of the charm enriched sample. The high p_t muon, which is used to enrich heavy quark events, also serves for triggering. Since we do not have this for the flavour inclusive dijets, a scattered electron detected in the electron tagger is used to trigger such events.

In the following the online and offline selection will be described.

5.1 Online Selection

For apparative details see chapter 3, in particular the H1 trigger system is described in section 3.2.5. Here only the most important details for this analysis will be mentioned.

L1 Trigger Selection

The charm enriched sample is triggered by a high p_t muon in the central muon detector (CMD) using subtriggers s19 and s22. Subtrigger s19 triggers muons in the barrel part of the CMD and takes the majority of the studied events (99 %). Events containing the muon in the forward or backward endcaps are triggered by s22. The most important trigger elements for both subtriggers are listed in table 5.1.

The flavour inclusive sample is triggered by the scattered electron detected in the electron tagger ET33. For that purpose subtrigger s83 is required and the trigger elements essential to that subtrigger are listed in table 5.1. The definition of the individual trigger elements can be found in table 5.2. In the following a short description will be given of the triggers, which provide the trigger elements entering the subtriggers used.

Subtrigger	Trigger Elements
s19	Mu_Bar && DCRPh_CNH && zVtx_sig>1
s22	Mu_ECQ && DCRPh_CNH && zVtx_sig>1
s83	DCRPh_Tc && zVtx_sig>1 && LU_ET && !LU_PD_low

Table 5.1: *The essential trigger elements in the definitions of the subtriggers. See table 5.2 for explanations. The symbols '&&' and '!&&' represent a logical AND and a logical AND NOT, respectively.*

Trigger Element (TE)	Definition
TE of the CMD:	
Mu_Bar	muon candidate in the barrel
Mu_ECQ	muon candidate in the forward outer endcap or backward outer endcap or backward inner endcap
TE of the CJC1 and CJC2:	
DCRPh_Tc	at least three fired track masks with $p_t \geq 450\,\mathrm{MeV/c}$
DCRPh_TNeg	at least one fired neg. track mask with $p_t \geq 450\,\mathrm{MeV/c}$
DCRPh_THig	at least one fired track masks with $p_t \geq 800\,\mathrm{MeV/c}$
DCRPh_CNH	shortcut for DCRPh_Tc && DCRPh_TNeg && DCRPh_THig
TE for the vertex significance:	
zVtx_sig>1	significant maximum in the z-vertex histogram
TE for the scattered electron:	
LU_ET	signal in the ET33
LU_PD_low	energy deposition in the PD

Table 5.2: *Definition of the trigger elements from table 5.1. The symbol '&&' represents a logical AND.*

- The **CMD trigger** uses five layers (3,4,5,8 and 12) of the instrumented iron system. The number of layers required to fire one of the CMD trigger elements Mu_Bar and Mu_ECQ (see table 5.2) differs for the different detector regions.

- The **DCRPh trigger** uses 10 out of 56 wire layers of the CJC. Each track coming from the nominal interaction point can be parametrised in the $r-\phi$ plane by a curvature κ an azimuthal angle ϕ at the point of closest approach to the vertex (DCA point). The signals caused by the measured tracks are compared to predefined masks in the two dimensional space in κ and ϕ for small values of DCA. Cosmic muons and beam induced background produce tracks with a large DCA to the event vertex. Validation of a mask leads to a positive trigger decision. It is possible to separate positive and negative tracks with low and high momentum (see table 5.2). More information can be found in [71, 72].

- The **z-vertex trigger** is based on the signals from the multiwire proportional chambers CIP, COP and FPC (see section 3.2.1). Each of them consists of two independent layers. The aim of the z-vertex trigger is to reconstruct online the primary interaction vertex along the beam axis. This is realised by building rays out of pad signals which can be connected by a straight line pointing to the z-axis (figure 5.1). The z-vertex histogram consists of 16 bins in ϕ and 16 bins in the z-coordinate. Each active ray contributes one entry to the z-vertex histogram. The histogram bin with most entries is expected to contain the interaction vertex of the *ep* collision, while the combinatorial background is randomly distributed. The trigger element zVtx_sig>1 fires, if the histogram shows a significant peak. More detailed information can be found in [73]

- The **scattered electron trigger** fires if an energy deposition above an adjustable threshold ($6-9\,\mathrm{GeV}$) is found in the ET33, and at the same time the energy deposition in the photon detector (PD) is smaller than a given threshold ($5-7\,\mathrm{GeV}$). This is done in the order to trigger events with a scattered electron in the ET33 and at the same time veto events from the Bethe-Heitler process.

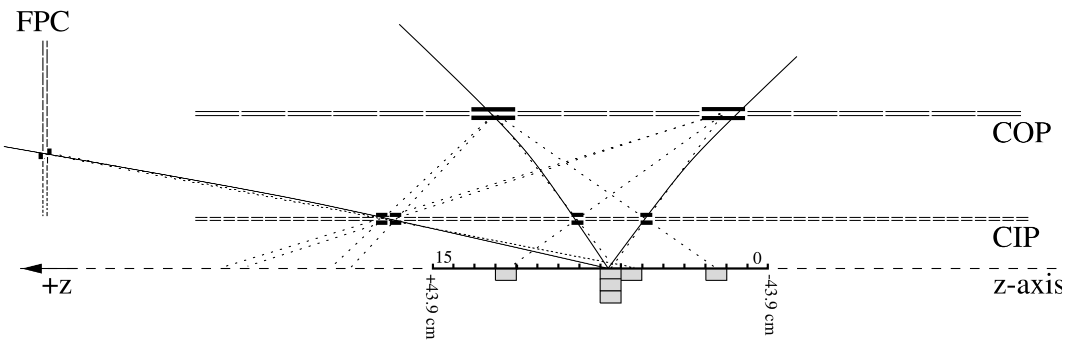

Figure 5.1: *The z-vertex trigger: Particle trajectories (full lines) cause hits in the double layers of CIP, COP, and FPC. Rays through pads (dotted lines) are extrapolated to the z-axis. Only rays from particle trajectories form a significant peak in the z-vertex histogram.*

The efficiencies of the trigger elements Mu_Bar, DCRPh_CNH and zVtx_sig>1 determined from the data are compared to the efficiencies from the Monte Carlo simulation in section 6.1.1. Trigger elements of the ET33 and PD are not simulated, but the effect is contained in the electron tagger acceptance, which is also discussed in section 6.1.1. Corrections of the data for trigger efficiencies are contained in the detector corrections (see section 6.5).

L4 Trigger Selection

On the fourth trigger level (L4), the obvious background is filtered out. For this purpose the complete event reconstruction is performed and the L1 trigger decision is verified. After the L1 trigger verification, an event classification is performed at L4.

For the events of both selected data samples, in addition to the L1 subtriggers triggers also the corresponding L4 verified subtrigger are required. There are no L4 subtriggers simulated for the MC events, only the L1 subtrigges are required for Monte Carlo. However, the applied offline cuts are tighter than the online cuts.

At L4, the events are either required to a have hard scale, such as high Q^2, E_t, E_t^{miss} or p_t^{jet}. If an event does not fulfill any of the hard selections it has to pass one of the approximately 45 exclusive final state finders. From the remaining events only each n-th is accepted, and it acquires a weight equal to n. This procedure is known as downscaling of the events. Thus there is a danger of losing events, when they are not classified properly. Although the analysis cuts are harder than the cuts of the L4 finders, a different calibrations are used at L4. Thus changes after applying the final calibration can occur and therefore it is necessary to monitor the situation, as it is also performed for this analysis.

The majority of events (99 %) from the charm enriched sample is accepted at L4 via the finder AOPEN from the heavy flavour class 16. It was designed to look for events including semileptonic decays of heavy quarks. The requirements are at least one muon measured in the CMD in the region $\theta^\mu > 18°$ with $p_t^\mu > 1.5\,\mathrm{GeV}$, and at least 4 central, forward or combined tracks. See figure 4.2 a) for definition of the track types.

The remaining 1 % of the events from the charm enriched sample is accepted by a jet class. None of the selected charm enriched events was found in the prescaled classes, that is of the events have a L4 weight equal to 1.

In the flavour inclusive sample the events are accepted in more classes, as for example jet class and multi-particle class. 0.6 % of the events were found with a weight equal to 10. They were classified as soft physics. Those events are included in the control plots and final result plots with the proper weight.

5.2 Offline Selection

Run Selection and Detector Status

In the years 1999/2000 H1 could be operated in stable conditions. There were neither significant changes in the trigger definitions, nor in L4 classification classes relevant for this analysis. From the collected data the so called 'minimum bias runs', for which special trigger settings were used, are excluded. Further runs with shifted vertex, where the bunches are not colliding at the nominal interaction point, are excluded.

Only runs classified at H1 as 'good' or 'medium' are used. Because of high requirements on the final state, all detector components relevant for this analysis like CST, CJC, CMD, CIP, COP, SpaCal and LAr were switched on for all selected charm enriched events.

Z-vertex Selection

The maximal accepted distance in z of the event vertex from the nominal vertex is 35 cm, to exclude events coming from collisions of the satellite bunches with oder bunches. The satellite bunches collide with other bunches before and after the nominal point. They arise during electron and proton injection into the HERA ring.

Luminosity Determination

For the selection discussed above, the integrated luminosity collected with subtriggers s19 and s22 was found to be $48\,pb^{-1}$. This number is already corrected for the averaged prescale 1.06 of the subtriggers [74].

Kinematic Selection

Both, the charm enriched and the flavour inclusive sample are studied in photoproduction. However, due to the different triggers, the event selection is different for these two samples.

The **charm enriched events are selected in untagged photoproduction**, i. e. by rejecting events with a scattered electron found in the SpaCal and LAr calorimeters. The scattered electron is searched for by the electron finder (see section 4.2). The photon virtuality is restricted for the selected events through the SpaCal acceptance to $Q^2 < 1\,\mathrm{GeV}^2$, with a mean value $\langle Q^2 \rangle = 0.05\,\mathrm{GeV}^2$.

Since the scattered electron is not measured, the kinematic variables are determined using the Jacquet-Blondel method [75]:

$$y_{JB} = \frac{\sum_{had}(E - p_z)}{2E_e} \tag{5.1}$$

where $\sum_{had}(E - p_z)$ is the difference between energy and longitudinal momentum summed over the entire hadronic final state system including the muon. E_e denotes the beam energy of the incoming electrons. The inelasticity region of $0.2 < y_{JB} < 0.8$ is chosen. The upper cut rejects background from DIS events, which have high inelasticity and correspondingly small scattered electron energies. The lower cut is applied to reject events in the extreme forward direction, in order to ensure a complete reconstruction of the final state.

Photoproduction events of the **flavour inclusive sample** are selected through detection of the **scattered electron** in the low angle ($\pi - \theta_{e'}$) electron tagger ET33. The energy deposition of the reconstructed electron candidate has to be above 4 GeV. A reliable measurement of the energy of the scattered electron $E_{e'}$ is obtained if the energy deposition is fully contained in the tagger. This is assured if the x-coordinate of the deposited energy fulfills $|x_{33}| < 6.5\,\mathrm{cm}$ [76].

Having measured the scattered electron, one can reconstruct the kinematic variables

$$Q_e^2 = 4\,E_e\,E_{e'}\,\cos^2\frac{\theta_{e'}}{2} \tag{5.2}$$

$$y_e = 1 - \frac{E_{e'}}{E_e}\sin^2\frac{\theta_{e'}}{2} \approx 1 - \frac{E_{e'}}{E_e}. \tag{5.3}$$

Requiring the scattered electron to be detected in the ET33, events with $Q^2 < 0.01\,\mathrm{GeV}^2$ are selected and the mean value of the Q^2 is $\langle Q^2 \rangle = 0.001\,\mathrm{GeV}^2$. For the inelasticity a cut of $0.3 < y_e < 0.65$ is applied to ensure an ET33 detector acceptance above 10 % (as shown in figure 5.2). The mean acceptance is about 40 % (see section 6.1.1).

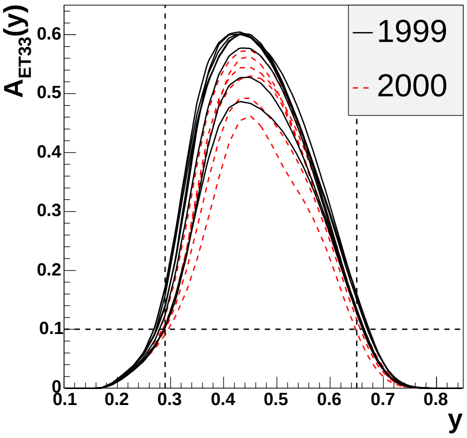

Figure 5.2: *Acceptance of ET33 for different run periods with different beam conditions as a function of the inelasticity y from [77]. Vertical lines indicate the inelasticity region, where the acceptance is greater than* $10\,\%$.

Dijet Selection

The jet reconstruction was described in detail in section 4.4. Our selection requires at least two jets with transverse momentum $p_t^{jet} > 7$ and $6\,\mathrm{GeV}$ in the angular range $20° < \theta < 160°$.

By applying all the cuts mentioned up to now, we have selected a **flavour inclusive event sample** which contains a 'normal mixture' of quarks. It is dominated by the production of light quarks. According to the inclusive PYTHIA simulation $3\,\%$ of the sample is due to beauty quark events and $30\,\%$ due to charm quark events. An overview of all cuts applied to select the flavour inclusive sample is given in table 5.3.

Muon Selection

Only for the **charm enriched sample** muons are required. The muon reconstruction was described in section 4.1. For this analysis only well measured muon candidates are selected, in order to keep the background from misidentified hadrons low. Tight cuts are used to enable an estimation of the charm purity by exploiting the long lifetime and high mass of the charm quark, as it will be explained later in this section.

The muon candidate has to have a well measured central track. The minimal radial length of the track measured by the central tracker has to be more than $22\,\mathrm{cm}$. A signal in the CMD has to span at least 5 central layers with measured hits in at least 4 layers, which are harder conditions than the default Lee West requirements [57]. Good matching of the tracks measured in the CMD and in the central tracking system is also required (link probability $> 10\,\%$).

Only those muons are selected for which at least two associated hits are found in both layers of the central silicon tracker (see section 3.2.1), thus providing a high spatial track resolution close to the ep collision vertex. This cut causes the majority of the event losses, that is about 35 %. The link probability between the central track and the CST hits has to exceed 10 % . Muon candidates fulfilling all the mentioned quality criteria are selected in the angular range $35° < \theta^{\mu} < 130°$, with a transverse momentum of $p_t^{\mu} > 2.5\,\mathrm{GeV}$. Such muons traverse the whole CMD and good identification is thus possible.

Events are accepted only when the selected muon candidate is contained in one of the two highest p_t jets, and an unambiguous determination of the so called **muon jet** is possible. According to the PYTHIA simulation of charm events[1], the muon jet is predicted to be initiated by a charm quark in 85 % of the selected events. The second, non muon jet, is initiated in 60 % of the selected events by a charm quark, in 30 % by a gluon and in 10 % by a light quark.

Charm Enrichment and Purity

After the selection discussed before, the background in the charm enriched sample consists of beauty events and light quark events. An event-by-event separation of signal and background is not possible. However, the **fraction of charm events can be determined on a statistical basis**. Two quantities are used to increase the fraction of charm events further and to determine the charm purity of the selected events. They exploit the different masses and lifetimes of charm, beauty and light quarks:

- The **relative transverse momentum** p_t^{rel} of the muon with respect to the axis of the associated jet (see figure 5.3 a) and equation 2.1). The higher the mass of the quark initiating the muon-jet, the higher the relative momentum of the muon to the jet axis. The p_t^{rel} distribution of beauty events has a maximum at higher values than that of the charm and light quark events (see figure 5.4). Therefore it is adequate to select lower p_t^{rel} in order to reject the beauty events. However, an another variable is needed to separate charm and light quark events.

- The decay length can be measured directly by measuring the distance between the primary and secondary vertex in the event. Here an other method is used - the impact parameter method. The magnitude of the **signed impact parameter of the muon** δ_{μ}, is given by the distance of closest approach of the track in the $r-\phi$ plane with respect to the primary event vertex. Its sign is positive if the intercept of the track with the jet axis is downstream of the primary vertex and negative otherwise. This is illustrated in figure 5.3 b). Decays of long-lived particles are signaled by positive impact parameters, whereas the finite track resolution yields a symmetric distribution centered on zero.

  First, the primary vertex in the $r-\phi$ plane is reconstructed from all tracks (with or without CST hits) including the muon candidate. The position and spread of the beam interaction region are taken into account. The transverse extensions of the beam interaction region are measured to be 145 μm in x and 25 μm in y for the data taking period considered here. The mean position of the beam is measured as the average over many events. The resulting error of $\sim 5\,\mu$m on the mean position

[1] In this thesis the flavour of a Monte Carlo event is defined as the flavour of the heaviest quark coming from the hard subprocess. Events where two gluons are coming from the hard subprocess are considered as being a light quark event.

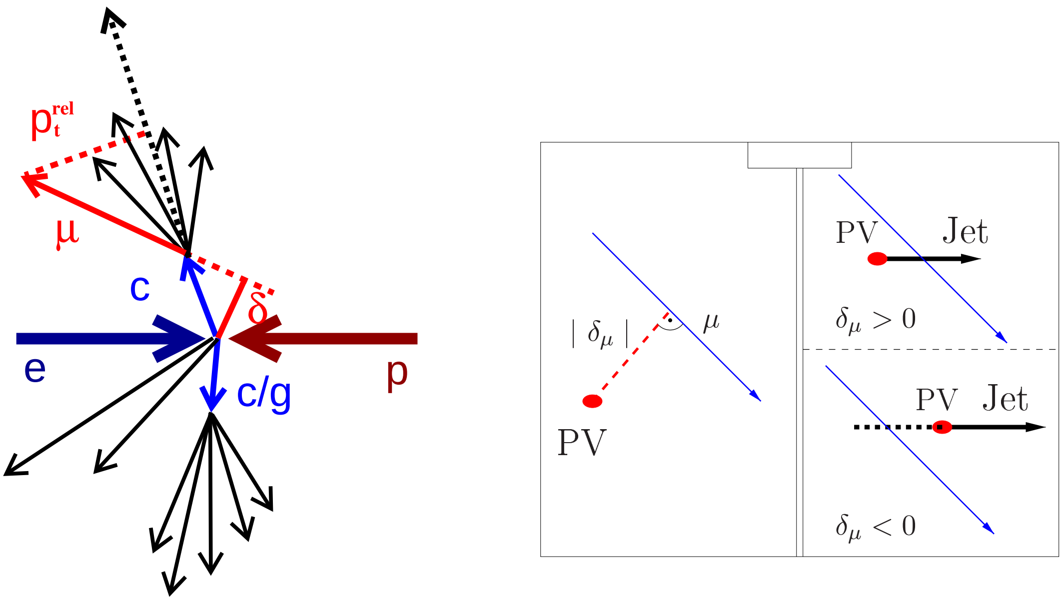

Figure 5.3: *a) Explanation of p_t^{rel}. b) Explanation of signed impact parameter of the muon δ_μ in the plane perpendicular to the beam axis. PV denotes the primary vertex.*

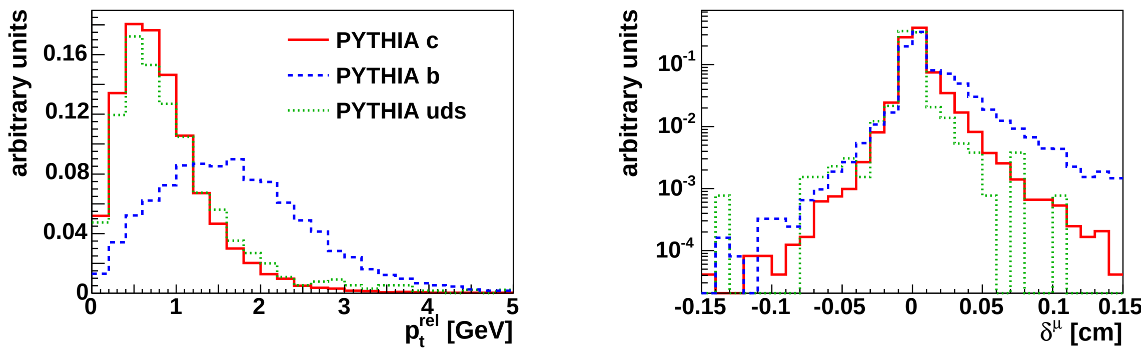

Figure 5.4: *The simulated shapes of the p_t^{rel} and δ_μ distributions for charm, beauty and light quark events used for the 2D fit. The distributions are area normalised.*

is small in comparison to the size of the beam interaction region.

The lifetime of charm hadrons (about 0.4 ps [3]) is about four times shorter than the lifetime of beauty hadrons. This leads to different decay lengths for charm hadrons (120 μm) and beauty hadrons (typically 450 μm), which enables a separation of charm and beauty production. A part of the light hadrons has negligible lifetimes in comparison to heavy flavored hadrons. The second part is represented by pions and kaons that have much larger lifetimes than the heavy hadrons (decay length of the order 10 m). In order to exclude a bias from light hadron decays it is adequate to select events with small magnitude of the impact parameter. The δ_μ distributions for beauty, charm and light quark events simulated by PYTHIA are shown in figure 5.4.

The distributions of p_t^{rel} and δ_μ for the selected charm enriched event sample are shown in Fig. 5.5. No cuts on p_t^{rel} and δ_μ are performed yet. The fractions of charm, beauty and uds events in the data are determined from a **combined fit** to the shape of two-dimensional distribution of p_t^{rel} and δ_μ using the distributions from the PYTHIA MC (figure 5.4) as templates. In the fit the relative weights of all three components are determined. A standard maximum likelihood fit is performed using Poisson statistics. However, the statistical errors of the template predictions are taken into account by the fitting program. For more details of the fit technique see [78]. The two dimensional fit is performed by fitting of the δ_μ distributions in bins od p_t^{rel} . The results of the fit are also shown in figure 5.5. The overall normalisation of the summed Monte Carlo contributions is adjusted to match the data. Both the p_t^{rel} and δ_μ distributions from the data are nicely described by the sum of the three contributions.

The PYTHIA MC simulation predicts that after muon selection about 50 % of the sample are charm events, the rest are beauty and light quark events. In order to enrich events with charm quark decays, a cut on the transverse momentum p_t^{rel} of the muon track relative to the momentum of the associated jet, $p_t^{rel} < 1\,\text{GeV}$, is imposed. In order to exclude events with light hadrons showing long decay lengths, events with δ_μ between -0.1 cm and 0.15 cm are selected. The final **charm enriched sample** contains about 800 events. The procedure of selecting a charm enriched sample is in first approximation independent of the production mechanism but only depends on the decay properties of the charm hadrons.

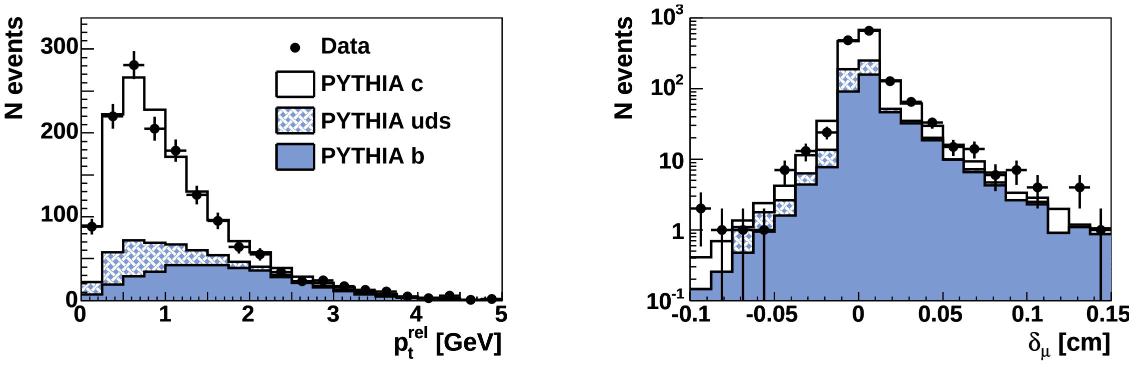

Figure 5.5: *Determination of the charm fraction in the selected charm enriched event sample. The distributions of the relative momentum p_t^{rel} of the muon w.r.t the jet-axis and the impact parameter δ_μ are shown. The white area below the solid line shows the charm contribution. The light (dark) shaded area indicate the contributions from light (beauty) quark events normalised using the results of the 2D fit to the data.*

The combined fit of p_t^{rel} and δ leads to a **charm purity** (i.e. the fraction of charm events in the sample) of 73 ± 3 % in the region of $p_t^{rel} < 1\,\text{GeV}$ compared to 71 ± 2 % expected from the PYTHIA Monte Carlo simulation. The remaining background due to beauty and light quark production is subtracted statistically in the studied distributions using the fractions predicted by PYTHIA, as explained in section 6.2. When background is not present in the distributions we talk about **charm sample**.

5.3 Event Selection Summary

The selection cuts for the flavour inclusive and charm enriched samples are summarised in table 5.3.

Control distributions for the charm enriched and the flavour inclusive samples, are shown in figures 5.6 and 5.8, where the data are compared to the PYTHIA Monte Carlo simulations. Variables for the investigated jet ('other jet' in case of the charm enriched sample and the two highest p_t jets for the flavour inclusive sample) are shown, like the polar angle θ^{jet}, transverse momentum p_t^{jet}, the number of jets found in the central region with $p_t^{jet} > 2.5\,\mathrm{GeV}$, the number of hadronic final state objects (HFS) per jet, the distance in R^2 of all the HFS objects in the event with respect to the axis of the investigated jet - $\Delta R^{HFS-jet}$, the fraction of the tranverse momentum of the investigated jet contained in a cone with a radius $r = 2$ are shown. Furthermore the variables x_γ^{obs}, the photon proton centre-of-mass-energy $W_{\gamma p}$ and ΔR^{jets} are shown. ΔR^{jets} is the distance in R between the two highest p_t jets in R. For the charm enriched sample the muon polar angle θ_μ, the transverse momentum p_t^μ and the transverse momentum of the jet associated to the muon $p_t^{\mu-jet}$ are shown additionally. The overall normalisation of PYTHIA is adjusted to match the data. For both samples the relative fractions of charm, beauty and light quark events are used, as predicted by PYTHIA.

The charm enriched data are described reasonably well by the PYTHIA simulation. In view of the measurement of the jet shapes in two regions of x_γ^{obs}, the control distributions for charm enriched sample are also shown for $x_\gamma^{obs} \leq 0.75$ (Fig. 5.7), where some deviations are visible. A typical event from the selected charm enriched sample is displayed in figure 5.9. The control distributions for the flavour inclusive sample are described by the Monte Carlo simulation reasonably well. Here the acceptance of the ET33 is taken into account.

Cut	**Charm Enriched Sample**	**Flavour Inclusive Sample**
Q^2 [GeV^2]	< 1	< 0.01
y	0.2 ... 0.8	0.3 ... 0.65
Jets		
#	$\geq$ 2	$\geq$ 2
p_t^{jet} [GeV]	$> 7(6)$	$> 7(6)$
θ^{jet}	20°...160°	20°...160°
Muon	in one of the jets	-
iron link probability	$> 10\,\%$	-
CST link probability	$> 10\,\%$	-
# CST hits	≥ 2	-
p_t^μ [GeV]	> 2.5	-
θ^μ	35°...130°	-
p_t^{rel} [GeV]	< 1.0	-
δ_μ [cm]	-0.1 .. 0.15	-
Subtrigger	s19, s22	s83
Analysed Jets	non muon jet	both highest p_t jets

Table 5.3: *The final selection cuts for the charm enriched data sample and the flavour inclusive data sample. The values are measured in the laboratory frame.*

[2] $R = \sqrt{\Delta\eta^2 + \Delta\phi^2}$

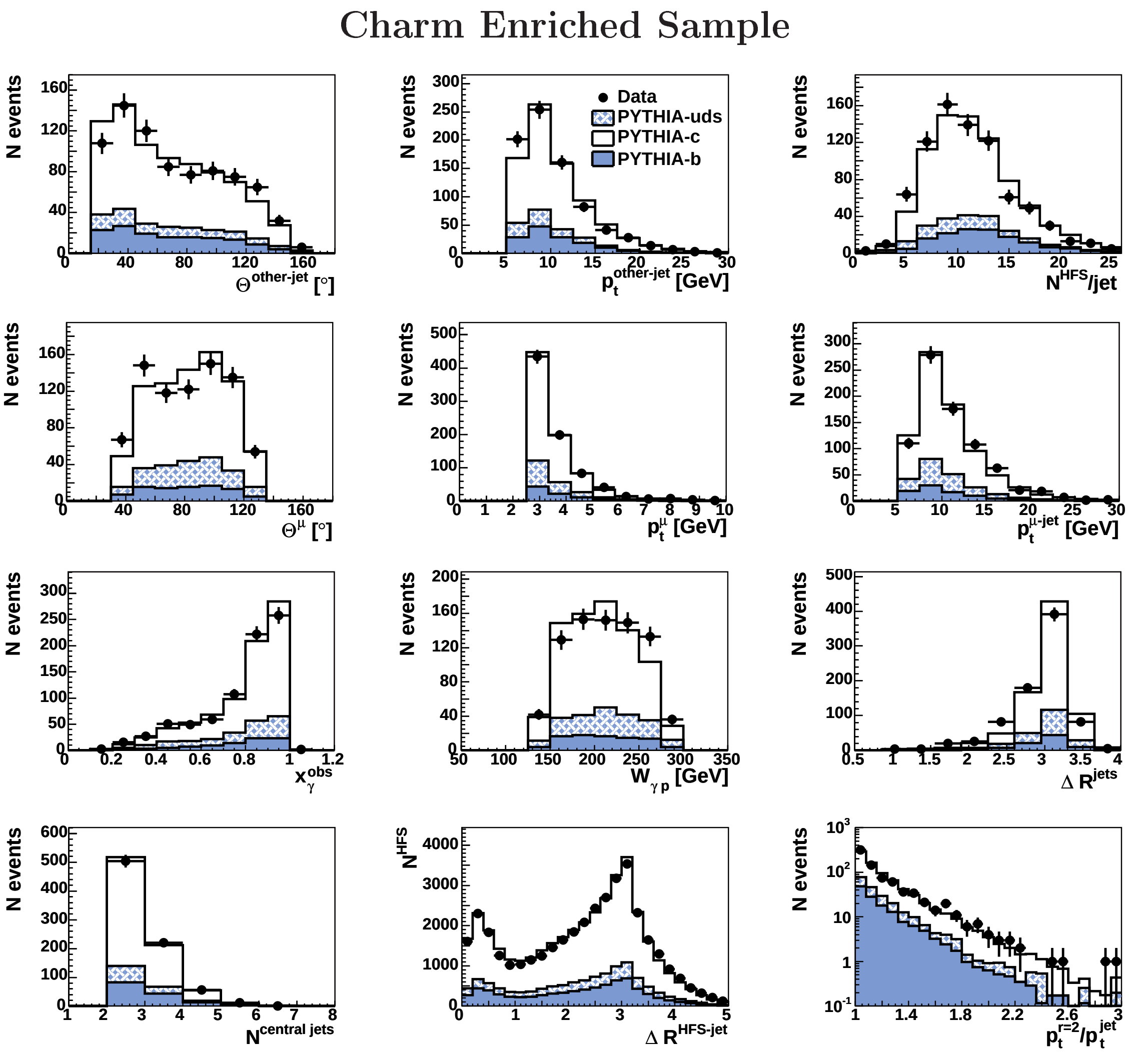

Figure 5.6: *Control distributions of various variables (see text) for the* ***charm enriched data sample****. The data (points) are compared with the PYTHIA Monte Carlo simulation (lines). The remaining background from beauty events and light quark events is shown separately.*

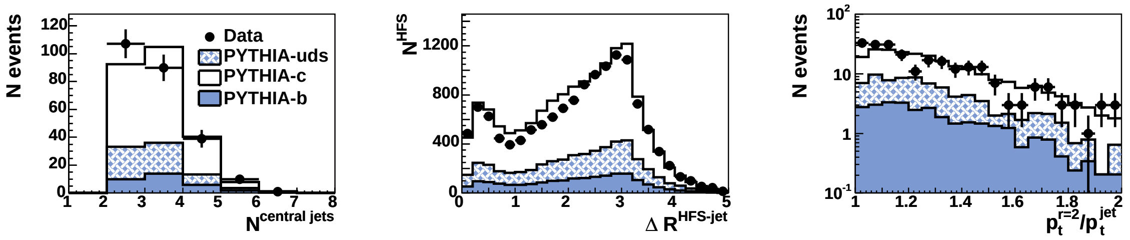

Figure 5.7: *Control distributions of selected variables (see text) for the events from* ***charm enriched sample*** *with $x_\gamma^{obs} \leq 0.75$. The data (points) are compared with the PYTHIA Monte Carlo simulation (lines). The remaining background from beauty events and light quark events is shown separately.*

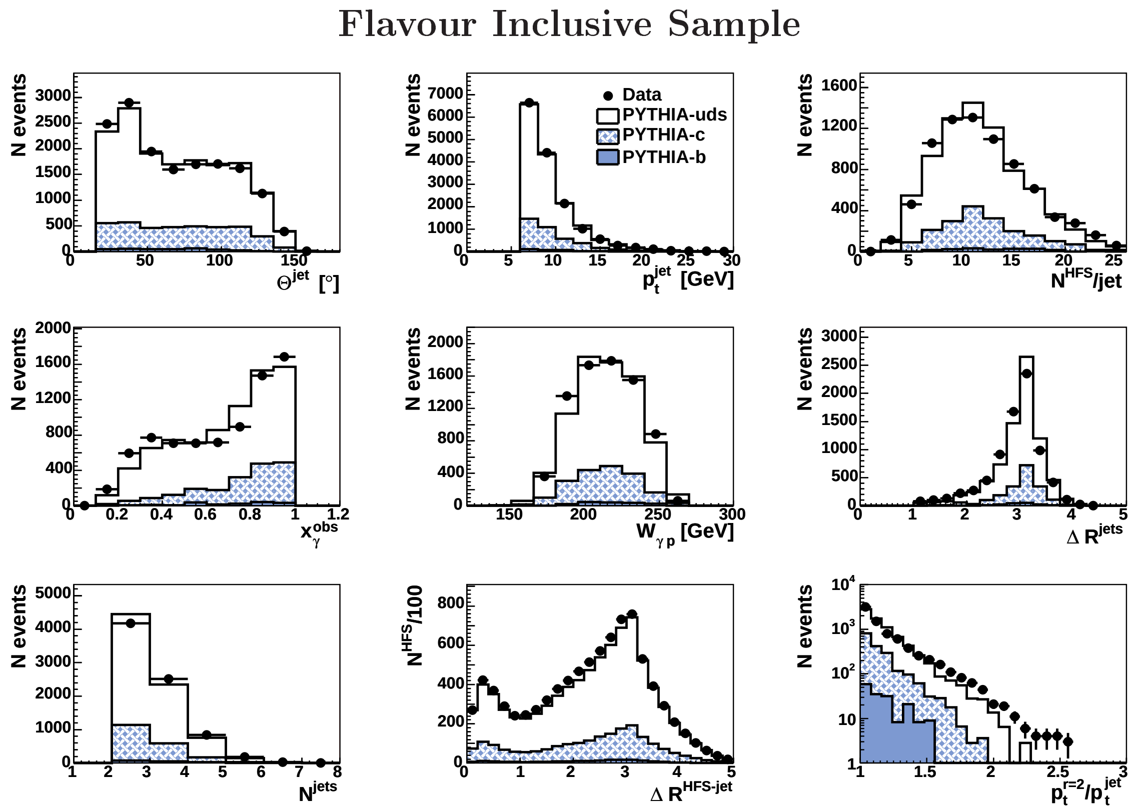

Figure 5.8: *Control distributions of various variables (see text) for the* ***flavour inclusive sample****. The data (points) are compared with the inclusive PYTHIA Monte Carlo simulation (lines). Separately shown are charm, light quark and beauty event contributions.*

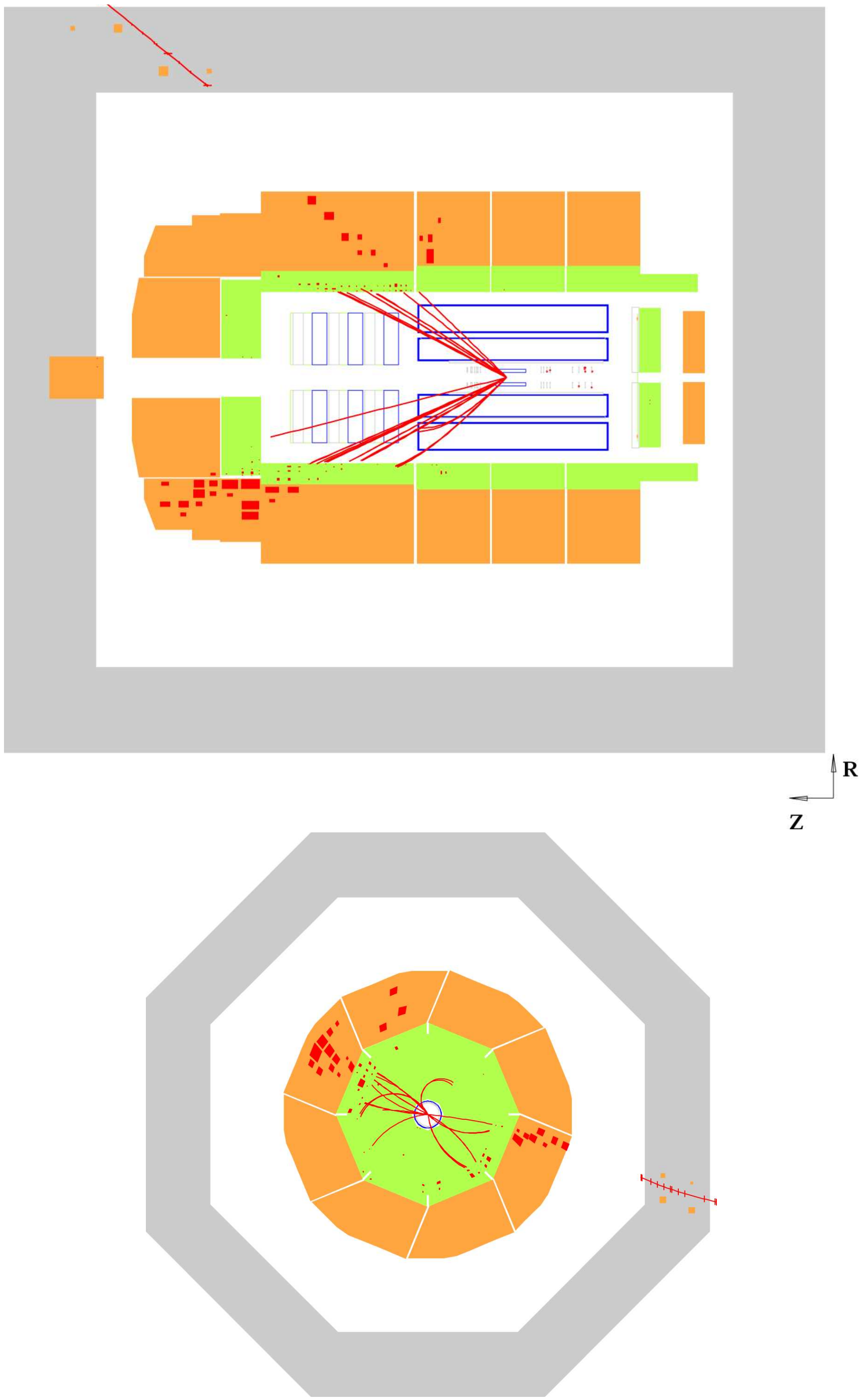

Figure 5.9: *Event display of a typical event from the charm enriched sample in the rz plane (top) and $r\phi$ plane (bottom) plane. Two jets and a muon with a signal in the CMD are visible.*

Chapter 6

Measurement of the Jet Structure

In this chapter the aspects of jet structure measurement are discussed including all systematic checks. In the first section of this chapter the results of quality checks of the measured variables are shown. They concern efficiency, correlation between reconstructed and generated variables, purity and stability of the selected data. Further, the background subtraction method for the charm enriched sample is explained. The measurements of the mean integrated jet shape at detector level are presented for the background corrected charm sample and for the flavour inclusive event sample. The method of detector corrections for the data and systematic uncertainties are discussed in the end.

6.1 Quality of the Reconstruction of the Kinematic Variables

In this analysis we measure the variable 'mean integrated jet shape' (see section 2.5 for the definition), where the efficiencies enter through the detector correction, as described in section 6.5 The efficiencies are investigated to ensure that the PYTHIA Monte Carlo description of the data is good enough to use it for the correction of the data to the hadron level.

Furthermore, the correlations between the reconstructed and generated variables and the resolutions are checked to confirm that the bin widths are not too narrow. Finally, the purities and stabilities prove that the migrations between the bins are not too large and that a relevant fraction of the reconstructed events was also generated in the same analysis bin.

6.1.1 Efficiency

The event losses due to the inefficiencies of the detector components and cuts of the event selection are characterised by $(1-\epsilon_{tot})$, where ϵ_{tot} is the **total efficiency**. It factorizes to

$$\epsilon_{tot} = \epsilon_{trig} \times \epsilon_{rec}, \tag{6.1}$$

where ϵ_{trig} denotes the trigger efficiency and ϵ_{rec} the reconstruction efficiency. Since the analysis cuts are harder than the cuts of the L4 finders, only L1 efficiencies are considered.

The **trigger efficiency** we define as the fraction of the events, satisfying the conditions listed in table 5.3, which are actually triggered. The Monte Carlo description of the efficiency of particular trigger elements is checked with the data. For this purpose a set of independent monitor triggers is needed, which do not require the studied trigger element. Usually, more then one monitor trigger is used in a logical 'or' combination. Then the trigger efficiency is given by the ratio of events that were triggered by, both, the investigated trigger element (TE) and the monitor trigger (moni) to the events that were triggered by the monitor trigger alone

$$\epsilon_{trig} = \frac{N_{TE\,\&\,moni}}{N_{moni}}. \tag{6.2}$$

In the data, both, actual L1 subtriggers and verified L4 subtriggers are required for monitor triggers. In the Monte Carlo only actual L1 subtriggers are required, since the relevant L4 trigger bits are not simulated.

In the following we discuss the efficiencies of the trigger elements Mu_Bar, DCRPh_CNH and zVtx_sig included in the definitions of subtriggers s19 and s22 (see table 5.1), which are used to trigger the charm enriched sample. The trigger elements of the luminosity system, used for the triggering of the flavour inclusive dijet sample, are contained in the electron tagger acceptance, which will be discussed later in this section.

As monitor triggers, subtriggers including the SpaCal trigger elements, the LAr trigger elements, the electron tagger trigger elements and the time-of-flight trigger elements are chosen (see table 6.1). To be able to use the trigger elements designed for the deep inelastic scattering events, the photoproduction cuts on Q^2 and y are dropped for this check.

Since a major fraction of the selected charm enriched sample is due to the charm events (about 70 %), we compare the trigger element efficiencies determined from the data to the efficiencies determined from the charm PYTHIA MC. It is checked that the efficiencies obtained using the beauty Monte Carlo are the same within the statistical errors. Binomial statistical errors are quoted

$$\sigma_{\epsilon_{trig}} = \sqrt{\frac{\epsilon_{trig} \cdot (1 - \epsilon_{trig})}{N_{moni}}}. \tag{6.3}$$

The efficiencies of the three trigger elements determined from the data, are compared to those from the charm PYTHIA MC simulation in figure 6.1.

Charm Enriched Sample

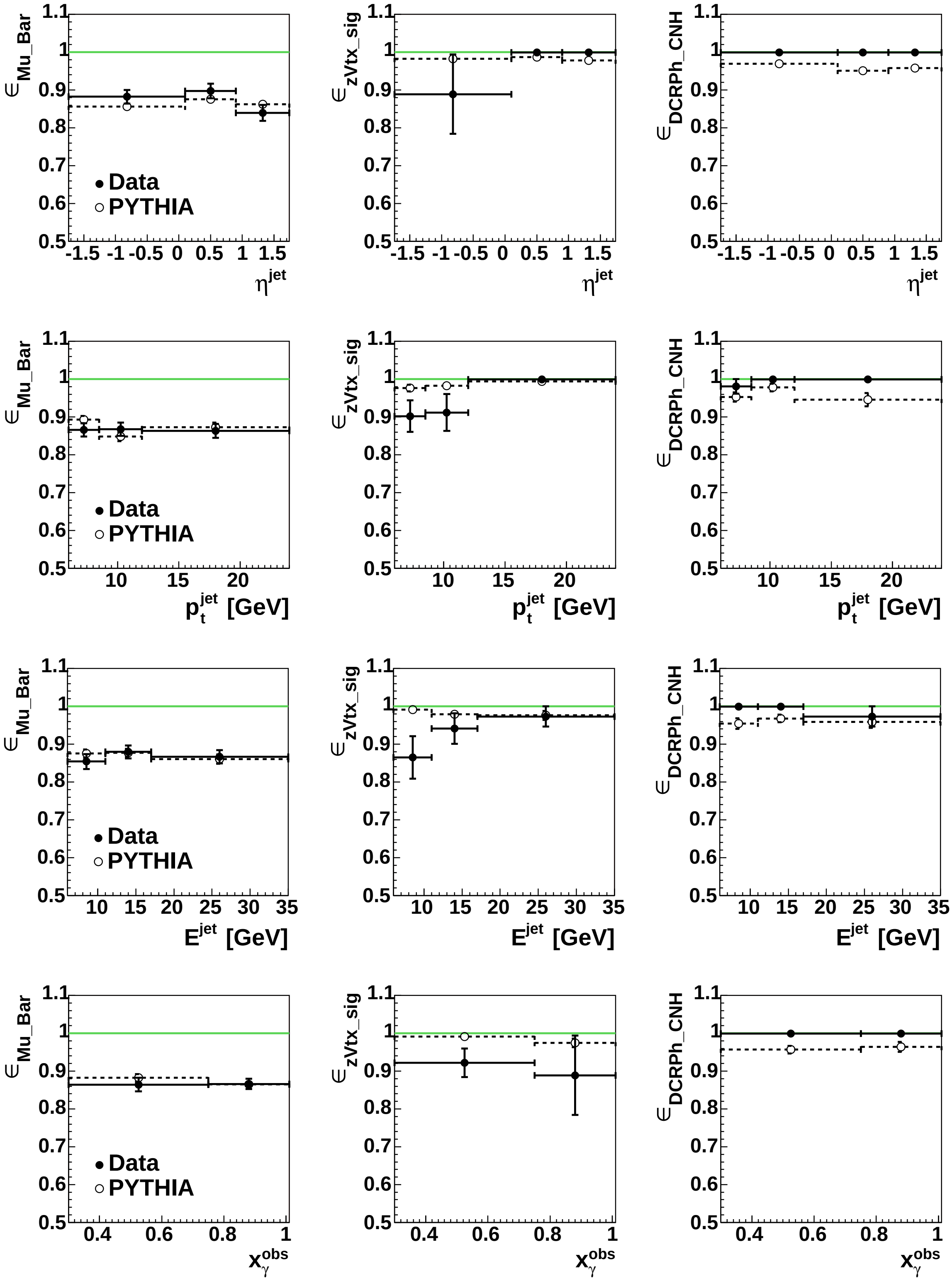

Figure 6.1: *The efficiency of the trigger elements Mu_Bar, zVtx_sig and DCRPh_CNH, for the charm sample as functions of the variables η^{jet}, p_t^{jet}, E^{jet} of the 'other jet' and the variale x_γ^{obs}. The description by the charm PYTHIA MC is also shown.*

In case of the element Mu_Bar a good agreement between the data and Monte Carlo is observed. In case of zVtx_sig a small disagreement is observed at low p_t^{jet} and E^{jet}. However, for this analysis the absolute magnitude of the trigger efficiency is not important. Relevant is a similar trigger efficiency for direct and resolved events rather than the absolute value. It ensures that the mixture of direct and resolved events in the data is not biased by the trigger selection, as it is also in the case of the efficiency of zVtx_sig, as shown in the lowest row of figure 6.1. The efficiency of the trigger element DCRPh_CNH is independent of all the variables in both data and the Monte Carlo, however in the data the efficiency is higher than in the Monte Carlo.

The overall efficiencies of the three investigated trigger elements are listed in table 6.1 for the data, the charm and the beauty Monte Carlo simulation PYTHIA.

Trigger Element	Monitor Triggers	ϵ_{trig}^{data}[%]	ϵ_{trig}^{cMC}[%]	ϵ_{trig}^{bMC}[%]
Mu_Bar	s0,s1,s2,s3,s4,s9,s35,s36,s37,s39, s42,s44,s71,s82,s83,s100,s101	86.5 ± 1.0	86.5 ± 0.3	87.3 ± 0.6
zVtx_sig	s0,s1,s3,s4,s5,s6,s7,s8	92.9 ± 2.4	98.2 ± 0.3	98.3 ± 0.5
DCRPh_CNH	s0,s1,s3,s4,s5,s6,s7,s8	99.1 ± 0.9	96.0 ± 0.4	95.9 ± 0.8

Table 6.1: *Average efficiencies of the trigger elements in subtrigger s19 are listed as well as the monitor triggers used, which do not contain the studied trigger elements. The efficiencies are calculated using the charm enriched data, charm and the beauty PYTHIA simulation. The subtriggers are defined in [79].*

The **reconstruction efficiency** includes the efficiency of all selection cuts (except of the trigger requirements) and the event reconstruction itself. It is determined by Monte Carlo and it is given by the fraction of the events reconstructed in the visible region after applying the selection cuts with respect to all generated events in the visible region:

$$\epsilon_{rec} = \frac{N_{rec|vis}}{N_{gen|vis}}. \tag{6.4}$$

The visible region is defined by the cuts in tables 5.3 and 6.3 for detector level and hadron level, respectively. Here 'detector level' denotes the level of measured particles and 'hadron level' the level of the decayed hadrons (see also figure 4.5). The reconstruction efficiency for the charm sample determined from the charm PYTHIA MC is shown in figure 6.2 as a function of the variables η^{jet}, p_t^{jet}, E^{jet} of the 'other jet' and the variable x_γ^{obs}. The overall reconstruction efficiency is independent of the variables in good approximation and only slightly higher for resolved events. It amounts to about 30 %.

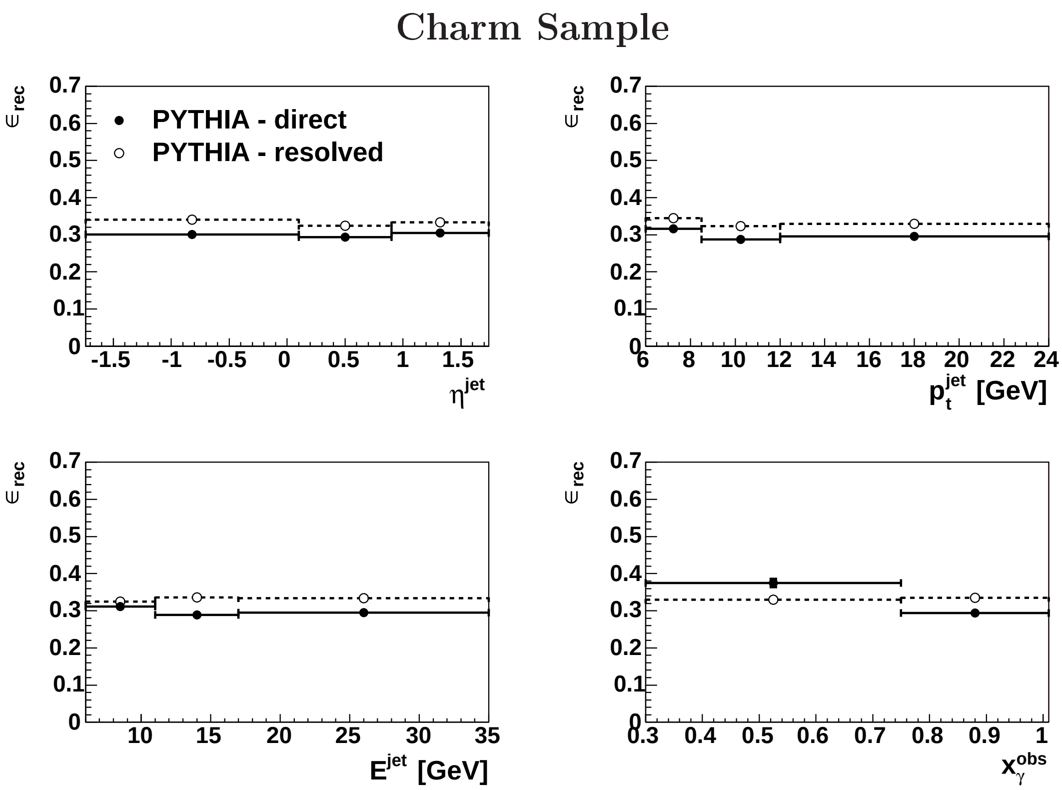

Figure 6.2: *The reconstruction efficiency for direct and resolved events as function of the variables η^{jet}, p_t^{jet} and E^{jet} of the 'other jet' and the variable x_γ^{obs}. The efficiencies are calculated using the charm PYTHIA MC.*

The **electron tagger acceptance** enters only for the flavour inclusive sample. Since the electron tagger is not simulated in the Monte Carlo, the generated events are weighted by the ET33 acceptance. In this analysis we adopt the method explained in [77]. The mean electron tagger acceptance is calculated by averaging the acceptance function over the visible region using the Monte Carlo simulation

$$\mathcal{A}_{ET33}^{MC} = \frac{\sum_i^{N_{rec}} a_{33}(y_i, r_i)}{N_{rec}}. \tag{6.5}$$

Here N_{rec} is the number of the Monte Carlo events reconstructed in the visible region, a_{33} is the measured acceptance parametrised as a function of the inelasticity y_i and the run period r_i of the reconstructed event. This acceptance also includes inefficiencies of the trigger elements LU_ET and LU_PD_low. The acceptance of the tagger ET33 for different run periods as a function of the inelasticity y is shown in figure 5.2. The total electron tagger acceptance in the visible region is about 40 % and it does not differ for direct and resolved events. The total electron tagger acceptance is independent of all the studied variables as expected.

6.1.2 Correlations Between Reconstructed and Generated Variables

The relationship between reconstructed and generated variables for the charm sample is studied separately for direct and resolved events in figures 6.3 and 6.4. The correlations for the variables p_t^{jet}, η^{jet}, E^{jet} of the 'other jet' and the variable x_γ^{obs} are shown. The plots are produced using the charm PYTHIA Monte Carlo, since the charm enriched data sample is dominated by charm events. The correlations are best in the variable η^{jet}, but the other variables are also well correlated. Similar correlations are observed for direct and resolved events.

The correlations for the flavour inclusive events are shown in figures 6.5 and 6.6. They are calculated for the two highest p_t jets. The figure contains one entry per jet. The correlations are comparable with the charm case, except of η^{jet}. In the flavour inclusive events the correlation for this variable is worse than in the charm events. The high p_t muon, which helps to distinguish the jets, is missing in the flavour inclusive sample.

More quantitatively, the difference between a generated and a reconstructed variable can be characterised by the relative deviation of the reconstructed variable from the generated variable. For η^{jet} it can be expresses as

$$\frac{\eta_{rec}^{jet} - \eta_{gen}^{jet}}{\eta_{gen}^{jet}}. \tag{6.6}$$

The distributions for all the variables used in this analysis are shown in figure 6.7 for the charm sample. The distributions for direct and resolved photon events are shown separately. The plots are obtained using the charm PYTHIA MC and considering only the 'other jet'. One can see that the resolution is comparable for direct and resolved events for p_t^{jet}, η^{jet}, and E^{jet}. The resolution in the variable x_γ^{obs} is worse for the resolved events. This may be expected from the different and more complex shape of the resolved events.

The resolutions are similar for the flavour inclusive events, as can be seen from the plots in figure 6.8. Only the resolution in η^{jet} is slightly worse than in the charm case, as already observed in the correlation plots. The inclusive PYTHIA MC is used for the resolution plots and only the highest p_t jet is chosen. The resolutions for the second highest p_t jet were also studied and found to be very similar to the resolutions for the highest p_t jet.

All the analysis bins used for the results in chapter 7 are broader than the full width at half maximum of the shown distributions. Resolution of the jet axis measurement is taken into account in the determination of the systematic uncertainties, as described in section 6.6.

Charm Sample

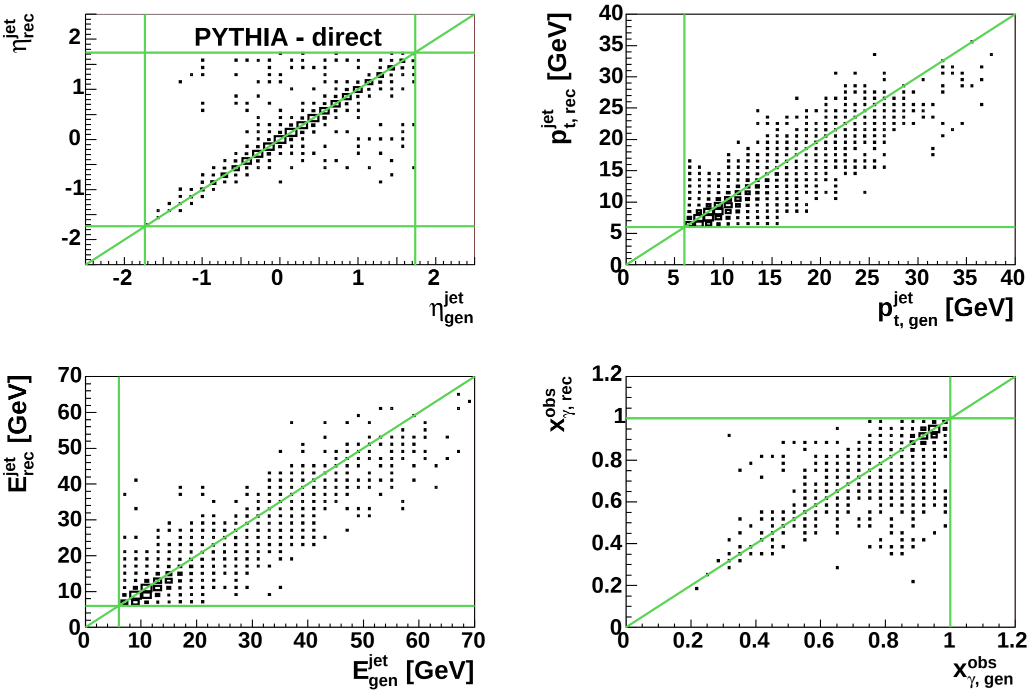

Figure 6.3: *Reconstructed versus generated variables for direct events as simulated by the charm PYTHIA MC. The variables η^{jet}, p_t^{jet} and E^{jet} are derived for the 'other jet'. Horizontal and vertical lines indicate the applied cuts.*

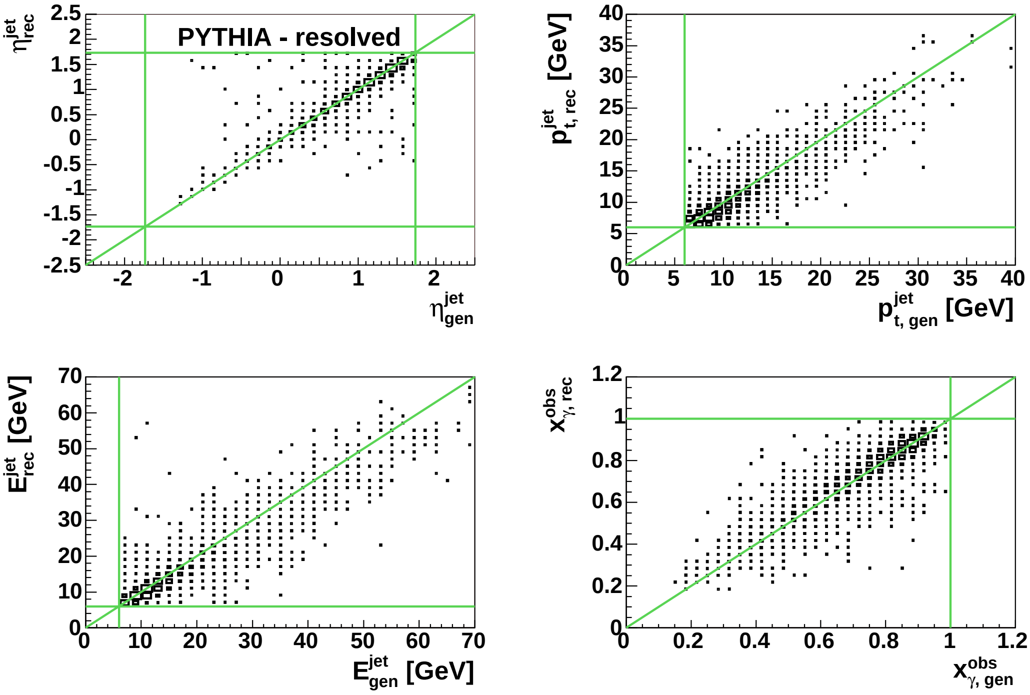

Figure 6.4: *Reconstructed versus generated variables for resolved events as simulated by the charm PYTHIA MC. The variables η^{jet}, p_t^{jet} and E^{jet} are derived for the 'other jet'. Horizontal and vertical lines indicate the applied cuts.*

Flavour Inclusive Sample

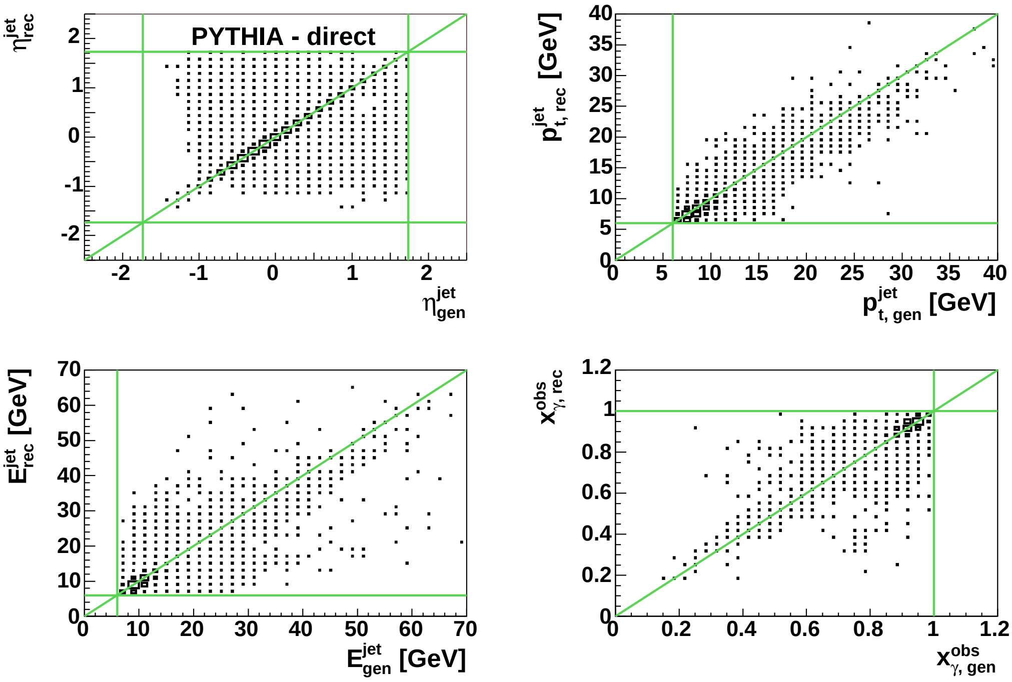

Figure 6.5: *Reconstructed versus generated variables for direct events as simulated by the inclusive PYTHIA MC. The figure contains one entry per each of the two highest p_t jets, the values are weighted by the ET33-acceptance. Horizontal and vertical lines indicate the applied cuts.*

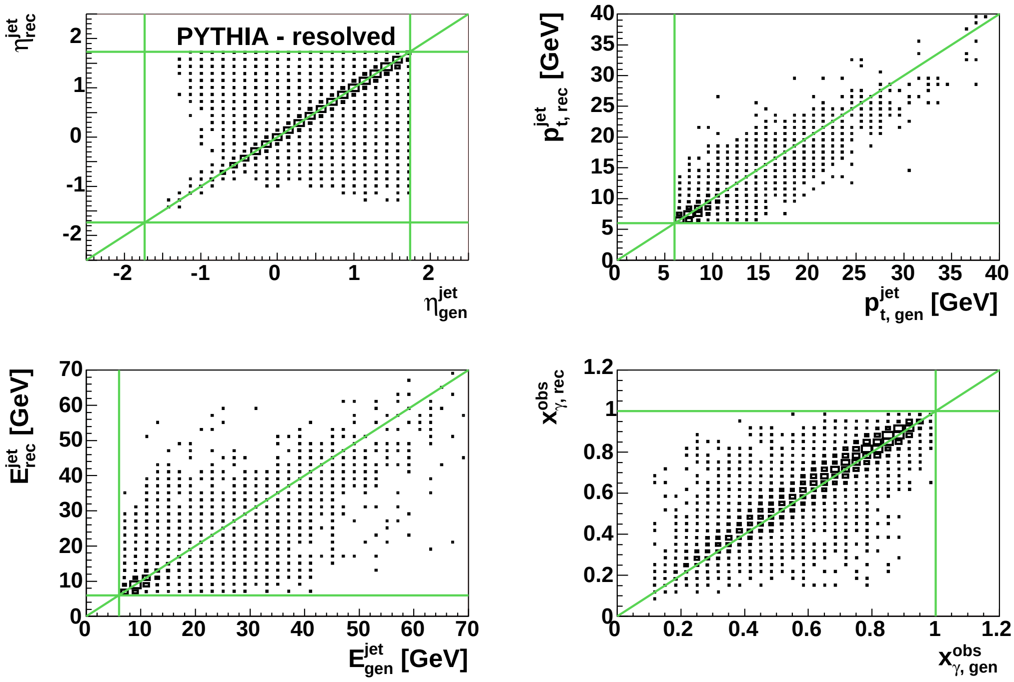

Figure 6.6: *Reconstructed versus generated variables for resolved events as simulated by the inclusive PYTHIA MC. The figure contains one entry per each of the two highest p_t jets, the values are weighted by the ET33-acceptance. Horizontal and vertical lines indicate the applied cuts.*

Charm Sample

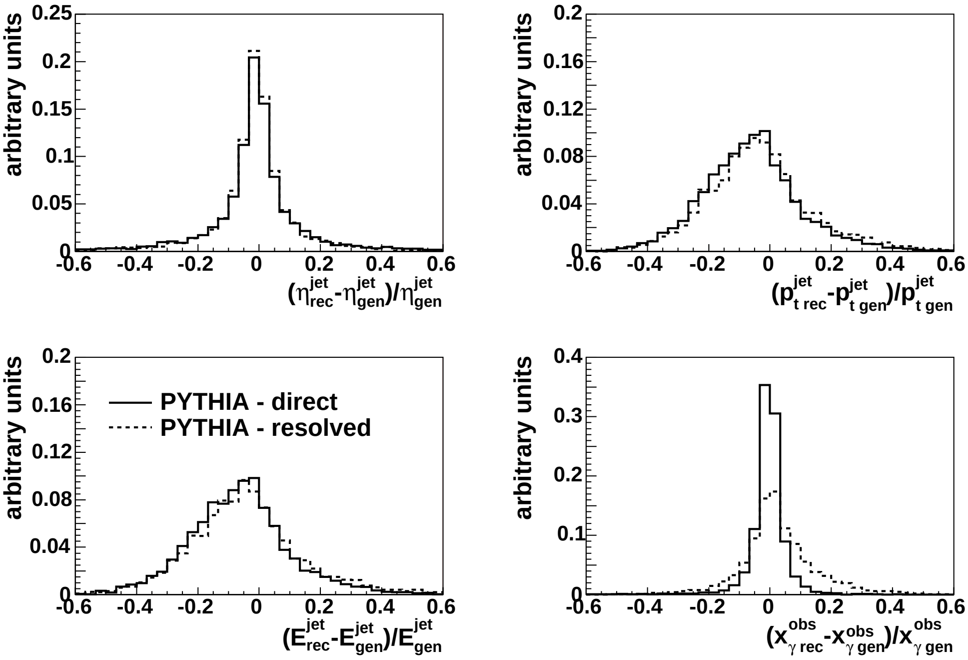

Figure 6.7: *The relative resolution in the variables η^{jet}, p_t^{jet} and E^{jet} of the 'other jet' and the variable x_γ^{obs}. The distributions are shown separately for direct and resolved events as simulated by the charm PYTHIA MC, normalised to the total number of events.*

Flavour Inclusive Sample

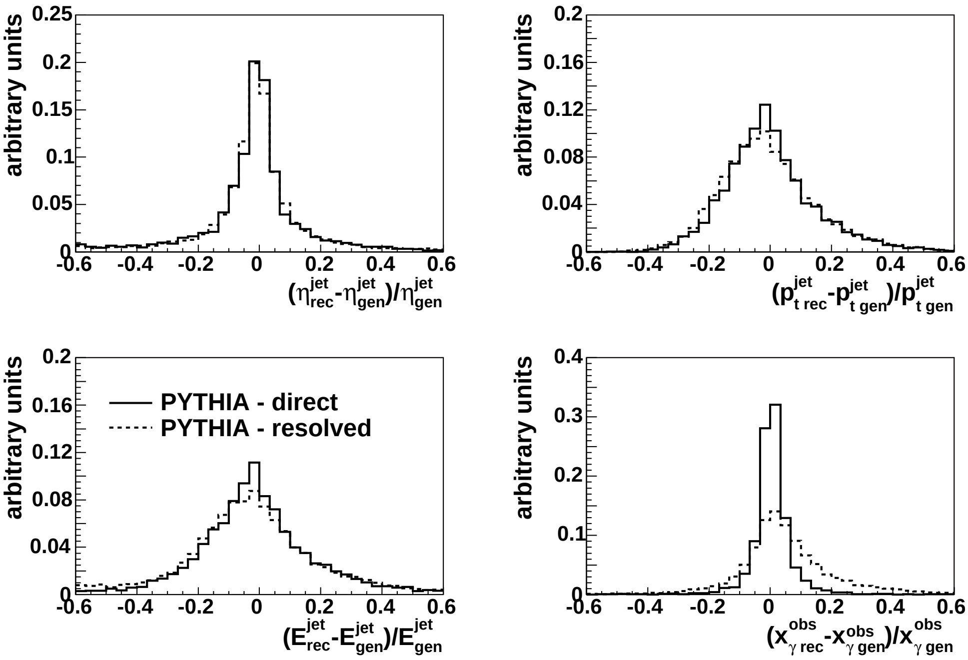

Figure 6.8: *The relative resolution in the variables η^{jet}, p_t^{jet} and E^{jet} of the highest p_t and the variable x_γ^{obs}, weighted by the ET33-acceptance. The distributions are shown separately for direct and resolved events as simulated by the inclusive PYTHIA MC, normalised to the total number of events.*

6.1.3 Purity and Stability

The migrations between the bins are characterised by the purity (stability) which is defined as the number of the simulated events which originate from a bin and which are reconstructed in it, divided by the number of reconstructed (generated) events in that bin. Thus purity (P_i) and the stability (S_i) are calculated for each bin i as

$$P_i = \left.\frac{N_{i,rec\,\&\,gen}}{N_{i,rec}}\right|_{vis}, \tag{6.7}$$

$$S_i = \left.\frac{N_{i,rec\,\&\,gen}}{N_{i,gen}}\right|_{vis}, \tag{6.8}$$

where $N_{i,gen}$ is the number of events with a variable generated in the bin i, $N_{i,rec}$ is the number of events with the same variable reconstructed in the bin i and $N_{i,rec\,\&\,gen}$ is the number of events with the value of the variable generated and reconstructed in the same analysis bin. Both, purity and stability are calculated using events reconstructed in the visible region of the measurement, which in this analysis is defined by the cuts in table 5.3. Both of them should be as large as possible. Ideally, in case of infinite resolution, they are equal to one. It has become customary to require purity and stability to be larger than 0.3.

The purities and stabilities for the variables η^{jet}, p_t^{jet} and E^{jet} of the 'other jet' and the variable x_γ^{obs} are shown in figures 6.9 and 6.10 respectively. Results of the charm Monte Carlo simulation PYTHIA are shown separately for direct and resolved events. The purities for the resolved events are lower than those of the direct events, except for the low x_γ^{obs} bin where the purity for the resolved events is higher. Purities in all bins are higher than 0.3 for both direct and resolved events. The lowest purity is obtained for the lowest p_t^{jet} bin. Stabilities are very similar for direct and resolved events and in all analysis bins well above 0.5.

Purities and stabilities for the highest p_t jet of the flavour inclusive sample are shown in figures 6.11 and 6.12 respectively. Only the highest p_t jet is considered. Results of the inclusive Monte Carlo simulation PYTHIA are shown separately for direct and resolved events. Purities are, like for the charm events, higher for direct events in most bins. Both purity and stability for η^{jet} are lower than in the charm case. This is caused by the worse resolution in the η^{jet} measurement in the flavour inclusive events (see section 6.1.2). The stabilities of the other variables do not differ much from the charm case.

Purities and stabilities for the second highest p_t jet of the flavour inclusive sample were also studied. In most bins the purity for the second highest p_t jet is slightly lower than for the highest p_t jet, however everywhere above 0.35. The stability is also slightly lower but still above 0.5 in all bins.

The high purities and stabilities together with the flat reconstruction efficiency, high trigger efficiency and well described control plots enable us to use the bin-by-bin corrections to correct the measured data for the detector effects, as will be explained in detail in section 6.5.

Charm Sample

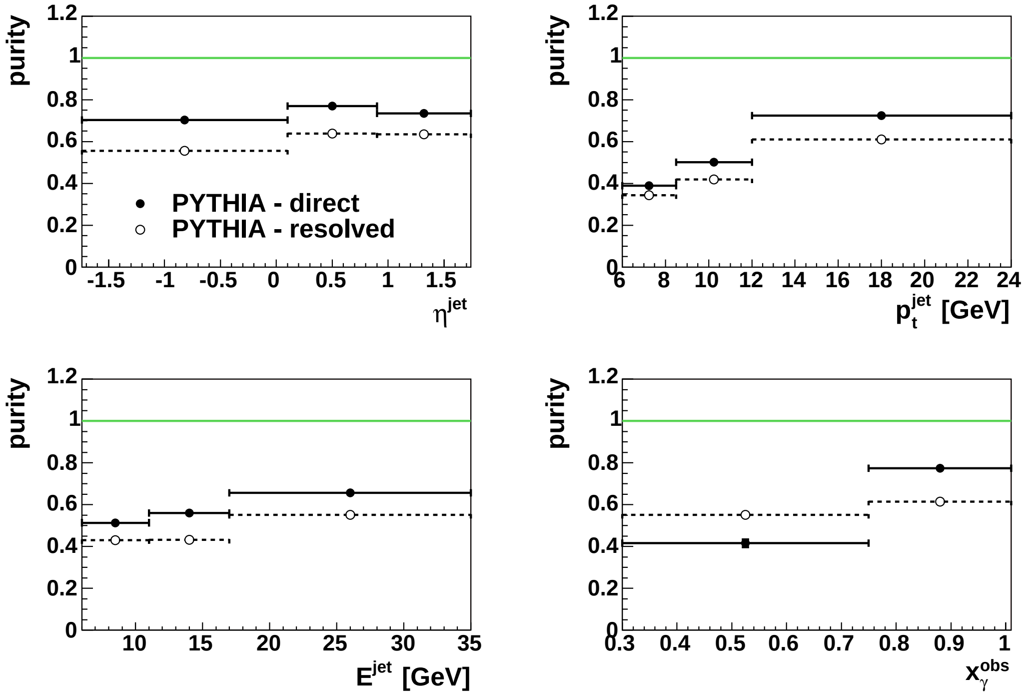

Figure 6.9: *The purities of the reconstructed events shown separately for direct and resolved processes as function of the variables η^{jet}, p_t^{jet} and E^{jet} of the 'other jet' and the variable x_γ^{obs}. The purities are calculated using the charm PYTHIA MC simulation.*

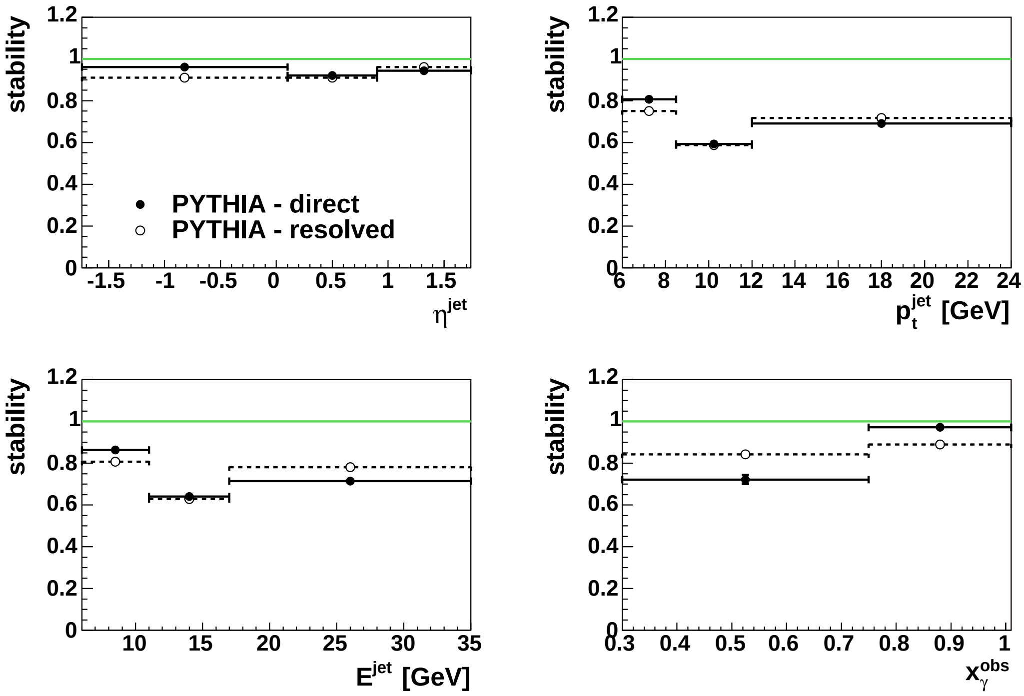

Figure 6.10: *The stabilities of the reconstructed events shown separately for direct and resolved processes as function of the variables η^{jet}, p_t^{jet} and E^{jet} of the 'other jet' and the variable x_γ^{obs}. The stabilities are calculated using the charm PYTHIA MC simulation.*

Flavour Inclusive Sample

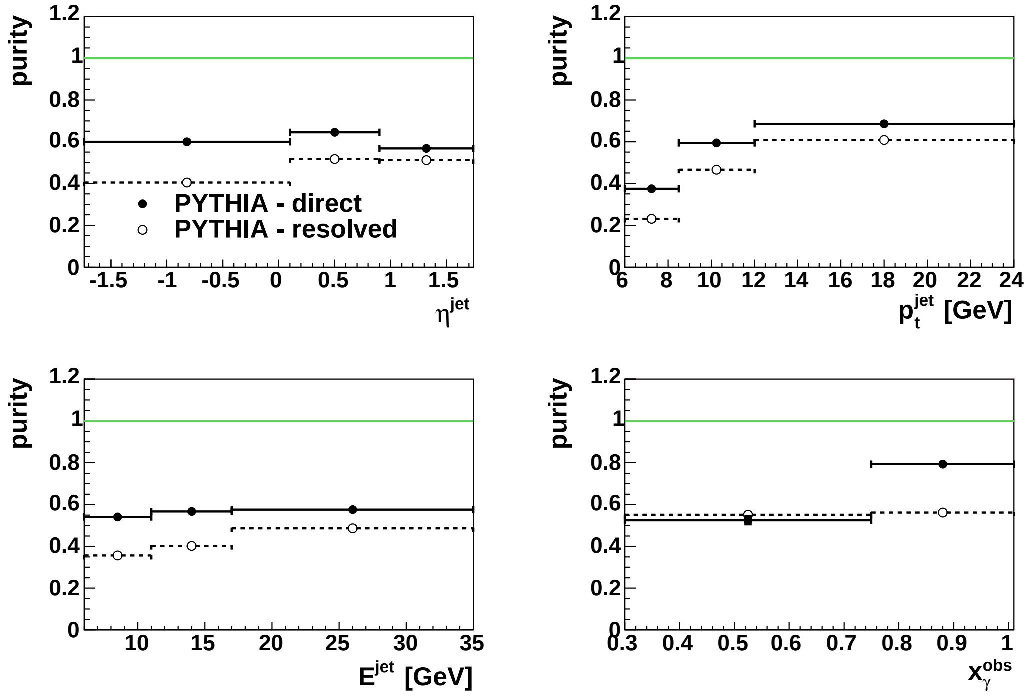

Figure 6.11: *The purities of the reconstructed events shown separately for direct and resolved processes as a function of η^{jet}, p_t^{jet}, E^{jet} for the jet with the highest p_t and x_γ^{obs}. The purities are calculated using the charm PYTHIA MC simulation.*

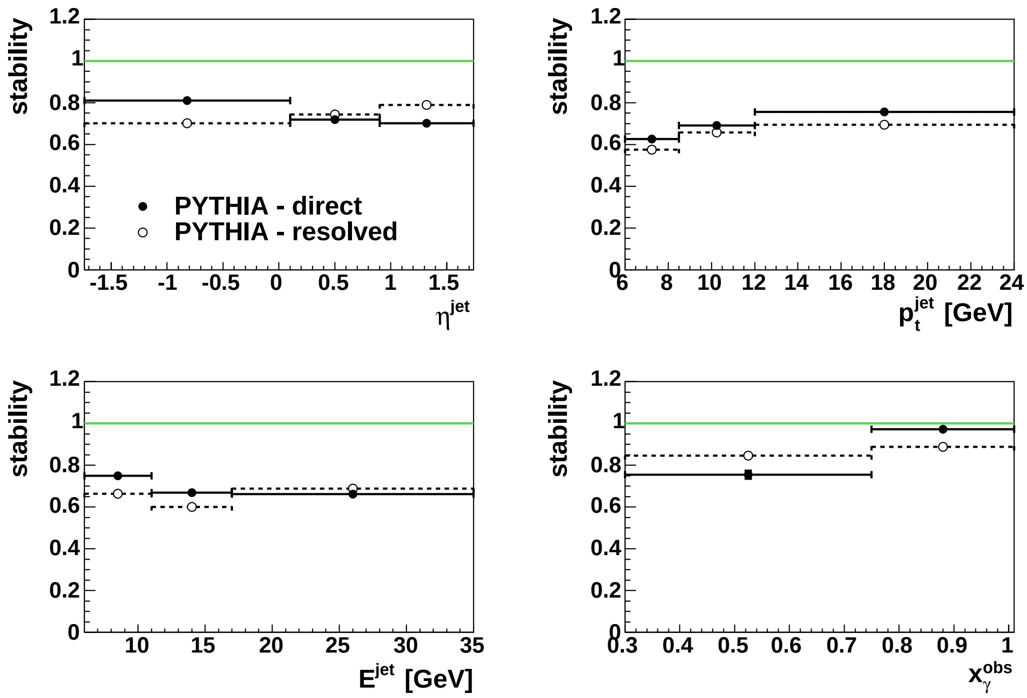

Figure 6.12: *The stabilities of the reconstructed events shown separately for direct and resolved processes as a function of η^{jet}, p_t^{jet}, E^{jet} for the jet with the highest p_t and x_γ^{obs}. The stabilities are calculated using the charm PYTHIA MC simulation.*

6.2 Background Subtraction for the Charm Enriched Sample

The charm enriched data sample, selected using the cuts listed in table 5.3, contains background events coming from beauty and light quark events, as already discussed in chapter 5. The background subtraction method explained in the present section is applied only on the charm data sample, the flavour inclusive events are not corrected for background since it does not contain any by definition.

In chapter 5 we showed that an overall two dimensional fit to the p_t^{rel} and δ_μ variables confirms the predictions of the inclusive PYTHIA Monte Carlo for the **fractions of beauty and light quark events**. These fractions are shown in figure 6.13 in all bins, as expected from the inclusive Monte Carlo PYTHIA. They are used for the background correction, as described below.

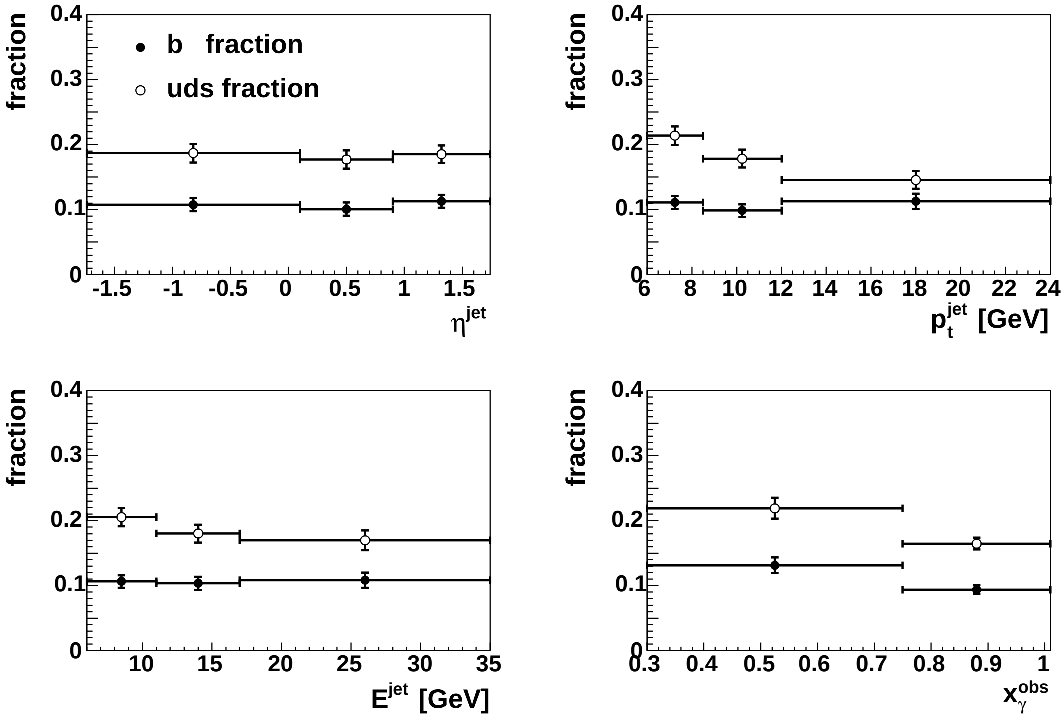

Figure 6.13: *Fractions of beauty and light quark events in the charm sample as function of the variables η^{jet}, p_t^{jet} and E^{jet} of the 'other jet' and the variable x_γ^{obs}. The prediction of the inclusive Monte Carlo PYTHIA with the statistical errors is shown.*

In figure 6.14 the data distributions for the variables p_t^{jet}, η^{jet}, E^{jet} of the 'other jet' and the variable x_γ^{obs} are shown together with the description by the inclusive PYTHIA Monte Carlo. The description of p_t^{jet}, E^{jet} and x_γ^{obs} is reasonable. Small differences appear only in the η^{jet} distribution. These are however related to the mixture of various direct and resolved processes, mainly in the charm sample, rather than to the fractions of charm, beauty and light quark events in the data sample. The slightly decreasing number of events versus η^{jet} cannot be well described by any combination of the shown charm and background distributions.

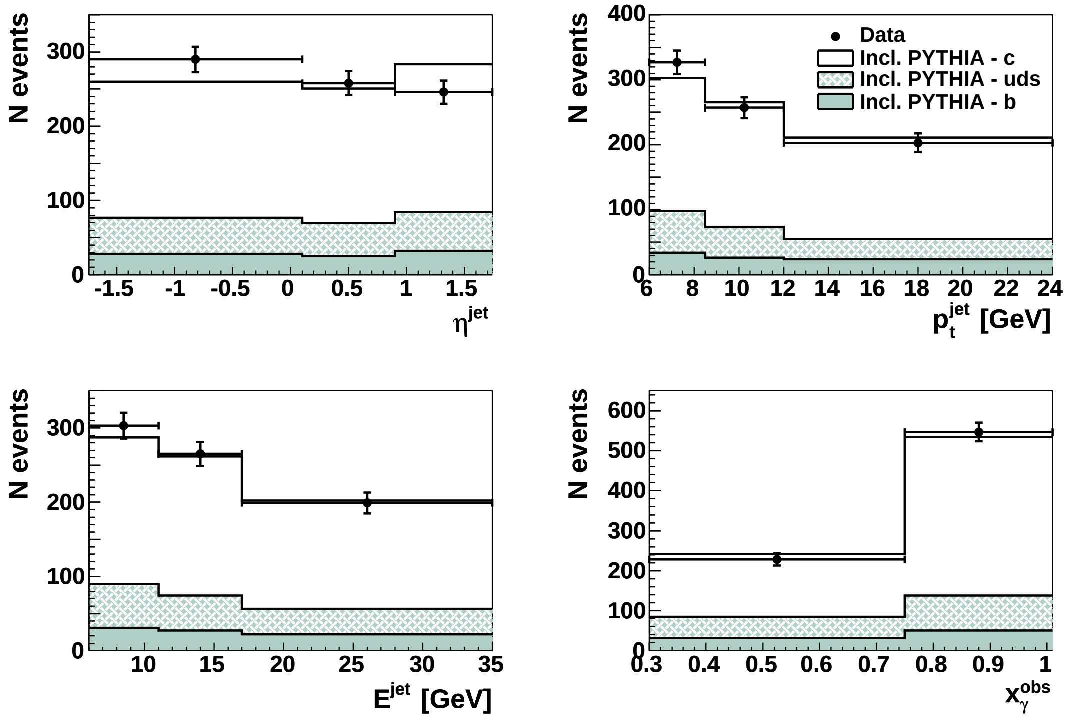

Figure 6.14: *Description of the charm enriched data sample before the background subtraction by the inclusive PYTHIA MC as function of the variables η^{jet}, p_t^{jet} and E^{jet} of the 'other jet' and the variable x_γ^{obs}. The shaded area represents the background due to jets from beauty events, the cross hatched area due to jets from light quark events. The total MC prediction is normalised to the number of the events in the data.*

The **correction for the background** is made using the method from [80]. Since the observable mean integrated jet shape $\langle\psi(r)\rangle$ is defined as an average of the measured integrated jet shapes over the events (see equation 2.5), the mean integrated jet shape measured in the data without background correction can be written as

$$\langle\psi(r)\rangle^{data} = f_c\langle\psi(r)\rangle^c + f_b\langle\psi(r)\rangle^b + f_{uds}\langle\psi(r)\rangle^{uds}, \tag{6.9}$$

where f_c, f_b and f_{uds} denote the fractions of charm, beauty and light quark events, respectively and their sum is equal to unity. The jet shapes for both background components, $\langle\psi(r)\rangle^b$ and $\langle\psi(r)\rangle^{uds}$, are determined from the PYTHIA MC in each analysis bin. Then $\langle\psi(r)\rangle^c$ can be expressed as

$$\langle\psi(r)\rangle^c = \frac{\langle\psi(r)\rangle^{data} - f_b\langle\psi(r)\rangle^b - f_{uds}\langle\psi(r)\rangle^{uds}}{1 - f_b - f_{uds}}. \tag{6.10}$$

The uncertainty on the background determination is included in the calculation of the systematic uncertainty, as described in the section 6.6.

The control distribution of $\psi(r = 0.5)$ for the **data before background subtraction** is shown in figure 6.15 together with the inclusive PYTHIA MC description in both bins of x_γ^{obs}. For the high x_γ^{obs} values (direct enriched events) the data are described well, but for the low x_γ^{obs} values (resolved enriched events) the description is not good. The discrepancy in the low x_γ^{obs} bin does not originate from the background composition, rather than the composition of the various resolved processes in the PYTHIA MC.

The control distribution of $\psi(r = 0.5)$ for the **data after background subtraction** is shown in figure 6.16 together with the prediction of the charm PYTHIA MC for both bins of x_γ^{obs}. For the low x_γ^{obs} values the MC description is good. For the low x_γ^{obs} values the data rise sharper versus ψ than both the direct and resolved PYTHIA predictions, thus having a higher mean value than the MC distributions. The difference between the distributions for direct and resolved events is very small at low x_γ^{obs}.

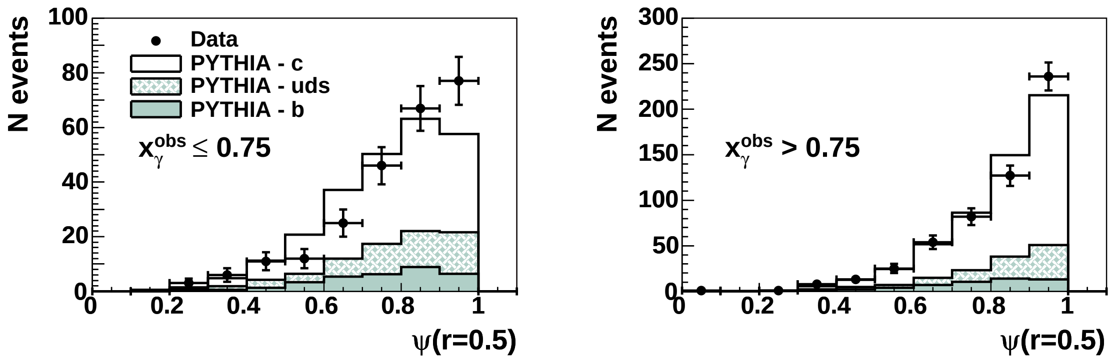

Figure 6.15: *The distribution of the integrated jet shape $\psi(r)$ for a cone radius r of 0.5 in the charm enriched data before the subtraction of background. A comparison with the inclusive PYTHIA simulation is shown. The background contributions by the beauty and light quark events are shown separately. The total MC prediction is normalised to the number of the events in the data.*

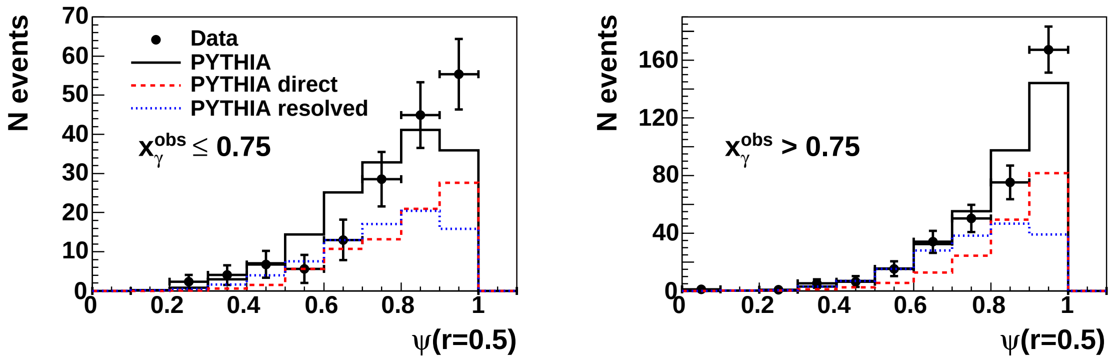

Figure 6.16: *The distribution of the integrated jet shape $\psi(r)$ for a cone radius r of 0.5 in the data after the subtraction of background. The description by the total charm PYTHIA MC is shown. The expected jet shapes for direct and resolved events are shown separately using an arbitrary normalisation for better visibility. The total MC prediction is normalised to the number of data events.*

6.3 Determination of the Statistical Errors

For the **flavour inclusive sample** the statistical error of the mean integrated jet shape $\langle\psi(r)\rangle$ measured in the data is determined as a standard deviation:

$$\sigma^{stat}_{\langle\psi(r)\rangle^{data}} = \sqrt{\frac{\sum_{i=1}^{N}(\psi(r)_i^{data} - \langle\psi(r)\rangle^{data})^2}{N-1}}, \tag{6.11}$$

where N is the number of events in the studied $\psi(r)^{data}$ distribution.

For the **charm enriched sample** the background subtraction is performed. In this case the statistical error contribution coming from the statistical uncertainty of the data is one magnitude higher than the statistical uncertainties of the MC background. Therefore the statistical error of the Monte Carlo can be neglected. The statistical error takes then the following form

$$\sigma^{stat}_{\langle\psi(r)\rangle} = \frac{1}{1 - f_b - f_{uds}}\,\sigma^{stat}_{\langle\psi(r)\rangle^{data}}, \tag{6.12}$$

where $\sigma^{stat}_{\langle\psi(r)\rangle^{data}}$ is determined using equation 6.11 according to the gaussian error propagation from the data distribution before the background is subtracted.

6.4 Measured Mean Integrated Jet Shape at Detector Level

We measure the mean integrated jet shape for both charm and flavour inclusive data samples. The data selection is described in chapter 5. The integrated jet shapes are calculated using equation 2.3 and the means are built according to equation 2.5. The charm data are corrected for background at each value of r using equation 6.10. No background corrections are applied to the flavour inclusive data. The measurements are compared to the PYTHIA MC simulation after detector simulation and reconstruction like the data.

In figure 6.17 the mean integrated jet shape $\langle\psi(r)\rangle$ measured in the **charm sample** as a function of the cone radius r are shown separately for $x_\gamma^{obs} \leq 0.75$ (**resolved enriched events**) and $x_\gamma^{obs} > 0.75$ (**direct enriched events**). The measured jet shapes are compared with the total prediction of the charm PYTHIA MC simulation. Additionally, the curves for direct and resolved photon MC events are shown separately. For the events at high x_γ^{obs} the description of the data by the PYTHIA prediction is good. At the low x_γ^{obs} values the jets in the data are more narrow than the jets from the PYTHIA simulation. The PYTHIA MC predicts a slower rise of $\langle\psi(r)\rangle$. However, the data suggest less gluon jets at low x_γ^{obs} and they are described reasonably by the pure direct PYTHIA prediction.

In order to find the source of the discrepancies in the low x_γ^{obs} bin, the mean differential jet shape $\rho(r)$ (see equation 2.4 for definition) as a function of the cone radius r is plotted in figure 6.18 in both x_γ^{obs} bins. However, the statistics is not large, therefore we do not consider the $\rho(r)$ distributions further in this analysis.

Charm Sample

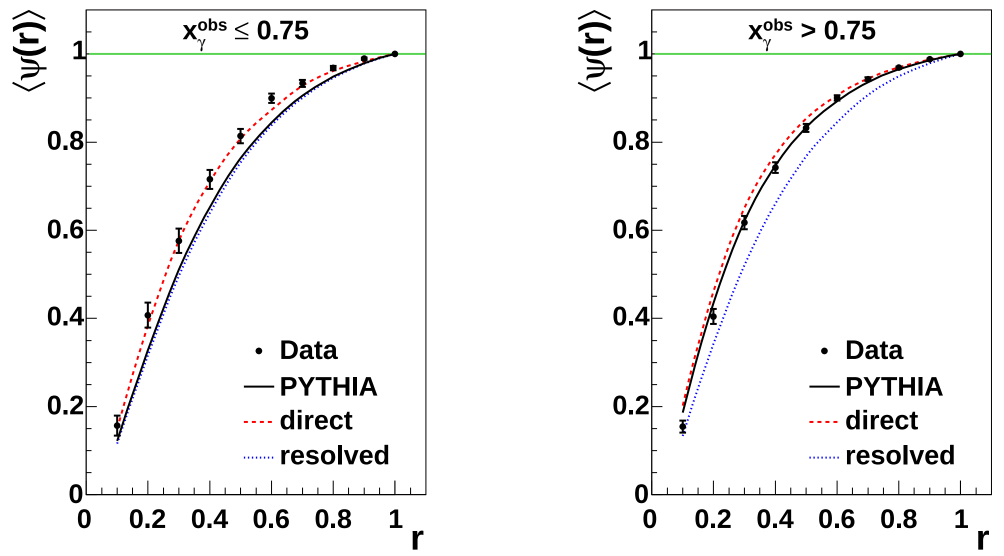

Figure 6.17: *The mean integrated jet shape $\langle\psi(r)\rangle$ of the 'other jet' in the charm event sample measured at detector level as a function of r for two different regions of x_γ^{obs}. The total prediction of the charm PYTHIA MC simulation is compared to the data. The expected curves for direct (dashed) and resolved (dotted) events from PYTHIA MC are shown separately. The statistical errors of the Monte Carlo predictions are negligible. Only statistical errors of the data are shown.*

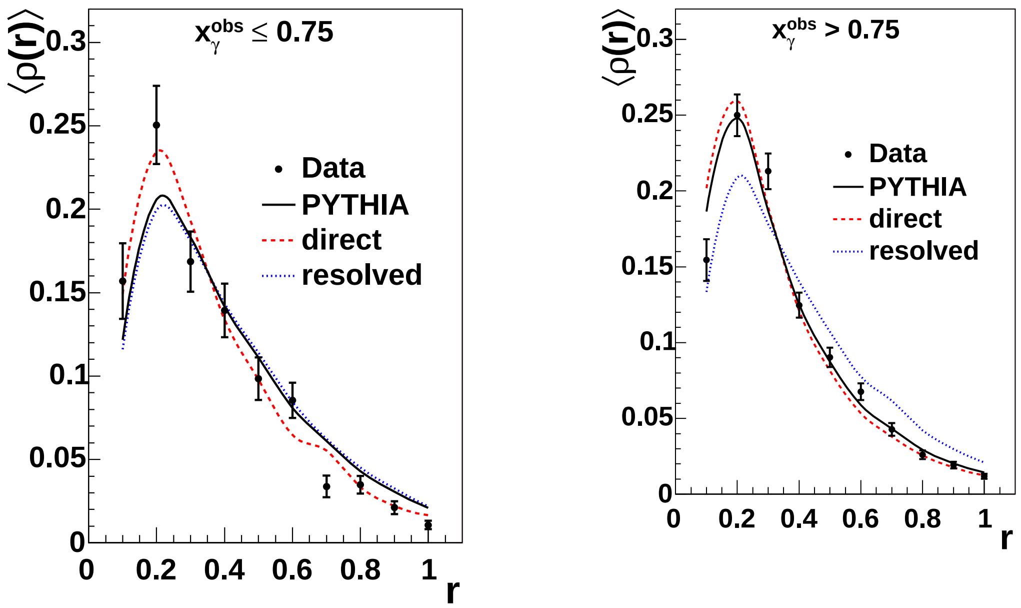

Figure 6.18: *The mean differential jet shape $\langle\rho\rangle$ of the 'other jet' in the charm event sample measured at detector level as a function of r for two different regions of x_γ^{obs}. The total prediction of the charm PYTHIA MC simulation is compared to the data. The expected curves for direct (dashed) and resolved (dotted) events from PYTHIA MC are shown separately. The statistical errors of the Monte Carlo predictions are negligible. Only statistical errors of the data are shown.*

Similarly, for the **flavour inclusive sample** we study the mean integrated jet shape $\langle\psi(r)\rangle$ as a function of the cone radius r (see figure 6.19). We observe a very good agreement of the measured mean integrated jet shape with the total inclusive PYTHIA MC prediction for both high and low values of x_γ^{obs}. According to the PYTHIA expectation, the low x_γ^{obs} flavour inclusive events are dominated by resolved processes, while at high x_γ^{obs} both kinds of events, direct and resolved, contribute.

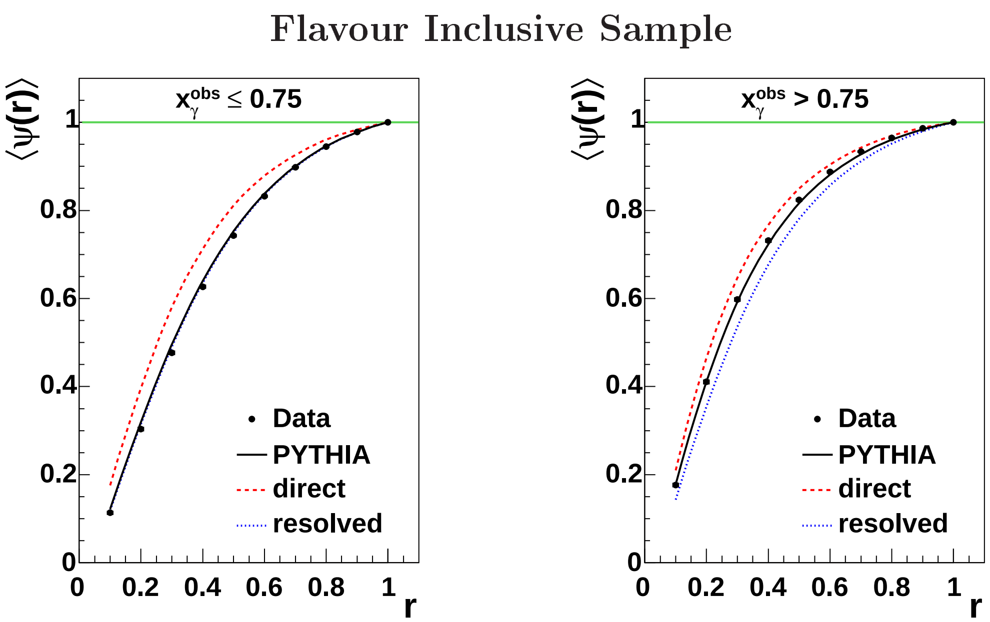

Figure 6.19: *The mean integrated jet shape $\langle\psi(r)\rangle$ of the two highest p_t jets in the flavour inclusive event sample measured at detector level as a function of r for two different regions of x_γ^{obs}. The total prediction of the charm PYTHIA MC simulation is compared to the data. The expected curves for direct (dashed) and resolved (dotted) events from PYTHIA MC are shown separately. The statistical errors of the Monte Carlo predictions are negligible. Only statistical errors of the data are shown.*

For a comparison of the mean integrated jet shape as a function of different physical variables a cone radius of 0.5 is chosen. The measurements of the mean integrated jet shape for the **charm sample**, $\langle\psi(r = 0.5)\rangle$, as a function of the variables η^{jet}, p_t^{jet}, E^{jet} of the 'other jet' and the variable x_γ^{obs} are shown in figure 6.20. The data points, as well as the points for the Monte Carlo predictions are plotted in the center of gravity of each bin (see tables B.2 and B.4 for the bin boundaries). The centers of gravity of the bins are not corrected for background, since the corrections are lower than 2 % of the bin width for each bin. In η^{jet}, p_t^{jet} and E^{jet} similar trends are observed in the data and in the total PYTHIA MC. Although all the data points are slightly above the total PYTHIA prediction, most of the differences are within the statistical errors. One can see that the large discrepancies observed at low x_γ^{obs} are accompanied by smaller discrepancies at high η^{jet}, low p_t^{jet} and high jet energies.

The same kind of measurements for the **flavour inclusive sample** is shown in figure 6.21. The two highest p_t jets are considered. For the flavour inclusive sample a good description of the data by the inclusive PYTHIA MC simulation is observed.

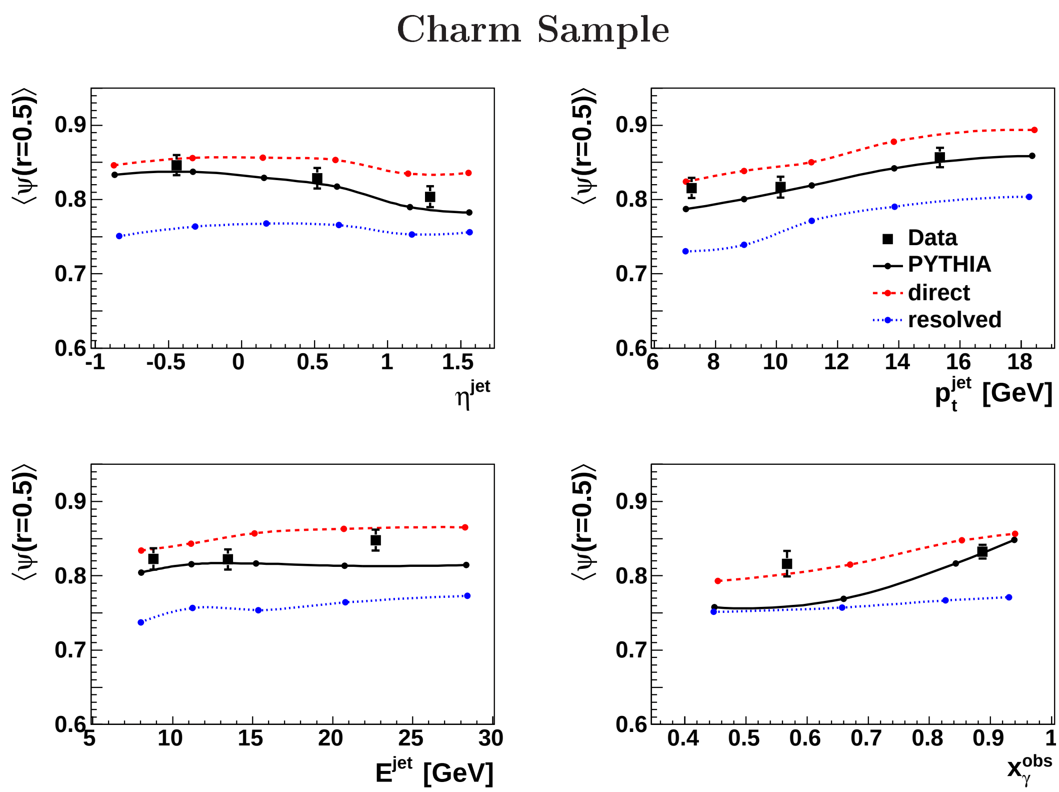

Figure 6.20: *Distributions of the mean integrated jet shape at fixed value of* $r = 0.5$, *measured at detector level for the charm sample as a function of the variables* η^{jet}, p_t^{jet} *and* E^{jet} *of the 'other jet' and the variable* x_γ^{obs}. *The predictions of the total charm PYTHIA MC simulation are compared to the data. The expectations for direct and resolved events from PYTHIA are shown separately. Smooth curves connecting the MC points are shown to guide the eye. The statistical errors of the MC predictions are negligible. Only statistical errors of the data are shown.*

In a similar jet shape analysis performed in the ZEUS experiment [80], the mean integrated jet shape for the 'other jet' was studied for the D^*-tagged charm dijet events as a function of E_t^{jet} and η^{jet}. In that analysis a fixed value of the cone radius, r=0.3, was chosen. In the present analysis we have chosen value of r=0.5, since the discrimination power for direct and resolved contributions of the data is higher at values of r larger than r=0.3. A maximum is reached at r=0.6, as can be seen from table 6.2. Additionally, the detector corrections are slightly lower for r=0.5 than for r=0.3, especially for the flavour inclusive events (see the following section). We also performed the analysis for r=0.3 (see figure 7.14) and observed similar trends as for r=0.5. The conclusions are unchanged, also concerning the x_γ^{obs} variable.

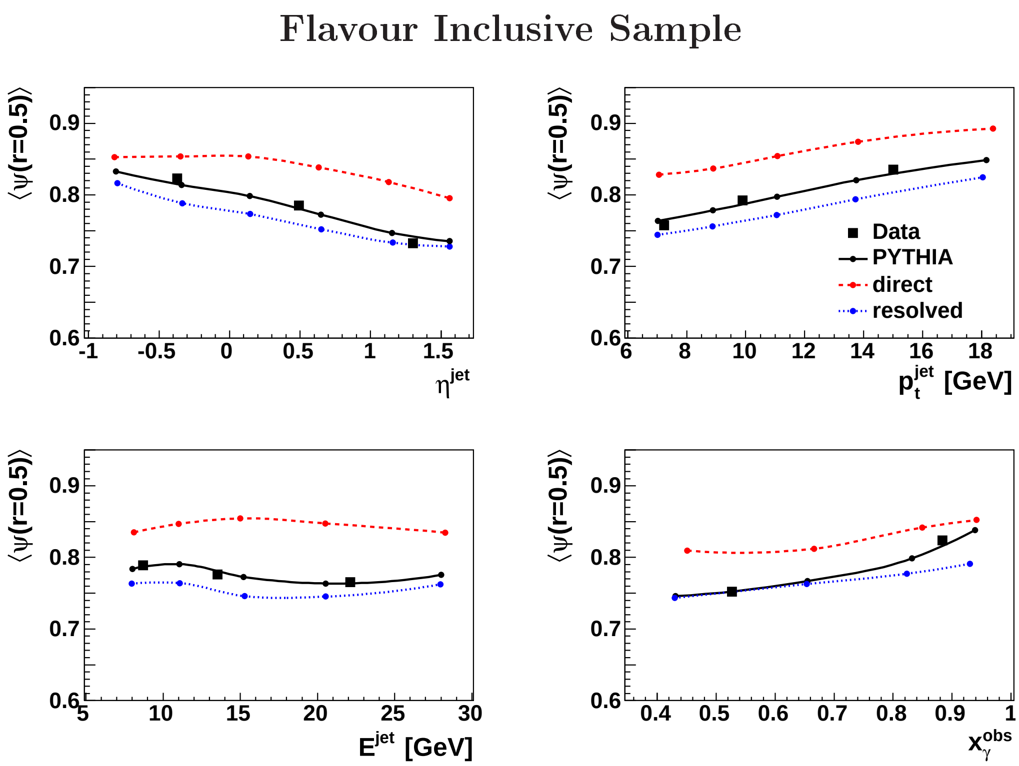

Figure 6.21: *Distributions of the mean integrated jet shape at fixed value of* $r = 0.5$ *measured at detector level for the flavour inclusive sample as a function of the variables* η^{jet}, p_t^{jet} *and* E^{jet} *of the two highest* p_t *jets and the variable* x_γ^{obs}. *The predictions of the total charm PYTHIA MC simulation are compared to the data. The expectations for direct and resolved events from PYTHIA are shown separately. Smooth curves connecting the MC points are shown to guide the eye. The statistical errors of the MC predictions are negligible. Only statistical errors of the data are shown.*

r	$(\langle\psi(r)\rangle^{dir} - \langle\psi(r)\rangle^{res})/\delta\langle\psi(r)\rangle^{Data}$	
	$x_\gamma^{obs} \leq 0.75$	$x_\gamma^{obs} > 0.75$
0.1	1.65	4.69
0.2	2.55	8.04
0.3	2.63	10.14
0.4	2.91	11.12
0.5	2.81	11.35
0.6	3.67	11.88
0.7	3.39	11.51
0.8	3.42	9.16
0.9	3.35	7.22

Table 6.2: *Estimation of the discrimination power of the data at various values of the cone radius* r. *The difference between the prediction of the mean integrated jet shape for direct and resolved events from the charm PYTHIA MC, divided by the statistical error of the data at the particular* r *is listed. The calculation is performed at hadron level, that is without detector simulation. The data show the highest discrimination power at* $r = 0.6$.

6.5 Detector Corrections

In this section the **detector corrections** are calculated, which are used to correct the measured data to the hadron level. The 'hadron level' is defined as the hadronic final state consisting of all stable[1] particles except of the scattered electron (neutrino in CC events) and photons radiated by the electron. Note that neutrinos coming from decays are included. Simulated particles at detector level are obtained after applying the detector simulation to particles at hadron level. The detector corrections make the results independent of the detector which it was performed with. Afterwards, it is possible to compare the data to the results of other experiments as well as theoretical predictions as implemented in MC generators. In this analysis the detector corrections compensate for geometrical acceptance, detector and trigger inefficiencies, limited resolutions, for the escaping neutrinos, particle interactions with the inactive material of the detector, efficiency and purity of the jet reconstruction and event selection. They also include corrections for the events lost due to the cuts on p_t^{rel} and δ_μ and thus make the measurement independent of those cuts.

To be able to correct the data using a Monte Carlo simulation, the Monte Carlo has to describe the data distributions reasonably well. As shown in chapter 5 and also in this chapter, this is the case for both data samples analysed here.

The corrected mean integrated jet shape in each bin i (of p_t^{jet}, η^{jet}, E^{jet}, x_γ^{obs}) and at each r is calculated as

$$\langle\psi(r)\rangle_i^{corr} = C_i^{MC} \times \langle\psi(r)\rangle_i^{meas}, \tag{6.13}$$

where $\langle\psi(r)\rangle^{meas}$ is the measured mean integrated jet shape discussed in the previous section. The correction factor C^{MC} is calculated using the Monte Carlo simulation:

$$C_i^{MC} = \frac{\langle\psi(r)\rangle_i^{MC_{had}}}{\langle\psi(r)\rangle_i^{MC_{det}}}, \tag{6.14}$$

where $\langle\psi(r)\rangle^{MC_{had}}$ and $\langle\psi(r)\rangle^{MC_{det}}$ are the mean integrated jet shapes simulated at hadron and detector level, respectively. The variable $\langle\psi(r)\rangle^{MC_{had}}$ considers jets built of the final decay products of hadrons, whereas $\langle\psi(r)\rangle^{MC_{det}}$ considers the reconstructed detector response in form of the jets of hadronic final state objects. In order to determine the correction factors, two largely overlapping Monte Carlo samples are selected. At the detector level all cuts listed in table 5.3 are applied. At the hadron level the phase-space cuts listed in table 6.3 are applied, but omitting the p_t^{rel} cut. Such extrapolation to the whole p_t^{rel} range can be made, since the data are well described by the PYTHIA MC, as show the control plots in figure 5.6 and especially the p_t^{rel} distribution in figure 5.5.

[1]Particles with lifetime $\tau \geq 0.33 \cdot 10^{-10}$ s are not decayed by the generators in the standard H1 MC event generation. Those particles are considered here as stable.

Cut	**Charm Sample**	**Flavour Inclusive Sample**
Q^2_{gen} [GeV^2]	< 1	< 0.01
y_{gen}	0.2 ... 0.8	0.3 ... 0.65
Jets		
#	$\geq$ 2	$\geq$ 2
$p_t^{jet\,gen}$ [GeV]	$> 7(6)$	$> 7(6)$
$\lvert\theta^{jet\,gen}\rvert$	20°...160°	20°...160°
Muon	in one of the jets	-
$p_t^{\mu\,gen}$ [GeV]	> 2.5	-
$\theta^{\mu\,gen}$	35°...130°	-
p_t^{rel} [GeV]	1.0	-

Table 6.3: *'Phase space selection cuts' determining the visible region for the charm MC sample and the flavour inclusive MC sample at hadron level and the p_t^{rel} cut, which is used only for charm sample control plots. Values are measured in the laboratory frame.*

For the charm sample, the charm PYTHIA MC is used to calculate the correction factors, since the data are already corrected for background and represent only charm events. For the flavour inclusive sample the inclusive PYTHIA MC is used.

The values of the detector correction factors for the integrated jet shape $\langle\psi(r)\rangle$ as functions of r in the two x_γ^{obs} bins are shown in figure 6.22 (charm sample) and 6.23 (flavour inclusive sample). They are also plotted separately for direct and resolved events for comparison. Deviations from 1.0 are observed especially at low values of r. Except of the first r bin, the correction factors deviate from 1.0 less than 5 % for both samples and converge to 1.0 as r increases.

Charm Sample

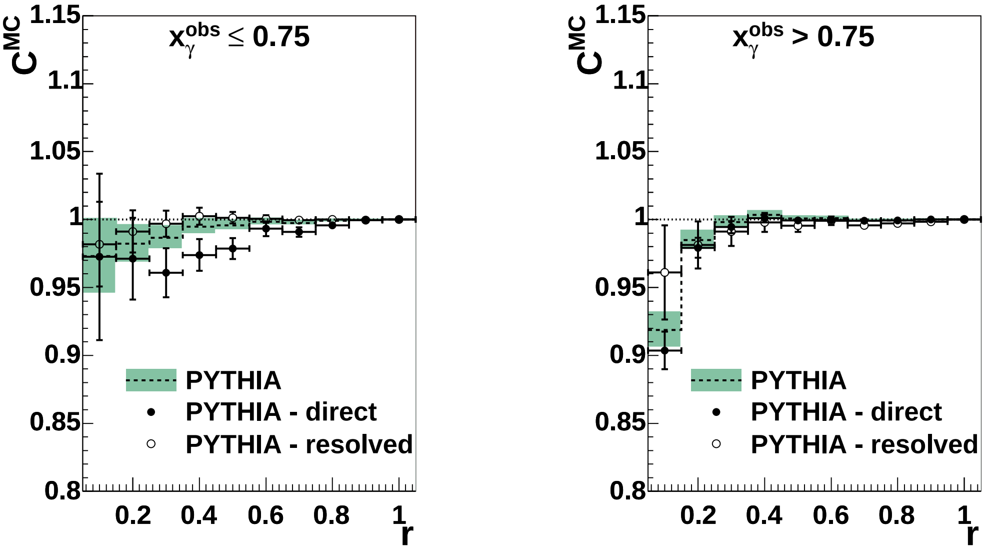

Figure 6.22: *Detector corrections for the mean integrated jet shape $\langle\psi(r)\rangle$ of the charm sample for the 'other jet' as a function of r for two different regions of x_γ^{obs}. The values were obtained using the charm PYTHIA MC. The factors are shown for the total charm PYTHIA MC simulation and separately for the direct and resolved components. The shaded band and the error bars represent the statistical uncertainty of the MC.*

Flavour Inclusive Sample

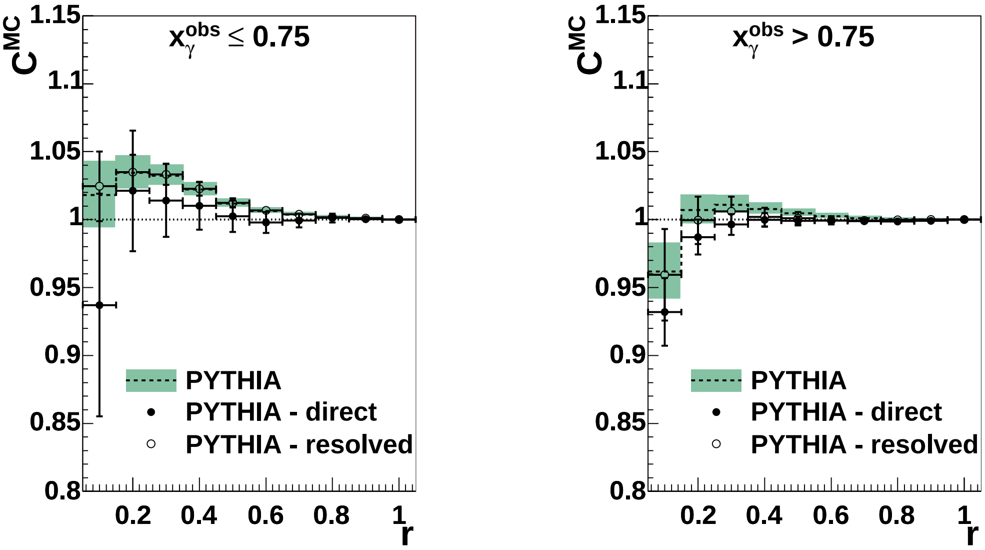

Figure 6.23: *Detector corrections for the mean integrated jet shape $\langle\psi(r)\rangle$ of the flavour inclusive sample for the two highest p_t jets as a function of r for two different regions of x_γ^{obs}. The values were obtained using the inclusive PYTHIA MC. The factors are shown for the total inclusive PYTHIA MC simulation and separately for the direct and resolved components. The shaded band and the error bars represent the statistical uncertainty of the MC.*

We also study the integrated jet shape $\langle\psi(r = 0.5)\rangle$ as a function of the variables η^{jet}, p_t^{jet}, E^{jet} and x_γ^{obs}. The detector corrections used to correct those measurements are shown in figure 6.24 for the charm sample and in figure 6.25 for the flavour inclusive sample.

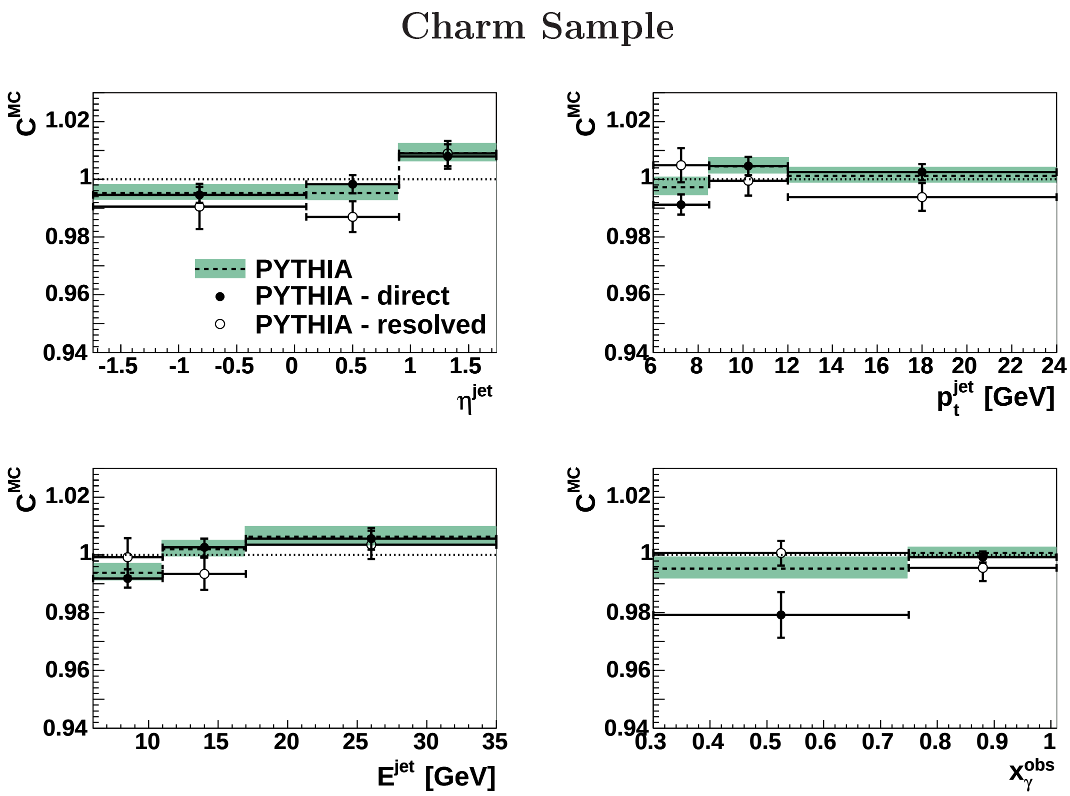

Figure 6.24: *Detector corrections for the mean integrated jet shape $\langle\psi(r = 0.5)\rangle$ for the charm sample as a function of the variables η^{jet}, p_t^{jet} and E^{jet} of the 'other jet' and the variable x_γ^{obs}. The corrections are calculated using the total charm PYTHIA MC. In addition to the correction derived from the total sample, the values for the direct and resolved component are shown separately. The shaded band and the error bars represent the statistical uncertainty of the MC.*

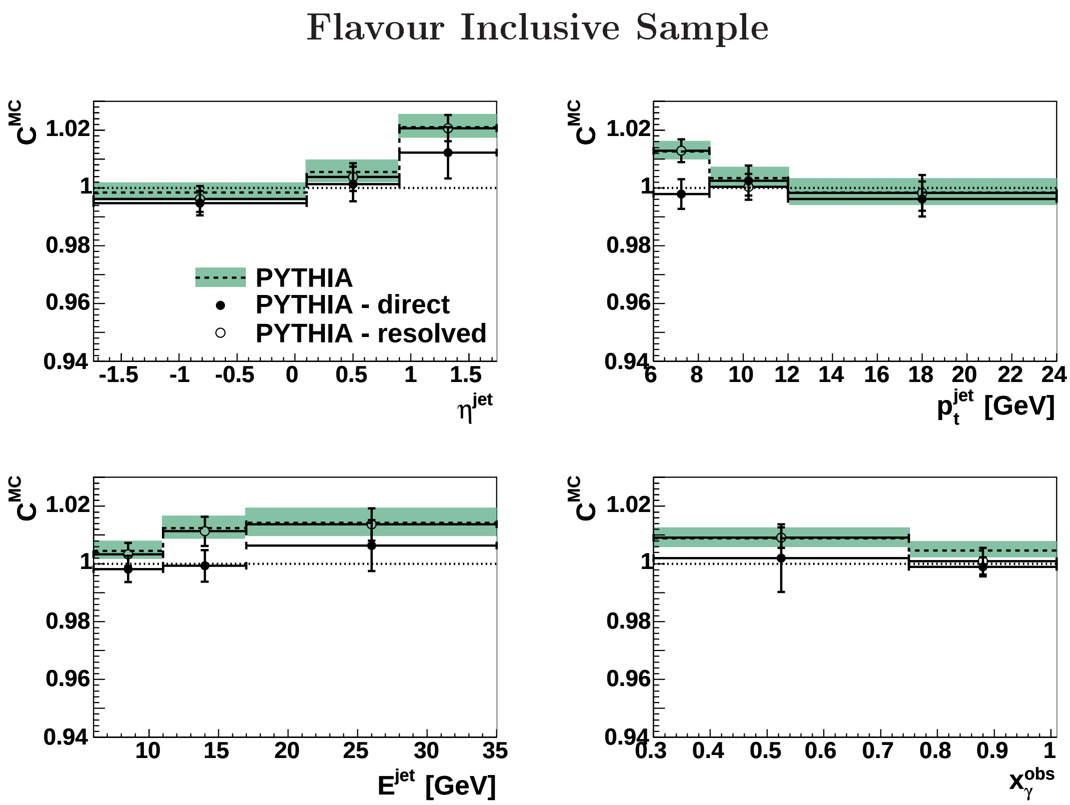

Figure 6.25: *Detector corrections for the mean integrated jet shape $\langle\psi(r=0.5)\rangle$ for the charm sample as a function of the variables η^{jet}, p_t^{jet} and E^{jet} of the two highest p_t jets and the variable x_γ^{obs}. The corrections are calculated using the total inclusive PYTHIA MC. In addition to the correction derived from the total sample, the values for the direct and resolved component are shown separately. The shaded band and the error bars represent the statistical uncertainty of the MC.*

The corrections are found to be small and the differences between the corrections for the direct and resolved events are not large. Therefore it is reasonable to use the f correction factors to correct the data. The overall correction is smaller than 1 % in all bins of p_t^{jet}, η^{jet}, E^{jet} and x_γ^{obs} for the charm data sample and smaller than 2.5 % for the flavour inclusive data sample. Systematic errors due to the uncertainty of the detector corrections are included in the calculation of the systematic uncertainties. They are estimated by the difference between the detector correction calculated using the CASCADE simulation and the detector correction calculated using the PYTHIA simulation as described in section 6.6.

6.6 Systematic Uncertainties

The following systematic studies have been carried out in order to estimate the systematic error of the measurements:

- **The jet axis is smeared** by 2.5° in both, polar angle θ and azimuthal angle ϕ. The choice of the value is motivated by the resolution in the jet axis measurement which is shown in figure 6.26.
- **The variation of the energy scale** of the hadronic final state objects by $\pm 4\,\%$ for pure clusters [81], $\pm 2\,\%$ for pure tracks and $\pm 3\,\%$ for combined objects (tracks and clusters). Pure cluster objects are found to contribute 40 % to the total jet transverse momenta, pure track objects 20 % and combined objects 40 %.
- **The variation of the background** due to beauty and light quark events is performed only for the charm sample. Both, the beauty event fraction and the light quark event fraction are varied by $\pm 20\,\%$, except of the bin $x_\gamma^{obs} \leq 0.75$, where is the light quark event fraction varied by $\pm 30\,\%$. Background fractions and their statistical uncertainties are shown in figure 6.13.
- **The uncertainty of the detector corrections** is estimated by using two different Monte Carlo generators, PYTHIA and CASCADE for calculating the corrections. The difference is taken as the systematic error on the detector correction. The detector corrections for the charm sample, as calculated using PYTHIA and CASCADE are shown in figures 6.27 and 6.28. For the flavour inclusive sample there is presently no inclusive CASCADE Monte Carlo sample available.

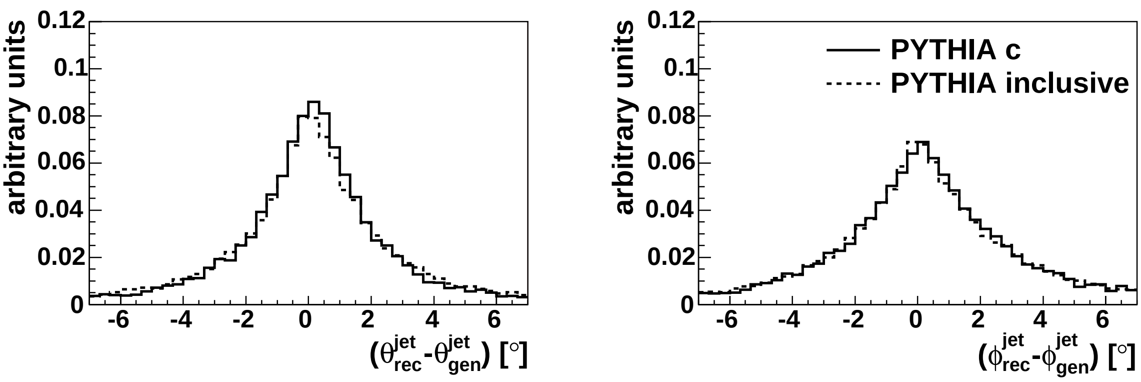

Figure 6.26: *Resolution of the variables θ^{jet} and ϕ^{jet}. The distributions are shown separately for the 'other jet' of the charm sample simulated by the charm PYTHIA MC and for the two highest p_t jets of the flavour inclusive sample simulated by the inclusive PYTHIA MC. They are normalised to the total number of events. The resolutions are in good approximation independent of the variables η^{jet}, p_t^{jet}, E^{jet} and x_γ^{obs}.*

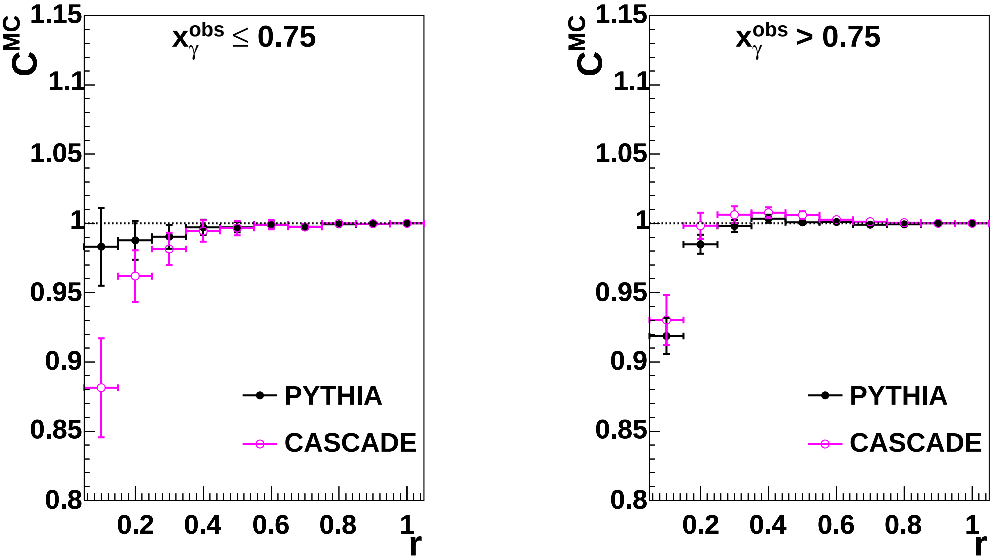

Figure 6.27: *Comparison of the detector corrections calculated using the PYTHIA MC and the CASCADE MC for the mean integrated jet shape $\langle\psi(r)\rangle$ for the 'other jet' of the charm sample as a function of the cone radius r for two different regions of x_γ^{obs}. The error bars represent the statistical uncertainty of the MC.*

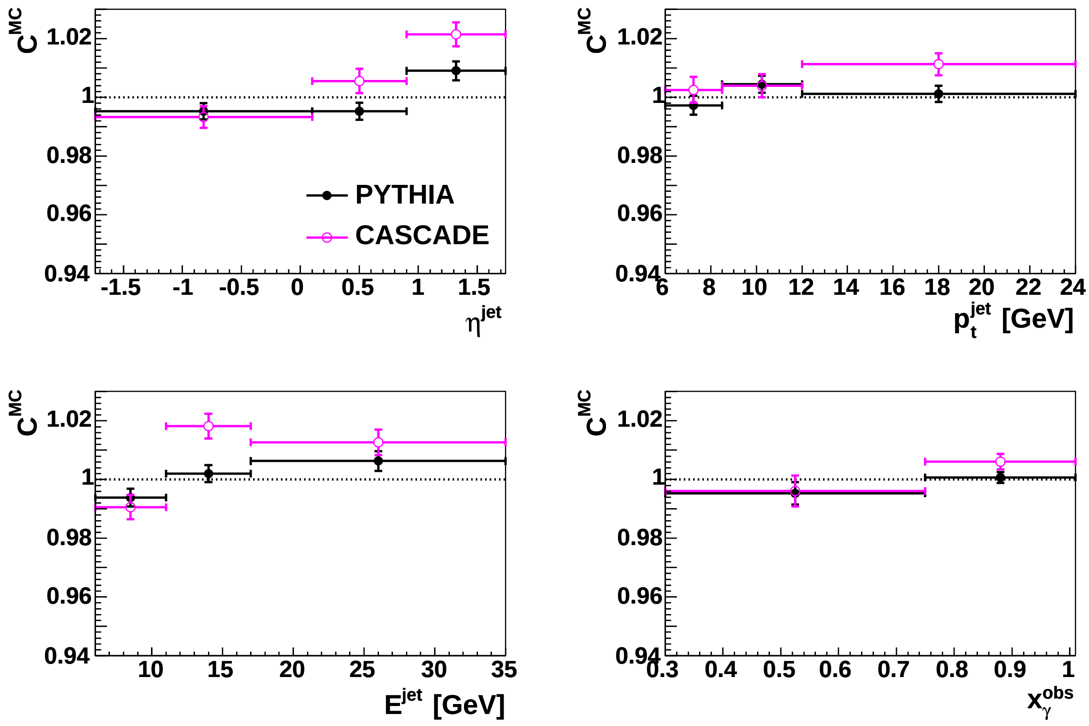

Figure 6.28: *Comparison of the detector corrections calculated using the PYTHIA MC and the CASCADE MC for the mean integrated jet shape $\langle\psi(r = 0.5)\rangle$ for the charm sample as a function of the variables η^{jet}, p_t^{jet} and E^{jet} of the 'other jet' and the variable x_γ^{obs}. The error bars represent the statistical uncertainty of the MC.*

The relative systematic uncertainty is defined as the deviation δ_{rel}^{syst} from the central value $\langle\psi\rangle^{central}$. It is calculated for jet axis smearing, variation of the energy scale and for background variation as

$$\delta_{rel}^{syst} = \frac{\langle\psi\rangle^{varied} - \langle\psi\rangle^{central}}{\langle\psi\rangle^{central}}, \tag{6.15}$$

where $\langle\psi\rangle^{varied}$ is the value of the mean integrated jet shape measured in the data which was changed due to the variation of one of the studied uncertainties. Variations are performed on the detector level that is before detector correction is applied. The uncertainty on the detector correction is determined as relative deviation of the correction calculated using the CASCADE MC from the correction calculated using the PYTHIA MC.

Additionally, the influence of the uncertainty of the flavour fractions was studied for the flavour inclusive sample. Since the beauty fraction is small (about 2 %), only the charm fraction was varied in the inclusive Monte Carlo by 10 % [82]. That variation was found to have negligible influence on the average jet shape in the flavour inclusive sample.

The values of the systematic errors of $\langle\psi(r = 0.5)\rangle$ are listed separately for $x_\gamma^{obs} \leq 0.75$ and $x_\gamma^{obs} > 0.75$ in table 6.4 for the charm sample and in table 6.5 for the flavour inclusive sample.

For the final estimation of the systematic error of each measurement point, the positive and negative contributions are added separately in quadrature, since the uncertainties are assumed to be independent. The larger absolute systematic error is taken as a final estimate of the systematic error. The largest relative systematic uncertainties for both samples are found at small cone radius r, about 15 %, and they decrease towards larger r. At $r = 0.5$ the systematic uncertainties are at the level of 1%. In order to determine the total error of the measurement, the statistical and systematic error are added in quadrature.

Source		$\delta\langle\psi\rangle_{x_\gamma^{obs}\leq 0.75}[\%]$	$\delta\langle\psi\rangle_{x_\gamma^{obs}>0.75}[\%]$
Jet axis smearing	$\phi \pm 2.5°$, $\theta \pm 2.5°$	-0.15	-0.84
Energy scale variation	$\pm 4\,\%$, $\pm 2\,\%$,$\pm 3\,\%$	∓ 0.01	< 0.01
b fraction variation	$\pm 20\,\%$	± 0.29	± 0.17
uds fraction variation	$\pm 20\,\%$ ($\pm 30\,\%$ for low x_γ^{obs})	± 0.50	< 0.01
Detector correction	PYTHIA/CASCADE diff.	-0.06	$+0.55$
Total systematic error		± 0.60	± 0.86
Statistical error		± 2.10	± 1.10
Total error		± 2.18	± 1.40

Table 6.4: *Results of systematic studies for the charm sample for* $\langle\psi(r = 0.5)\rangle$.

Source		$\delta\langle\psi\rangle_{x_\gamma^{obs}\leq 0.75}[\%]$	$\delta\langle\psi\rangle_{x_\gamma^{obs}>0.75}[\%]$
Jet axis smearing	$\phi \pm 2.5°$, $\theta \pm 2.5°$	-0.81	-0.91
Energy scale variation	$\pm 4\%$, $\pm 2\,\%$,$\pm 3\,\%$	< 0.01	< 0.01
Total systematic error		± 0.81	± 0.91
Statistical error		± 0.28	± 0.22
Total error		± 0.86	± 0.94

Table 6.5: *Results of systematic studies for the flavour inclusive sample for* $\langle\psi(r = 0.5)\rangle$.

Chapter 7

Results

In the following the distributions discussed already in section 6.4 are now presented with the detector corrections described in section 6.5. Different Monte Carlo models are compared to the data including systematic errors.

7.1 Jet Shape as Function of the Cone Radius r in Two Regions of x_γ^{obs}

7.1.1 Charm Sample

The mean integrated jet shape measured for the charm sample is shown in figure 7.1 for resolved enriched events ($x_\gamma^{obs} \leq 0.75$) and for direct enriched events ($x_\gamma^{obs} > 0.75$). The PYTHIA MC predictions are shown with the data. In addition to the total prediction, the curves for the direct and resolved photon events are shown separately. The data are well described by the total PYTHIA prediction at high x_γ^{obs}. A disagreement is observed at low x_γ^{obs}, as already seen without the detector corrections (see section 6.5). The PYTHIA simulation predicts a slower rise of $\langle\psi(r)\rangle$ at low x_γ^{obs} due to the presence of broad gluon jets in the resolved photon sample which originate predominantly from the excitation processes. However, the data suggest less gluon jets at low x_γ^{obs} and they are described reasonably by the pure direct PYTHIA prediction which does contain very little gluon jets. Numerical values for the data and Monte Carlo predictions are listed in table B.1.

In figure 7.2 the same results as in figure 7.1 are shown, here as a ratio of the data over the total charm PYTHIA prediction. The PYTHIA predictions for direct and resolved events are also shown as a ratio over the total charm PYTHIA MC. Here the difference between the description in the two x_γ^{obs} bins can be clearly seen. At high x_γ^{obs} starting from $r = 0.3$ the data agree very well with the total PYTHIA prediction. At low x_γ^{obs} the data disagree with the total PYTHIA prediction over the whole range of r and are compatible with the pure direct sample.

To investigate this disagreement, comparisons of the same charmed data with various models follow in figures 7.3 - 7.6.

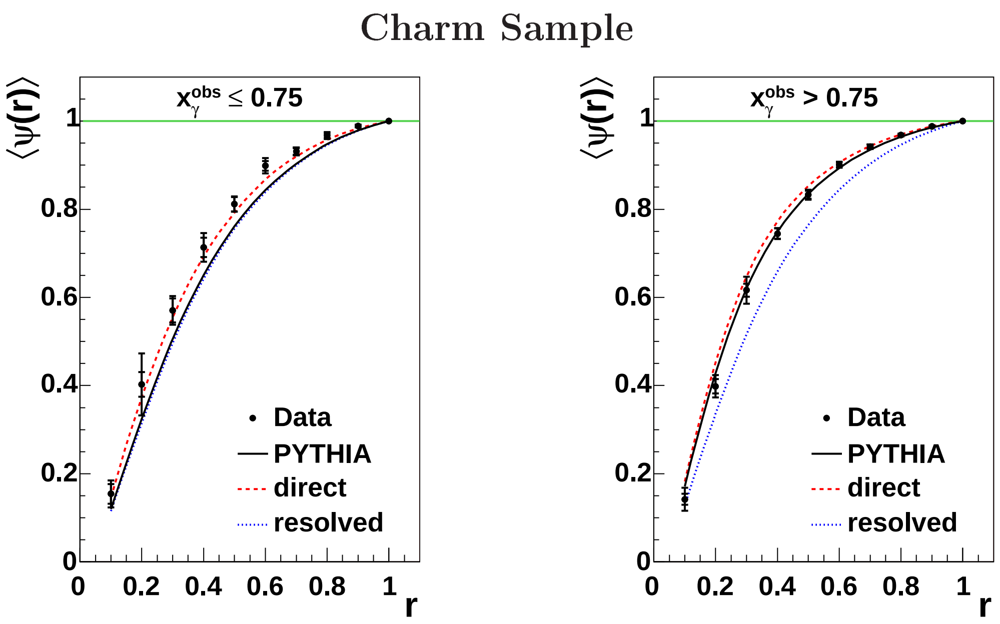

Figure 7.1: *The mean integrated jet shape $\langle\psi(r)\rangle$ for the 'other jet' in the charm event sample measured as a function of r in two different regions of x_{γ}^{obs}. The data, corrected for detector effects, are compared to the total prediction from the charm PYTHIA MC simulation (full line). The expected curves for direct photon events (dashed) and resolved photon events (dotted) from PYTHIA are shown separately. The statistical errors of the Monte Carlo predictions are negligible. The inner error bars of the data points represent the statistical uncertainty and the outer error bars the statistical and systematic errors added in quadrature.*

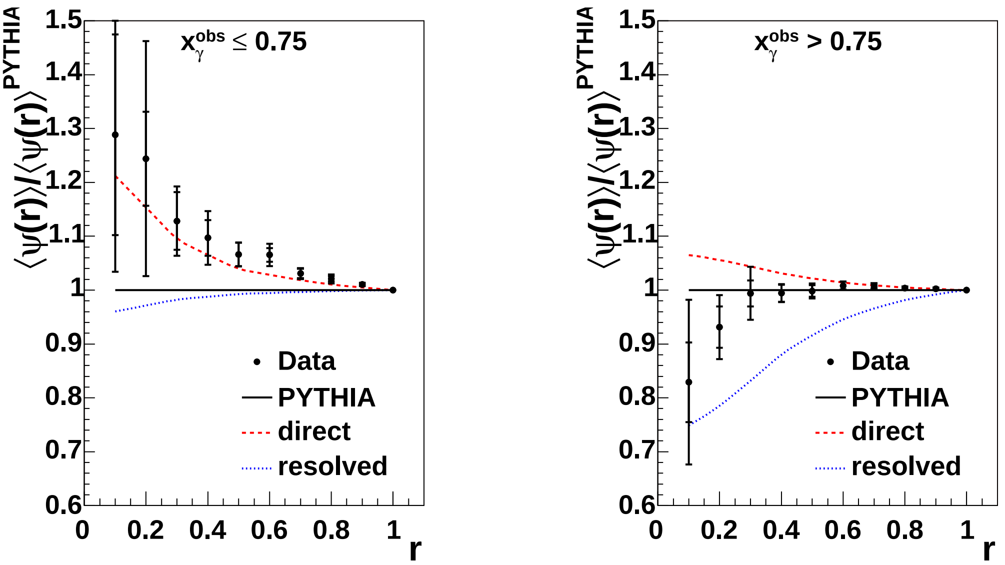

Figure 7.2: *Ratio of the data points relative to the total charm PYTHIA MC prediction. The same corrected data as in figure 7.1 are shown. The expected curves for direct photon and resolved photon events from PYTHIA are shown separately, also relative to the total PYTHIA prediction.*

PYTHIA Simulation Without Multiple Interactions

Interactions between the photon and proton remnants, in addition to the hard interaction, are called multiple interactions (MI). They may be important for resolved events. As default the MI are included in the PYTHIA MC simulation used here.

The two main parameters controlling the MI modelation are the minimum relative transverse momentum between the two outgoing partons (parameter 'PARP 81') and the impact parameter [83]. In the PYTHIA Monte Carlo predictions used for this analysis the value of the minimum relative transverse momentum 1.4 GeV/c (default value) was used. The simulation of the probability of the MI is made independent of the impact parameter by setting the parameter 'MSTP 82' to 1. The regularisation scale (parameter 'PARP 82') was set to 1.2 GeV/c. Those are default parameters in H1.

In figure 7.3 we compare the measured charm data with the PYTHIA simulation with and without MI. The ratio of the data over the standard PYTHIA simulation including MI is plotted. The ratio of the prediction of the PYTHIA MC with MI switched off to the standard PYTHIA simulation is shown as well. We observe that the description of the data in the low x_γ^{obs} bin improves significantly by switching off the MI, although it is still too low. In this case the jets get narrower, since there are fewer particles from the underlying event which can be falsely assigned to the jet. The description of the high x_γ^{obs} events gets slightly worse when excluding the MI. However, other analyses showed [84] that MI are important to be able to describe distributions of other variables. Therefore we do not regard the PYTHIA MC without MI as the correct model for the measured charm data.

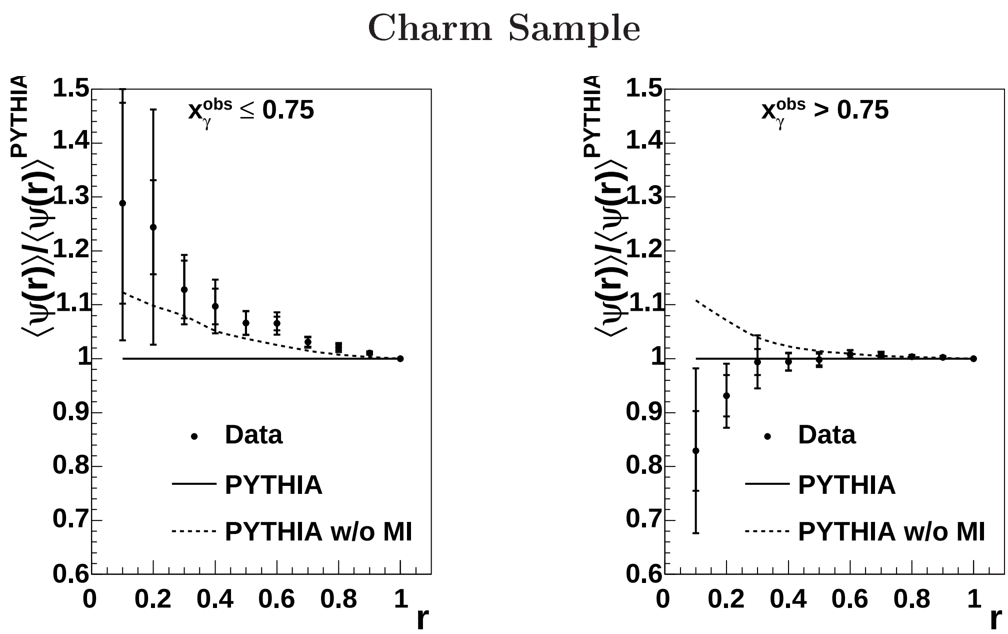

Figure 7.3: *The same data as in figure 7.2. The total PYTHIA MC includes multiple interactions (full line). The prediction of the PYTHIA MC without MI (dashed line) is also shown relative to the total PYTHIA prediction.*

PYTHIA Simulation with Different Peterson Fragmentation Parameters

The default value of the Peterson fragmentation parameter ϵ_c in this analysis is set to 0.058, as recommended in [18]. The Peterson fragmentation parameter is varied between 0.03 and 0.08 in figure 7.4. The data are divided by the PYTHIA prediction with $\epsilon_c = 0.03$. The PYTHIA prediction with $\epsilon_c = 0.08$ is also divided by the PYTHIA prediction with $\epsilon_c = 0.03$. Changes caused by the variation of the Peterson fragmentation parameter ϵ_c are found to be very small and cannot explain the big discrepancies between the data and the Monte Carlo simulation.

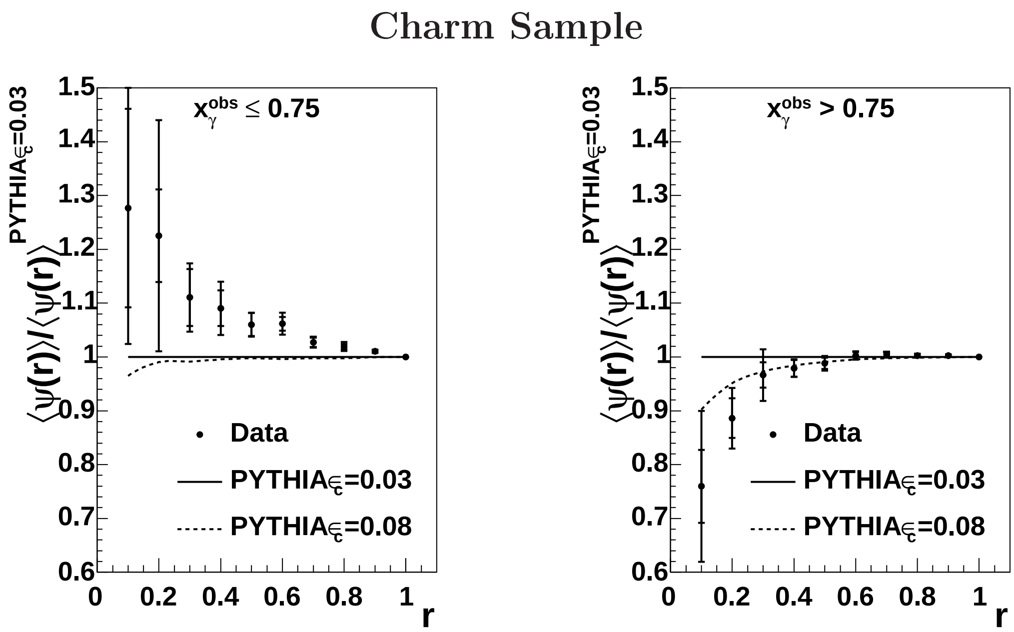

Figure 7.4: . *Ratio of the charm data points corrected for detector effects for the mean integrated jet shape $\langle\psi(r)\rangle$ for the 'other jet' in two different regions of x_{γ}^{obs} measured as a function of r relative to the total prediction of the PYTHIA MC with charm Peterson fragmentation parameter $\epsilon_c = 0.03$ (full line). The prediction of the PYTHIA MC with $\epsilon_c = 0.08$ (dashed line) is also shown relative to the full line. The inner error bars of the data points represent the statistical uncertainty and the outer error bars the statistical and systematic errors added in quadrature.*

PYTHIA with a Different Photon Structure Function

The photon structure function GRV-LO is used in the PYTHIA simulation as a standard for this analysis. In figure 7.5 we compare the data over the standard PYTHIA simulation with the ratio of the PYTHIA prediction using the SaS 1D photon structure function over the standard PYTHIA simulation. At low x_γ^{obs} we observe only a very slight improvement of the data description as a result of the use of the SaS 1D structure function. At high x_γ^{obs} the changes in the description are negligible. Using the SaS 1D photon structure function in the PYTHIA simulation shows that the observed discrepancy is not specially due to the choice of the GRV-LO photon structure function.

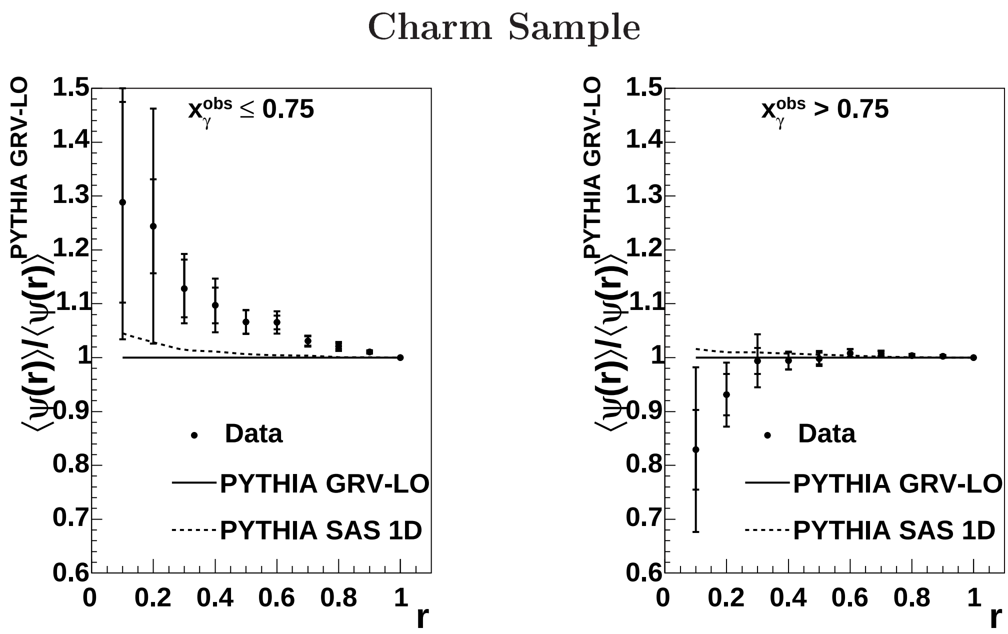

Figure 7.5: *The same data as in figure 7.2. The total prediction of the charm PYTHIA MC using GRV-LO photon structure function (default, used also in the previous plots) is shown as full line. The prediction of the charm PYTHIA MC using SAS 1D photon structure function is shown as dashed line, also relative to the full line.*

CASCADE simulation

The charm data over the standard PYTHIA prediction are shown again in figure 7.6 together with the ratio of the prediction of the CASCADE model over the standard PYTHIA prediction. In the CASCADE MC no explicit resolved component is generated. k_t-factorisation includes already a hadronic photon component. The CASCADE prediction describes the data equally good as the PYTHIA prediction in the high x_{γ}^{obs} region. In the low x_{γ}^{obs} region the CASCADE prediction is closer to the data than the PYTHIA prediction. However, CASCADE is still lower than the data at low x_{γ}^{obs}.

Charm Sample

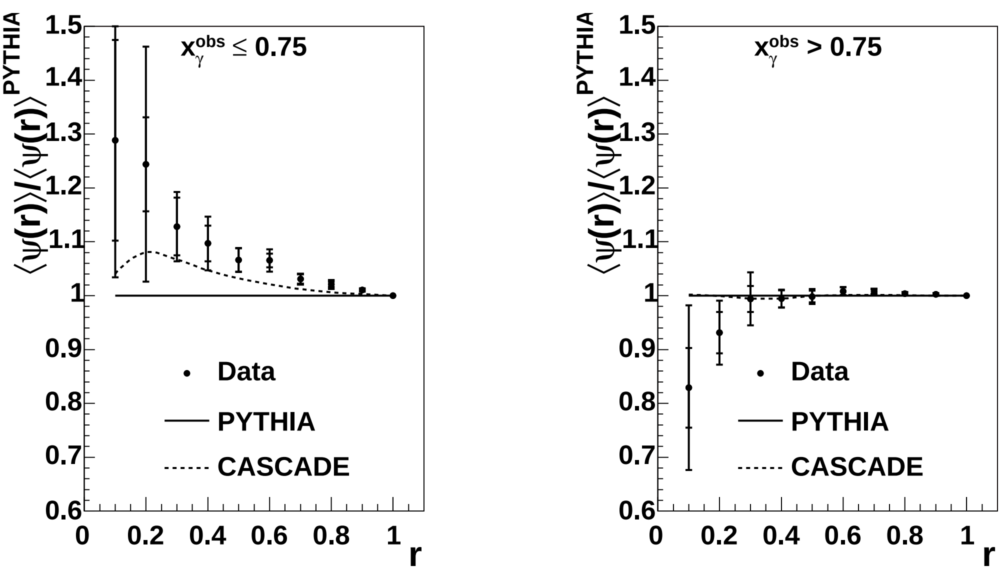

Figure 7.6: *The same data as in figure 7.2. Prediction of the CASCADE MC (dashed line) relative to the PYTHIA prediction (full line) is shown.*

7.1.2 Flavour Inclusive Sample

In figure 7.7 the measurement of the mean integrated jet shape as a function of the cone radius r for the light quark dominated flavour inclusive sample is shown. Good agreement between data and PYTHIA prediction can be observed at both low and high x_{γ}^{obs} values. A more precise look at the situation is taken in figure 7.8, where the ratio of the data over the total inclusive PYTHIA MC confirms a perfect description in the high x_{γ}^{obs} bin. In the low x_{γ}^{obs} bin the data are slightly lower than the inclusive PYTHIA prediction. Numerical values for the data and Monte Carlo predictions are listed in table B.3.

Flavour Inclusive Sample

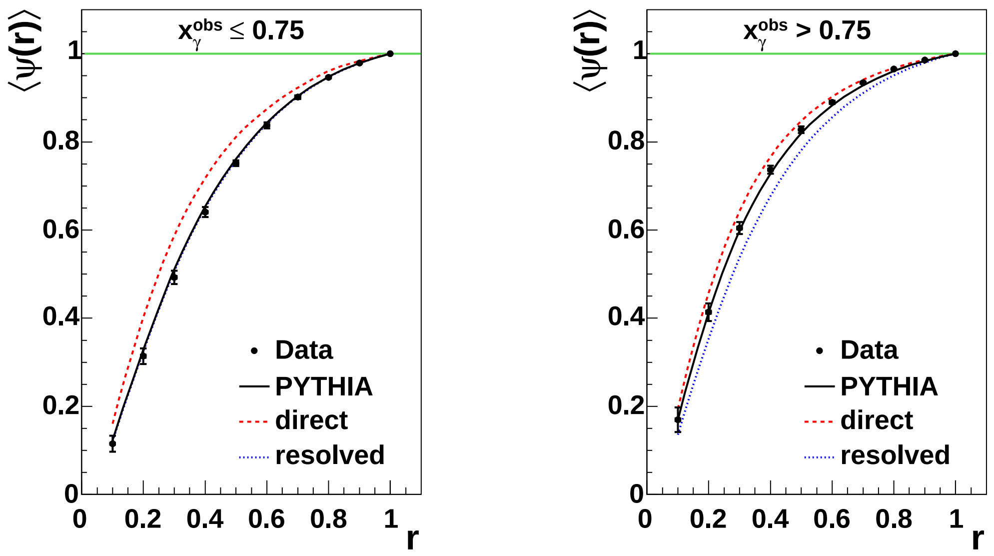

Figure 7.7: *The mean integrated jet shape $\langle\psi(r)\rangle$ for the two highest p_t jets in the flavour inclusive event sample measured as a function of r for two different regions of x_γ^{obs}. The data corrected for detector effects are compared to the total prediction of the inclusive PYTHIA MC simulation (full line). The expected curves for the direct photon (dashed) and the resolved photon (dotted) events from PYTHIA are shown separately. The statistical errors of the Monte Carlo predictions are negligible. The inner error bars of the data points represent the statistical uncertainty and the outer error bars the statistical and systematic errors added in quadrature.*

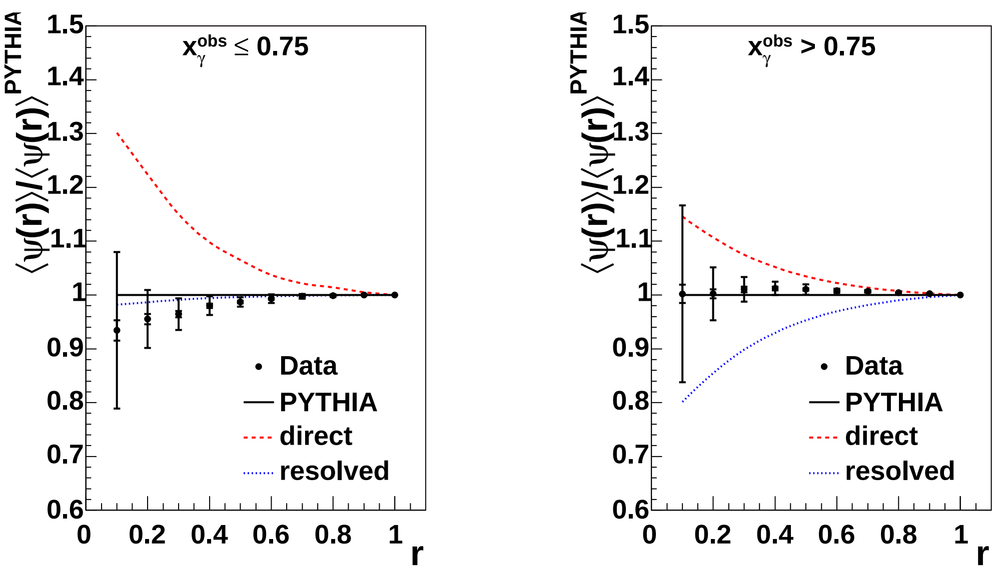

Figure 7.8: *The same measurement as in figure 7.7. Here the ratio of the data points is plotted relative to the total inclusive PYTHIA MC prediction (full line). The expected curves for direct photon (dashed line) and resolved photon (dotted line) events from PYTHIA are shown, also relative to the total PYTHIA prediction.*

7.2 Jet Shape at Fixed Value of the Cone Radius r

7.2.1 Charm Sample

In figure 7.9 the mean integrated jet shape at $r = 0.5$ is shown for the charm sample as a function of the variables η^{jet}, p_t^{jet}, E^{jet} of the 'other jet' and the variable x_γ^{obs}. The distributions as functions of η^{jet} and p_t^{jet} are well described. However, deviations are seen at high jet energy and low x_γ^{obs}. Numerical values for the data and Monte Carlo predictions are listed in table B.2.

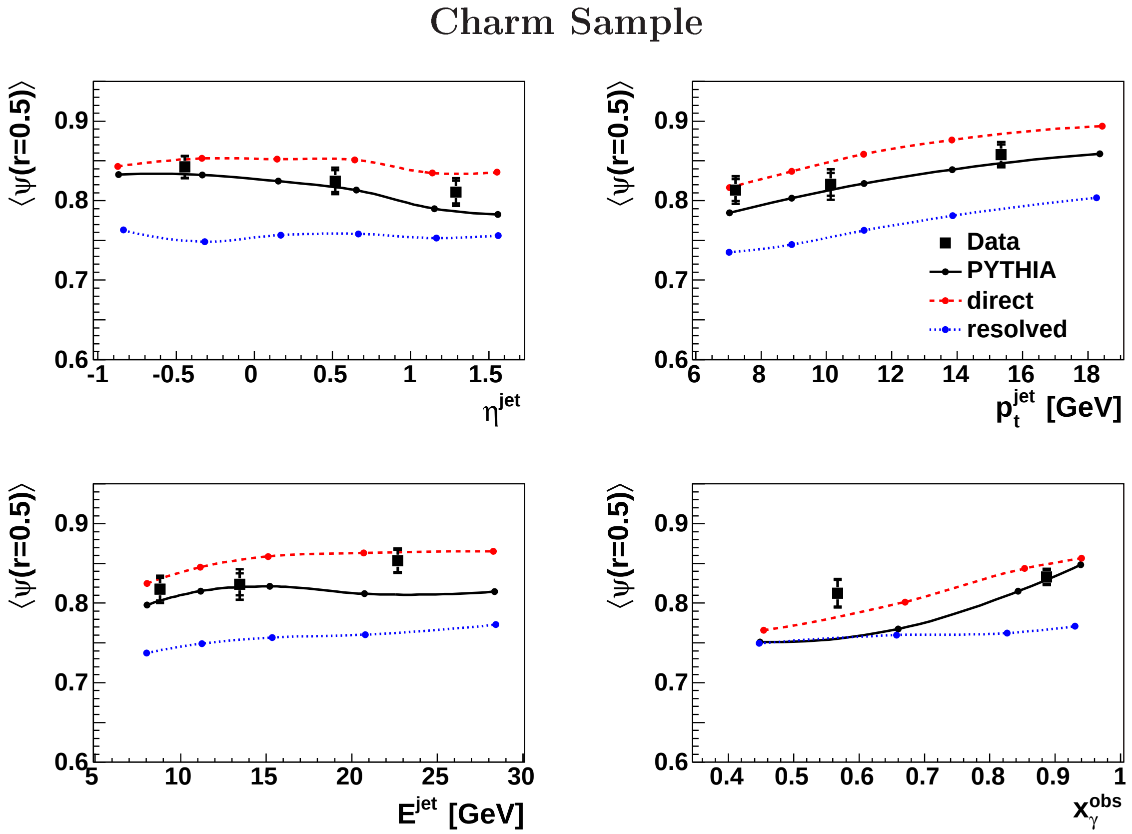

Figure 7.9: *Distributions of the mean integrated jet shape at a fixed value of $r = 0.5$ after detector corrections measured for the charm sample as a function of the variables η^{jet}, p_t^{jet} and E^{jet} of the 'other jet' and the variable x_γ^{obs}. The predictions of the total charm PYTHIA MC simulation (full line) are compared to the data. The expectations for the direct photon events (dashed line) and the resolved photon events (dotted line) from PYTHIA are shown separately. Smooth curves connecting the MC points are shown to guide the eye. The statistical errors of the MC predictions are negligible. The inner error bars of the data points represent the statistical uncertainty and the outer error bars the statistical and systematic errors added in quadrature.*

In figure 7.10 the charm data are shown again with the predictions of the PYTHIA and CASCADE models. CASCADE is closer to the data at low x_γ^{obs}, however at high jet energy CASCADE predicts the same value as PYTHIA. Omitting the simulation of multiple interactions has a significant effect on the jet shapes. The PYTHIA simulation without multiple interactions is somewhat closer to the data at low x_γ^{obs}, while the description at high x_γ^{obs}, forward η^{jet} and high jet energy remains good.

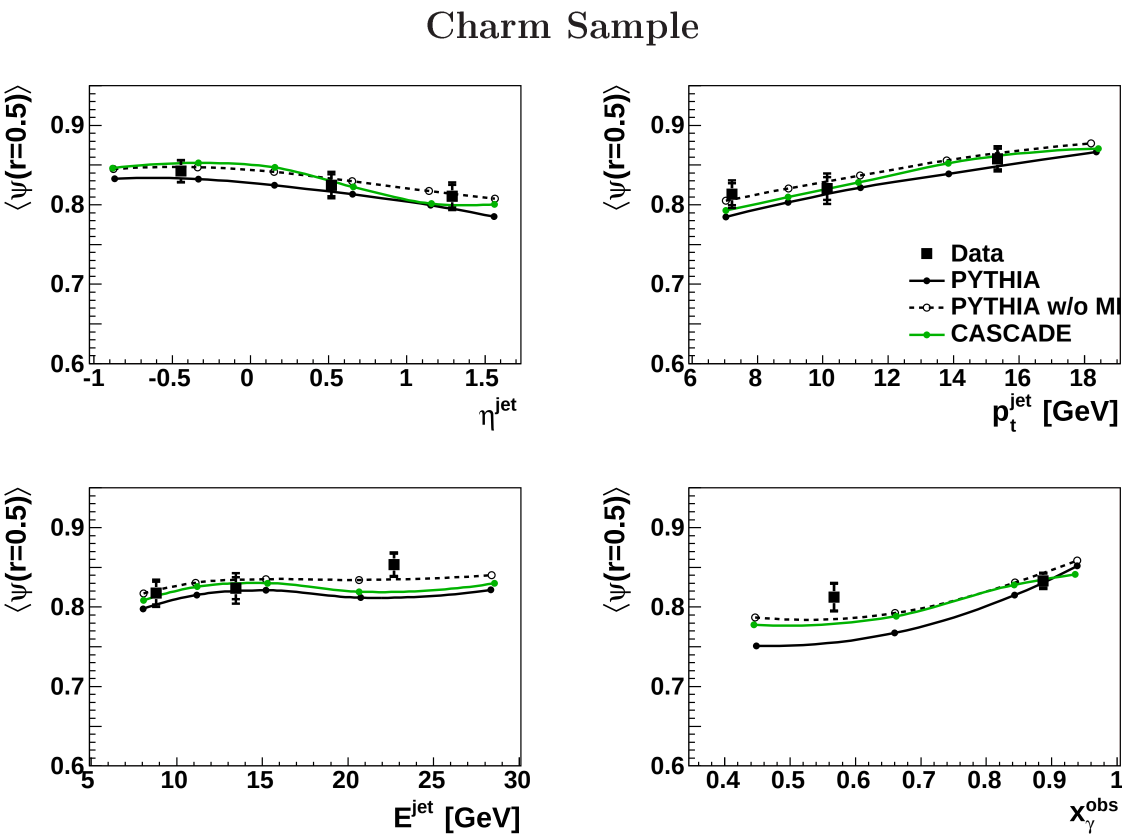

Figure 7.10: *The same data points as in figure 7.9 are compared with the predictions of the PYTHIA MC simulation with (full line) and without (dashed line) multiple interactions and with the CASCADE model (grey line). Smooth curves connecting the MC points are shown to guide the eye. The statistical errors of the MC predictions are negligible.*

7.2.2 Flavour Inclusive Sample

In figure 7.11 the mean integrated jet shape at $r = 0.5$ is shown for the flavour inclusive sample as a function of the variables η^{jet}, p_t^{jet}, E^{jet} of the two highest p_t jets and the variable x_γ^{obs}. PYTHIA simulation describes the flavour inclusive data well everywhere and confirms the growing contribution of the resolved events towards the forward region and lower x_γ^{obs} values. Numerical values for the data and Monte Carlo predictions are listed in table B.4.

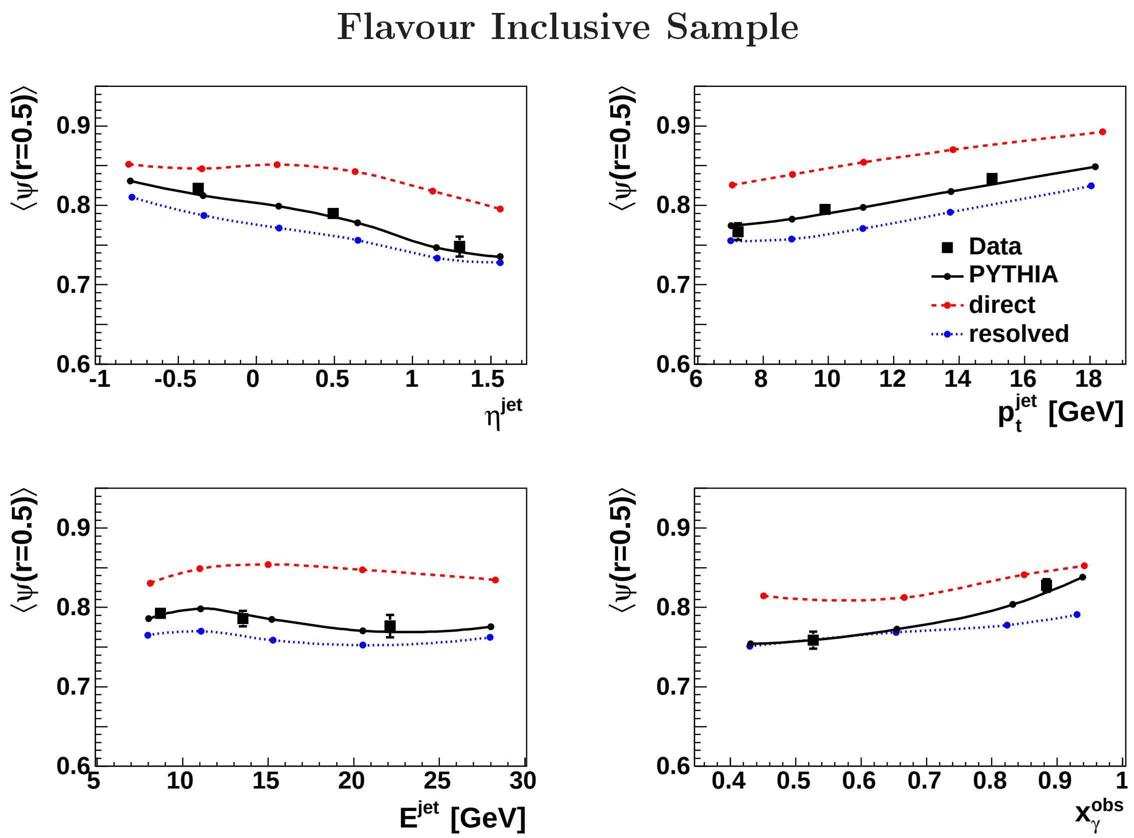

Figure 7.11: *Distributions of the mean integrated jet shape at a fixed value of* $r = 0.5$ *after detector corrections measured for the flavour inclusive sample as function of the variables* η^{jet}, p_t^{jet}, E^{jet} *of the two highest* p_t *jets and the variable* x_γ^{obs} *. The predictions from the charm PYTHIA MC simulation are compared to the data. The expectations for direct photon and resolved photon events from PYTHIA are shown separately. Smooth curves connecting the MC points are shown to guide the eye. The statistical errors of the MC predictions are negligible. The inner error bars of the data points represent the statistical uncertainty and the outer error bars the statistical and systematic errors added in quadrature.*

7.3 Comparison of the Charm Sample and the Flavour Inclusive Sample

Finally a direct comparison of the jet shapes measured in charm data and flavour inclusive data is shown in figures 7.12 and 7.13.

In figure 7.12, where the mean integrated jet shape as a function of the cone radius r is shown, a clear difference between both data samples is seen at low values of x_γ^{obs}. The jets from charm events are significantly narrower than the jets from the flavour inclusive events. That indicates a lower fraction of gluon jets in the charm sample than in the flavour inclusive sample at low x_γ^{obs}. At high x_γ^{obs} no significant differences are found.

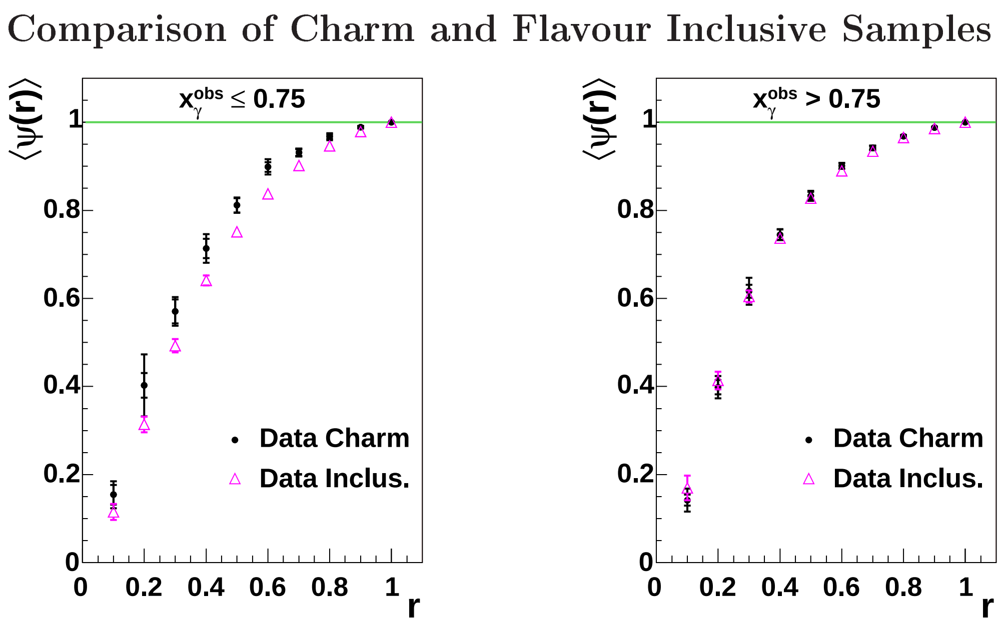

Figure 7.12: *Comparison of the mean integrated jet shape $\langle\psi(r)\rangle$ corrected for detector effects for the charm data sample ('other jet' is analysed) and flavour inclusive data sample (both highest p_t jets are analysed) in two different regions of x_γ^{obs}. The inner error bars of the data points represent the statistical uncertainty and the outer error bars the statistical and systematic errors added in quadrature.*

As can be seen in figure 7.13, the differences between the flavour inclusive and the charm sample at a cone radius $r = 0.5$ are increasing towards the forward region, towards higher jet energies and at low x_γ^{obs}. The PYTHIA predictions for the mean integrated jet shape as a function of x_γ^{obs} are very similar for both samples. However, while the flavour inclusive data are well described by the PYTHIA MC, the charm data show a significant deviation at low x_γ^{obs}, as already discussed.

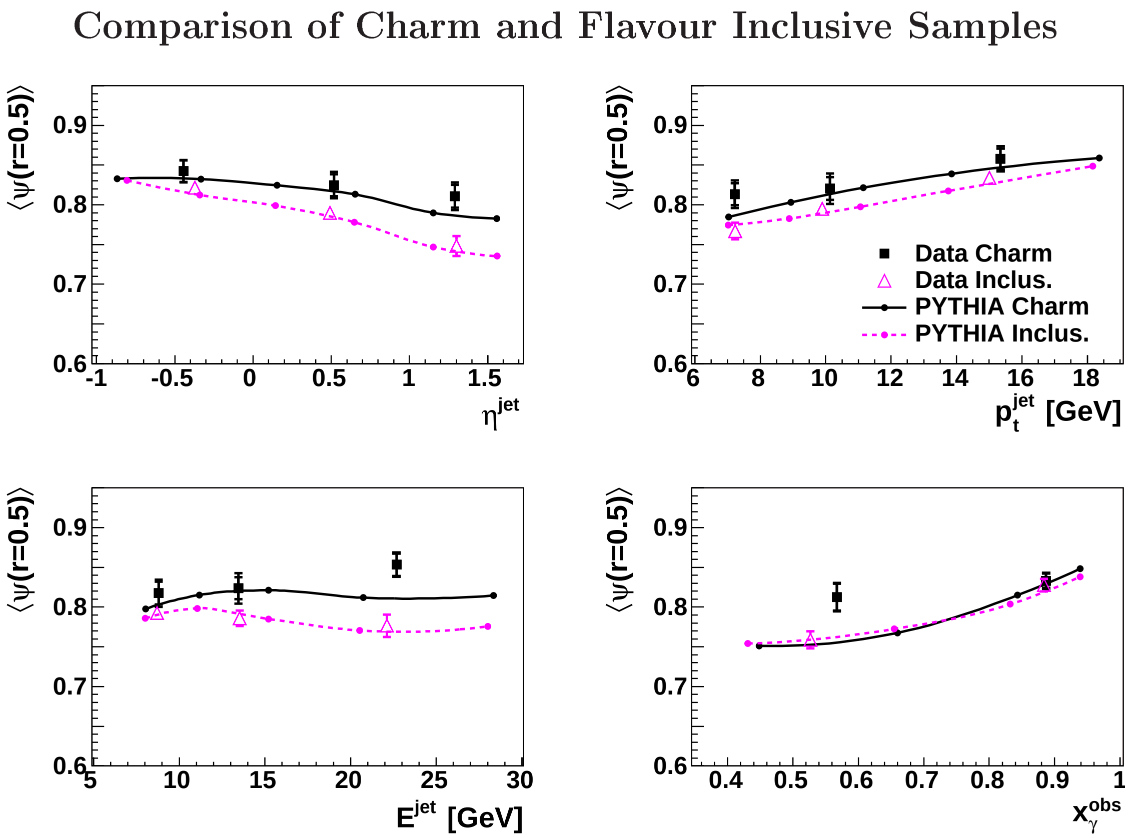

Figure 7.13: *Comparison of distributions of the mean integrated jet shapes at a fixed value of $r = 0.5$ as a function of η^{jet}, p_t^{jet} and E^{jet} and x_γ^{obs} for the charm sample ('other jet' are analysed) and for the flavour inclusive sample (two highest p_t jets are analysed). The measurements are corrected for detector effects. The PYTHIA predictions for the charm (full line) and the flavour inclusive dijets (dashed line) are shown with the data. Smooth curves connecting the Monte Carlo points are shown to guide the eye. The statistical errors of the MC predictions are negligible. The inner error bars of the data points represent the statistical uncertainty and the outer error bars the statistical and systematic errors added in quadrature.*

7.4 Summary of the Results

We measured the mean integrated jet shape $\langle\psi(r)\rangle$ in the charm sample and in the flavour inclusive sample. These measurements are sensitive to the ratio of the gluon initiated jets to the quark initiated jets and thus to the composition of different processes.
The measured values for the charm sample and the corresponding PYTHIA predictions in the two regions of x_γ^{obs} are:

$$\langle\psi(r=0.5)\rangle^{meas}_{x_\gamma^{obs}\le 0.75} = 0.812 \pm 0.017 \pm 0.005 \qquad \langle\psi(r=0.5)\rangle^{PYTHIA}_{x_\gamma^{obs}\le 0.75} = 0.761$$

$$\langle\psi(r=0.5)\rangle^{meas}_{x_\gamma^{obs}>0.75} = 0.833 \pm 0.009 \pm 0.007 \qquad \langle\psi(r=0.5)\rangle^{PYTHIA}_{x_\gamma^{obs}>0.75} = 0.834$$

The statistical errors for the Monte Carlo predictions are negligible. We observe a disagreement for the charm sample with the total charm PYTHIA prediction for the data at low x_γ^{obs}. The data are about three standard deviations over the PYTHIA prediction at the cone radius $r = 0.5$. The data at high x_γ^{obs} are well described. For the flavour inclusive data sample we observe a good agreement of the data with the total inclusive PYTHIA MC prediction over the whole range of x_γ^{obs}.

The probabilities of various processes as simulated by PYTHIA for the charm MC and for the inclusive MC are listed in table 1.1, page 24. The distributions studied for the flavour inclusive data sample are well described with the present composition of the processes in the PYTHIA MC. However, this is not the case for the charm sample Also none of the performed variations of the PYTHIA parameters succeeded in describing the data satisfactory. We found the CASCADE simulation to describe the data better at low x_γ^{obs} (discrepancy of two standard deviations), while the description of other measured points is as good as the PYTHIA one.

The summary tables of all the measured data points, together with their uncertainties and PYTHIA Monte Carlo predictions are listed in the tables in appendix B for the charm and flavour inclusive sample.

In appendix C the additional measurements of the mean integrated jet shape as a function of the cone radius r in bins of η^{jet}, p_t^{jet} and E^{jet} are shown for the charm sample and for the flavour inclusive sample. The data are compared with predictions of the PYTHIA Monte Carlo simulation.

7.5 Comparison with other Measurements

It is interesting to consider the results presented in this thesis in context of the recent measurements of the charm photoproduction at HERA. A similar measurement of jet shapes was performed by the ZEUS experiment [80] for the 'other jet' of D^*-tagged charm photoproduction events. There it was observed (see Fig. 7.14 b), that the data sample is consistent with a pure sample of quark jets along the whole η^{jet} range, except of the most forward η^{jet} bin, where a deviation from the pure quark sample was observed. It was concluded that the deviation is caused by the presence of gluon initiated jets coming from excitation processes. Moreover, the effect could be localised not to come from the region of high x_γ^{obs} events.

The mean integrated jet shape as a function of η^{jet} for the cone radius $r = 0.3$ (as in the ZEUS analysis) determined from this analysis is shown in figure 7.14 a). Only statistical errors of the measurement are shown. The results are in agreement with the results of the discussed ZEUS analysis, as can be seen in figure 7.14. However, we do not access the very forward region of the ZEUS results. Unfortunately, the jet shapes for low x_γ^{obs} events were not extracted separately in the ZEUS analysis.

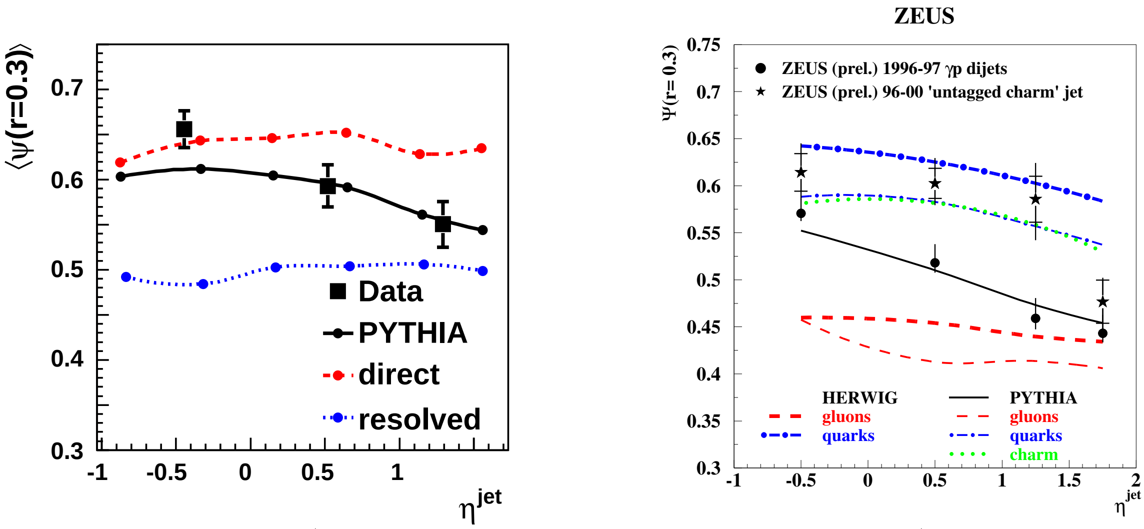

a) b)

Figure 7.14: *Comparison of the results of the present analysis (a) with the results of a similar ZEUS analysis [80] (b). Distributions of the mean integrated jet shape at a fixed value of* $r = 0.3$ *corrected for detector effects are shown for the charm samples as a function of the* η^{jet} *for the non charm tagged jet. In figure a) only statistical errors of the data are shown. For more details see text.*

A different analysis was performed at H1, concerning the measurement of differential cross sections of photoproduction events containing a D^* meson and a jet [39]. It was found that the cross section as a function of η^{D^*} falls in the forward direction whereas the cross section as a function of η^{jet} is almost constant. They conclude on a significant contribution form a further parton, most likely a gluon in the forward direction which initiates the jet, but does not contribute to the D^* cross section. Combining that result with the results of this analysis, only a majority of light quark initiated jets going into forward direction would agree with the results of both analyses.

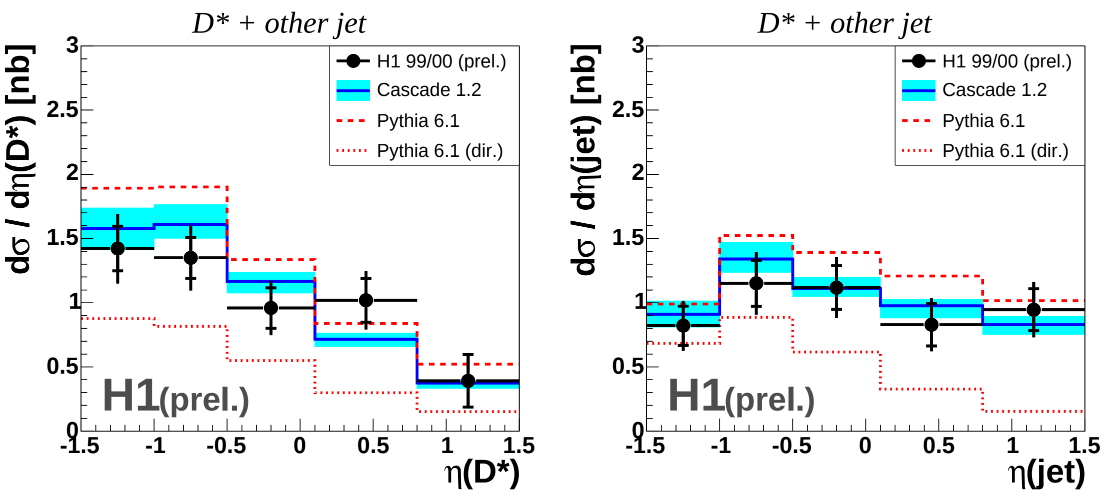

Figure 7.15: *D^*+jet cross sections in bins of the pseudorapidity of the D^* (a) and of the jet (b), together with the predictions of the PYTHIA and CASCADE Monte Carlo simulations. The figures are taken from [39]. For more details see text.*

Chapter 8

Summary

In this analysis production mechanisms involved in charm photoproduction are studied. In previous analyses a good description of charm production cross section by the theoretical models was found. The topic of this thesis is the investigation of various processes contributing to the production cross section.

Charm production in ep collisions at HERA is dominated by boson-gluon fusion processes. In addition to direct photon processes ($\gamma g \to c\bar{c}$), resolved photon processes can contribute significantly in photoproduction. Here the photon can act as a source of quarks and gluons which participate in the hard interaction. In the 'normal resolved' processes ($gg \to c\bar{c}$) a charm quark pair is produced in the hard interaction. In contrast to that, in the excitation processes ($cg \to cg$ and $cq \to cq$), which are supposed to represent the largest fraction of the resolved photon processes, one charm quark and another parton are produced. The different contributions to the cross section are investigated experimentally by a study of the jet shapes of the high p_t jets emerging from photoproduction reactions. Since the jet shape depends mainly on the nature of the parton that initiated the jet, the average jet shape is sensitive to the relative composition of the production processes, particularly to various resolved processes.

The data analysed here were collected with the H1 detector at HERA in the years 1999-2000 and correspond to an integrated luminosity of $48\,\mathrm{pb}^{-1}$. Charm dijet events were tagged in the semileptonic decay channel using a high p_t muon in one of the jets. Jets were built from hadronic final state objects using the inclusive $k_\perp$ clustering algorithm and the p_t-weighted recombination scheme. Two jets in the central rapidity range with $p_t^{jet} > 7$ and $6\,\mathrm{GeV}$ were required. The kinematical region of the analysis is defined as $Q^2 < 1\,\mathrm{GeV}^2$ and $0.2 < y < 0.8$. A cut on the relative momentum of the muon with respect to the jet axis ($p_t^{rel} < 1\,\mathrm{GeV}$) was used to increase the fraction of charm events in the studied data sample. The final results were corrected for the event losses due to the p_t^{rel} cut as well as for the remaining background originating from beauty and light quark events and detector effects. The distributions for a pure charm event sample were extracted. For comparison a flavour inclusive dijet sample, which is dominated by light quark production, was studied.

In case of the charm sample, the high p_t muon associated to a jet is used to tag a jet initiated by a charm quark. The shape of the second jet, not containing the muon, was investigated and compared with predictions of a leading order PYTHIA Monte Carlo simulation including parton showers, which contains both direct and resolved photon events as well as with the CASCADE Monte Carlo. CASCADE does not contain resolved events explicitly.

For the purpose of the jet shape studies the mean integrated jet shape $\langle\psi(r)\rangle$ was used. The dependence of $\langle\psi(r)\rangle$ on the variables η^{jet}, p_t^{jet} and E^{jet} was compared to both Monte Carlo models mentioned above. The data are described well by both of them, similar trends are observed except for the deviation from the MC prediction at high E^{jet}.

The variable $\langle\psi(r)\rangle$ was also investigated in two regions of x_γ^{obs}. For events with $x_\gamma^{obs} > 0.75$, which are dominated by the direct photon component, the description of the data by the MC simulations is good. In the region $x_\gamma^{obs} \leq 0.75$, dominated by resolved events, a discrepancy of three standard deviations with respect to the PYTHIA simulation is found. The resolved component in PYTHIA is dominated by charm excitation processes, where in addition to the charm quark jet (tagged by the muon) a gluon initiated jet is expected, which is on average broader than a charm jet. However, the measured data do not agree with the PYTHIA prediction of a significantly lower mean integrated jet shape for the resolved enriched sample, due to significantly more gluon initiated jets in the region of low x_γ^{obs} values present in PYTHIA. The disagreement may be explained by a different mixture of the various contributing resolved photon processes. Another possibility is that the observed discrepancy occurs due to missing higher orders in the massless simulation.

The proper simulation of the final state parton showers for the charm quark initiated jets is indicated by agreement of the data and the MC at high values of x_γ^{obs}. The good description of the x_γ^{obs} distribution indicates agreement between the data and the MC concerning the ratio of direct to resolved processes. Since the other control data distributions are also described well by the Monte Carlo, the simulated topologies seem to be the same as seen in the data. However, the description is worse for the events with $x_\gamma^{obs} \leq 0.75$.

In the framework of this thesis we made several attempts to understand the discrepancies found for $\langle\psi(r)\rangle$ in the low x_γ^{obs} region between the data and the PYTHIA simulation. They included variations of the Peterson fragmentation parameter, usage of the SaS 1D photon structure function instead of the default GRV-LO and switching off the multiple interactions (MI) which can occur between the photon and proton remnants. None of the models succeeded in describing the data satisfactory. The only significant changes in the direction of the data are seen in switching off the MI and when using the CASCADE simulation. The biggest change in the PYTHIA simulation for the low x_γ^{obs} was observed when switching off the MI, which are otherwise included. Thus fewer particles coming from the underlying events are present in the final state and jets get somewhat narrower. However, other analyses showed the necessity of including the MI in the simulation in order to describe other measured quantities. The most plausible explanation of the data by the tested models was found in the CASCADE model. The CASCADE prediction is about two standard deviations below the data at low x_γ^{obs}, the description of the high x_γ^{obs} data is about as good as the PYTHIA one.

For comparison, flavour inclusive dijet events were analysed in tagged photoproduction. Here the high p_t muon requirement was omitted and the two highest p_t jets were analysed. The jet shapes measured in the flavour inclusive sample are in agreement with the inclusive PYTHIA prediction containing a large fraction of gluon jets in the resolved photon sample and thus predicting broader jets for events at low x_γ^{obs}.

Chapter 9

Outlook

Starting from the measurements presented in this thesis, we discuss here possible improvements which could contribute to the explanation of the observed discrepancies from both experimental and theoretical points of view.

Since the statistics of the charm data sample represents the dominant error of the mean integrated jet shape measurement, a larger data sample would help to constrain the models further. An improvement in this direction is expected from the HERA II data, where already now the collected luminosity exceeds the data sample studied here. However, a high data quality is necessary for such a complex analysis.

A further experimental test could be an independent study of jet shapes in charm events which can be performed selecting charm photoproduction in the D^*-tagged events. Significant progress in this direction is expected due to the new Fast Track Trigger, which is still under development. It allows triggering on particular track topologies and invariant masses and thus collecting a large D^*-event photoproduction sample in the coming HERA II data.

Concerning the theoretical explanation of the results presently measured for the charm sample, none of the studied models succeeds in describing the data well. The next step would be to try to adjust the fractions of the various resolved PYTHIA MC processes such that the description of the mean integrated jet shape at low x_γ^{obs} improves. However, the problem has many free parameters. One has to keep in mind that the fraction of the direct processes has to stay unchanged, since this is well constrained not only by the jet shape measurement, but even more by the description of the x_γ^{obs} variable by PYTHIA. The variable $\cos\Theta^*$, being the dijet scattering angle in the dijet rest frame, which is sensitive to gluon propagator effects of the partonic subprocess, has to be also described well. Other variables, which have not been considered in this analysis, have to be also described well. Among them the number of central jets, the distribution of the distance of the event particles from the jet axis and the distribution of the fraction of the transverse momentum of the non muon jet contained in a cone with a radius $r > 1$. In case of those variables, distributions for different processes differ considerably, as is shown in the following appendix. While the distributions are described well for the whole charm enriched sample this is not the case anymore for the resolved enriched events, as shown earlier in this thesis.

Some other theoretical approaches might also bring interesting insights to the problem. It is known that the massive next-to-leading order (NLO) calculation implemented in the FMNR program (see appendix D) contains a much smaller fraction of the processes called 'resolved' than the PYTHIA simulation, whereas in the NLO calculation jets initiated by a hard gluon can appear also in the direct processes. The good description of the absolute magnitude of the charm photoproduction cross section by the FMNR program as well as the good description of various differential angular distributions in the charm photoproduction data, are in favor of such a model. However, presently only the outgoing partons from the hard subprocess are available for a user of this program. Therefore the jet structure of the data cannot be compared to the predictions of the FMNR program. It could, however, still be interesting to derive the fraction of gluon initiated jets in such a calculation.

Another challenging approach is represented by the MC@NLO program, which is presently under development for HERA physics. This may bring a new insight into the problem of resolved events in charm production.

Appendix A

Previous Studies

The goal of the study, which preceeded the work presented of this thesis was to bring possibly most information on the abundance of various processes contributing to the production of heavy quarks at HERA. It was a natural further step after the heavy flavour production cross sections at HERA were measured in recent years [39, 70, 85, 86, 87]. Those measurements showed that the fraction of direct and resolved processes is described reasonably well by various models. Additionally one might ask, whether also the composition of the resolved processes in the models correspond to the reality. In particular, the distinction of the normal resolved processes (where gluon is picked up from the photon) and excitation processes (where charm quark is picked up from the photon) is presently of a big interest.

A **large number of processes** contribute to heavy quark production at HERA. An overview of the leading order processes is given in table A.1. Distributions in different variables for the three most important processes according to the PYTHIA MC are shown in figure A.1. One can see that the situation is complicated, since the differences between the processes are not large.

In addition to the large number of contributing processes, a further difficulty is represented by the **complicated background composition**. The starting point of the study was the selection of heavy quark enriched events using a muon and two jets, as established in [70]. The selection was kept fixed during the whole study. The photoproduction event sample obtained after that selection consists of approximately 50 % charm events, 30 % beauty events and 20 % light quark events [70]. Each of these flavour contributions comprises of a number of processes, as already mentioned in case of charm production. This gives many degrees of freedom for any analysis investigating particular processes. Therefore fitting the distributions in figure A.1 did not seem to be a good approach, but some other technique had to be chosen.

Process	**Name**	**Generator number**	**Type**
$\gamma g \to Q\bar{Q}$	direct	135	direct
$gg \to Q\bar{Q}$	normal resolved	53	resolved
$Qg \to Qg$ + conjugate	excitation	28	resolved
$Qq \to Qq$ + conjugate	light quark component	11	resolved
$q\bar{q} \to Q\bar{Q}$	-	12	resolved
$\gamma Q \to gQ$ + conjugate	-	131	direct

Table A.1: *Processes contributing to the production of heavy quarks at HERA. Here Q denotes heavy quark, q light quark, γ stands for photon and g for gluon. In some cases also conjugate processes occur. For this processes both quark and antiquark can take part in the process. Generator numbers listed here label the process in the PYTHIA MC.*

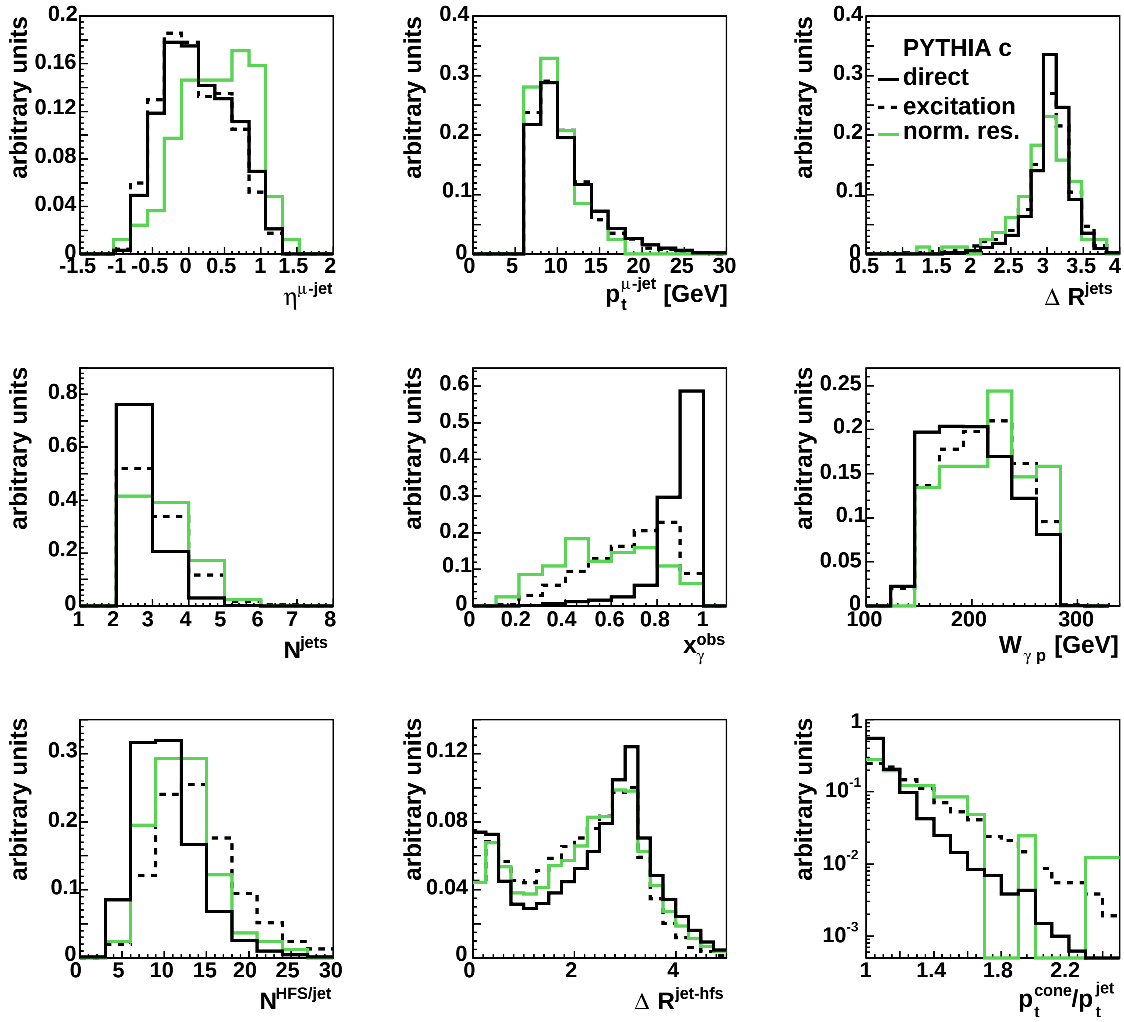

Figure A.1: *Distributions in different variables for direct, excitation and normal resolved processes (see table A.1) simulated by the charm PYTHIA MC. The variables are described on page 68. The used cuts are listed in table 5.3. The distributions are normalised to the total number of events. Most of the distributions of the light quark component is similar to the distributions of the normal resolved events.*

An investigation of the jet structure was found to be a very promising method to distinguish various processes. The studies in this thesis are based on the fact, that gluon jets are in general broader than the quark jets, as already described earlier. This is the case for light and charm quark initiated jets. In case of beauty quark initiated jets the differences to gluon jets are already negligible due to the high mass of the beauty quark. Therefore **charm quark production** is best suited for the jet structure method.

However, in the field of the jet structure study one has a whole variety of possible approaches to follow. We investigated some of them and the results are summarised in this appendix.

A.1 Discriminating Variables

Selection of the Variables

We investigated a number of candidate variables sensitive to differences between charm and gluon jets. Some of them were not used later: jet charge, number of HFS objects/jet, electromagnetic and LAr fraction of the jet, fragmentation function, relative magnitude of p_t^{jet} of the muon jet to the non-muon jet, p_t of the muon jet. These studies also included tuning of parameters which occur in definitions of some of the variables.

Soon it was clear that the high p_t muon causes a bias in the structure of the jet. Therefore we have chosen only the non-muon jet, called the 'other jet', to be investigated. With respect to the identification of the contributing processes this choice is favorable, since the 'other jet' has a high chance not to be initiated by the charm quark.

Studying the shape of the 'other jet' in the charm Monte Carlo, we chose in the end four variables, which seemed to be most promising:

- **Jet spread** (J_s) representing the p_t-weighted jet radius

$$J_s = \frac{\sum_i^N p_{t_i}^{\kappa} r_i}{\sum_i^N p_{t_i}^{\kappa}}, \tag{A.1}$$

  where the sum runs over all N jet particles. Performing a variation of the parameter κ between 0.1 and 1.0 it was found that the value of 0.3 provides the best separation between charm and gluon initiated jets.

- **Number of subjets** (N_{subj}) is obtained by running the jet finder on the particles of the studied jet. The matching is stopped when all $E_T^{subjet} \geq \sqrt{y_{cut}} E_T^{jet}$. Here y_{cut}, which controls the number of resolved subjets (see figure A.2), was chosen to be 5.10^{-4}.

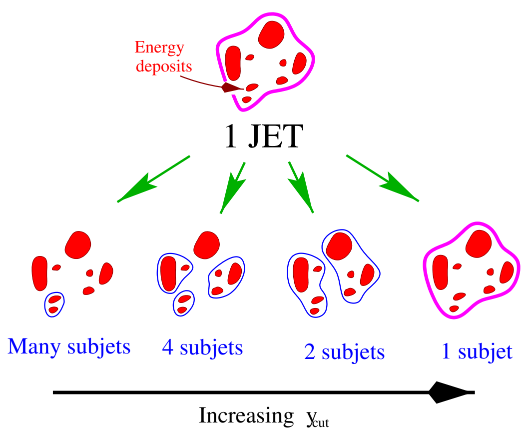

Figure A.2: *The internal jet structure can be studied by resolving jet-like structures ('subjets') in a single jet. As the resolution scale y_{cut} decreases an increasing number of subjets is resolved. Figure taken from [88].*

- **Longitudinal energy fraction** (L_E) was motivated by fragmentation. It is defined as:

$$L_E = \frac{\sum_i^N p_{l_i}}{N\, E^{jet}}, \tag{A.2}$$

where p_{l_i} is the longitudinal momentum of the particle i with respect to the jet axis.

- The usage of the **jet mass** (M^{jet}) is based on the assumption, that the gluon jets, which are wider, will have a higher mass than the quark jets. The jet mass is calculated from the sum of the four vectors of the jet particles: $\mathbf{p}_i$:

$$M^{jet} = \sqrt{(\sum_i^N \mathbf{p}_i)^2} \tag{A.3}$$

assuming the proper mass for identified electrons and muons, a pion mass for the rest tracks and a zero mass for single cell clusters.

In case of the two last mentioned variables, the logarithm of the variable was considered. Figure A.3 shows distributions of the discriminating variables for the charm PYTHIA MC separately for charm quark and gluon jets. Gluon jets have a higher jet spread, a larger number of subjets, softer fragmentation and higher mass than charm quark jets. For the definition of charm quark and gluon jets see section A.4, here the scheme JC1 is used.

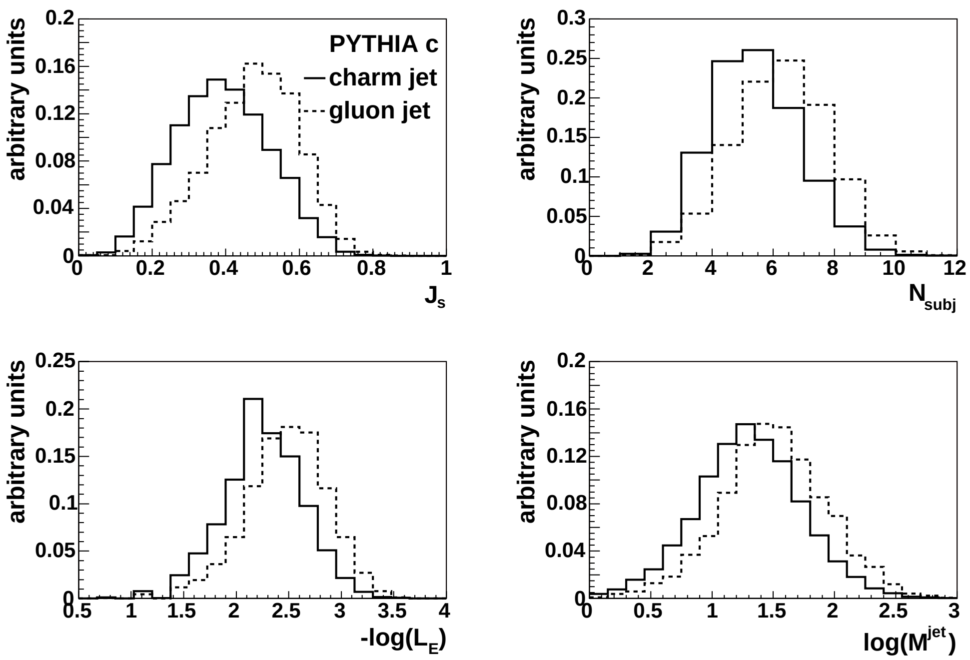

Figure A.3: *Distributions of the discriminating variables J_s, $N_{subjets}$, $-\log(L_E)$ and $\log(M^{jet})$ for charm and gluon jets as simulated by the charm PYTHIA MC, normalised to the total number of events. The jet classification in charm quark and gluon jets JC1 (see section A.4) is used.*

Figure A.4 shows the distribution of gluon and quark jets as functions of the variables η^{jet}, p_t^{jet}, E^{jet} of the 'other jet' and the variable x_γ^{obs}, as simulated by the charm PYTHIA MC. We chose to study the jet shape as a function of x_γ^{obs}, because this variable is constructed to be sensitive to direct and resolved processes. Jets from resolved processes are expected to occur in the forward region, therefore we chose also η^{jet}. Additional variables E^{jet} and p_t^{jet} are kinematical variables, which might help to understand the sample and possible discrepancies.

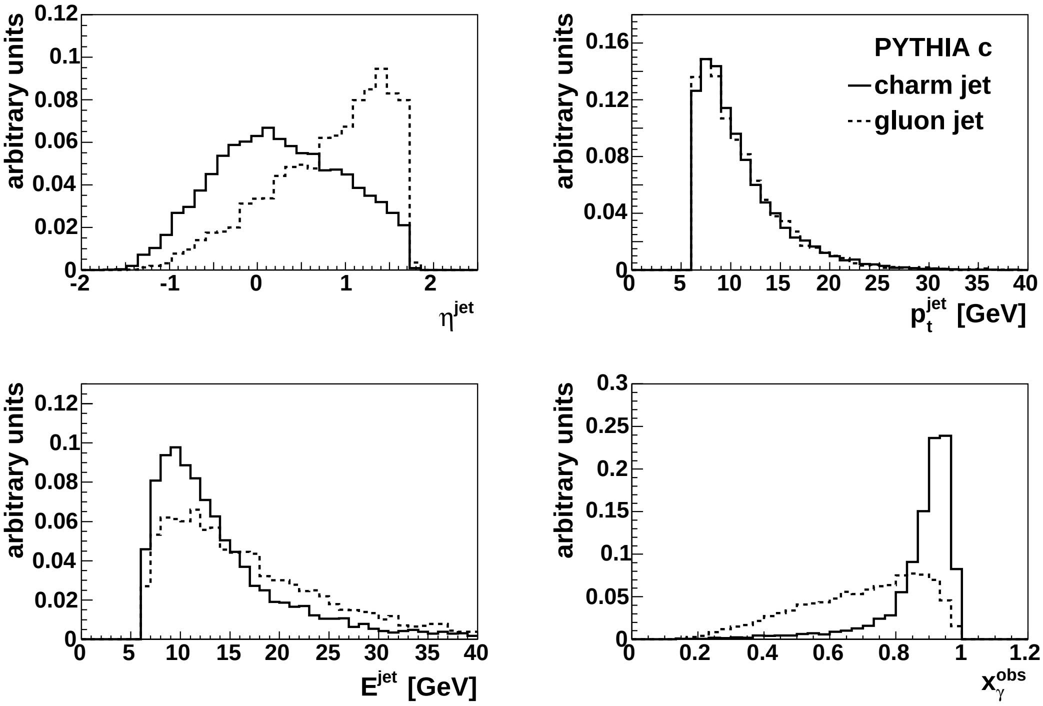

Figure A.4: *Distributions of gluon and charm jets as a function of the variables η^{jet}, p_t^{jet} , E^{jet} of the 'other jet' and the variable x_γ^{obs} as simulated by charm PYTHIA MC. They are normalised to the total number of events. Jet classification to charm quark and gluon jets JC1 (see section A.4) is used.*

An ideal variable for a direct study of the excitation processes is the dijet scattering angle in the dijet rest frame

$$\cos\Theta^* = \tanh\Big(\frac{\eta^{jet_1} - \eta^{jet_2}}{2}\Big), \tag{A.4}$$

which is sensitive to the type of the propagator in the hard subprocess (gluon or quark) [38]. Unfortunately, to ensure that this variable is not biased by the phase-space selection, one needs to apply additional cuts, which reduce the statistics of the sample considerably. Since the number of events of our selected sample is already quite limited, we decided not to use this, otherwise very interesting, variable.

Combination of the Variables - Fisher Discriminant

Since the variables are highly correlated, one needs to combine them taking the correlations into account. There is a number of approaches to combine multiple discriminating variables, for example neural networks and multivariate analyses. We decided to use a simple and efficient method based on a **Fisher discriminant** [89] to exploit the available discriminative power. In this method the discriminative variables are combined, taking into account the correlations between them. The correlations are obtained from the Monte Carlo models.

The Fisher discriminant D_F is defined as a linear combination of the discriminating variables x_i. For an arbitrary number of variables N_{var}

$$D_F = \sum_{i=1}^{N_{var}} a_i \, x_i, \tag{A.5}$$

where a_i are coefficients chosen such that the separation between gluon and charm jets is maximal. The procedure of determination of the coefficients a_i will be described briefly: We label the hypothesis that a jet is a gluon jet by H_0 and the hypothesis that a jet is a charm jet by H_1. In the first step the mean values μ_i^k of discriminating variables are calculated for each hypothesis H_k, k=0,1 and for each variable x_i, $i = 1, ..., N_{var}$. The charm PYTHIA MC was used to carry out this step.

Each hypothesis H_k has the expectation value for D_F:

$$d_k = \sum_{i=1}^{N_{var}} a_i \, \mu_i^k. \tag{A.6}$$

Our aim is to maximize the differences between the expectation values for both hypotheses, $|d_0 - d_1|$. It can be shown (see [90]) that this is the case for

$$a_i = W_{ij}^{-1}(\mu_j^0 - \mu_j^1), \tag{A.7}$$

where

$$W_{ij} = V_{ij}^0 + V_{ij}^1. \tag{A.8}$$

V^k represents the covariance matrix for the hypothesis H_k. The components of the V^k matrix are calculated as

$$V_{ij}^k = \langle (\mu_i^k - x_i)(\mu_j^k - x_j) \rangle \tag{A.9}$$

The Fisher discriminant method works best for variables which have Gaussian distributions. For such variables the results are comparable to neural networks. Therefore, some of our variables were modified using simple functions to resemble as close as possible to a Gaussian form. Thus we used $-\log(L_E)$ and $\log(M^{jet})$ instead of L_E and M^{jet}.

Problems can occur, when the matrix W to be inverted is singular. However, this was not the case in our analysis. For more details about the method see [90].

Using this combined discriminating variable D_F, the charm enriched sample can be divided into **charm-quark-enriched and gluon-enriched** subsamples by cutting on D_F (see Fig. A.5). Gluon enriched jets were defined by $D_F < -1.9$ and charm enriched jets by $D_F > -1.9$.

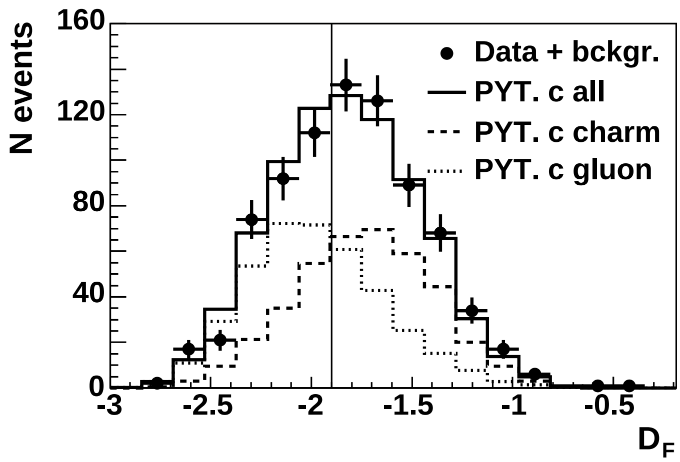

Figure A.5: *Distribution of the data as a function of the Fisher discriminant D_F. The data, which are not corrected for the background, are compared to the charm PYTHIA MC simulation including all processes. The data and the Monte Carlo are normalised to the same number of events. Curves for charm jets and gluon jets are also shown. They are normalised arbitrary. The line at $D_F = -1.9$ indicates the cut used to divide jets into charm enriched and gluon enriched samples.*

The aim was to measure cross sections of charm and gluon enriched jets as functions of the variables η^{jet}, p_t^{jet}, E^{jet} and x_γ^{obs}. Differences were observed between the gluon-enriched and charm-enriched data, as shown in figure A.6. They are very similar to the clean gluon/charm jets distributions shown in figure A.4. Gluon enriched jets were found to be predominantly in forward region and at lower values of x_γ^{obs} than charm enriched jets.

Although the results seemed to be nice and clear, the following problem was discovered: Applying the D_F-cut on pure charm Monte Carlo jets were divided into 'charm-enriched' and 'gluon-enriched' jets. Such selected 'gluon-enriched' jets were distributed in η^{jet}, p_t^{jet}, E^{jet} and x_γ^{obs} as expected for real gluon jets, although the sample was supposed to contain only charm induced jets (see figure A.7). This effect is probably due to η^{jet}, p_t^{jet} and E^{jet} dependence of two of the four variables: $-\log(L_E)$ and $\log(M^{jet})$, as it can be seen in figure A.8. Therefore, we decided to change the analysis strategy to the one described in the next section.

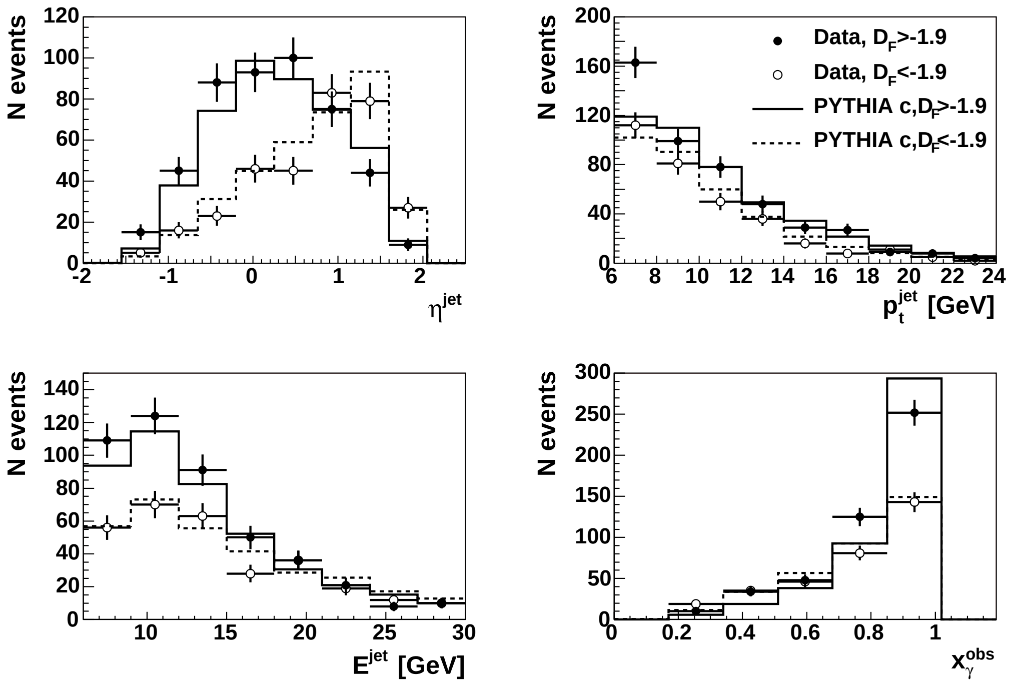

Figure A.6: *Distributions of gluon enriched and charm enriched jets as functions of the variables η^{jet}, p_t^{jet}, E^{jet} of the 'other jet' and the variable x_γ^{obs}. Data (not background corrected) are compared to the charm PYTHIA MC.*

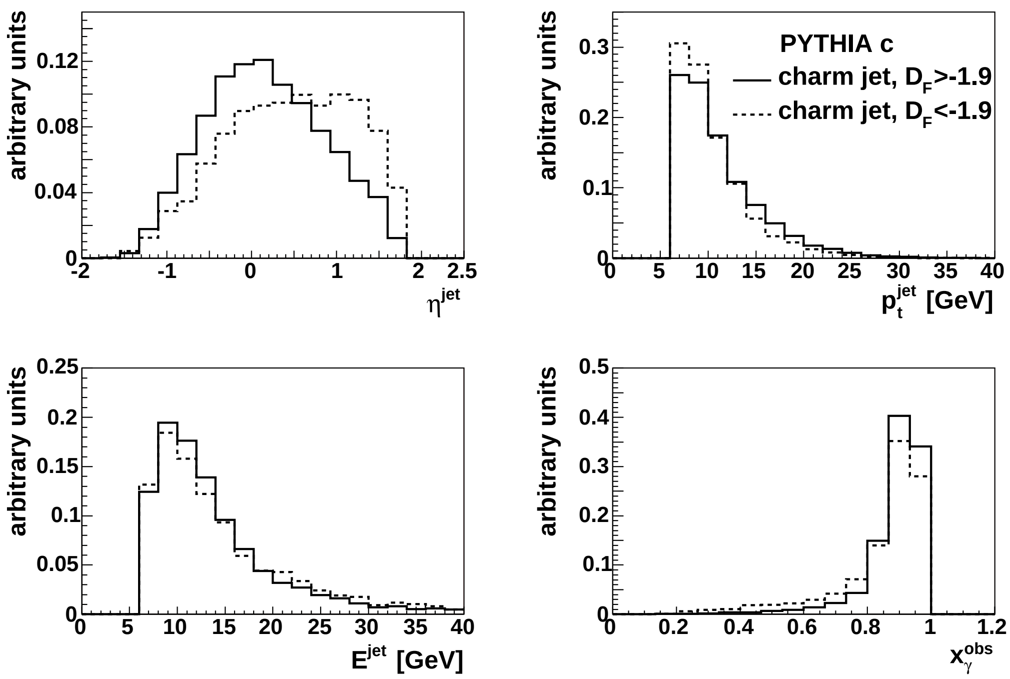

Figure A.7: *Charm jets (according to JC1) are divided by the cut on D_F into 'charm enriched' jets ($D_F > -1.9$) and 'gluon enriched' jets ($D_F < -1.9$). Distributions of 'gluon enriched' jets as functions of the variables η^{jet}, p_t^{jet}, E^{jet} of the 'other jet' and the variable x_γ^{obs}, normalised to the total number of events, show similar trends as gluon jets selected according to JC1 (see figure A.4).*

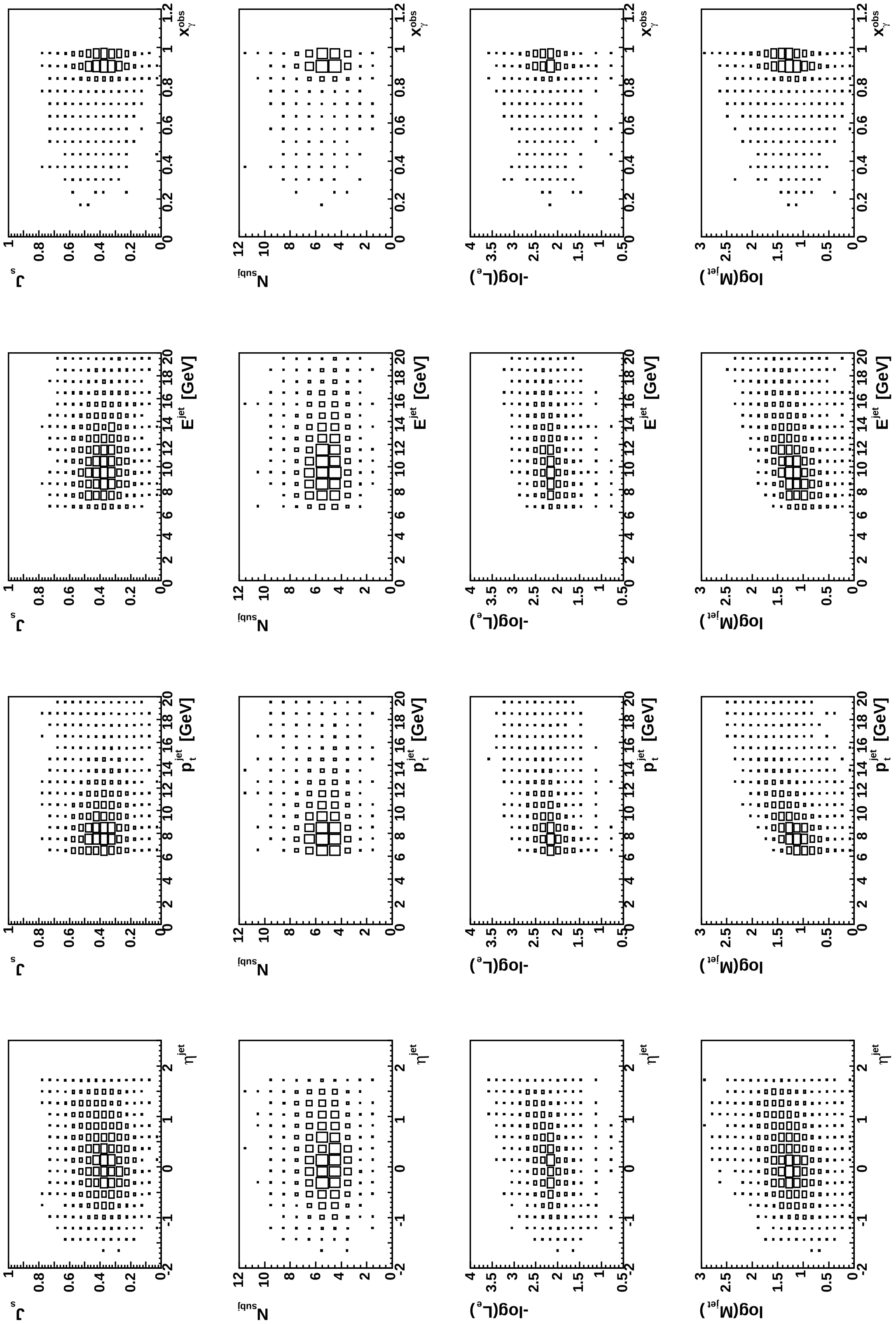

Figure A.8: *Correlations of the discriminating variables entering the Fisher discriminant* (J_s, N_{subj}, $-\log(L_e)$ *and* $\log(M^{jet})$) *with* η^{jet}, p_t^{jet}, E^{jet} *and* x_γ^{obs} *as simulated by direct charm PYTHIA MC.*

A.2 Charm and Gluon Jet Total and Differential Cross Sections

Instead of cutting on the Fisher discriminant D_F, another approach was followed. It was assumed that the jet shapes as well as the correlations between the discriminating variables, mentioned in the previous section, are correctly simulated in the Monte Carlo. Fitting of the MC templates of D_F for charm and gluon jets to the data would enable us to determine the fraction of gluon and charm jets. In this way one could obtain distributions of clean gluon and charm jets, in contrast to gluon-enriched and charm-enriched jets in case of a cut as in section A.1.

As a first step it was necessary to **correct the data for the background**. This was performed by subtraction of the simulated background templates from the D_F distributions. The fractions of beauty and light quark events were obtained from the inclusive MC. The beauty and light quark MC templates, scaled according to those fractions, were kept fixed during the fit. The distribution of D_F in the data was then **fitted by charm and gluon templates** using a standard likelihood fit with Poisson statistics [78] (see also section 5.2, page 67). Two parameters, the contributions of the charm and gluon component, were free during the fit and two parameters, the beauty and the light quark component, were fixed. The templates from the charm MC together with the templates for the background are shown in figure A.9. In such a fit it is possible to determine the overall **gluon fraction**, as well as the gluon fractions in bins of certain kinematic variables. The **total visible cross section for gluon and charm jets** is determined by:

$$\sigma^{vis}_{quark\ jets} = \frac{N_{events} f_q}{\mathcal{L}\epsilon_q} \tag{A.10}$$

$$\sigma^{vis}_{gluon\ jets} = \frac{N_{events} f_g}{\mathcal{L}\epsilon_g} \tag{A.11}$$

where N_{events} is the number of events in the selected data sample, f_q and f_g are the fractions of charm and gluon jets, respectively. $\mathcal{L}$ denotes the luminosity of the data and ϵ_q and ϵ_g are the total efficiencies for the charm and gluon jets, respectively.

Results of the fit to the D_F-distribution for the total data sample are shown in figure A.10. They can be compared with the PYTHIA prediction of the D_F-distribution, shown in figure A.11. The plots suggest that gluon jets are overestimated in PYTHIA and the fit describes the data better. Quantitative results on the charm and gluon jet fraction in the total selected data sample are given in table A.2. They are compared with the numbers from PYTHIA and CASCADE Monte Carlo models.

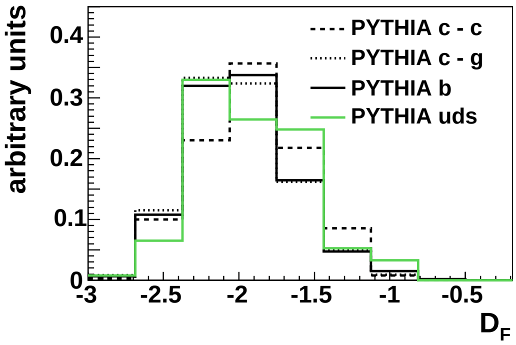

Figure A.9: *Four templates used to describe the data: charm and gluon jets (JC1) simulated by the charm PYTHIA MC, jets from light quark events simulated by the inclusive PYTHIA MC (mixture of light quark and gluon jets) and jets from beauty events (mixture of b-quark and gluon jets) simulated by the beauty PYTHIA MC. All histograms are normalised to the total number of events. Note that beauty and gluon jets are very similar.*

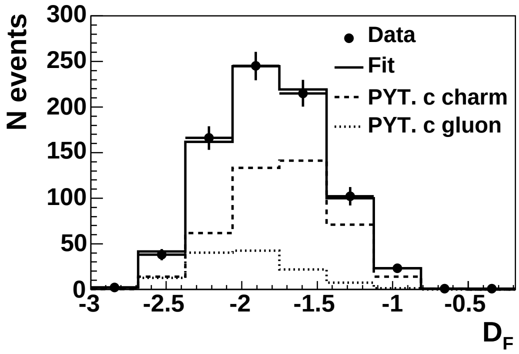

Figure A.10: *Description of the data as a function of the Fisher discriminant D_F by the fit to D_F. Background (not shown) is taken into account. The distributions of charm and gluon jets, which were used as templates for the fit, are shown additionally.*

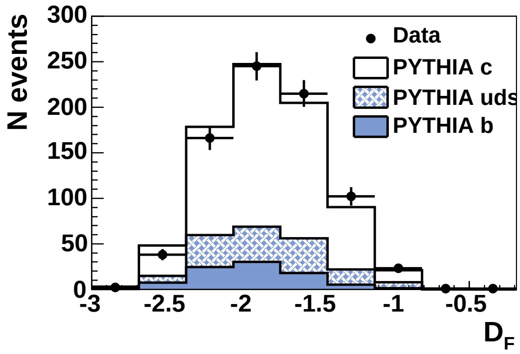

Figure A.11: *The data as a function of the Fisher discriminant D_F and description by the PYTHIA MC. Background from beauty and light quark events is taken into account.*

	Charm jets	Gluon jets
Pythia	63 %	37 %
Cascade	73 %	27 %
Fit	77 %	23 %

Table A.2: *Fractions of charm and gluon jets in the total selected charm data sample as predicted by Monte Carlo models PYTHIA and CASCADE and results from the fit.*

Analogous fits were performed in bins of η^{jet}, p_t^{jet}, E^{jet} of the 'other jet' and the variable x_γ^{obs}. The **differential cross sections** using results of this fit, together with the PYTHIA MC predictions, are shown in figure A.12. Although the PYTHIA MC is about a factor of 1.5 lower than the data, similar trends in the data and PYTHIA simulation are obvious. The contribution of gluon jets is observed to rise towards the forward region. Lower fraction of gluon jets in the data than in the PYTHIA MC is obvious. Description of the high x_γ^{obs} bin is reasonable. Most of the fits were good, however the most interesting low x_γ^{obs} bin was found to be problematic. At low x_γ^{obs} the difference between the templates is very small and there is no linear combination that would be able to describe the data, as shown in figure A.13.

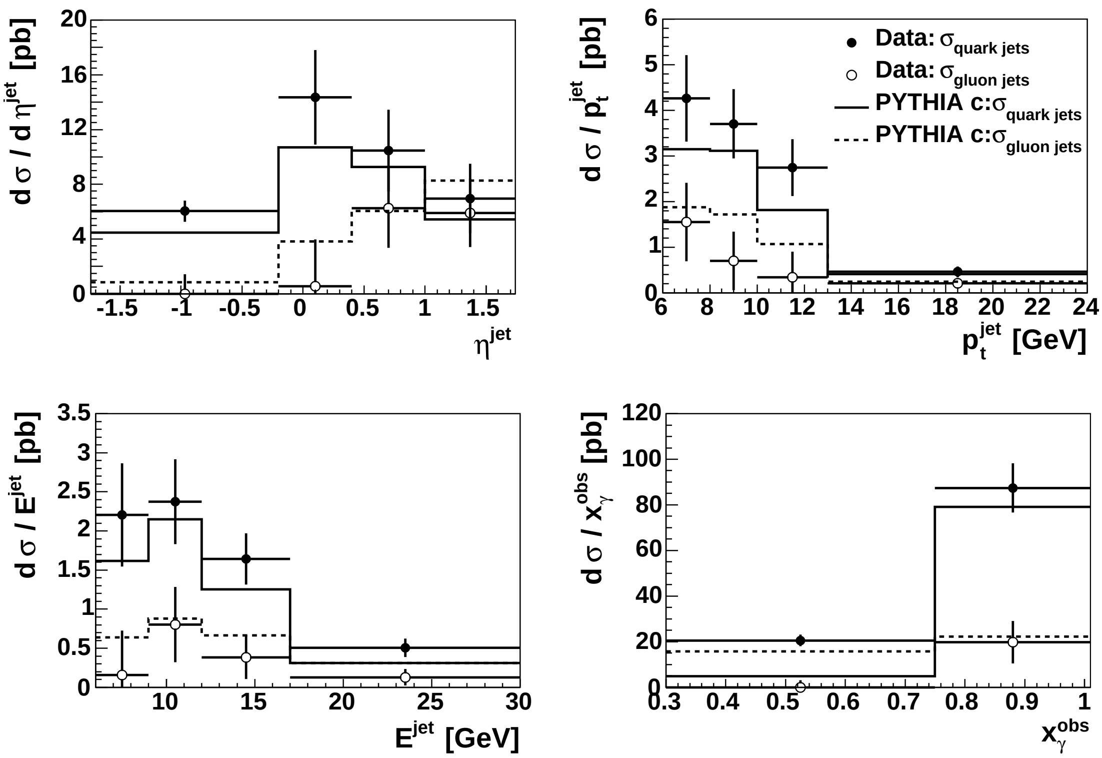

Figure A.12: *Differential cross sections as functions of the variables η^{jet}, p_t^{jet}, E^{jet} of the 'other jet' and the variable x_γ^{obs} are shown. They are obtained from the data by fitting of Fisher discriminant in the bins. Only the statistical errors of the fit are shown. In case of the Monte Carlo prediction explicit JC1 jet classification is used.*

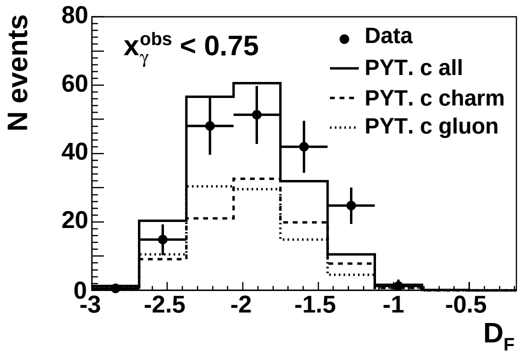

Figure A.13: *Distribution of the data (background corrected) for $x_\gamma^{obs} < 0.75$ as a function of the Fisher discriminant D_F. They are compared to the charm PYTHIA MC simulation. Data and the total MC prediction are normalised to the same number of events. Distributions for charm and gluon jets are also shown, with arbitrary normalisation. No combination of these templates is able to describe the data.*

Using this analysis method the **light quark component**, additionally to the charm and gluon component was found to be important. This topic will be discussed in detail in section A.3. But fitting of three components would make the situation much more complicated.

Although having high statistics charm MC (1850 pb^{-1}), the **fit results** were not stable (up to 50 % when using different subsamples of the MC) and had large errors. Additionally, it is not obvious that the jet shapes in the MC correspond to the reality. Therefore, the fit would not be reliable.

There was still a remaining problem with the **energy and pseudorapitidy dependence** of the two of four discriminating variables, as discussed earlier. The charm PYTHIA simulation predicts that the energy spectrum of charm and gluon jets is different. However, it is difficult to check, whether the simulated spectra of charm and gluon jets correspond to the reality.

Due to these reasons we looked for a less energy dependent variable with similar discrimination power. It was decided to **change the discriminant** and use the well established **integrated jet shape** variable instead of the Fisher discriminant. This variable is independent of η^{jet}, p_t^{jet}, E^{jet} and x_γ^{obs} and it provides a similar discriminative power as D_F. Using only one variable reduces also possible sources of uncertainties.

Because of the suspicion of the incorrect jet classification (see section A.4) it was decided to **change the method** and **compare the data and the MC** instead of fitting them by the MC templates. The final results of this thesis are presented in such way.

A.3 Light Quark Jets in Charm Events

We realised and also saw in the Monte Carlo that a third component is present in the charm event sample, additional to gluon and charm jets. Light quark initiated jets originate from processes, as shown in figure 1.9 e), where a light quark from the proton interacts via a gluon with a charm quark coming from the photon. The contribution of such processes to charm production depends on the light quark density in the proton and the charm quark density in the photon. A comparison of light quark and gluon densities, as they are in CTEQ5L, is shown in figure 1.7. According to the charm PYTHIA MC, these processes contribute about 10 % to the charm production cross section in the visible region. In the final plots those processes are included in the resolved curves, since they belong to the excitation component and thus to the resolved photon events.

A.4 Jet Classification

A jet classification is a prescription for the MC events which enables us to say, whether the selected jet was initiated by a charm quark, a gluon, a light quark or by a beauty quark. The jet classification was one of the major challenges during the development of this analysis. The reason is that the association of a detector level jet to a parton level jet can be ambiguous. Already the number of jets at the parton level and detector level can differ. Therefore, kinematical differences are expected as well. We tried three approaches, which are briefly described in the following:

- In the **JC1** approach a parton level[1] jet is found first, which is closest to the jet, from which we would like to determine its flavour. If the associated parton jet contains a charm quark, then the detector level jet is classified as a charm jet. Otherwise the jet is classified as a gluon jet.

  The obvious problem of this classification is that it does not take into account light quark jets. In this approach they are classified as gluon jets. In an attempt to improve this situation the second method was developed.

- In **JC2**, as in the previous method, the corresponding parton level jet is found first. However, in this method a closer and more detailed look is taken at the parton jet:
  1) If it contains a c or $\bar{c}$ quark the jet is classified as a charm jet and is excluded from the further classification.
  2) If it contains a b or $\bar{b}$ quark the jet is classified as a beauty jet and is excluded from the further classification.
  3) If it contains an odd number of light quarks (and an arbitrary number of gluons) the jet is classified as a light quark jet.
  4) If it contains an even number of light quarks (or 0) the jet is classified as a gluon jet.

[1]Parton level = all hadronic final state particles after the parton shower and before the hadronisation step.

This method has some positive features. All jets can be classified in this way as exactly one of the four possibilities: gluon, charm, beauty and light quark jet. It was checked that the fractions of those jets correspond to the fractions of the processes as generated by PYTHIA. Jets containing both charm and beauty quarks were not found.

Unfortunately, also this method has negative features. It does not care of cases which can occur when a few more/less partons are matched to the investigated parton level jet by the jet algorithm. It still relies on perfect one-to-one matching of detector level jets to parton level jets, which can be quite far away in R in reality.

- Approach **JC3** was motivated by [91]. This algorithm considers both highest p_t jets at the detector level (jet 1 and jet 2), which are then matched with the partons from the hard interaction (parton A and parton B) in the following way:
  1) The distances ΔR_{1A}, ΔR_{1B}, ΔR_{2A}, ΔR_{2B} are calculated where is $\Delta R = \sqrt{\Delta\eta^2 + \Delta\phi^2}$.
  2) The minimum of $\Delta R_{1A} + \Delta R_{2B}$ and $\Delta R_{2A} + \Delta R_{1B}$ is found. If the minimum is
     - $\Delta R_{1A} + \Delta R_{2B}$, then jet 1 is associated to the parton A and jet 2 is associated to the parton B.
     - $\Delta R_{1B} + \Delta R_{2A}$, then jet 1 is associated to the parton B, jet 2 is associated to the parton A.

  Such association is considered to be reliable when the sum of the distances is small enough. An event is accepted for a template only when the sum of the distances is less than 0.5. This cut was optimised in order not to accept too many falsely classified events and not to exclude a high number of events.

  This method has the best performance from the three investigated, but it is still not perfect. It ignores the possibility that one of the two highest p_t jets in the central region can come from initial/final state gluon radiation or from the photon remnant. Unclassified jets are not evenly distributed in the phase-space. There are more unclassified events at low p_t^{jet}, in forward region, and at lower x_γ^{obs}.

The approaches of JC2 and JC3 methods are displayed in figure A.14.

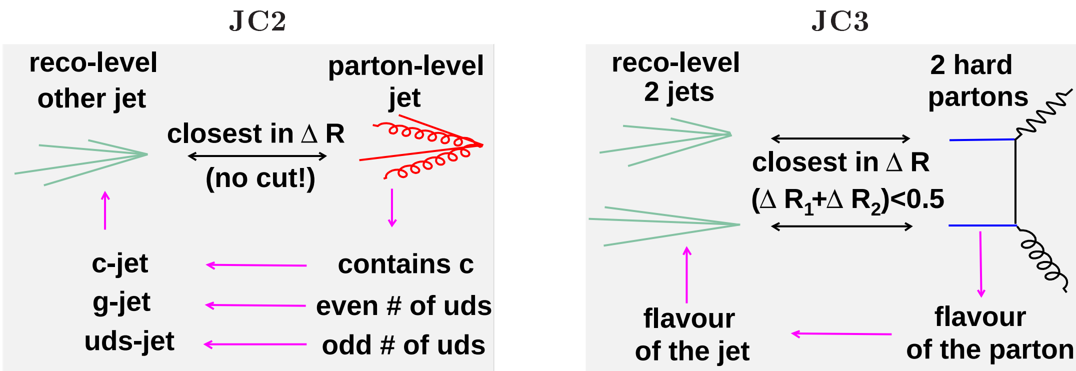

Figure A.14: *Graphical explanation of methods JC2 and JC3 for the jet classification.*

The three different classifications are compared in figureA.15. Various differences between the templates for gluon and charm jets appear in different phase space regions. Also the most sofisticated one, the JC3, we do not consider as reliable. **therefore**, to avoid ambiguities, we **dropped the jet classification** to charm and gluon jets and in the final plots are the Monte Carlo events divided only to direct and resolved events, which is an unambiguous association based on the generator information.

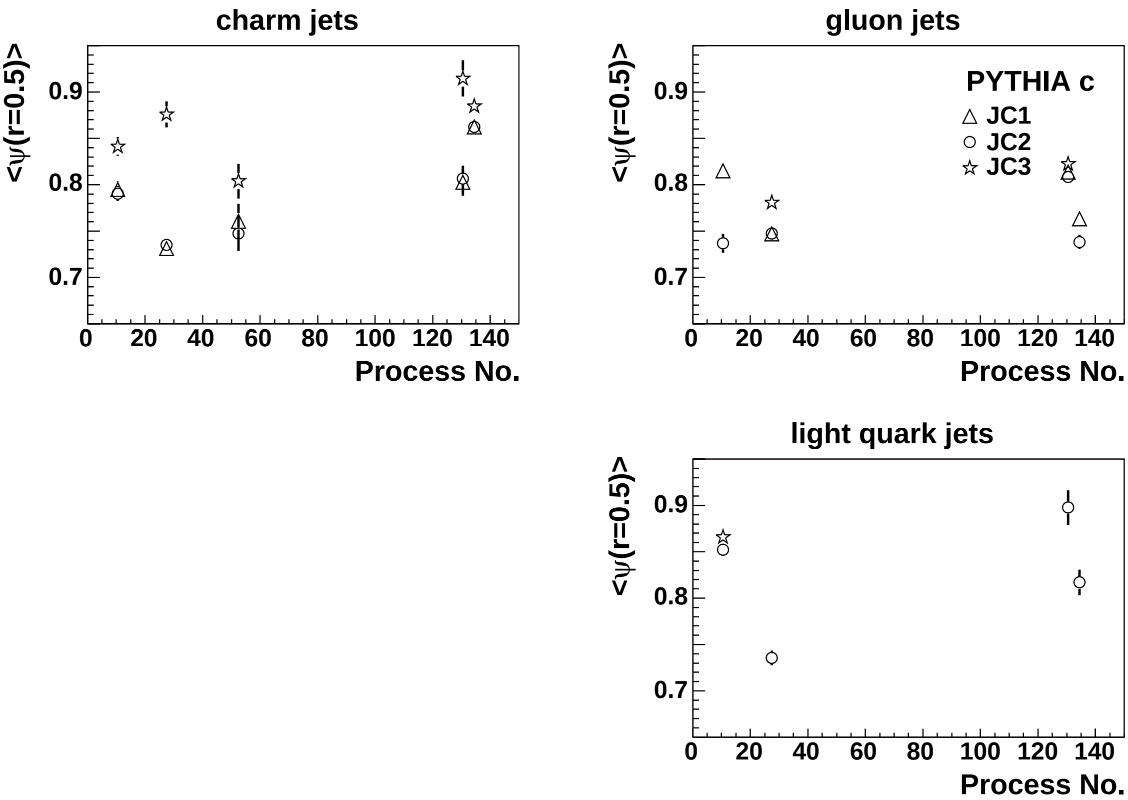

Figure A.15: *Comparison of the three jet classification methods JC1, JC2 and JC3. The mean integrated jet shape for the 'other jet' classified as charm (gluon, light quark) jet by the various methods is shown as a function of the process number (see table A.1). For an ideal classification, all charm jets would show up at one high constant value of $\langle\psi(r=0.5)\rangle$. Similarly, all gluon jets would group at one low value of $\langle\psi(r=0.5)\rangle$. Since the jet shape is independent of energy. This is not the case for any of the studied approaches, although the JC3 classification is clearly the best one.*

Remark on the Flavour Inclusive Sample

There was a suspicion that the observed discrepancies can be caused by the method itself. Therefore, a need to check the method on an independent sample led to a separate analysis. For this purpose the flavour inclusive dijet sample was chosen, which is dominated by light quark events. Results of the integrated jet shape studies of the flavour inclusive events are included in the result chapter of this thesis.

Appendix B

Tables of Results

This appendix contains tables with values of the measured data points with their uncertainties, which are presented in chapter 7. Results for the charm sample are given in tables B.1 and B.2, results for the flavour inclusive sample in tables B.3 and B.4. Values for the total, direct and resolved PYTHIA Monte Carlo predictions are listed, together with the ratios of the data over theory.

Charm Sample

$x_\gamma^{obs} \leq 0.75$

r	$\langle\psi(r)\rangle^{Data}$	$\langle\psi(r)\rangle^{MC}$	$\langle\psi(r)\rangle^{MC}_{dir}$	$\langle\psi(r)\rangle^{MC}_{res}$	$\frac{\langle\psi(r)\rangle^{Data}}{\langle\psi(r)\rangle^{MC}}$
0.1	$0.154 \pm 0.022 \pm 0.021$	0.120	0.145	0.115	1.29
0.2	$0.403 \pm 0.028 \pm 0.065$	0.324	0.373	0.314	1.24
0.3	$0.571 \pm 0.027 \pm 0.018$	0.506	0.554	0.497	1.13
0.4	$0.714 \pm 0.022 \pm 0.024$	0.650	0.693	0.642	1.20
0.5	$0.812 \pm 0.017 \pm 0.005$	0.761	0.792	0.756	1.07
0.6	$0.899 \pm 0.011 \pm 0.014$	0.843	0.868	0.839	1.07
0.7	$0.931 \pm 0.008 \pm 0.005$	0.903	0.920	0.900	1.03
0.8	$0.967 \pm 0.005 \pm 0.006$	0.948	0.957	0.946	1.02
0.9	$0.989 \pm 0.003 \pm 0.001$	0.979	0.983	0.978	1.01
1.0	$1.000 \pm 0.000 \pm 0.000$	1.000	1.000	1.000	1.00

$x_\gamma^{obs} > 0.75$

r	$\langle\psi(r)\rangle^{Data}$	$\langle\psi(r)\rangle^{MC}$	$\langle\psi(r)\rangle^{MC}_{dir}$	$\langle\psi(r)\rangle^{MC}_{res}$	$\frac{\langle\psi(r)\rangle^{Data}}{\langle\psi(r)\rangle^{MC}}$
0.1	$0.142 \pm 0.013 \pm 0.023$	0.171	0.182	0.128	0.83
0.2	$0.398 \pm 0.017 \pm 0.019$	0.428	0.452	0.336	0.93
0.3	$0.616 \pm 0.015 \pm 0.027$	0.620	0.647	0.516	0.99
0.4	$0.745 \pm 0.012 \pm 0.004$	0.749	0.772	0.659	0.99
0.5	$0.833 \pm 0.009 \pm 0.007$	0.834	0.853	0.764	1.00
0.6	$0.901 \pm 0.006 \pm 0.003$	0.894	0.906	0.845	1.01
0.7	$0.942 \pm 0.004 \pm 0.003$	0.935	0.943	0.903	1.02
0.8	$0.968 \pm 0.003 \pm 0.001$	0.965	0.970	0.947	1.00
0.9	$0.988 \pm 0.002 \pm 0.002$	0.986	0.988	0.977	1.00
1.0	$1.000 \pm 0.000 \pm 0.000$	1.000	1.000	1.000	1.00

Table B.1: *The mean integrated jet shape $\langle\psi(r)\rangle$ for the different values of the cone radius r at hadron level in two bins of the variable x_γ^{obs} as measured for the charm sample, inclusive the statistical and the systematical errors. The predictions of the charm PYTHIA MC simulation for all events, for direct events and for resolved events are also listed. In the last column the ratio of the mean jet shape in the data over the MC value is given. The errors for the Monte Carlo predictions are negligible. The values correspond to the points in figures 7.1 and 7.2.*

Bin	Center	$\langle\psi(0.5)\rangle^{Data}$	$\langle\psi(0.5)\rangle^{MC}$	$\langle\psi(0.5)\rangle^{MC}_{dir}$	$\langle\psi(0.5)\rangle^{MC}_{res}$	$\frac{\langle\psi(0.5)\rangle^{Data}}{\langle\psi(0.5)\rangle^{MC}}$
$-1.74 < \eta^{jet} \leq 0.1$	-0.44	$0.842 \pm 0.013 \pm 0.004$	0.832	0.850	0.754	1.01
$0.1 < \eta^{jet} \leq 0.9$	0.52	$0.825 \pm 0.014 \pm 0.009$	0.816	0.852	0.757	1.01
$0.9 < \eta^{jet} \leq 1.74$	1.29	$0.811 \pm 0.014 \pm 0.010$	0.794	0.842	0.761	1.02
$6.0 < p_t^{jet} \leq 8.5\,\mathrm{GeV}$	7.22	$0.813 \pm 0.014 \pm 0.011$	0.787	0.819	0.736	1.03
$8.5 < p_t^{jet} \leq 12.0\,\mathrm{GeV}$	10.13	$0.820 \pm 0.014 \pm 0.013$	0.813	0.848	0.754	1.01
$12.0 < p_t^{jet} \leq 24.0\,\mathrm{GeV}$	15.35	$0.858 \pm 0.013 \pm 0.009$	0.848	0.885	0.790	1.01
$6.0 < p_t^{jet} \leq 11.0\,\mathrm{GeV}$	8.80	$0.818 \pm 0.014 \pm 0.010$	0.803	0.831	0.739	1.02
$11.0 < p_t^{jet} \leq 17.0\,\mathrm{GeV}$	13.45	$0.824 \pm 0.014 \pm 0.013$	0.820	0.853	0.755	1.00
$17.0 < p_t^{jet} \leq 35.0\,\mathrm{GeV}$	22.68	$0.853 \pm 0.014 \pm 0.006$	0.817	0.867	0.768	1.04
$0.30 < x_\gamma^{obs} \leq 0.75$	0.57	$0.812 \pm 0.017 \pm 0.006$	0.761	0.792	0.756	1.07
$0.75 < x_\gamma^{obs} \leq 1.00$	0.89	$0.833 \pm 0.009 \pm 0.005$	0.834	0.853	0.764	1.00

Table B.2: *The mean integrated jet shape $\langle\psi(r = 0.5)\rangle$ for the different values of the variables η^{jet}, p_t^{jet}, E^{jet} of the 'other jet' and the variable x_γ^{obs} at hadron level as measured for the charm sample, inclusive the statistical and the systematical errors. The predictions of the charm PYTHIA MC simulation for all events, for direct events and for resolved events are also listed. In the last column the ratio of the mean jet shape in the data over the MC value is given. The errors for the Monte Carlo predictions are negligible. The values correspond to the points in figure 7.9.*

Flavour Inclusive Sample

$x_\gamma^{obs} \leq 0.75$

r	$\langle\psi(r)\rangle^{Data}$	$\langle\psi(r)\rangle^{MC}$	$\langle\psi(r)\rangle^{MC}_{dir}$	$\langle\psi(r)\rangle^{MC}_{res}$	$\frac{\langle\psi(r)\rangle^{Data}}{\langle\psi(r)\rangle^{MC}}$
0.1	$0.115 \pm 0.002 \pm 0.018$	0.124	0.161	0.121	0.93
0.2	$0.314 \pm 0.003 \pm 0.017$	0.328	0.402	0.324	0.96
0.3	$0.492 \pm 0.003 \pm 0.015$	0.511	0.587	0.506	0.96
0.4	$0.641 \pm 0.003 \pm 0.011$	0.654	0.718	0.650	0.98
0.5	$0.752 \pm 0.002 \pm 0.006$	0.761	0.811	0.758	0.99
0.6	$0.837 \pm 0.001 \pm 0.007$	0.843	0.875	0.841	0.99
0.7	$0.901 \pm 0.001 \pm 0.004$	0.904	0.923	0.903	1.00
0.8	$0.947 \pm 0.001 \pm 0.002$	0.948	0.961	0.947	1.00
0.9	$0.979 \pm 0.000 \pm 0.001$	0.979	0.984	0.978	1.00
1.0	$1.000 \pm 0.000 \pm 0.000$	1.000	1.000	1.000	1.00

$x_\gamma^{obs} > 0.75$

r	$\langle\psi(r)\rangle^{Data}$	$\langle\psi(r)\rangle^{MC}$	$\langle\psi(r)\rangle^{MC}_{dir}$	$\langle\psi(r)\rangle^{MC}_{res}$	$\frac{\langle\psi(r)\rangle^{Data}}{\langle\psi(r)\rangle^{MC}}$
0.1	$0.170 \pm 0.003 \pm 0.028$	0.169	0.194	0.136	1.00
0.2	$0.414 \pm 0.003 \pm 0.020$	0.413	0.457	0.353	1.00
0.3	$0.604 \pm 0.003 \pm 0.013$	0.598	0.643	0.537	1.01
0.4	$0.737 \pm 0.002 \pm 0.008$	0.728	0.766	0.677	1.01
0.5	$0.828 \pm 0.002 \pm 0.008$	0.819	0.848	0.781	1.01
0.6	$0.890 \pm 0.001 \pm 0.003$	0.883	0.903	0.856	1.01
0.7	$0.934 \pm 0.001 \pm 0.002$	0.928	0.941	0.911	1.01
0.8	$0.965 \pm 0.001 \pm 0.001$	0.961	0.968	0.951	1.00
0.9	$0.986 \pm 0.000 \pm 0.001$	0.984	0.987	0.980	1.00
0.1	$1.000 \pm 0.000 \pm 0.000$	1.000	1.000	1.000	1.00

Table B.3: *The mean integrated jet shape $\langle\psi(r)\rangle$ for the two jets with the highest p_t per event for the different values of the cone radius r at hadron level in two bins of the variable x_γ^{obs} as measured for the flavour inclusive sample, inclusive the statistical and the systematical errors. The predictions of the inclusive PYTHIA MC simulation for all events, for direct events and for resolved events are also listed. In the last column the ratio of the mean jet shape in the data over the MC value is given. The errors for the Monte Carlo predictions are negligible. The values correspond to the points in figures 7.7 and 7.8.*

Bin	Center	$\langle\psi(0.5)\rangle^{Data}$	$\langle\psi(0.5)\rangle^{MC}$	$\langle\psi(0.5)\rangle^{MC}_{dir}$	$\langle\psi(0.5)\rangle^{MC}_{res}$	$\frac{\langle\psi(0.5)\rangle^{Data}}{\langle\psi(0.5)\rangle^{MC}}$
$-1.74 < \eta^{jet} \leq 0.1$	-0.37	$0.822 \pm 0.002 \pm 0.003$	0.817	0.852	0.790	1.01
$0.1 < \eta^{jet} \leq 0.9$	0.49	$0.790 \pm 0.002 \pm 0.004$	0.785	0.844	0.762	1.01
$0.9 < \eta^{jet} \leq 1.74$	1.30	$0.748 \pm 0.003 \pm 0.012$	0.758	0.823	0.747	1.00
$6.0 < p_t^{jet} \leq 8.5\,\mathrm{GeV}$	7.23	$0.767 \pm 0.002 \pm 0.008$	0.776	0.828	0.756	1.00
$8.5 < p_t^{jet} \leq 12.0\,\mathrm{GeV}$	9.90	$0.795 \pm 0.002 \pm 0.005$	0.789	0.847	0.763	1.01
$12.0 < p_t^{jet} \leq 24.0\,\mathrm{GeV}$	15.00	$0.834 \pm 0.003 \pm 0.004$	0.827	0.879	0.799	1.01
$6.0 < p_t^{jet} \leq 11.0\,\mathrm{GeV}$	8.71	$0.792 \pm 0.002 \pm 0.004$	0.791	0.837	0.768	1.00
$11.0 < p_t^{jet} \leq 17.0\,\mathrm{GeV}$	13.53	$0.786 \pm 0.003 \pm 0.007$	0.792	0.853	0.763	0.99
$17.0 < p_t^{jet} \leq 35.0\,\mathrm{GeV}$	22.12	$0.776 \pm 0.003 \pm 0.010$	0.777	0.852	0.759	1.00
$0.30 < x_\gamma^{obs} \leq 0.75$	0.53	$0.759 \pm 0.002 \pm 0.008$	0.764	0.815	0.761	0.99
$0.75 < x_\gamma^{obs} \leq 1.00$	0.88	$0.828 \pm 0.002 \pm 0.006$	0.820	0.849	0.782	1.01

Table B.4: *The mean integrated jet shape $\langle\psi(r = 0.5)\rangle$ for the different values of the variables η^{jet}, p_t^{jet}, E^{jet} and the variable x_γ^{obs} at hadron level for the two jets with the highest p_t per event. as measured for the flavour inclusive sample, inclusive the statistical and the systematical errors. The predictions of the inclusive PYTHIA MC simulation for all events, for direct events and for resolved events are also listed. In the last column the ratio of the mean jet shape in the data over the MC value is given. The statistical errors for the Monte Carlo predictions are negligible. The values correspond to the points in figure 7.11.*

Appendix C

Jet Shape in Bins of η^{jet}, p_t^{jet}, E^{jet}

In chapter 7 measurements of the mean integrated jet shape $\langle\psi(r)\rangle$ at hadron level are presented as a function of the cone radius r in two bins of the x_γ^{obs} variable. In this appendix the picture is completed by the measurement of the jet shape as a function of r in bins of η^{jet}, p_t^{jet} and E^{jet}.

Detector Corrections

The method for calculating the detector corrections was discussed in section 6.5. In figure C.1 the detector corrections are shown for the integrated jet shape $\langle\psi(r)\rangle$ for the charm sample as function of the cone radius r in bins of η^{jet}, p_t^{jet} and E^{jet}. They are plotted separately for direct and resolved events to be able to estimate the differences between them. Corrections are obtained also using the charm PYTHIA MC. In figure C.2 the corresponding corrections for the flavour inclusive event sample are shown. These are obtained using the inclusive PYTHIA MC.

Generally, for both the charm and the flavour inclusive sample the corrections are largest at low cone radii and decrease as the cone radius increases. At cone radii $r \geq 0.3$ the corrections in all analysis bins are found to be smaller than 2 % for the total charm sample and smaller than 6 % for the total flavour inclusive event sample. For $r < 0.3$ the detector corrections deviate from unity considerably.

In the **charm event sample** the corrections for direct and resolved events are compatible for forward and backward rapidities. For central rapidities the corrections are larger for resolved events than for direct events. At low jet energies and momenta the corrections for direct and resolved events show a completely different behavior. While the former are lower than unity, the later are larger. The differences get smaller at higher jet energies.

In the **flavour inclusive event sample** the differences between the detector corrections for direct and resolved events are not significant in any η^{jet} bin, although for high η^{jet} they differ considerably. In the p_t^{jet} bins the detector correction for the flavour inclusive sample show a similar behavior as those for charm events. The behavior of the detector corrections for the flavour inclusive sample in bins of the jet energy is different from the ones observed in the charm event case.

Charm Sample

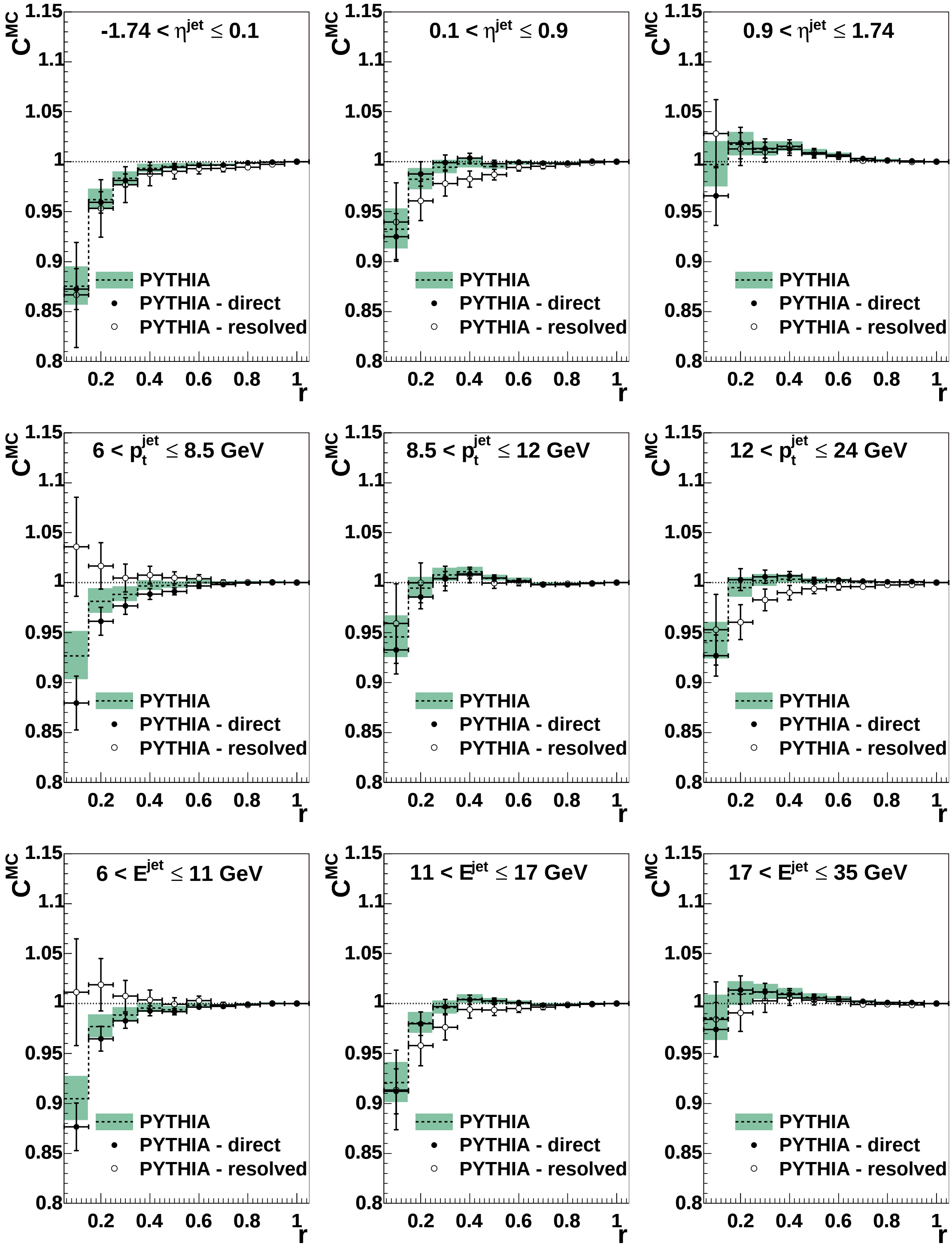

Figure C.1: *Detector corrections for the mean integrated jet shape $\langle\psi(r)\rangle$ for the 'other jet' in the charm sample as a function of the cone radius r in bins of η^{jet}, p_t^{jet} and E^{jet}. The corrections are calculated using the charm PYTHIA MC. The factors are shown for the total charm PYTHIA MC simulation and separately for the direct and resolved components. The shaded band and the error bars represent the statistical uncertainty of the MC.*

Flavour Inclusive Sample

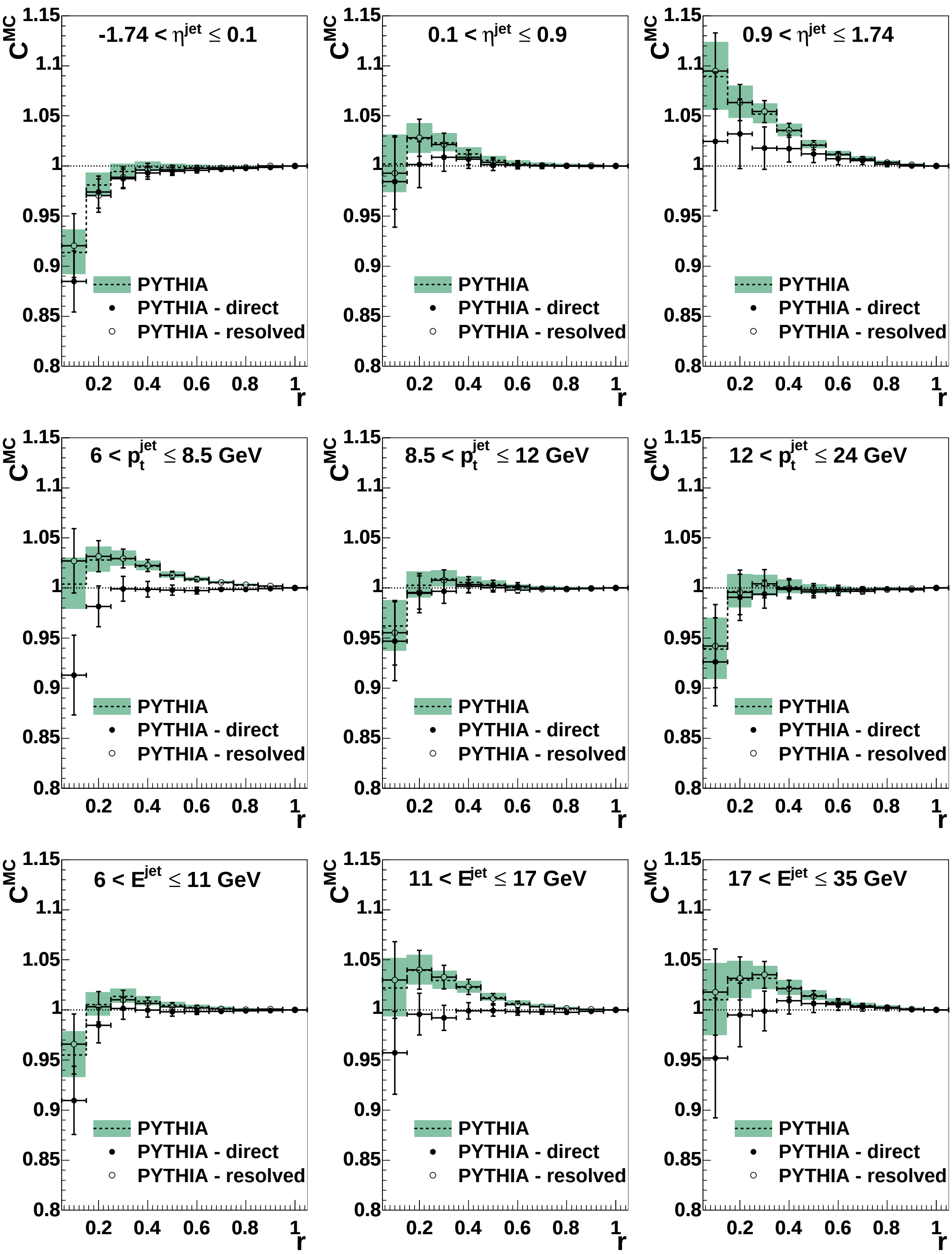

Figure C.2: *Detector corrections for the mean integrated jet shape $\langle\psi(r)\rangle$ for the two highest p_t jets in the flavour inclusive sample as a function of the cone radius r in bins of η^{jet}, p_t^{jet} and E^{jet}. The corrections are calculated using the inclusive PYTHIA MC. The factors are shown for the total inclusive PYTHIA MC simulation and separately for the direct and resolved components. The shaded band and the error bars represent the statistical uncertainty of the MC.*

Results of the Mean Integrated Jet Shape Measurements

Background corrected measurements of the mean integrated jet shape $\langle\psi(r)\rangle$ as function of the cone radius r for the **charm event sample** at hadron level in bins of η^{jet}, p_t^{jet} and E^{jet} are shown in figure C.3. To be able to compare the situation at different r, the measurements are shown as a ratio of the data over the total charm PYTHIA simulation. Additionally, the same analysis as for the data has been performed on the PYTHIA MC events. The curves direct and resolved events are shown separately, also as a ratio to the total charm PYTHIA MC. Only statistical errors of the data are shown.

While in the backward region the charm data are compatible with a pure direct sample, in the central and forward bin the presence of resolved events in the data is visible. The most significant differences between the direct and resolved MC curves with respect to the statistical error of the data can be observed for $r = 0.6 - 0.7$. The largest systematic differences between the data and the PYTHIA MC are found in the lowest p_t^{jet} bin and highest E^{jet} bin, consistent with the measurement of the jet shape at the fixed value of $r = 0.5$ presented in chapter 7. Especially at the lowest p_t^{jet} the data deviate from the overall PYTHIA prediction in course of the direct events.

The jet shapes measured in the **flavour inclusive event sample** in the same bins of η^{jet}, p_t^{jet} and E^{jet} are shown in figure C.4, relative to the total PYTHIA prediction. They are compared to the inclusive PYTHIA MC simulation. Integrated jet shapes for direct and resolved events are also shown separately. The data points are well described by the PYTHIA MC simulation. All the plots show that the flavour inclusive event sample is clearly dominated by the resolved events and the resolved event enrichment grows towards the forward region, and high energies.

Charm Sample

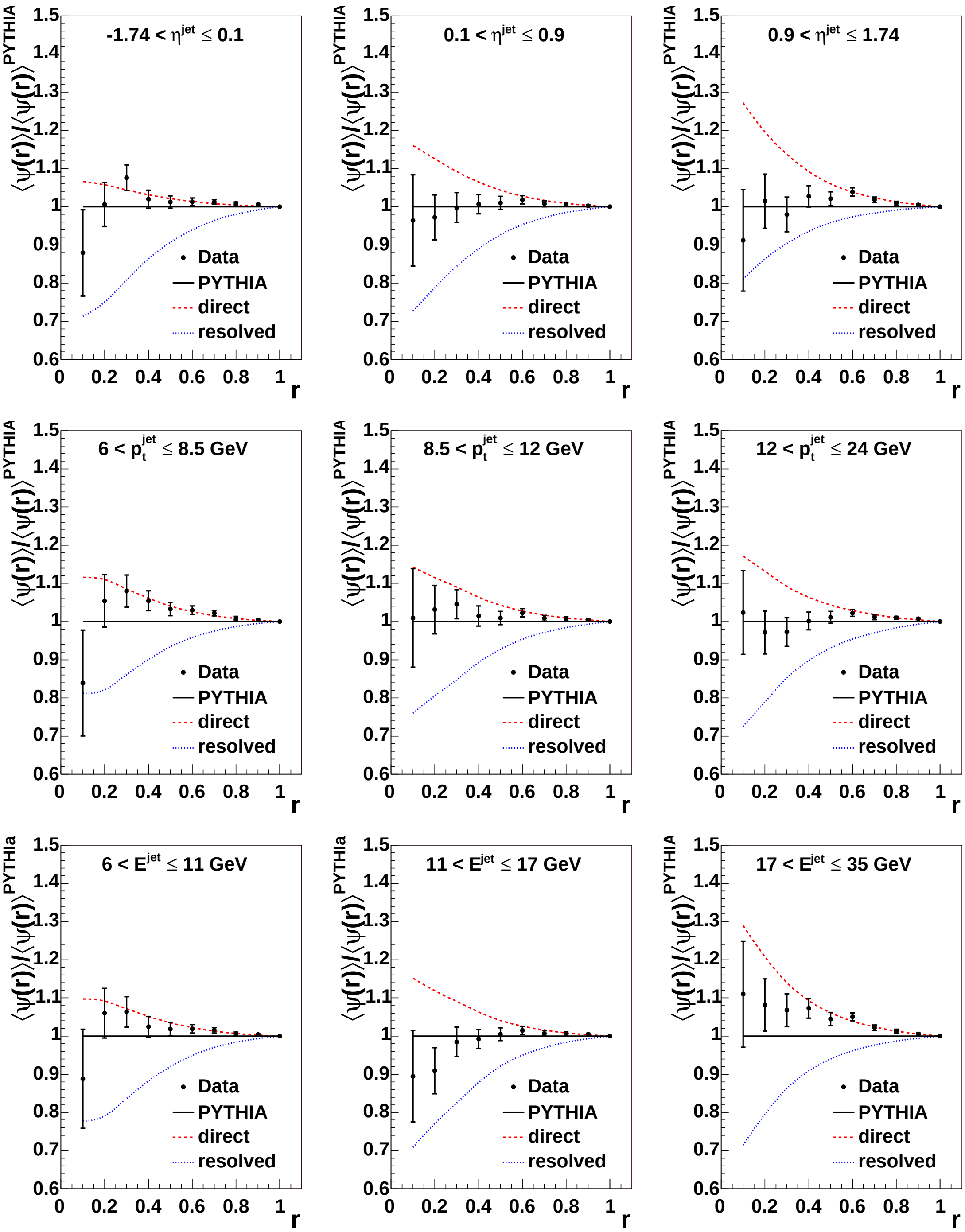

Figure C.3: *The ratio of the integrated jet shape $\langle\psi(r)\rangle$ for the 'other jet' in the charm event sample as a function of the cone radius r relative to the total charm PYTHIA MC. Measurements are performed in bins of η^{jet}, p_t^{jet} and E^{jet} and are corrected for detector effects. The MC predictions for direct events (dashed line) and resolved events (dotted line) are also shown relative to the total charm PYTHIA prediction (full line). The errors of the Monte Carlo predictions are negligible.*

Flavour Inclusive Sample

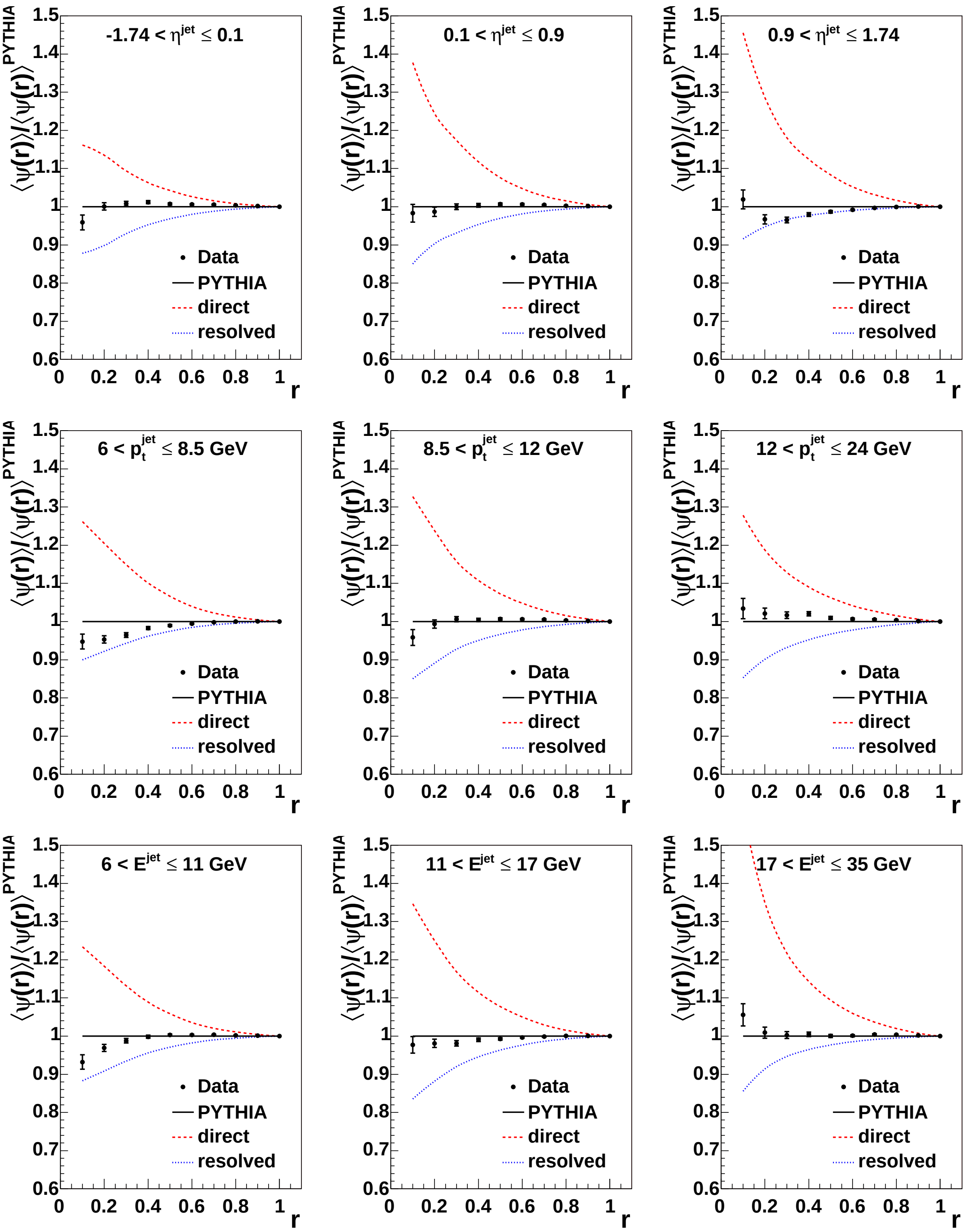

Figure C.4: *The ratio of the integrated jet shape $\langle\psi(r)\rangle$ for the two highest p_t jets in the flavour inlcusive event sample as a function of the cone radius r relative to the total inclusive PYTHIA MC. Measurements are performed in bins of η^{jet}, p_t^{jet} and E^{jet} and are corrected for detector effects. The MC predictions for direct events (dashed line) and resolved events (dotted line) are also shown relative to the total inclusive PYTHIA prediction (full line). The errors of the Monte Carlo predictions are negligible.*

Appendix D

The FMNR Program

The FMNR program [27] calculates total and exclusive cross sections for charm and beauty quark production in photoproduction at leading order (LO) and next-to-leading order (NLO) QCD.

Program Description

FMNR implements a **fixed order massive** calculation, which means that heavy quarks are not active flavors in the proton and the photon but are produced perturbatively in the hard subprocess, like e.g. boson-gluon fusion (BGF). This fixed flavour number scheme with three flavors is believed to be valid for the cases where the transverse momentum of the quark is of the same order of magnitude as the quark mass [37]. Here the mass of the heavy quark determines the scale near the threshold, enabling the description of the hard subprocess by perturbative QCD. Corrections to this scheme are expected in the domain of large p_t of the quarks, since terms of the form $\alpha_s^n log^n(p_t^q/m^q)$ (corresponding to n-gluon emissions) are not resummed [92]. This resummation is performed in **massless** calculations (not included in the FMNR program) where heavy quarks are considered to be massless and are active flavors in the photon and proton (see Fig. D.1).

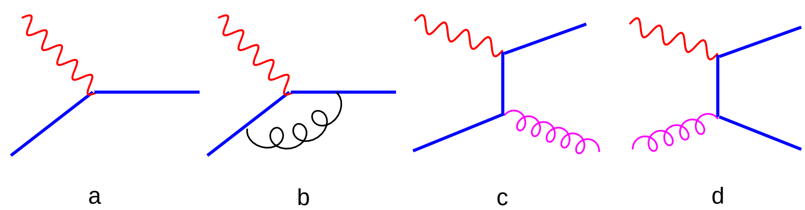

Figure D.1: *Feynman diagrams of the massless scheme. Only diagram d) is implemented in the FMNR program. Diagrams a), b) and c) are not implemented, since the proton does not contain charm or beauty quarks in the massive scheme.*

In photoproduction the incoming almost real photon may fluctuate into a hadronic state before undergoing a hard collision. The corresponding contribution to the cross section is referred to as **resolved** or hadronic, in contrast with the case where the photon interacts directly with the proton, called **direct** or pointlike. Diagrams a) and b) from Fig. 1.9 are implemented in the FMNR program. Diagrams c) - e) are not implemented, since there the heavy quarks come from the photon. A differential photon-hadron cross section can be written as a sum of direct and resolved photon contributions [37]:

$$d\sigma^{\gamma p}(P_\gamma, P_p) = d\sigma^{\gamma p}_{dir}(P_\gamma, P_p) + d\sigma^{\gamma p}_{res}(P_\gamma, P_p),$$

where P_γ and P_p denote the momenta of the photon and proton respectively. The two contributions can be expressed as

$$d\sigma^{\gamma p}_{dir}(P_\gamma, P_p) = \sum_i \int dx\ f^p_j(x, \mu_F)\ d\hat{\sigma}_{\gamma j}(P_\gamma, xP_p, \alpha_s(\mu_R), \mu_R, \mu_F, \mu_\gamma)$$

$$d\sigma^{\gamma p}_{res}(P_\gamma, P_p) = \sum_{ij} \int dx\ dy\ f^\gamma_i(y, \mu_\gamma)\ f^p_j(x, \mu'_F)\ d\hat{\sigma}_{ij}(yP_\gamma, xP_p, \alpha_s(\mu'_R), \mu'_R, \mu'_F, \mu_\gamma)$$

here f^γ_i and f^p_j are the photon and proton parton density functions. The separation of a cross section into a direct and resolved component is ambiguous beyond leading order, because different choices of the factorisation schemes lead to different definitions of the two components [37]. The contribution from resolved processes to the total cross section is about 5 % in the FMNR calculation, depending on the selected phase-space.

In FMNR the following **partonic subprocesses** relevant for heavy quark photoproduction at the order $\alpha_{em}\alpha_s^2$ are implemented:

$$\gamma p \to Q\bar{Q}$$
$$\gamma p \to Q\bar{Q}g$$
$$\gamma p \to Q\bar{Q}q$$

where $Q(\bar{Q})$ denotes a heavy quark (antiquark) and q a light quark. γ stands for the photon, p for the proton and g for gluon. It is possible to calculate the cross section in LO or NLO, where NLO refers to a sum of contributions of leading order and next-to-leading order diagrams. The divergences of the coefficient functions calculated to the order $O(\alpha_s^2)$ due to **soft gluon emissions** (Fig. D.2) are compensated by contributions from **virtual gluon exchange** (Fig. D.3) using the subtraction method.

Available are routines to compute **total**, **single inclusive** (considering one hard parton) and **double differential** (considering both hard partons) cross sections. In leading order partons can be generated only in one plane without influence on the important physical distributions like p_t or θ of the parton. Here the $p_y - p_z$ plane was chosen and partons are generated in LO with $p_x = 0$. In NLO there is a small spread around zero due to possible light parton (mainly gluon) radiation.

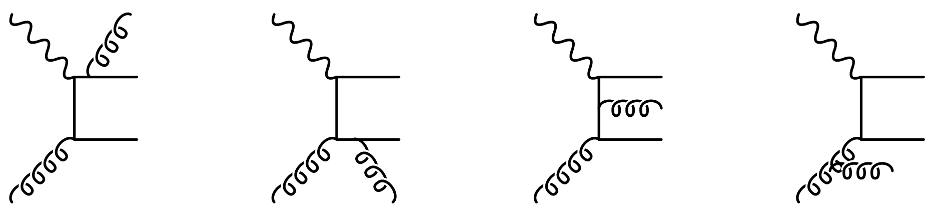

Figure D.2: *Gluon radiation corrections considered in direct NLO.*

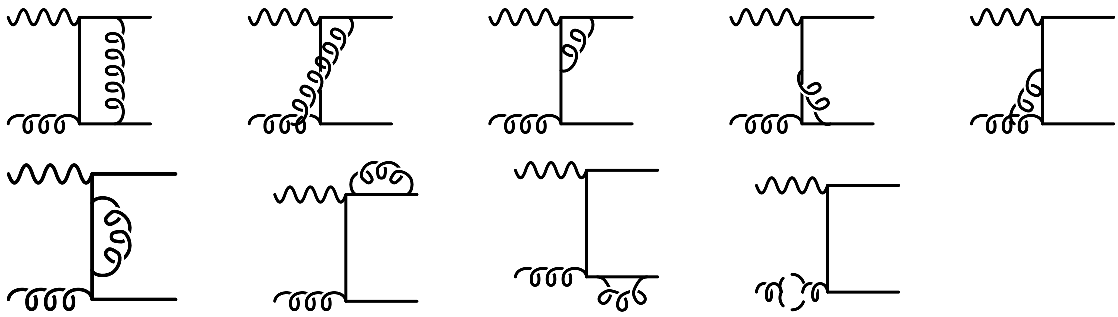

Figure D.3: *Virtual corrections considered in direct NLO.*

The FMNR program is an **cross section integration program**[1], not an event generator like PYTHIA. As explained in [26], cross section integration programs use a prescription for calculating a cross section of the form:

$$d\sigma(ep \to X) = f(\theta, \phi, ...), \tag{D.1}$$

where f includes matrix elements and phase space factors. First the phase space has to be sampled, which in this case is a multi-dimensional hypercube which spans over all of the degrees of freedom (for example 2-D space $-1 < \cos\theta < 1,\ 0 < \phi < 2\pi$). The procedure of choosing $cos\theta$ and ϕ is said to define candidate event. The candidate event's differential cross section, called **event weight**, $d\sigma$ is calculated from equation D.1 and is directly related to the probability of this event occurring. The average over many candidate event weights $\langle d\sigma \rangle$ is an approximation of the integral $\int d\sigma$ and converges to the calculated cross section.

At this point the candidate events are distributed flat in phase space and there is no physics information in the distributions. This is contained in the event weights which can be used to fill histograms representing physical distributions. A histogram of some relevant observable (e.g. p_t of the quark) is filled using the event weights from a large number of candidate events. In the limit of an infinite number of candidate events, the distribution is exactly the same, as predicted by equation D.1. Since in the leading order only positive weights occur, in NLO also negative weights are needed. The combination of events with both positive and negative weights then gives finite results (positive or negative).

The problems arising from **soft and collinear divergences** are dealt with by generating an appropriate sequence of **correlated events**, so that the cancellation of collinear and soft singularities takes place for any well-defined physical distribution (i.e. distributions that are insensitive to soft and collinear emission). It does not require any artificial regularisation of the cross section [36].

[1]The program VEGAS [93] is used for integration.

The **renormalisation scale** in FMNR for single differential cross sections is given by $\mu_R = \sqrt{m_q^2 + p_{t\,q}^2}$ and in the double differential case by $\mu_R = \sqrt{m_q^2 + (p_{t\,q1}^2 + p_{t\,q2}^2)/2}$. The FMNR choice for the **factorisation scale** is $\mu_F = 2\mu_R$ for charm and $\mu_F = \mu_R$ for beauty.

The **Weizsäcker-Williams formula** [94] is used[2] to describe the photon flux from the electron:

$$f_\gamma^e(y) = \frac{\alpha_{em}}{2\pi}\frac{(1+(1-y)^2)}{y} log\frac{Q_{eff}^2}{m_e y^2} + 2(1-y)(\frac{m_e^2 y}{Q_{eff}^2} - \frac{1}{y}). \tag{D.2}$$

Application for the Prediction of the $B \rightarrow \mu X$ Cross Section

The FMNR program was used to calculate total and differential NLO predictions in the visible range for the analysis of beauty production using events with muons and jets [70].

The **quantities available for the user** are the event weight, inelasticity y and x_{gluon}. Furthermore the transverse momentum vector (p_x, p_y) and rapidity of the heavy quark, heavy antiquark and for the light parton in the e^+p rest frame are provided. Any other quantities have to be calculated from these variables.

For the $B \rightarrow \mu X$ analysis, in the first step four momenta of the partons (two or three) are passed to the **jet finding routine** JETFIND, which uses the jet finder from HZTOOL [95]. The jet finder contains the k_t-clustering algorithm with the p_t-weighted recombination scheme, used in the laboratory frame. The jet algorithm and the recombination scheme should be the same as used in the data analysis and in the MC treatment. Then all possible effects coming from the jet algorithm are 'absorbed' into the hadronisation corrections. We didn't observe any significant differences on the NLO level when changing between the E-recombination scheme and p_t-recombination scheme. The output of the jet finder is the number of found jets as well as the kinematic variables of the found jets. Only if the third parton ends up in a separate jet it does make sense to ask for its kinematics.

In the second step a **semileptonic decay of the heavy hadron** coming from the heavy quark is simulated. For that purpose the four momenta of both original quarks are modified such, that they represent the four momenta of B-hadrons[3]. The Peterson fragmentation function with the parameters $\epsilon_b = 0.0033$ and $\epsilon_c = 0.035$ is used in a frame where $p_z^{q1} = -p_z^{q2}$. Subsequently the momentum of the hadron is modified[4] to represent the four momentum of the muon coming from the semimuonic decay. In the hadron rest frame, where the decay is isotropic, ϕ and $\cos\theta$ are randomly chosen, as well as the absolute value of the momentum (according to the muon momentum spectrum, which is adopted from the JETSET simulation). Direct decays $b \rightarrow \mu$, cascade decays $b \rightarrow c \rightarrow \mu$ or a combination of both can be chosen. A Lorentz boost back into the laboratory frame is performed then. Afterwards cuts on the p_t and η of the muon can be imposed.

[2] The Weizsäcker-Williams formula is implemented in the function PHDISTR.

[3] The fragmentation is implemented in the routine FRAGM.

[4] The semileptonic decay of the heavy hadrons is implemented in the routine SEMDEC.

In order to obtain the muon cross section, the right approach is to let both hadrons decay with muons in the final state using the appropriate branching ratio. The processes listed in table D.1 are considered. The value for the branching ratio used here, 0.21, is close to the sum of branching ratios of the mentioned processes (0.2105) and also corresponds to the value from PYTHIA (0.207).

In the FMNR program it is possible to choose a **proton parton density funtion**, for example CTEQ5D. One can choose between the DIS or $\overline{MS}$ scheme according to the used PDF. The **photon PDFs** are needed only in the resolved case, in the direct case the Weizsäcker-Williams Approximation (equation D.2) is used. The photon structure functions integrated over the photon flux, called **electron structure functions**, have to be determined within a given visible range (Q^2, y). In the resolved case the variable y is not directly accessible. So there is **no possibility to cut explicitly on y** of the photon since this cut is convoluted with the Q^2 cut in the photon PDF.

The unavailability of y causes an additional difficulty in the calculation of the variable x_γ^{obs}. Partons coming from the photon are generated via the photon structure function, not via photon generation. So it is not possible to use directly the formula 4.12 to compute the x_γ^{obs}. Neither is it possible to use

$$x_\gamma^{obs} = \frac{\sum_{2\ jets}(E - p_z)}{\sum_{all\ jets}(E - p_z)}, \tag{D.3}$$

since the photon remnant is not simulated. Instead one can produce results for resolved events by using the γp mode and sampling the y distribution in separate calculations with the appropriate electron structure functions. In that case it is possible to use equation 4.12.

The **cross section** can be calculated as integral of any differential distribution (histogram filled with the event weight) on the appropriate level (e.g after jet cuts or after muon cuts). The result is in μb.

To obtain the **uncertainty of the calculation**, the standard variations in the $B \to \mu X$ analysis are performed simultaneously. For $m_b = 4.5 - 5.0\,\mathrm{GeV}$, the scales are varied by the factors of 0.5-2.0. For the PDF uncertainty we assign 8 % and add it in quadrature. According to our experience, a linear addition of varied values gives in a good approximation the same value as simultaneous variations up ($m_b = 4.5\,\mathrm{GeV}$ and multiplication of scales by factor of 0.5) and down ($m_b = 5.0\,\mathrm{GeV}$ and multiplication of scales by factor of 2.0). The separate variation of mass and scales and quadratic addition gives lower values of uncertainties.

More details concerning the practical usage of the FMNR program can be found in [96].

Process	Branching ratio
$b \to \mu$	0.1095
$b \to \bar{c} \to \mu$	0.08
$b \to c \to \mu$	0.016
$b \to \tau \to \mu$	0.0043
$b \to J/\psi \to \mu X$	0.0007

Table D.1: *Decays of beauty flavored hadrons including a muon in the final state.*

Acknowledgments

At this place I would like to thank everybody who supported me during my work on this thesis and/or helped me in some way.

First of all I thank Prof. Dr. Beate Naroska for offering me the opportunity to become a member of the group of Hamburg University and to work on the H1 experiment. At the same time I thank her for the many ideas during the whole three years of my stay at DESY as well as for her careful reading of the thesis draft.

Prof. Dr. Peter Schleper I wish to thank for his readiness to examine this work.

I would like to thank Dr. Carsten Niebuhr for accepting me to work within the FH1 group and DESY for the financial support to participate in summer schools and conferences.

My thanks go to all the members of the H1 collaboration, especially the members of the heavy flavour group, who contributed with ideas and opinions to the analysis presented in this thesis. I am thankful to Dr. Olaf Behnke for his enthusiasm for this analysis, fruitful discussions and and his willingness in answering all my questions.

I would like to thank Dr. Juraj Braciník, Dr. Jörg Gayler and Dr. Hannes Jung for the proof-reading of the manuscript of this thesis.

Further thanks go to Lars Finke, my office colleague, for his helpfulness and discussions in the course of solving the daily working problems as well as for the friendly and quiet working atmosphere in our office. Henning Lüders and other present and previous members of the H1-Uni group I thank for the company through my three years at DESY.

A special thank belongs to Rainer for his untiring support in all the difficult situations which appeared. The discussions with him and his helpful physics tips as well as the careful proof-reading of the manuscript of the thesis were of big importance for this work.

Moja najväčšia vďaka patrí mojej najbližšej rodine, ktorá ma neúnavne podporovala, napriek vzdialenosti stála vždy pri mne a bezvýhradne vo mňa verila v každej situácii.

Bibliography

[1] Mark I Collaboration, G. Hanson *et al.*, *Evidence for Jet Structure in Hadron Production by e^+e^- Annihilation*, Phys. Rev. Lett. **35** (1975) 1609.

[2] TASSO Collaboration, R. Brandelik *et al.*, *Evidence for Planar Events in e^+e^- Annihilation at High Energies*, Phys. Lett. **86B** (1979) 243.
MARK-J Collaboration, D. P. Barber *et al.*, *Discovery of Three-Jet Events and a Test of Quantum Chromodynamics at PETRA*, Phys. Rev. Lett. **43** (1979) 830.
PLUTO Collaboration, C. Berger *et al.*,*Evidence for Gluon Bremsstrahlung in e^+e^- Annihilation at High Energies*, Phys. Lett. **86B** (1979) 418.
JADE Collaboration, W. Bartel *et al.*, *Observation of Planar Three-Jet Events in e^+e^- Annihilation and Evidence for Gluon*, Phys. Rev. Lett. **91B** (1980) 142.

[3] Particle Data Group, S. Eidelman *et al.*, *The Review of Particle Physics*, Phys. Lett. **B592** (2004 and 2005) 1.

[4] J. E. Augustin *et al.*, *Discovery of a Narrow Resonance in e^+e^- Annihilation*, Phys. Rev. Lett. **33** (1974) 1406.

[5] ZEUS Collaboration, *Precision Measurements of α_s at HERA*, proceedings of the DIS 2005, Madison, Wisconsin, USA, arXiv:hep-ex/0506035.

[6] R. P. Feynman, *Very High Energy Collisions of Hadrons*, Phys. Rev. Lett. **23** (1969) 1415;
J. D. Bjorken, *Asymptotic Sum Rules at Infinite Momentum*, Phys. Rev. **179** (1969) 1547.

[7] J. C. D. Collins, D. E. Soper and G. Sterman, *Factorisation for Short Distance Hadron-Hadron Scattering*, Nucl. Phys. **B261** (1985) 104.

[8] L. Lai *et al.*, *Global QCD Analysis of Parton Structure of the Nucleon: CTEQ5 Parton Distributions*, arXiv:hep-ph/9903282.

[9] F. Lenz, H. Gießhammer, D. Stoll, *Lectures on QCD - Applications*, Springer, Berlin/Heidelberg/New York, 1999.

[10] V. N. Gribov and L. N. Lipatov, *Deep Inelastic e- p Scattering in a Perturbative Theory*, Sov. J. Nucl. Phys. **15** (1972) 438;
V. N. Gribov and L. N. Lipatov, *e^+e^- Pair Annihilation and Deep Inelastic ep Scattering in Perturbation Theory*, Sov. J. Nucl. Phys. **15** (1972) 675;
L. N. Lipatov, *The Parton Model and Perturbation Theory*, Sov. J. Nucl. Phys. **20** (1975) 94;
G. Altareli and G. Parisi, *Asymptotic Freedom in Parton Language*, Nucl. Phys.

B126 (1977) 298;
Y. L. Dokshitzer, *Calculation of Structure Functions of Deep-inelastic Scattering and e^+e^- Annihilation by Perturbation Theory in Quantum Chromodynamics*, Sov. Phys. JETP **46** (1977) 641.

[11] E. A. Kuraev, L. N. Lipatov and V. S. Fadin, *The Pomeranchuk Singularity in Non-abelian Gauge Theories*, Sov. Phys. JETP **45** (1977) 199;
I. I. Balitsky and L. N. Lipatov, *The Pomeranchuk Singularity in Quantum Chromodynamics*, Sov. J. Nucl. Phys. **28** (1978) 822.

[12] M. Ciafaloni, *Coherence Effects in Initial Jets At Small Q^2/s*, Nucl. Phys. **B296** (1988) 49;
S. Catani, F. Fiorani and G. Marchesini, *QCD Coherence in Initial State Radiation*, Phys. Lett. **B234** (1990) 339;
Small-x Behavior of Initial State Radiation in Perturbative QCD, Nucl. Phys. **B336** (1990) 18;
G. Marchesini, *QCD Coherence in the Structure Function and Associated Distributions at Small x*, Nucl. Phys. **B445** (1995) 49.

[13] H1 Collaboration, C. Adloff *et al.*, *Forward Jet and Particle Production at HERA*, Nucl. Phys. **B538** (1999) 3, arXiv:hep-ex/9809028.

[14] H1 Collaboration, *Forward Jet Production at HERA*, Proceedings of the Symposium on Lepton-Photon Interactions at High Energy, Uppsala, 2005.

[15] L. M. Jones and H. W. Wyld, *Charmed-Particle Production by Photon-Gluon Fusion*, Phys. Rev. **D17** (1978) 159.

[16] B. Andersson, G. Gustafson, G. Ingelman and T. Sjöstrand, *Parton Fragmentation and String Dynamics*, Phys. Rept. **97** (1983) 31.

[17] C. Peterson, D. Schlatter, I. Schmitt, and P. M. Zerwas, *Scaling Violations in Inclusive e^+e^- Annihilation Spectra*, Phys. Rev. **D27** (1983) 105.

[18] P. Nason and C. Oleari, *A Phenomenological Study of Heavy-Quark Fragmentation Functions in e^+e^- Annihilation*, Nucl. Phys. **B565** (2000) 245, arXiv:hep-ph/9903541.

[19] R. K. Ellis, W. J. Stirling and B. R. Webber, *QCD and Collider Physics*, Cambridge University Press (1996).

[20] DELPHI Collaboration, P. Abreu *et al.*, *The Scale Dependence of the Hadron Multiplicity in Quark and Gluon Jets and a Precise Determination of C_A/C_F*, Phys. Lett. **B449** (1999) 383.

[21] OPAL Collaboration, G. Abbiendi *et al.*, *Experimental Properties of Gluon and Quark Jets from a Point Source*, Eur. Phys. J. **C11** (1999) 217, arXiv:hep-ex/9903027.

[22] G. Sterman and S. Weinberg, *Jets form Quantum Chromodynamics*, Phys. Rev. Lett. **39** (1977) 1436.

[23] OPAL Collaboration, G. Alexander *et al.*, *A Comparison of b and (u d s) Quark Jets to Gluon Jets*, Z. Phys. **C69** (1996) 543.

[24] ZEUS Collaboration, M. Derrick *et al.*, *Measurement of Multiplicity and Momentum Spectra in the Current Fragmentation Region of the Breit Frame at HERA*, Z. Phys. **C67** (1995) 93, arXiv:hep-ex/9501012.

[25] TASSO Collaboration, M. Althoff *et al.*, *Properties of Charm Jets Produced in e^+e^- Annihilation near* 34 GeV, Phys. Lett. **135B** (1984) 243.

[26] M. A. Dobbs *et al.*, *Les Houches Guidebook to MC Generators for Hadron Collider Physics*, presented at the workshop 'Physics at TeV Colliders', Les Houches, France, May 2003, arXiv:hep-ph/0403045.

[27] S. Frixione, M. L. Mangano, P. Nason, G. Ridolfi, *Total Cross Sections for Heavy Flavour Production at HERA*, Phys. Lett. **B348** (1995) 633.

[28] B. W. Harris and J. Smith, *Heavy Quark Correlations in Deep Inelastic Electroproduction*, Nucl. Phys. **B452** (1995) 109, arXiv:hep-ph/9503484.

[29] W.-K. Tung, S. Kretzer and C. Schmidt, *Open Heavy Flavor Production in QCD - Conceptual Framework and Implementation Issues*, J. Phys. **G28** (2002) 983, arXiv:hep-ph/0110247.

[30] H1 Collaboration, A. Aktas *et al.*, *Measurement of $F_2^{c\bar{c}}$ and $F_2^{b\bar{b}}$ at High Q^2 using the H1 Vertex Detector at HERA*, Eur. Phys. J. **C40** 349 (2005), arXiv:hep-ex/0411046.

[31] T. Sjostrand, *High-Energy Physics Event Generation with PYTHIA 5.7 and JETSET 7.4*, Comput. Phys. Commun. **82** (1994) 74.

[32] R. Brun *et al.*, *GEANT 3 Users Guide*, (1987) CERN-DD/EE/84-1;
CERN, *GEANT, Detector Description and Simulation Tool*, CERN Program Library, Long Writeup W5013 (1993), `http://wwwasd.web.cern.ch/wwwasd/geant/`.

[33] H. Jung and G. P. Salam, *Hadronic Final State Predictions from CCFM: The Hadron-Level Monte Carlo Generator CASCADE*, Eur. Phys. J. **C19** (2001) 351, arXiv:hep-ph/0012143.

[34] H. Jung, *The CCFM Monte Carlo Generator CASCADE*, Comput. Phys. Commun. **143** (2002) 100, arXiv:hep-ph/0109102.

[35] M. Glück, E. Reya and A. Vogt, *Parton Structure of the Photon Beyond the Leading Order*, Phys. Rev. **D45** (1992) 3986;
M. Glück, E. Reya and A. Vogt, *Photonic Parton Distributions*, Phys. Rev. **D46** (1992) 1973.

[36] S. Frixione, M. L. Mangano, P. Nason, G. Ridolfi, *Heavy-Quark Correlations in Photon-Hadron Collisions*, Nucl. Phys. **B412** (1994) 225, arXiv:hep-ph/9304289.

[37] G. Ridolfi, *Photoproduction of Heavy Quarks at HERA*, J. Phys. **G25** (1999) 1313.

[38] ZEUS Collaboration, S. Chekanov *et al.*, *Dijet Angular Distributions in Photoproduction of Charm at HERA*, Phys. Lett. **B565** (2003) 87, arXiv:hep-ex/0302025.

[39] H1 Collaboration, *Photoproduction of $D^{*}\pm$ Mesons Associated with a Jet at HERA*, XXII International Symposium on Lepton-Photon Interactions at High Energy, June 30 (2005), Uppsala.

[40] LEP Heavy Flavour Working Group, *Input Parameters for the LEP/SLD Electroweak Heavy Flavour Results for Summer 1998 Conferences*, LEP note, January 1998, LEPHF/98-01.

[41] O. Behnke, private communication, 2005.

[42] J. Kroseberg, *A Measurement of Beauty Production in High-Energy Positron-Proton Scattering*, Dissertation, Universität Zürich, December 2002.

[43] CDF Collaboration, F. Abe *et al.*, *A Measurement of Jet Shapes in $p\bar{p}$ Collisions at $\sqrt{s}$ = 1.8 TeV*, Phys. Rev. Lett. **70** (1993) 713.

[44] H1 Collaboration, C. Adloff *et al.*, *Measurement of Internal Jet Structure in Dijet Production in Deep-Inelastic Scattering at HERA*, arXiv:hep-ex/9901010.

[45] ZEUS Collaboration, S. Chekanov *et al.*, *Substructure Dependence of Jet Cross Sections at HERA and Determination of α_s*, arXiv:hep-ex/0407050.

[46] ZEUS Collaboration, *Measurements of Jet Substructure in Inclusive and Charm-Induced Dijet Photoproduction at HERA*, proceedings of the EPS 2001, Budapest.

[47] H1 Collaboration, I. Abt *et al.*, *The Tracking, Calorimeter and Muon Detectors of the H1 Experiment at HERA*, Nucl. Instrum. Meth. **A386** (1997) 310 and 348.

[48] H1 Collaboration, *H1 Track Detectors*, `http://www-h1.desy.de/h1det/tracker.`

[49] D. Pitzl *et al.*, *The H1 Silicon Vertex Detector*, Nucl. Instrum. Meth. **A454**, (2000) 334, arXiv:hep-ex/0002044.

[50] H1 Calorimeter Group, B. Andrieu *et al.*, *The H1 Liquid Argon Calorimeter System*, Nucl. Instrum. Meth. **A336**, (1993) 460.

[51] H1 SPACAL Group, R. D. Apphun *et al.*, *The H1 Lead/Scintilating-Fibre Calorimeter*, Nucl. Instrum. Meth. **A386**, (1997) 397.

[52] H1 Collaboration, *The Central Muon Detector of H1*, `http://www-h1.desy.de/h1/www/h1det/muon/c_muon/digmuohome.html`.

[53] H. Bethe, W. Heitler, *On the Stopping of Fast Particles and on the Creation of Positive Electrons*, Proc. Roy. Soc. **A146** (1934) 83.

[54] H1 Collaboration, S. Aid et al., *Luminosity Measurement in the H1 Experiment at HERA*, contributed paper pa17-026 to ICHEP 1996, Warsaw.

[55] H1 Collaboration, *H1REC: Reconstruction Program*, H1 internal documentation, `https://www-h1.desy.de/icas/imanuals/h1rec/h1rec9/h1rec.html`.

[56] The H1 OO Group, *The H1 OO Physics Analysis Project*, H1 internal documentation, `https://www-h1.desy.de/icas/oop/`.

[57] L. West, *How to use the Heavy Flavour Working Group Track, Muon and Electron Selection Code*, H1 internal software manual, 1997.

[58] S. Schiek, *Untersuchung der Inelastischen Photoproduction von J/ψ Mesonen im H1-Detektor bei HERA*, Dissertation, December 1996.

[59] B. Naroska, S. Schiek, G. Schmidt, *Lepton identification in the H1 Detector at Low Momenta*, H1 internal note (1997), H1-05/97-518.

[60] P. Bruel, *Recherche d'interactions au-dela du Modele Standard a HERA*, Dissertation, University Paris XI, Orsay, May 1998.

[61] M. Peez, B. Portheault and E. Sauvan, *An Energy Flow Algorithm for Hadronic Reconstruction in OO: Hadroo2*, H1 internal note (2005), H1-01/05-616.

[62] J. E. Huth *et al.*, *Proceedings of the 1990 Summer Study on High Energy Physics*, Snowmass, Colorado, edited by E. L. Berger, World Scientific, Singapore, (1992) 134.

[63] JADE Collaboration, W. Bartel *et al.*, *Experimental Studies on Multi - Jet Production in e^+e^- Annihilation at Petra Energies*, Z. Phys. **C33** (1986) 23;
S. Bethke et al., *Experimental Investigation of the Energy Dependence of the Strong Coupling Strength*, Phys. Lett. **213B** (1988) 235.

[64] S. Catani, Y. L. Dokshitzer, M. H. Seymour and B. R. Webber, *Longitudinally-Invariant $k_\perp$ Clustering Algorithms for Hadron-Hadron Collisions*, Nucl. Phys. **B406** (1993) 187.

[65] M. H. Seymour, *Searches for New Particles Using Cone and Cluster Jet Algorithms: a Comparative Study*, Z. Phys. **C62** (1994) 127.

[66] J. M. Butterworth, J. P. Couchman, B. E. Cox and B. M. Waugh, *KtJet: A C++ Implementation of the $k_\perp$ Clustering Algorithm*, Comput. Phys. Commun. **153** (2003) 85, arXiv:hep-ph/0210022.

[67] S. D. Ellis and D. E. Soper, *Successive Combination Jet Algorithm for Hadron Collisions*, Phys. Rev. **D48** (1993) 3160, arXiv:hep-ph/9305266.

[68] M. H. Seymour, *Jets in QCD*, arXiv:hep-ph/9506421.

[69] R. Brun *et al.*, *Root, An Object-Oriented Data Analysis Framework*, `http://root.cern.ch/`.

[70] H1 Collaboration, A. Aktas *et al.*, *Measurement of Beauty Production at HERA Using Events with Muons and Jets*, arXiv:hep-ex/0502010.

[71] T. Wolff *et al.*, *A Driftchamber Track Finder for the First Level Trigger of H1*, H1 internal note (1992), H1-02/92-213.

[72] J. Reidberger, *The H1 Trigger with Emphasis on Tracking Triggers*, H1 internal note (1995), H1-01/95-419.

[73] H. Beck, *Principles and Operation of the z-Vertex Trigger*, H1 internal note (1996). H1-05/96-479.

[74] J. Wagner, *Charm and Beauty Production at HERA with D^*-Muon Events*, Dissertation, Universität Hamburg, Jun 2004.

[75] F. Jacquet and A. Blondel, *Report from the Study Group on Detectors for Charged Current Events*, in Proc. of the Study for an ep Facility for Europe, edited by U. Arnaldi, (1979) 377, DESY-79-048.

[76] H1 Collaboration, S. Aid *et al.*, *Measurement of the Total Photon-Proton Cross-Section and its Decomposition at 200 GeV Center-of-Mass Energy*, Z. Phys. **C69** (1995) 27, arXiv:hep-es/9509001.

[77] G. Flucke, *Photoproduction of D^* Mesons and D^* Mesons Associated with Jets at HERA*, Dissertation, Universität Hamburg, Jun 2005.

[78] R. Barlow and C. Beeston, *Fitting Using Finite Monte Carlo Samples*, Comp. Phys. Comm. **77** (1993) 219.

[79] *https://www-h1.desy.de/icgi-trigger/trigchange.cgi*

[80] M. Milite, *The Internal Structure of Charmed Jets in Photoproduction at HERA and Tests of the ZEUS Microvertex Silicon Sensors*, Dissertation, Universitäet Hamburg, May 2001.

[81] B. Reisert, *Elektron-Proton-Streuung bei hohen Impulsüberträgen am H1-Experiment*, Dissertation, University München, December 2000.

[82] H1 Collaboration, *Measurement of Beauty and Charm Photoproduction at H1 using inclusive lifetime tagging*, proceedings of the DIS 2005, Madison, Wisconsin, USA.

[83] T. Sjöstrand, *PYTHIA 5.7 and JETSET 7.4 Physics and Manual*, LU TP 95-10, December 1998, hep-ph/9508391.

[84] R. Lemrani-Alaoui *Prompt photon production at HERA*, Dissertation, University Hamburg, March 2003.

[85] H1 Collaboration, A. Aktas *et al.*, *Measurement Charm and Beauty Photoproduction at HERA using $D^*\mu$ Correlations*, arXiv:hep-ex/0503038.

[86] H1 Collaboration, C. Adloff *et al.*, *Measurement of D^* Meson Cross Sections at HERA and Determination of the Gluon Density in the Proton using NLO QCD*, Nucl. Phys. **B545** (1999) 21, arXiv:hep-ex/9812023.

[87] H1 Collaboration, *Inclusive $D^{*\pm}$ Meson and Associated Dijet Production in Deep-Elastic Scattering*, ICHEP04, Beijing.

[88] M. Vazquez, *Jet Production in CC DIS at HERA*, Dissertation, Madrid University, March 2003.

[89] R. A. Fisher, *The Use of Multiple Measurements in Taxonomic Problems*, Annals of Eugenics **7**, (1936) 179.

[90] G. Cowan, *Statistical Data Analysis*, Clarendon Press, Oxford, 1998.

[91] L. Sonnenschein, *Untersuchung Interner Jet-Struktur in Tief-Inelastischer Streuung im H1-Experiment*, Diploma, III. Phys. Inst. RWTH Aachen, January 1998.

[92] *Open Heavy Quark Production*, MC generators for HERA physics workshop, Proceedings of the workshop 1998/99.

[93] G. P. Lepage, *A New Algorithm for Adaptive Multidimensional Integration*, Journal of Comp. Phys. **27** (1978) 192.

[94] S. Frixione, M. L. Mangano, P. Nason, G. Ridolfi, *Improving the Weizsäcker-Williams Approximation in Electron-Proton Collisions*, Phys. Lett. **B319** (1993) 339, arXiv:hep-ph/9310350.

[95] HZTOOL, `http://www.desy.de/~carli/hztool.html`.

[96] M. Martišíková, *About FMNR Program*, H1 internal document.